Surface characteristics scheme for the neutron transport equation in extruded and non-conformal 3D geometries

Arthur Le Bars

université PARIS-SACLAY

Surface characteristics scheme for the neutron transport equation in extruded and non-conformal 3D geometries.

Schéma aux caractéristiques de surface pour l'équation du transport de neutrons dans des géométries 3D extrudées et non conformes

Thèse de doctorat de l'université Paris-Saclay

École doctorale n°576, particules, hadrons, énergie et noyau : instrumentation, imagerie, cosmos et simulation (PHENIICS)
Spécialité de doctorat : Physique Nucléaire
Graduate School : Physique. Référent : Faculté des sciences d'Orsay

Thèse préparée dans l'unité de recherche
Service d'Études des Réacteurs et de Mathématiques Appliquées
(Université Paris-Saclay, CEA),
sous la direction de **Sandra DULLA**, Professeure
et le co-encadrement de **Simone SANTANDREA**, Ingénieur-chercheur

Thèse soutenue à Paris-Saclay, le 06 décembre 2024, par

Arthur LE BARS

Composition du jury

Membres du jury avec voix délibérative

Bruno DESPRES Professeur, Laboratoire Jacques-Louis Lions	Président
Alain HEBERT Professeur, Polytechnique Montréal	Rapporteur & Examinateur
Benoit FORGET Professeur, Massachussets Institute of Technology	Rapporteur & Examinateur
Jean RAGUSA Professeur, Texas A&M University	Examinateur
Cheikh M. DIOP Professeur, CEA Saclay	Examinateur

THESE DE DOCTORAT

NNT : 2024UPASP162

université PARIS-SACLAY

ÉCOLE DOCTORALE
Particules, hadrons, énergie et noyau : instrumentation, imagerie, cosmos et simulation (PHENIICS)

Titre : Développement d'un schéma aux caractéristiques surfaciques pour la résolution de l'équation du transport de neutrons

Mots clés : transport de neutrons, méthode des caractéristiques, accélération synthetique DP_n, schéma d'ordre supérieur, géométries 3D extrudées

Résumé : Le travail de la thèse se compose de deux parties. La première partie se focalise sur le développement d'un schéma (transport + accélération) aux caractéristiques linéaire surfacique pour la résolution de l'équation du transport sur des géométries 3D extrudées. À présent, seule l'approximation constante peut être utilisée. La différence entre les deux méthodes réside dans le fait que pour l'une la vitesse de convergence au maillage est linéaire (approximation constante) alors qu'elle est quadratique pour l'autre méthode (approximation surfacique linéaire). Pratiquement, la dernière méthode permet de réaliser des calculs avec une même précision qu'avec l'approximation constante tout en réduisant le nombre de mailles, et donc le temps de calcul. Le schéma doit aussi permettre de développer le flux sur une base polynomiale dans la direction axiale, et les sections efficaces ; ce qui importe si l'on veut faire des calculs en évolution. Notez que contrairement à la plupart des approximations linéaires, la source, dans ce schéma, est définie sur les surfaces verticales des régions de calcul. La valeur de la source sur les surfaces horizontales est obtenue à partir d'une interpolation linaire au vol entre les valeurs définies sur les surfaces verticales. L'avantage de cette approche est de pouvoir se débarrasser de l'intégration par le traçage des grandeurs définies sur les surfaces horizontales.

Un bilan sur les moments volumiques du flux angulaire est utilisé pour tester la convergence des itérations internes. A cette fin, un opérateur géométrique est définie de manière à construire une source volumique à partir de la source surfacique. La conservation par région est forcée par correction.

Concernant l'accélération du transport, le choix a été fait d'implémenter une accélération synthétique de type DP_n. La méthode repose sur le développement sur la base des harmoniques sphériques du flux angulaire définie sur les surfaces d'une région de calcul mais peut être vu comme un préconditionnement d'un schéma itératif de type Richardson. Plusieurs arguments motivent ce choix . Le rayon spectral de l'opérateur associé à l'accélération est inférieur à d'autres accélérations comme la diffusion synthetic acceleration (DSA) ou des accélérations non-lineaires de type Coarse mesh finite difference (CMFD), y compris pour des milieux à fort chemins optiques. Par ailleurs, la construction du système d'équation repose sur la même discrétisation spatiale que le transport et limite la nécessité d'une normalisation de certaines grandeurs d'intérêts qui pourraient apparaître avec d'autres méthodes. Enfin, l'utilisation de la forme intégrale du transport rend la méthode attractive pour son utilisation sur des configurations géométriques complexes et des maillages non-structurées.

La seconde partie porte sur la correction d'instabilités numériques qui apparaissent lorsque l'on augmente l'ordre de développement spatial du flux. En milieu homogène infini, le terme de fuite issue de l'équation intégro-différentielle doit être nul. Ce n'est pas le cas pour des régions de calcul où la quantité de cordes avec un chemin optique suffisamment faible dépasse une certaine limite. Ce phénomène pénalise la convergence des méthodes du TDT-MOC et la rend impossible s'il est trop important.

Ces travaux sont vérifiés sur différentes configurations géométriques.

Title: Development of a surface characteristics scheme for solving the neutron transport equation

Keywords: neutron transport, characteristics method, DP$_n$ synthetic acceleration, higher order scheme, 3D extruded geometries

Abstract: The thesis work consists of two parts. The first part focuses on developing a linear surface characteristics scheme (transport + acceleration) for solving the transport equation on extruded 3D geometries. Currently, only the constant approximation can be used. The difference between the two methods lies in the fact that the convergence speed for the mesh is linear (constant approximation) for one, whereas it is quadratic for the other method (linear surface approximation). Practically, the latter method allows calculations with the same accuracy as the constant approximation while reducing the number of meshes, and thus the computation time. The scheme should also allow the flux to be developed on a polynomial basis in the axial direction, as well as cross sections, which is important for depletion calculations. Note that unlike most linear approximations, the source in this scheme is defined on the vertical surfaces of the calculation regions. The value of the source on the horizontal surfaces is obtained from an on-the-fly linear interpolation between the values defined on the vertical surfaces. The advantage of this approach is to eliminate the need for tracking-based integration of quantities defined on the horizontal surfaces.

A balance on the volume moments of the angular flux is used to test the convergence of the inner iterations. To this end, a geometric operator is defined to construct a volume source from the surface source. Conservation per region is enforced by correction.

Regarding transport acceleration, the choice was made to implement a DP$_n$-type synthetic acceleration. The method is based on the spherical harmonics expansion of the angular flux defined on the surfaces of a calculation region but can be seen as a preconditioning of a Richardson-type iterative scheme. Several arguments motivate this choice. The spectral radius of the operator associated with the acceleration is lower than other accelerations such as diffusion synthetic acceleration (DSA) or nonlinear accelerations like Coarse Mesh Finite Difference (CMFD), including for media with high optical paths. Furthermore, the construction of the equation system relies on the same spatial discretization as the transport and limits the need for normalization of certain quantities of interest that might appear with other methods. Finally, the use of the integral form of transport makes the method attractive for use in complex geometric configurations and unstructured meshes.

The second part deals with correcting numerical instabilities that appear when increasing the spatial development order of the flux. In an infinite homogeneous medium, the leakage term from the integro-differential equation should be zero. This is not the case for calculation regions where the number of chords with sufficiently low optical paths exceeds a certain limit. This phenomenon penalizes the convergence of TDT-MOC methods and makes it impossible if it is too significant.

These works are verified and tested on different geometric configurations.

A mes parents,

Remerciements

La thèse ne s'est pas faite toute seule et il serait exagéré de dire que le mérite associé au titre de docteur revient uniquement au thésard travaillant seul dans son bureau. En ce sens, je tiens à remercier les personnes qui ont contribué au bon déroulement de cette thèse.

Je remercie les chefs de service et les chefs de laboratoire du SERMA et du LLPR pour m'avoir permis de réaliser cette thèse au CEA. Je remercie mes deux rapporteurs, Benoit Forget et Alain Hebert, pour l'attention portée à mon manuscrit, ainsi que pour vos remarques et propositions de corrections. Je remercie mes trois examinateurs, Bruno Despres, Cheick Diop et Jean Ragusa, d'avoir accepté de faire partie de mon jury. Je suis fier d'avoir défendu ma thèse devant vous cinq.

Je remercie ma directrice de thèse, Sandra Dulla, d'avoir accepté de diriger la thèse. Je remercie Simone Santandrea, mon encadrant, pour m'avoir donné l'occasion de travailler avec lui, pour m'avoir partagé ses connaissances et pour m'avoir soutenu lorsque j'en avais besoin.

Je remercie les doctorants pour les discussions, les cafés pas très bons, les repas à 11h30 et ceux du soir au CEA. Je pense aussi aux quelques bars et aux quelques pressions qui m'auront permis de faire diminuer, la pression. Certaines rencontres transforment et vous font voir les choses différemment.

Je souhaite aux prochains doctorants tout le courage nécessaire à la réussite de leur thèse. Le désespoir est à regarder droit dans les yeux et à tordre par le travail. Croyez en vous !

Table of Contents

List of Figures

List of Tables

1 - Introduction

The general objective of this thesis work is to improve numerical simulations for solving neutron transport in extruded and unstructured 3D geometries.

1.1 . From fission to nuclear power plants

The nuclear industry as we know it today is based on discoveries made less than a century ago. The beginning of neutron reactor physics can be traced back to the 1930s. Leo Szilard envisioned the nuclear chain reaction in 1933 and patented the idea of the first nuclear reactor based on thermal neutrons in 1936. At the end of 1938, Otto Hahn and Fritz Strassmann discovered nuclear fission from an experimental perspective, while Lise Meitner and Otto Frisch provided its theoretical interpretation in 1939. [9, 10]. A few months before the start of World War II, the two physicists demonstrated that lighter chemical elements could be obtained from uranium bombarded with neutrons. A year later, in 1939, the French scientist Joliot-Curie understood that multiple neutrons are emitted as a result of this reaction. These two discoveries are fundamental as they paved the way for the birth of this industry: the fission reaction emits several neutrons that can in turn be absorbed by fissile nuclei – such as uranium-235 – leading to subsequent fissions. Knowing this, it became conceivable to construct a reactor capable of sustaining these chain reactions. This was the bold vision of severals physicists and engineers of the time. By the 1940s, the design of the first nuclear reactor had commenced [11].

It is interesting to note that fissile nuclei are a dense source of energy. For example, the fission of a uranium-235 nucleus releases around 200 MeV of energy [12]. While 200 MeV may not seem significant to many, to put this into a more tangible context, with so much energy released by reaction, the energy needs of one person for a year are satisfied with just 6g of natural uranium. This result is obtained by applying the formula (1.1) and the numerical values considered for the calculation are listed below.

$$m_g = \frac{\rho \times Q n_a}{\eta \times \mathrm{E} \xi \mathcal{N}_a}, \tag{1.1}$$

with

- $\rho = 238\,\mathrm{g.mol}^{-1}$: Molar mass of natural uranium.
- $Q = 10,000\,\mathrm{J}$: Daily energy consumption per individual.
- $n_a = 365$: Number of days in a year.
- $\eta = 0.7\,\%$: Enrichment of natural uranium in uranium-235.
- $\mathrm{E} = 200$ MeV: Energy released by the fission of one uranium-235 nucleus.
- $\xi = 1.602 \times 10^{-19}$: Number of joules per eV.
- $\mathcal{N}_a = 6.02 \times 10^{23}\,\mathrm{mol}^{-1}$: Number of particles per mole (Avogadro's number).

— m_g: Mass of natural uranium consumed in one year by an individual with a daily energy consumption of Q.

This is very little compared to other energy sources such as coal or gas. These arguments, although not exhaustive, partly justify the construction of nuclear reactors that has taken place up to the present day.

Since the post-war years, several reactor technologies have been developed. In this thesis, we will limit our study to Pressurized Water Reactors (PWRs) [13].

If we now want to simulate these reactors numerically, it is necessary to understand how they operate. We can start by noting that they consist of three thermohydraulic circuits: the primary circuit, the secondary circuit, and the tertiary circuit. Water at 320°C, kept in a liquid state under a pressure of 155 bar and heated by the nuclear reactions occurring in the reactor core, circulates in the primary circuit. Heat is then transferred through a steam generator to the secondary circuit. The produced steam powers a turbine, which, coupled with an alternator, generates the electricity distributed to the grid. Finally, the cooling circuit supplies cold water to the condenser, which re-liquefies the steam from the secondary circuit before it passes through the steam generator again [13].

In the context of this thesis, we focus particularly on the simulation of neutron transport. Therefore, it is essential to model the reactor core. Several types of PWRs are in operation in France, but for the purpose of this example, we will focus on the design of the European Pressurised Reactor (EPR), intended to replace first and second generation reactors. The core geometry is as follows: the core consists of 241 fuel assemblies. Each fuel assembly can be seen as a 17×17 Cartesian grid of fuel cells composed of fuel, void, a zircaloy cladding, and water. There are seven types of assemblies with different enrichments in uranium-235. The assemblies, with a width of 21.4 cm and an active height of 420 cm, are composed of 265 fuel pins and 24 guide tubes. The pin pitch is 1.2598 cm [13, 14]. A diagram showing the three scales (core, assembly, and fuel cell) is proposed in figure 1.1.

It is well understood that multiple physical phenomena interact within such a system: the heat generated from fission causes the materials to expand, changes in the core temperature alter the water density and modify the absorption probabilities (the Doppler effect [15]), neutrons weaken the materials of the reactor vessel, and so on. Research reactors have been constructed to characterize these interactions. In France, notable examples include the **Osiris** and **Cabri** reactors. However, it is important to note that these experiments are costly, time-consuming, and the advent of computers allows a significant portion of these studies to be replaced by numerical simulations.

1.2 . Numerical methods for reactor physics

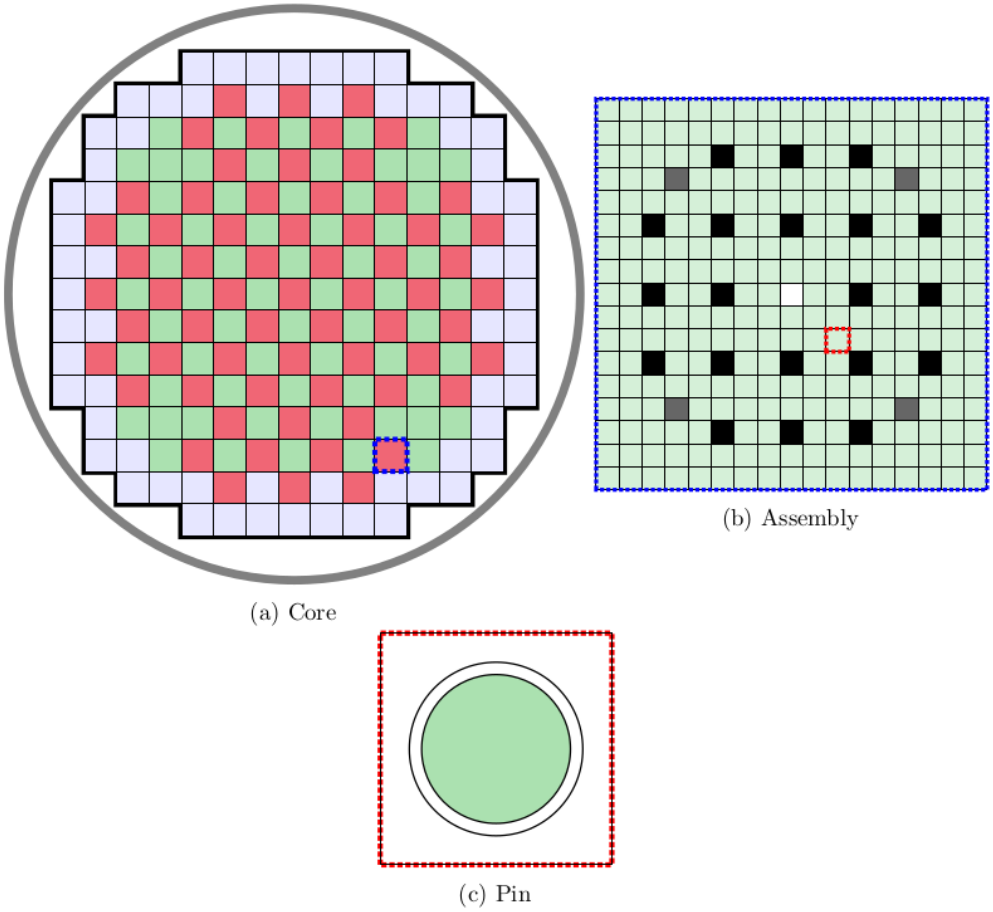

Figure 1.1 – Scheme of a Pressurized Water Reactor core. The core (a) is composed of assemblies (b), which in turn consist of fuel cells (c) [1].

Thus, for a given nuclear reactor, with its geometry and material composition, the focus is on determining the distribution of the neutron population in space, energy, and direction, and its depletion over time. To this end, certain physical quantities such as the neutron flux distribution (proportional to neutron density), neutron disappearance (absorption), and neutron production are particularly examined. These quantities will be defined in the main body of the manuscript. What is important to understand from the outset is that this information is obtained from solving the neutron transport equation—also known as the neutron formulation of the Boltzmann equation, an integro-differential problem that can be viewed as a local balance. Thus, the entire effort revolves around solving this equation. However, even though analytical solutions exist for simple cases, such as in an infinite homogeneous medium, most of the time analytical resolution of the equation is not feasible.

To circumvent this issue, numerical solution methods are employed and consolidated into a set of interconnected algorithms known as computational codes. Today, two families

of codes exist. On one side, there are stochastic Monte Carlo codes, and on the other side, deterministic codes.

Monte Carlo codes obtain a solution to the neutron transport equation by simulating a large number of particles governed by probabilistic analog laws. They rely on two fundamental results: **the law of large numbers** and **the central limit theorem** [16]. TRIPOLI-4® [17], TRIPOLI-5® [18], MCNP® [19, 20], OpenMC® [2], and Serpent-2® [21] are examples of such codes.

Deterministic codes, unlike probabilistic codes, do not rely on stochastic processes but rather on linear algebra. The neutron transport equation is formulated as a generalized eigenvalue problem and solved using direct or iterative numerical methods developed for this type of problem. More specifically, the first step involves transforming the continuous energy problem into a multi-group problem consisting of several equations defined over an energy interval. The problem data are then energy-condensed before solving the transport equation. The first step is handled by self-shielding algorithms, and the second by flux solvers. Finally, it is important to note that, unlike Monte Carlo codes, the self-shielding step introduces errors in deterministic calculations.

Several approaches exist for performing core calculations. The most direct approach involves conducting an (accelerated) transport calculation applied to the entire reactor, known as **whole core calculations**. Examples capable of this include OpenMOC® [22, 23], DeCART® [24, 25], and nTRACER® [26, 27], MOCkingbird® [28]. However, industrial practices often prefer a **two-step calculations** approach where multiple lattice calculations are repeated for various state parameters (such as burn-up, temperature, boron concentration, void fraction) to generate multi-parameter libraries used in diffusion core calculations. APOLLO3® [29, 30], DRAGON® [31], and CASMO5® [32, 33] are examples of codes that utilize this approach.

1.3 . APOLLO3® platform

APOLLO3® is a deterministic transport code developed at CEA in collaboration with EDF and Framatome since 2007 [34]. A portion of the code integrates algorithms inherited from CEA codes of previous generation. From the perspective of the two-step scheme used by industry, the code is structured into two main parts:

- A lattice physics part consisting of self-shielding methods, flux solvers and homogenization and condensation [35] part for macroscopic reaction rates and diffusion parameter calculations. The self-shielding methods currently available in APOLLO3® for thermal reactors include the equivalence-based method [36] and subgroup methods [37, 38]. The lattice flux solvers currently available in APOLLO3® are NYMO [39, 40, 41, 42], IDT [43, 44, 45, 46, 47], and TDT [48, 49, 50, 51, 6, 7].
- A core part consisting of various solvers: Minos [52], Minaret [53, 54], and NYMO.

The method developed during the thesis has been implemented within the TDT solver.

1.4 . TDT solver

The TDT solver utilizes the Method of Characteristics (MOC) or the collision probability method (Pij) to solve the neutron transport equation from its integral form. The treatment of the angular variable relies on the S_n method, which discretizes the unit sphere into a finite number of directions. An assumption about the spatial variation of the neutron source is necessary to evaluate the integral numerically. Several approximations are available in TDT. In two dimensions, constant (SC) [48] and linear surface (LS) approximations are available [55, 49]. In three dimensions, a polynomial approximation in the axial direction is available for both the source and cross sections [56, 57]; radially, the source is assumed constant.

A synthetic acceleration method known as DP$_n$, based on spherical harmonic expansions of the angular flux on surfaces within a calculation region, is also available in the solver for the same approximations used in transport [58, 50, 59].

Efforts have also been made to reduce memory usage associated with tracking. Two techniques include chords classification and hit surface sequence optimization [5]. Shared-memory parallelism using OpenMP has been implemented to reduce computation times [60]. Finally, the solver can handle both structured and unstructured 3D meshes using the ALAMOS® API [61].

The thesis work focuses on three main points:
- Extending the linear surface scheme for handling 3D extruded geometries, with the capability to develop the source using a polynomial basis in the axial direction.
- Extending coherent surface acceleration alongside transport.
- Reformulating the transmission equation for chords with low optical path lengths to preserve numerical stability of the power iteration method.

These developments aim to perform calculations with a certain precision on reaction rate distributions for a given machine memory and operation frequency, while reducing computational mesh density without increasing computation times. This capability would make it easier to process larger geometries, such as MOX assembly surrounded by UOX assemblies. Such calculations could produce homogenized and condensed diffusion coefficients and cross sections that more accurately represent core heterogeneities. Therefore, the present utilisation context of TDT is that of two-step core calculation or to produce benchmark results in small dimensional cases.

1.5 . Structure of Thesis

The thesis structure is detailed below.

Chapter 2: In this chapter, the reactor physics concepts necessary for understanding the manuscript are introduced. The chapter details some properties of neutrons and their interactions with matter in a Pressurized Water Reactor (PWR), before introducing important quantities of interest and the Boltzmann equation applied to neutrons.

Chapter 3: Chapter 3 introduces the multi-group transport equation and summarizes various deterministic methods for solving the transport equation. The chapter focuses particularly on the Method of Characteristics used in the thesis. A bibliography of different known codes using this method is also provided at the end of the chapter.

Chapter 4: Chapter 4 details the specific features of the TDT solver. It briefly reviews how 3D tracking is performed in the solver. Subsequently, the different approximations available for the neutron flux and source are specified. Some important results and properties of the existing schemes are also recalled.

Chapter 5: Chapter 5 specifies important approximations of the linear surface transport scheme: linear variation of the source between two surfaces of a region in the radial direction, and polynomial variation of the source in the axial direction. Based on these assumptions, the numerical expressions of the transmission and conservation equations are specified.

Chapter 6: Chapter 6 begins with a comparison of acceleration methods used to reduce the convergence time of transport schemes. This justifies the implementation of the DP$_n$ acceleration. Finally, the equations specific to this acceleration and adapted to the assumptions of the transport scheme are detailed.

Chapter 7: Chapter 7 validates the transport scheme on a 3x3 PWR mini-assembly. It shows that the scheme converges to the mesh more rapidly than the scheme where the source is assumed constant per region. Additionally, it demonstrates that numerical divergence may appear when the polynomial development in the axial direction exceeds 1.

Chapter 8: Chapter 8 details the theoretical solution that stabilizes numerical divergence when the order of spatial development in the axial direction increases. The issue is treated in the case of a radially uniform angular flux.

2 - Modelling neutron transport for reactor physics problems

In order to model the neutron population in a reactor, it is essential to understand its properties and modes of interaction with the fuel and structural materials present in the core. It is only through this study and the defined assumptions that we can construct a theoretical model of the system we seek to comprehend.

This is the focus of this chapter. We begin by justifying some approximations, then we introduce the phase space before defining the concept of cross sections, which are used to model neutron-matter reactions in a nuclear reactor. Finally, the Boltzmann equation applied to neutron transport is introduced. The deterministic methods for solving the equations are detailed in Chapter 3.

Contents

2.1 . Generalities

2.1.1 . Preliminary approximations

The neutron is a subatomic particle, electrically neutral, that composes the atomic nucleus alongside the proton. Its mass is 1.674×10^{-27} kg, and its mean lifetime is 878.4 seconds. Various nuclear reactions emit neutrons: nuclear fusion, $\beta-$ decay, neutron emission, spontaneous fission, and induced fission [62].

Induced fission of uranium-235 is the most important reaction for PWRs ; it is the primary source of neutrons, with an average of 2.47 neutrons emitted per reaction, and energy. The neutrons are emitted with an energy that follows a specific probability density. Experimental measurements have allowed for an analytical expression of these probabilities. The Watt spectrum shown in figure (2.1) is an example [63, 64]. For uranium, the analytical expression of the spectrum is:

$$\chi(\mathrm{E}) = 0.484 \mathrm{sinh}(\sqrt{2\mathrm{E}})\, e^{-\mathrm{E}}\ \mathrm{MeV}^{-1} \tag{2.1}$$

Thus, it can be shown that the average energy of a neutron resulting from the fission of

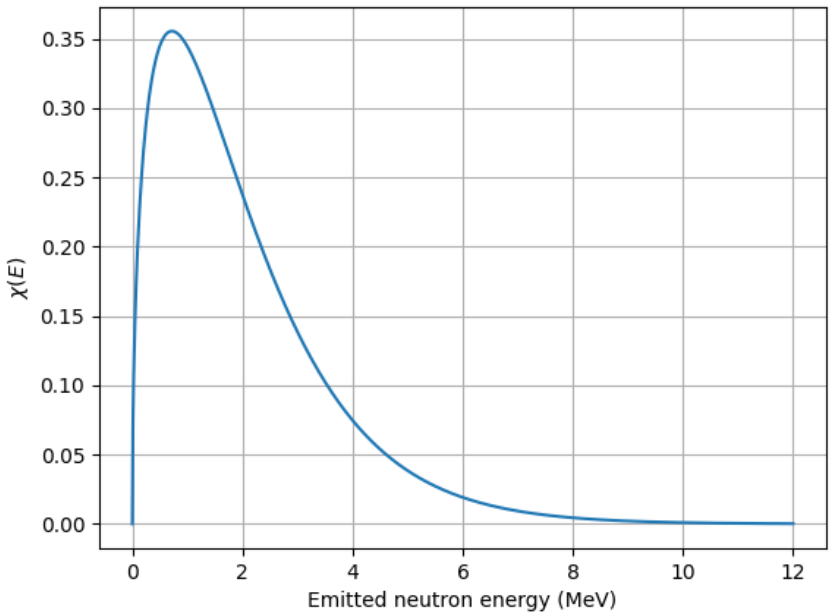

Figure 2.1 – Thermal fission spectrum for uranium-235, approximated by the Watt formula (2.1).

uranium-235 is 1.98 meV. Investigating the properties of the particle in a reactor allows for a better understanding of its behavior. For example, in a thermal reactor, it is known that the majority of neutrons ranges from energies between meV and hundreds of eV, knowing that the equilibrium thermal energy is 0.025eV. These two bounds correspond to the energies of fission neutrons and thermal neutrons, respectively. This is depicted in figure (2.2), where the neutron flux spectrum, proportional to the neutron density, is plotted for a PWR cell. It is observed that neutrons are most prevalent at fission energies and thermal energies. The spectrum is calculated from an OpenMC [2] data set.

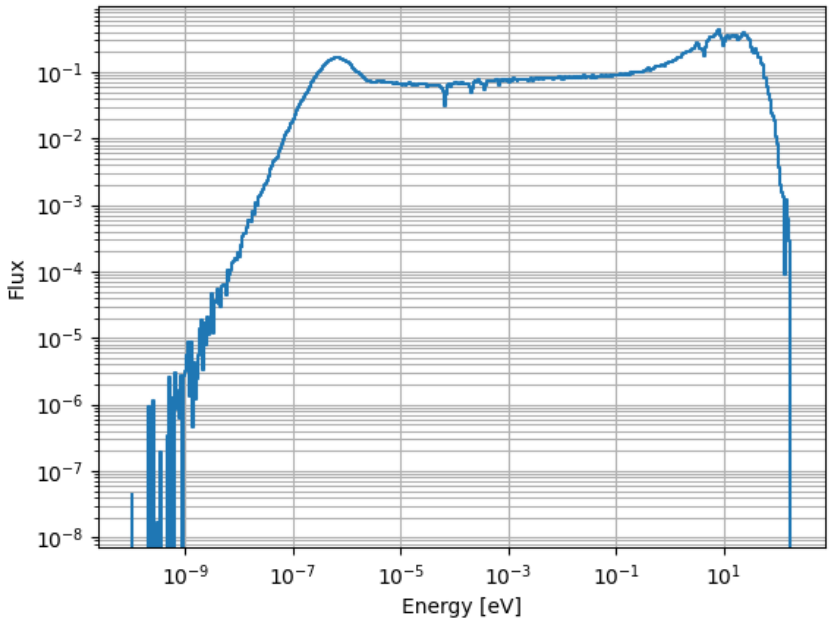

Figure 2.2 – Neutron spectrum for a PWR cell calculated with OpenMC [2]. The flux is normalized per source particle simulated.

Moreover, it is interesting to compare the volumetric density of neutrons and atoms in a thermal reactor. If we consider a reactor with a flux of 10^{16} cm$^{-2}\cdot$ s^{-1}, then it can be shown that the volumetric density of neutrons is on the order of 10^{11} cm^{-3}. This is small compared to nuclear densities, which are on the order of 10^{22} nuclei cm^{-3} in solids. The numerical values are taken from Bell and Glasstone [65]. Thus, **neutron-neutron interactions can be neglected**.

2.1.2 . Phase space

A priori, a neutron is defined by its position, its velocity (i.e., its direction and energy), and the time t at which the state of the reactor is observed. To characterize the distribution of the neutron population within a reactor, one uses a Cartesian coordinate system $\mathcal{R}$. The particle

position in space is expressed as follows:

$$\boldsymbol{r} = x\boldsymbol{e}_x + y\boldsymbol{e}_y + z\boldsymbol{e}_z, \tag{2.2}$$

with $\boldsymbol{e}_x$, $\boldsymbol{e}_y$, and $\boldsymbol{e}_z$ being the canonical vectors of $\mathbb{R}^3$, and x, y, z representing the coordinates of the point $\boldsymbol{r}$. The direction $\boldsymbol{\Omega}$ belongs to the unit sphere $\mathbb{S}_2$, defined as the set of unit vectors in space.

$$\mathbb{S}_2 = \left\{(x, y, z) \in \mathbb{R}^3, x^2 + y^2 + z^2 = 1\right\}. \tag{2.3}$$

Each solid angle in $\mathbb{S}_2$ is parameterized by an azimuthal angle $\varphi \in [0, 2\pi]$ and a polar angle $\theta \in [0, \pi]$. For simplicity, we may write $\boldsymbol{\Omega} = (\varphi, \theta)$ when convenient. We denote by $\mathbb{S}_{2+}$ (respectively, $\mathbb{S}_{2-}$) the set of directions for which $\theta \in [0, \pi/2[$ (respectively, $\theta \in [\pi/2, \pi]$). A graphical representation of the Cartesian coordinate system is provided in figure (2.3). Finally, it may be useful to define the differential element $\mathrm{d}^2\Omega$ for integral calculations. It is expressed as follows:

$$\mathrm{d}^2\Omega = \sin(\theta)\mathrm{d}\theta\mathrm{d}\varphi \tag{2.4}$$

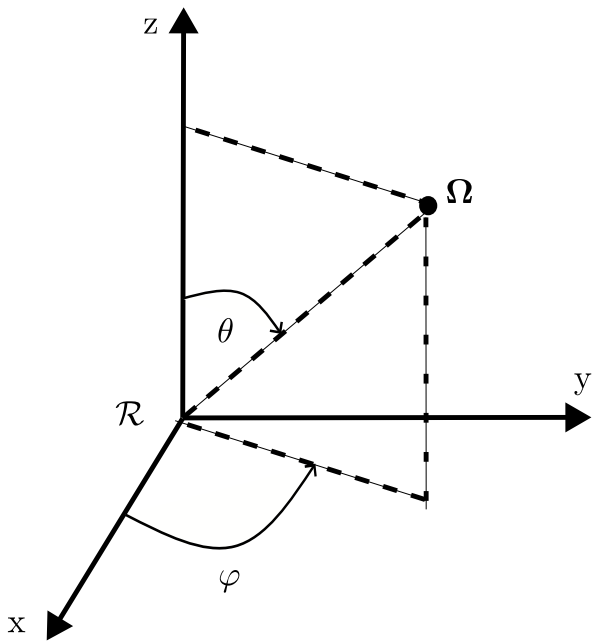

Figure 2.3 – Parametrization of the solid angle $\boldsymbol{\Omega}$ in the Cartesian coordinate system $\mathcal{R}$.

2.2 . Overview of nuclear reactions

The neutron-matter interaction occurs through nuclear reactions. The reactions that most significantly impact on the neutron population in a thermal reactor are listed in figure (2.4).

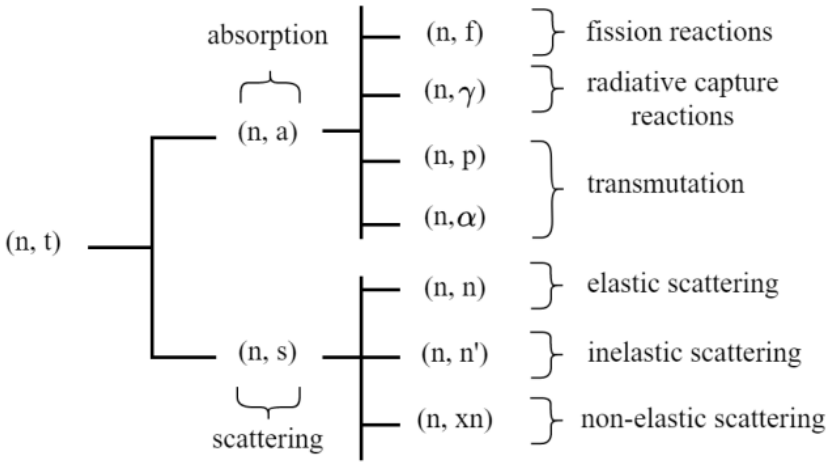

Figure 2.4 – Main nuclear reactions considered in a nuclear power plant [3].

Elastic scattering (n,n): Elastic scattering can be viewed as a collision between two billiard balls. The incident neutron with direction $\mathbf{\Omega}'$ and energy E' is scattered into the direction $\mathbf{\Omega}$ with energy E.

Non-elastic scattering (n,xn): In such reactions, it is not just one, but x neutrons that are emitted from the reaction.

Fission (n,f): A fission reaction is defined as a process in which the absorbing nucleus disintegrates into two fission fragments, with the emission of photons and neutrons. Some of these fission fragments, known as precursors, will in turn emit a small fraction of neutrons referred as delayed. For instance, in the case of uranium-235 fission, only 660 pcm of neutrons are emitted in a delayed manner. Neutrons emitted directly from the fission reaction are called prompt neutrons. On the other hand, neutrons emitted by the precursors are referred to as delayed neutrons.

Radiative capture (n,γ): Radiative capture reactions are those in which the absorbing nucleus de-excites by emitting a photon.

Physically, these reactions are modeled by probability densities known as microscopic cross sections, denoted by σ. Their unit is the barn, with the relation $1\,\text{barn} = 10^{-24}\,\text{cm}^2$. Typically, cross sections are indexed according to the type of reaction considered. Thus, σ_s,

σ_a, and σ_f denote the cross sections for scattering, absorption, and fission, respectively.

The profiles of the fission, elastic scattering, and capture cross sections at $293\mathrm{K}$ are plotted in figures (2.5) and (2.6) for uranium-235 and uranium-238, respectively. The data are sourced from the JEFF3.3 library and were obtained in CSV format from the JANIS website. Upon examining these images, several observations can be made. Firstly, it is evident that our attention is drawn to the regions where the cross sections vary significantly over a narrow energy range. These large amplitude variations characterize the resonances in the cross sections. For a more detailed understanding of the origin of these resonances, additional explanations can be found in Chapter 2 of Alain Hébert's book [66]. This behavior must be accounted for in deterministic calculation schemes, where the energy range is discretized into several groups (see section 3.1).

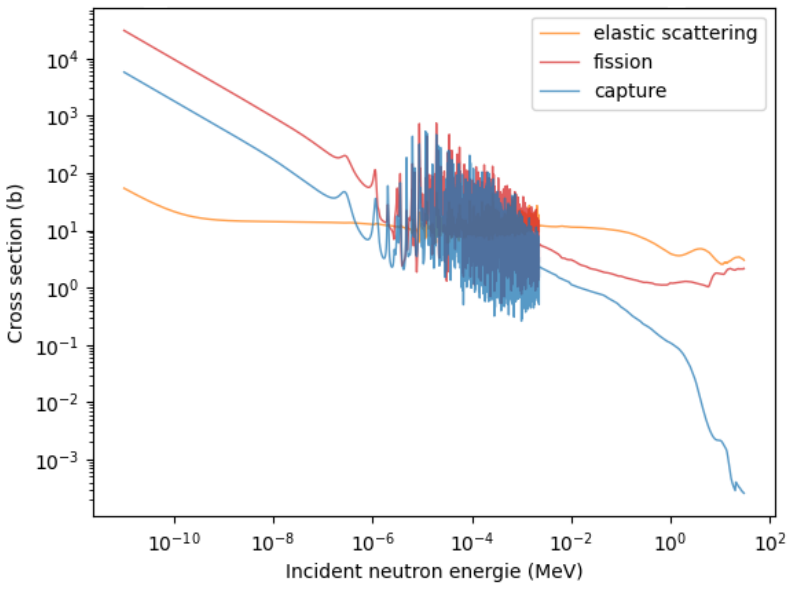

Figure 2.5 – Microscopic fission, elastic scattering and capture for uranium-235 at $293\,\mathrm{K}$.

Furthermore, note that, for thermal energies, the ratio σ_f/σ_c is much greater than 1 for uranium-235. This is not the case for uranium-238; around $0.1,\mathrm{eV}$, $\sigma_f/\sigma_c \simeq 10^{-06}$. However, the ratio becomes greater than unity around the MeV range. This difference between fissile isotopes, that are in average "multiplicative", and other that remain "absorbent", makes the enrichment of the fissile species necessary as it is done customarily in the industry.

Finally, the energy range is typically divided into three regions, from the lowest to the highest energies: the resolved low-energy region, the unresolved region up to intermediate energies, and finally the continuous region. Definitions of the different regions are provided

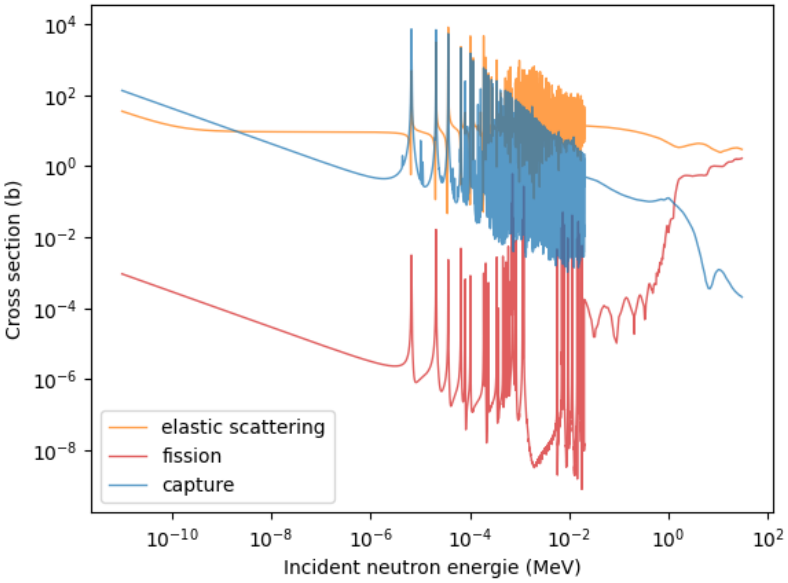

Figure 2.6 – Microscopic fission, elastic scattering and capture for uranium-238 at $293\,\mathrm{K}$.

below:

— **Resolved Resonance Region (RRR)**: At relatively low energies, individual peaks (resonances) can be observed in the energy-dependent cross sections; this energy region is referred to as the "resolved-resonance region."
— **Unresolved Resonance Region (URR)**: At higher energies, the natural widths of the resonances are comparable to their spacing, making it impossible to distinguish one peak from another; this is known as the "unresolved-resonance region."
— **Continuous Region**: The continuous region extends from the end of the unresolved region to higher energies. In this domain, cross sections vary smoothly with energy.

A few definitions now:

Definition: **Total Microscopic Cross Section.** Let i be an isotope and Π a set of neutron-induced reactions. The total microscopic cross section is defined as the sum of the cross sections for the reactions $\rho \in \Pi$:

$$\sigma_{i,t} = \sum_{\rho \in \Pi} \sigma_{i,\rho}. \tag{2.5}$$

In practice, microscopic cross sections are not directly used in the calculation of the transport equation. Instead, macroscopic cross sections are preferred, which are defined as the

product of the microscopic cross sections and the density of the isotope i considered in a given volume, N_i, in cm^{-3}.

Definition: **Partial Macroscopic Cross Section.** Let i be an isotope with density N_i in a given geometry and let ρ be a reaction. The partial macroscopic cross section for isotope i and reaction ρ is defined as the product:

$$\Sigma_{i,\rho} = \mathrm{N}_i \sigma_{i,\rho}. \tag{2.6}$$

It may also be useful to define macroscopic cross sections for an isotopic mixture. The unit of this cross section is cm^{-1}.

Definition: **Macroscopic Cross Section for a Mixture.** Let I be a mixture of isotopes and ρ a reaction. The macroscopic cross section of the mixture for reaction ρ is defined as:

$$\Sigma_\rho = \sum_i \mathrm{N}_i \sigma_{i,\rho}. \tag{2.7}$$

In a manner similar to microscopic cross sections, a total macroscopic cross section Σ_t can be defined for a given isotope by summing the partial cross sections. Additionally, the probability $\mathrm{P}(l)\mathrm{d}l$ that a neutron will travel a distance l before its first collision in a homogeneous medium can be defined as

$$\mathrm{P}(l)\mathrm{d}l = \Sigma_t e^{-\Sigma_t l}\mathrm{d}l. \tag{2.8}$$

Calculating the expectation of this probability density involves determining the mean free path Λ, which represents the average distance a neutron travels before undergoing its first collision.

$$\Lambda = \int_0^{+\infty} \mathrm{d}l \mathrm{P}(l) l = \frac{1}{\Sigma_t}. \tag{2.9}$$

In pressurized water reactors, the mean free path of a neutron in water is on the order of centimeters in the thermal range [67].

2.2.1 . Temperature dependence of microscopic cross sections

As the temperature of the fuel increases, resonances broaden, thereby increasing the probabilities of neutron-matter interactions. This is the case for the resonant absorption of uranium-238 at 6.67 eV, as shown in figure (2.7). This phenomenon is known as the Doppler

effect [15].

If the core temperature increases, capture reactions become, on average, mere significant than fissions and therefore the thermal power decreases. This leads to a temperature reduction. This is referred to as the Doppler feedback. It is an intrinsic safety feature of PWRs.

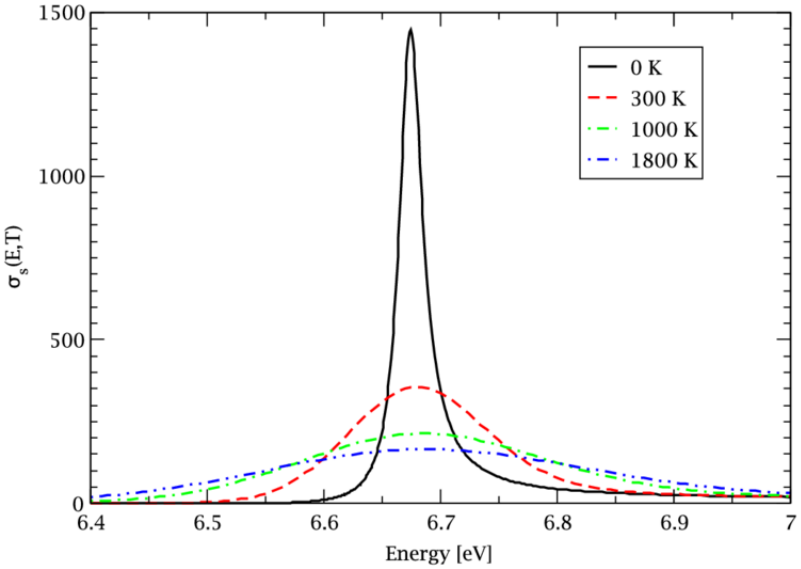

Figure 2.7 – Doppler broadening of the uranium-238 6.67 eV absorption resonance. [4]

2.2.2 . Time dependence of macroscopic cross sections

The set of nuclear reactions and radioactive decays alters the isotopic inventory of the reactor. To model these changes in concentrations, computational codes use so-called depletion solvers. Such a solver finds a solution to the Bateman equation [68], which describes these changes in concentrations. Using the notation from the article [69], the Bateman equation is expressed as follows:

$$\frac{dn_i}{dt}(t) = -(\lambda_i + \tau_{i,i})\, n_i(t) + \sum_{ji}(b_{j,i}\lambda_j + \tau^r_{j,i})\, n_j(t) + \sum_k(\gamma_{k,i} + \tau^f_k)\, n_k(t), \tag{2.10}$$

$$n_i(0) = n^0_i. \tag{2.11}$$

with

- n^0_i : Initial concentration of nuclide i at time $t = 0$
- λ_i : Radioactive decay constant of nuclide i
- $b_{j,i}$: Decay branching ratio from nuclide j to nuclide i
- $\gamma_{k,i}$: Fission product yield from fissile nuclide k to nuclide i

— $\tau_{i,i}$: Disappearance reaction rate of nuclide i due to neutron-induced reactions
— $\tau^r_{j,i}$: Neutron reaction rate from nuclide j to nuclide i
— τ^f_k : Fission reaction rate of nuclide k

Numerically, the equation is solved as a linear system by grouping the concentrations of each nuclide i into a vector $\boldsymbol{n}$. This results in a first-order homogeneous differential equation:

$$\frac{d\boldsymbol{n}}{dt}(t) = \boldsymbol{\Phi}_a(t)\boldsymbol{n}(t), \tag{2.12}$$

$$\boldsymbol{n}(0) = \boldsymbol{n}^0, \tag{2.13}$$

where $\boldsymbol{\Phi}_a$ is the matrix that implicitly encompasses all the pathways for the creation and destruction of isotopes. Historically, equation (2.12) has been solved using a fourth-order Runge-Kutta scheme [70], but other solution methods exist, such as matrix exponential methods or the Chebyshev Rational Approximation Method (CRAM) [71]. In the APOLLO3® code, depletion calculations are performed by sending the flux and cross sections to the depletion solver MENDEL® [72], which solves equation (2.12).

Moreover, macroscopic cross sections vary over time because multi-group microscopic cross sections vary due to the flux variations. Thus, one needs to perform cross section self-shielding (see 3.1.4) as the burn-up increases.

2.2.3 . Space dependence of macroscopic cross sections

As mentioned earlier, the macroscopic cross sections evolve over time due to radioactive decay on one hand, and collisions on the other. The collision terms are functions of the non-uniform flux. Thus, the depletion of isotopic concentrations does not occur uniformly, even for assemblies of the same composition placed symmetrically within the reactor.

2.3 . Neutron transport equation

2.3.1 . Quantities of interest

The cross sections introduced in the previous section determine the behavior of the neutron population in a reactor. However, they do not provide direct information about the depletion of this population. In this section, we introduce the quantities defined to characterize both the local and global depletion of this population.

An important measure is the effective multiplication factor, denoted k_{eff}, which is an integral measure that indicates whether the neutron population in a multiplying system is increasing or decreasing over time. To provide a physical definition of k_{eff}, it can be described

as the ratio of the number of neutrons produced in the $(i+1)^{\text{th}}$ generation of fissions to the number of neutrons produced in the i^{th} generation [73]:

$$k_{\text{eff}} = \frac{\text{Neutrons produced in the fission generation } i+1}{\text{Neutrons produced in the fission generation } i}. \tag{2.14}$$

The quantity can also be defined as the ratio between the neutrons produced and the neutrons that disappear from the considered system. This yields the expression:

$$k_{\text{eff}} = \frac{\text{Production}}{\text{Absorption} + \text{Leakage}}. \tag{2.15}$$

One can distinguish three cases:

- $k_{\text{eff}} < 1$: The reactor is subcritical. The initial neutron population decreases over time.
- $k_{\text{eff}} = 1$: The reactor is critical. The initial neutron population remains constant over time.
- $k_{\text{eff}} > 1$: The reactor is supercritical. The initial neutron population increases over time.

Another important quantity is the neutron distribution in phase space, n, known as the density, which depends on the particle position $\boldsymbol{r}$, direction $\boldsymbol{\Omega}$, energy E, and time t. In practice, it is often preferable to use the angular flux. This quantity is defined as follows.

Definition: **Angular Flux.** The angular flux is defined as the distribution obtained by multiplying the density of the neutrons by their velocity.

$$\psi(\boldsymbol{r}, \boldsymbol{\Omega}, \mathrm{E}, t) = V_{\mathrm{E}}\, n(\boldsymbol{r}, \boldsymbol{\Omega}, \mathrm{E}, t), \tag{2.16}$$

where V_{E} is the velocity of the neutron packet with energy E. Its unit is neutrons $\cdot\, \mathrm{cm}^{-2} \cdot \mathrm{s}^{-1} \cdot \mathrm{sr}^{-1} \cdot \mathrm{eV}^{-1}$. As mentioned in [66], the flux itself does not have a direct physical meaning. However, it is the unknown in the transport equation, as the number of collisions in a small volume per unit time depends on both the density of neutrons in the volume and the amount of neutrons arriving in the volume.

It is also useful to define the angular moments that arise when decomposing the flux using the basis of real spherical harmonics. These functions are defined in Appendix (10.4.2), see 10.42.

Definition: **Angular Moments of the Flux.** The angular moments of the flux are defined as the projections of the angular flux onto the basis of spherical harmonics.

$$\phi_k^l(\boldsymbol{r}, \mathrm{E}, t) = \frac{1}{4\pi} \int_{\mathbb{S}_2} \mathrm{d}\boldsymbol{\Omega} A_k^l(\boldsymbol{\Omega}) \psi(\boldsymbol{r}, \boldsymbol{\Omega}, \mathrm{E}, t). \tag{2.17}$$

The first moment, $\phi_0^0(\boldsymbol{r}, \mathrm{E}, t)$, is commonly referred to as the scalar flux. This quantity appears in the definition of the fission source in equation (2.31). Thus, if we consider an expansion of the angular flux up to order K, we obtain:

$$\psi(\boldsymbol{r}, \boldsymbol{\Omega}, \mathrm{E}, t) = \sum_{k=0}^{\mathrm{K}} \sum_{l=-k}^{k} \phi_k^l(\boldsymbol{r}, \mathrm{E}, t) A_k^l(\boldsymbol{\Omega}). \tag{2.18}$$

Definition: **Angular Current.** The angular current is defined as the quantity:

$$\mathbf{J}(\boldsymbol{r}, \boldsymbol{\Omega}, \mathrm{E}, t) = \boldsymbol{\Omega}\, \psi(\boldsymbol{r}, \boldsymbol{\Omega}, \mathrm{E}, t). \tag{2.19}$$

It is possible to integrate the previous quantity to obtain the outgoing current, which can be viewed as the neutron density leaving the position $\boldsymbol{r}$ through the angle $\boldsymbol{\Omega}$, per unit time.

$$\mathrm{J}^+(\boldsymbol{r}, \mathrm{E}, t) = \int_{\boldsymbol{\Omega}\cdot\boldsymbol{n}>0} \mathrm{d}\boldsymbol{\Omega} (\boldsymbol{\Omega} \cdot \boldsymbol{n}) \psi(\boldsymbol{r}, \boldsymbol{\Omega}, \mathrm{E}, t). \tag{2.20}$$

Definition: **Volumetric reaction rate.** The volumetric reaction rate for reaction ρ and isotope i is defined as the product:

$$\mathrm{T}_{i,\rho}(\boldsymbol{r}, \boldsymbol{\Omega}, \mathrm{E}, t) = \Sigma_{i,\rho}(\boldsymbol{r}, \mathrm{E}) \psi(\boldsymbol{r}, \boldsymbol{\Omega}, \mathrm{E}, t). \tag{2.21}$$

Its unit is the number of reactions $\cdot\, \mathrm{cm}^{-3} \cdot \mathrm{s}^{-1}$ of type ρ involving isotope i. To obtain the total number of reactions within a specific volume, one simply integrates equation (2.21) over the volume V under consideration.

Definition: **Reaction Rate.** The reaction rate for reaction ρ and isotope i is defined as the product:

$$\mathrm{T}_{i,\rho}(\boldsymbol{\Omega}, \mathrm{E}, t) = \int_{\mathrm{V}_i} \mathrm{d}\boldsymbol{r} \Sigma_{i,\rho}(\boldsymbol{r}, \mathrm{E}) \psi(\boldsymbol{r}, \boldsymbol{\Omega}, \mathrm{E}, t), \tag{2.22}$$

which is the number of reactions $\cdot\, s^{-1}$ of type ρ involving isotope i.

2.3.2 . Eigenvalue problem

The transport equation applied to neutrons is a local conservation equation. It can be derived by performing a particle balance over an infinitesimal volume of phase space over a time interval Δt. The general idea is to state that the temporal change in neutron population is the algebraic sum of neutron production and neutron loss. The temporal change can be expressed as:

$$\eta_1 = \left(n(\boldsymbol{r}, \boldsymbol{\Omega}, \mathrm{E}, t + \Delta t) - n(\boldsymbol{r}, \boldsymbol{\Omega}, \mathrm{E}, t)\right) \mathrm{d}\boldsymbol{r}\mathrm{d}\boldsymbol{\Omega}\mathrm{dE}. \tag{2.23}$$

We denote by η_2 the quantity of neutrons that leave the volume $\mathrm{d}\boldsymbol{r}$ during the time interval Δt.

$$\eta_2 = \boldsymbol{\nabla} \cdot \boldsymbol{\Omega}\psi(\boldsymbol{r}, \boldsymbol{\Omega}, \mathrm{E}, t)\mathrm{d}\boldsymbol{r}\mathrm{d}\boldsymbol{\Omega}\mathrm{dE}\Delta t. \tag{2.24}$$

We denote by η_3 the quantity of neutrons that disappear due to collisions during the time interval Δt.

$$\eta_3 = \Sigma_t(\boldsymbol{r}, \mathrm{E})\psi(\boldsymbol{r}, \boldsymbol{\Omega}, \mathrm{E}, t)\mathrm{d}\boldsymbol{r}\mathrm{d}\boldsymbol{\Omega}\mathrm{dE}\Delta t. \tag{2.25}$$

We denote by η_4 the quantity of neutrons that appear in the system during the time interval Δt, due to the neutron source Q.

$$\eta_4 = Q(\boldsymbol{r}, \boldsymbol{\Omega}, \mathrm{E}, t)\mathrm{d}\boldsymbol{r}\mathrm{d}\boldsymbol{\Omega}\mathrm{dE}\Delta t. \tag{2.26}$$

Once all the production and loss terms have been defined, we write that the change η_1 corresponds to the neutron production minus the loss. That is,

$$\eta_1 = -\eta_2 - \eta_3 + \eta_4. \tag{2.27}$$

Thus, by dividing both sides by $\mathrm{d}\boldsymbol{r}\mathrm{d}\boldsymbol{\Omega}\mathrm{dE}\Delta t$ and recalling that the angular flux is defined in terms of neutron density and velocity, we can directly write:

$$\frac{1}{V_{\mathrm{E}}}\frac{\partial}{\partial t}\psi(\boldsymbol{r},\boldsymbol{\Omega},\mathrm{E},t)+\boldsymbol{\Omega}\cdot\boldsymbol{\nabla}\psi(\boldsymbol{r},\boldsymbol{\Omega},\mathrm{E},t)+\Sigma_t(\boldsymbol{r},\mathrm{E})\psi(\boldsymbol{r},\boldsymbol{\Omega},\mathrm{E},t)=Q(\boldsymbol{r},\boldsymbol{\Omega},\mathrm{E},t). \tag{2.28}$$

Throughout the remainder of the thesis, we will assume a steady-state regime where the angular flux no longer depends on time. Thus:

$$\boldsymbol{\Omega}\cdot\boldsymbol{\nabla}\psi(\boldsymbol{r},\boldsymbol{\Omega},\mathrm{E})+\Sigma_t(\boldsymbol{r},\mathrm{E})\psi(\boldsymbol{r},\boldsymbol{\Omega},\mathrm{E})=Q(\boldsymbol{r},\boldsymbol{\Omega},\mathrm{E}). \tag{2.29}$$

We now need to define the neutron source Q. We consider a framework where neutrons appearing in the phase space volume arise either from scattering or fission, with an external source assumed to be zero. Let $\mathcal{H}$ and $\mathcal{F}$ denote the operators for scattering and fission, respectively:

$$\mathcal{H}\psi(\boldsymbol{r},\boldsymbol{\Omega},\mathrm{E})=\int_{\mathbb{S}_2}\mathrm{d}\boldsymbol{\Omega}'\int_0^{+\infty}\mathrm{dE}'\Sigma_s(\boldsymbol{r},\boldsymbol{\Omega}'\to\boldsymbol{\Omega},\mathrm{E}'\to\mathrm{E})\psi(\boldsymbol{r},\boldsymbol{\Omega}',\mathrm{E}'). \tag{2.30}$$

where notations $\boldsymbol{\Omega}'\to\boldsymbol{\Omega}$ and $\mathrm{E}'\to\mathrm{E}$ designates neutrons that scatters on a nuclide with an entering direction and energy, $\boldsymbol{\Omega}'$ and E', and an exiting direction and energy, $\boldsymbol{\Omega}$ and E. Fission reactions can be assumed as isotropic, and the number of emitted neutrons is assumed to be independent of the incident neutron energy. Let χ_i represent the fission spectrum of the fissile nuclide i, which describes the energy distribution of the emitted neutrons, and let n_i denote the number of fissile nuclides. The fission source term can be expressed as:

$$\mathcal{F}\psi(\boldsymbol{r},\boldsymbol{\Omega},\mathrm{E})=\sum_{i=1}^{n_i}\chi_i(\mathrm{E})\int_0^{+\infty}\mathrm{dE}'\nu\Sigma_{f,i}(\boldsymbol{r},\mathrm{E}')\phi_0^0(\boldsymbol{r},\mathrm{E}'). \tag{2.31}$$

The equation is generally written using operators, with the terms related to leakage and collisions grouped under the operator $\mathcal{L}$ such that:

$$\mathcal{L}\psi(\boldsymbol{r},\boldsymbol{\Omega},\mathrm{E})=\boldsymbol{\Omega}\cdot\boldsymbol{\nabla}\psi(\boldsymbol{r},\boldsymbol{\Omega},\mathrm{E})+\Sigma_t(\boldsymbol{r},\mathrm{E})\psi(\boldsymbol{r},\boldsymbol{\Omega},\mathrm{E}). \tag{2.32}$$

The operator $\mathcal{B}$ is defined as the difference between the loss and the scattering terms

$$\mathcal{B}\psi(\boldsymbol{r},\boldsymbol{\Omega},\mathrm{E})=\mathcal{L}\psi(\boldsymbol{r},\boldsymbol{\Omega},\mathrm{E})-\mathcal{H}\psi(\boldsymbol{r},\boldsymbol{\Omega},\mathrm{E}). \tag{2.33}$$

The steady-state transport equation (2.29) can thus be written as a generalized eigenvalue problem

$$\mathcal{B}\psi(\boldsymbol{r}, \boldsymbol{\Omega}, \mathrm{E}) = \frac{1}{k_{\text{eff}}}\mathcal{F}\psi(\boldsymbol{r}, \boldsymbol{\Omega}, \mathrm{E}). \tag{2.34}$$

where k_{eff} is the value scaling the fission so that the neutron population is stable over time. Iterative methods exist for solving this class of problems. In reactor physics, the power iteration method is traditionally used [66]. It will be detailed when we discuss the multi-group problem (3.1).

2.3.3 . Scattering anisotropy

To account for the anisotropy of scattering, some additional developments are made. First, the medium is considered isotropic. Thus, the scattering cross section depends on the cosine μ of the angle between $\boldsymbol{\Omega}$ and $\boldsymbol{\Omega}'$. Moreover, the dependence can be expanded using Legendre polynomials (10.4.1).

$$\Sigma_s(\boldsymbol{r}, \mu, \mathrm{E}' \to \mathrm{E}) = \frac{1}{4\pi}\sum_{k=0}^{\mathrm{K}} \Sigma_{s,k}(\boldsymbol{r}, \mathrm{E}' \to \mathrm{E})\mathcal{P}_k(\mu). \tag{2.35}$$

where the anisotropic moments $\Sigma_{s,k}$ are defined as

$$\Sigma_{s,k}(\boldsymbol{r}, \mathrm{E}' \to \mathrm{E}) = 2\pi(2k+1)\int_{-1}^{1} \mathrm{d}\mu \Sigma_s(\boldsymbol{r}, \mu, \mathrm{E}' \to \mathrm{E})\mathcal{P}_k(\mu), \tag{2.36}$$

and where the Legendre polynomials satisfy the property

$$\mathcal{P}_k(\mu) = \sum_{l=-k}^{k} A_k^l(\boldsymbol{\Omega})A_k^l(\boldsymbol{\Omega}'). \tag{2.37}$$

Thus, by substituting equations (2.35) and (2.37) into (2.30), the final expression is obtained:

$$\mathcal{H}\psi(\boldsymbol{r}, \boldsymbol{\Omega}, \mathrm{E}) = \sum_{k=0}^{\mathrm{K}}\sum_{l=-k}^{k} A_k^l(\boldsymbol{\Omega}) \int_0^{+\infty} \mathrm{dE}'\Sigma_{s,k}(\boldsymbol{r}, \mathrm{E}' \to \mathrm{E})\phi_k^l(\boldsymbol{r}, \mathrm{E}'). \tag{2.38}$$

2.3.4 . Integral form of the transport equation

The integro-differential equation, representing the local particle balance, can be viewed as a conservation equation along trajectories called characteristics. The starting point to obtain the integral formulation is to rewrite the streaming term. Initially, recall that:

$$\frac{\mathrm{d}}{\mathrm{d}s} = \frac{\mathrm{d}x}{\mathrm{d}s}\frac{\partial}{\partial x} + \frac{\mathrm{d}y}{\mathrm{d}s}\frac{\partial}{\partial y} + \frac{\mathrm{d}z}{\mathrm{d}s}\frac{\partial}{\partial z} + \frac{\mathrm{d}t}{\mathrm{d}s}\frac{\partial}{\partial t}.$$

Next, consider a point $\boldsymbol{r}$ in space with coordinates (x, y, z) and a point $\boldsymbol{r}'$ with coordinates (x', y', z'), defined as $\boldsymbol{r}' = \boldsymbol{r} + s\boldsymbol{\Omega}$. By projecting $\boldsymbol{r}'$ onto the basis vectors, it directly follows that:

$$\frac{\mathrm{d}x'}{\mathrm{d}s} = \Omega_x, \tag{2.39}$$

and similarly for the other components. It follows that:

$$\frac{\mathrm{d}}{\mathrm{d}s} = \boldsymbol{\Omega} \cdot \boldsymbol{\nabla}.$$

The equation can therefore be written in its characteristics form as:

$$\frac{\mathrm{d}}{\mathrm{d}s}\psi(\boldsymbol{r} + s\boldsymbol{\Omega}, \boldsymbol{\Omega}, \mathrm{E}) + \Sigma_t(\boldsymbol{r} + s\boldsymbol{\Omega}, \mathrm{E})\psi(\boldsymbol{r} + s\boldsymbol{\Omega}, \boldsymbol{\Omega}, \mathrm{E}) = Q(\boldsymbol{r} + s\boldsymbol{\Omega}, \boldsymbol{\Omega}, \mathrm{E}), \tag{2.40}$$

which integrates for an infinite domain as

$$\psi(\boldsymbol{r}, \boldsymbol{\Omega}, \mathrm{E}) = \int_0^\infty \mathrm{d}t Q(\boldsymbol{r} - t\boldsymbol{\Omega}, \boldsymbol{\Omega}, \mathrm{E}) e^{-\tau(t, \mathrm{E})}, \tag{2.41}$$

and for finite domain

$$\psi(\boldsymbol{r}, \boldsymbol{\Omega}, \mathrm{E}) = \psi(\boldsymbol{r} - l\boldsymbol{\Omega}, \boldsymbol{\Omega}, \mathrm{E}) e^{-\tau(l, \mathrm{E})} + \int_0^l \mathrm{d}t Q(\boldsymbol{r} - t\boldsymbol{\Omega}, \boldsymbol{\Omega}, \mathrm{E}) e^{-\tau(t, \mathrm{E})}, \tag{2.42}$$

with the optical path τ, considering that the integration from 0 to t is performed over the segment from $\boldsymbol{r} - t\boldsymbol{\Omega}$ to $\boldsymbol{r}$, is defined as

$$\tau(t, \mathrm{E}) = \int_0^t \mathrm{d}t' \Sigma_t(t', \mathrm{E}). \tag{2.43}$$

2.3.5 . Boundary conditions

The resolution of the transport equation requires imposing an incoming flux at the boundary of the domain. This is referred to as a boundary condition. We are considering a domain D with boundary ∂D and normal vector $\boldsymbol{n}$. The boundary $\Gamma = \partial D \times \mathbb{S}_2$ is divided into an incoming boundary and an outgoing boundary, denoted respectively by Γ_- and Γ_+, defined as follows:

$$\Gamma_- = \{(\boldsymbol{r}, \boldsymbol{\Omega}) \in \partial D \times \mathbb{S}_2,\, \boldsymbol{\Omega} \cdot \boldsymbol{n}(\boldsymbol{r}) < 0\}\,, \tag{2.44}$$
$$\Gamma_+ = \{(\boldsymbol{r}, \boldsymbol{\Omega}) \in \partial D \times \mathbb{S}_2,\, \boldsymbol{\Omega} \cdot \boldsymbol{n}(\boldsymbol{r}) > 0\}\,. \tag{2.45}$$

Then, it is useful to define a boundary for each computational region i. Following the same logic as in the first paragraph, we denote $\Gamma_i = \partial i \times \mathbb{S}_2$ and $\Gamma_{i,-}$ and $\Gamma_{i,+}$ as

$$\Gamma_{i,-} = \{(\boldsymbol{r}, \boldsymbol{\Omega}) \in \partial i \times \mathbb{S}_2,\, \boldsymbol{\Omega} \cdot \boldsymbol{n}(\boldsymbol{r}) < 0\}\,, \tag{2.46}$$
$$\Gamma_{i,+} = \{(\boldsymbol{r}, \boldsymbol{\Omega}) \in \partial i \times \mathbb{S}_2,\, \boldsymbol{\Omega} \cdot \boldsymbol{n}(\boldsymbol{r}) > 0\}\,. \tag{2.47}$$

The boundary condition is imposed on Γ_-. These conditions can be classified into two categories: homogeneous conditions on one side, and heterogeneous conditions on the other.

Homogeneous boundary conditions:

The homogeneous boundary condition is also called the vacuum boundary condition. It is written as follows:

$$\psi(\boldsymbol{r}, \boldsymbol{\Omega}, E) = 0. \tag{2.48}$$

Heterogeneous boundary conditions:

The albedo boundary condition is the one where the entering flux is isotropic and multiplied by the beta quantity. It is written as follows:

$$\psi(\boldsymbol{r}, \boldsymbol{\Omega}, E) = \beta\psi(\boldsymbol{r}, \boldsymbol{\Omega}', E). \tag{2.49}$$

The specular reflection boundary condition corresponds to the case where $\beta = 1$. In practice, the exiting direction $\boldsymbol{\Omega}'$ is defined solely based on the entering direction $\boldsymbol{\Omega}$ and the normal vector $\boldsymbol{n}$ using the following relation:

$$\begin{aligned} \boldsymbol{\Omega} \cdot \boldsymbol{n}(\boldsymbol{r}) &= -\boldsymbol{\Omega}' \cdot \boldsymbol{n}(\boldsymbol{r}), \\ (\boldsymbol{\Omega} \times \boldsymbol{\Omega}') \cdot \boldsymbol{n}(\boldsymbol{r}) &= 0. \end{aligned}$$

with $\times$ the cross product in $\mathbb{R}^3$. Note that the vacuum and specular reflection conditions can be seen as special cases of the more general albedo condition.

In order to define periodic boundary conditions, we define an infinite lattice of d-dimensional cells with $d \in \{1, 2, 3\}$ with side length $\Delta \boldsymbol{e}_d$, constructed from the infinite repetition of the elementary cell of geometric motion $\Delta \boldsymbol{e}_d$, such as the one shown in figure 2.8. Then, we consider a point r of cell i and a point $\boldsymbol{r} + \Delta \boldsymbol{r}$ of cell i', with $\Delta \boldsymbol{r} = \sum_d k_d \Delta \boldsymbol{e}_d$ and where k_d are non-zero integers. Thus, the periodic boundary condition can then be written as

$$\psi(\boldsymbol{r} + \Delta \boldsymbol{r}, \boldsymbol{\Omega}, E) = \psi(\boldsymbol{r}, \boldsymbol{\Omega}, E), \tag{2.50}$$

for every values of k_d.

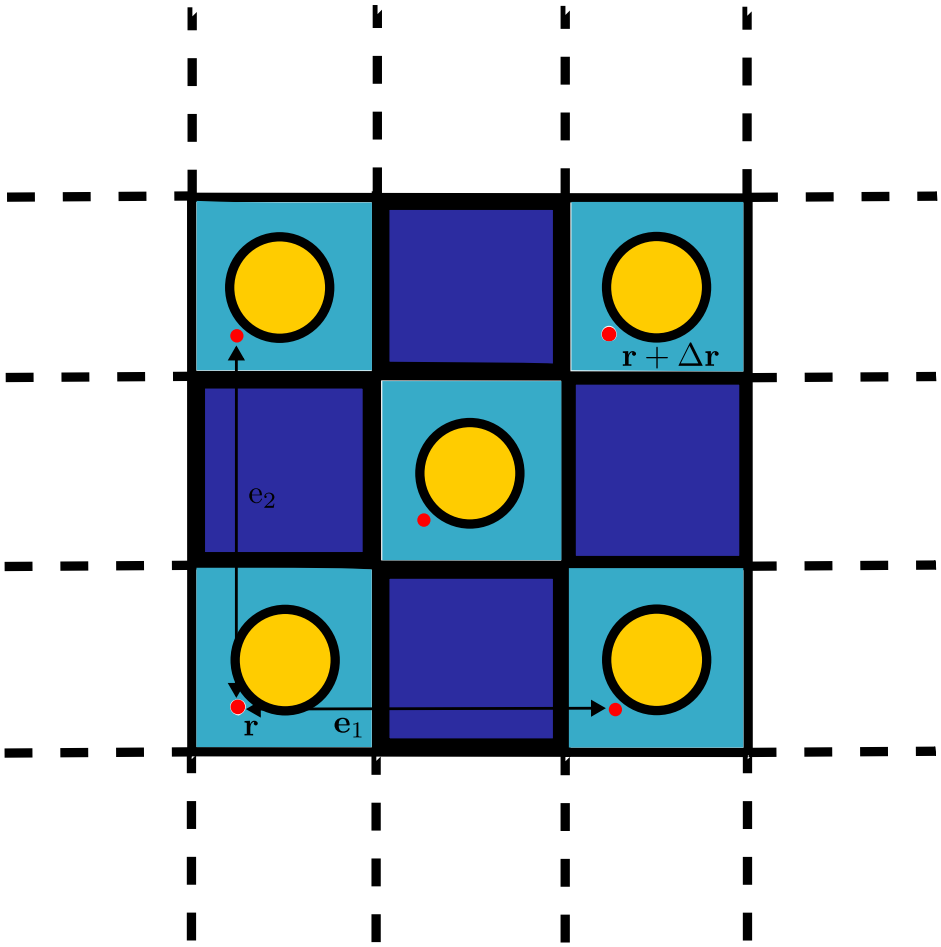

Figure 2.8 – Representation of a cartesian infinite two-dimensional lattice. Each color represents a different material composition. The angular flux on each red point is the same. Here $\Delta \boldsymbol{r} = \Delta \boldsymbol{e}_1 + \Delta \boldsymbol{e}_2$.

3 - Deterministic resolution of the transport equation

Deterministic methods for solving the transport equation rely on a discretization of the phase space. Traditionally, the continuous equation is first discretized in energy, resulting in a system of equations that are coupled with each other; this is referred to as a multi-group problem. In this chapter, we will present the general framework defining these equations and then, at the end of chapter, the method of characteristics.

Contents

3.1 . Multi-group problem

3.1.1 . Energy discretization

Deterministic methods rely on a discretization of the energy interval $[\mathrm{E}_{\mathsf{min}}, \mathrm{E}_{\mathsf{max}}]$ into n_g groups such that

$$\mathrm{E}_{\mathsf{min}} = \mathrm{E}_{n_g} < \cdots < \mathrm{E}_1 < \mathrm{E}_0 = \mathrm{E}_{\mathsf{max}},$$

ordered by decreasing energy. Thus, group g contains the energy neutrons situated between E_g and E_{g-1}. Several energy meshes exist, with different numbers of groups and ways of defining the energy intervals.

At the CEA, most applications for thermal reactors rely on the SHEM-281 mesh [74], which originates from the XMAS-172g mesh [75]. The SHEM-281 mesh introduces a finer discretization below 22.5 eV to avoid need of self-shielding and to improve the representation of mutual self-shielding effets. Subsequently, the SHEM-281 mesh was refined between 22.5 eV and 11.5 keV to enable use of subgroup methods and to improve the accuracy of self-shielding processing. 80 groups were added for this purpose, resulting in the SHEM-361 mesh [76]. Users of CASMO-5 and OpenMOC sometimes use a 70-group library [77], although since 2021, a 586-group library is available [78].

To generate continuous energy cross sections before condensation, the data must be reconstructed from processing codes like NJOY21 [79] or FUDGE [80]. At the CEA, the developed code is called GALILEE [81, 82] and is used by TRIPOLI-4® and APOLLO3®. This approach ensures consistent comparisons between Monte Carlo codes and deterministic codes, as they rely on the same nuclear data processing.

3.1.2 . The multi-group transport equation

The continuous energy transport equation is decomposed into a coupled system of n_g equations. To achieve this, equation (2.29) is integrated over each energy interval, denoted as:

$$\int_g \mathrm{dE}\, \cdot = \int_{\mathrm{E}_g}^{\mathrm{E}_{g-1}} \mathrm{dE}\, \cdot \tag{3.1}$$

For all energy groups g, we write:

$$\boldsymbol{\Omega} \cdot \boldsymbol{\nabla} \int_g \mathrm{dE}\psi(\boldsymbol{r}, \boldsymbol{\Omega}, \mathrm{E}) + \int_g \mathrm{dE}\Sigma_t(\boldsymbol{r}, \mathrm{E})\psi(\boldsymbol{r}, \boldsymbol{\Omega}, \mathrm{E}) = \int_g \mathrm{dE}Q(\boldsymbol{r}, \boldsymbol{\Omega}, \mathrm{E}). \tag{3.2}$$

Then, we define

$$\psi^g(\boldsymbol{r}, \boldsymbol{\Omega}) = \int_g \mathrm{dE}\psi(\boldsymbol{r}, \boldsymbol{\Omega}, \mathrm{E}), \tag{3.3}$$

$$\Sigma_t^g(\boldsymbol{r}, \boldsymbol{\Omega})\psi^g(\boldsymbol{r}, \boldsymbol{\Omega}) = \int_g \mathrm{dE}\Sigma_t(\boldsymbol{r}, \mathrm{E})\psi(\boldsymbol{r}, \boldsymbol{\Omega}, \mathrm{E}), \tag{3.4}$$

$$Q^g(\boldsymbol{r}, \boldsymbol{\Omega}) = \int_g \mathrm{dE}Q(\boldsymbol{r}, \boldsymbol{\Omega}, \mathrm{E}). \tag{3.5}$$

It is important to note that the energy condensation of the macroscopic total cross section (3.4) introduces an angular dependence, as it is calculated from the angular flux. Historically, lattice calculations have been performed without this dependence. Specifically, it is assumed that energy and direction are independent in the expression of the angular flux. Thus, the angular flux, only for (3.4), is expressed as the product of the scalar flux and a weighting function u that depends on angle and space. Practically, we write:

$$\psi(\boldsymbol{r}, \boldsymbol{\Omega}, \mathrm{E}) \simeq \phi(\boldsymbol{r}, \mathrm{E})u(\boldsymbol{r}, \boldsymbol{\Omega}). \tag{3.6}$$

Then, if we substitute the hypothesis (3.6) into (3.4) and use (3.3) to express $\psi^g(\boldsymbol{r}, \boldsymbol{\Omega})$, we obtain an expression where u cancels out. As a result, we derive a macroscopic cross section that is independent of the direction $\boldsymbol{\Omega}$:

$$\Sigma_t^g(\boldsymbol{r}) = \frac{\displaystyle\int_g \mathrm{dE}\Sigma_t(\boldsymbol{r}, \mathrm{E})\phi(\boldsymbol{r}, \mathrm{E})}{\displaystyle\int_g \mathrm{dE}\phi(\boldsymbol{r}, \mathrm{E})}. \tag{3.7}$$

Several studies exist to quantify the error associated with (3.6) [83]. Following the same principle, the scattering and fission cross sections are defined as

$$\Sigma_{s,k}^{g'\to g}(\boldsymbol{r}) = \frac{\displaystyle\int_g \mathrm{dE} \int_{g'} \mathrm{dE}' \nu\Sigma_{s,k}(\boldsymbol{r}, \mathrm{E}\to \mathrm{E}')\phi(\boldsymbol{r}, \mathrm{E}')}{\displaystyle\int_{g'} \mathrm{dE}'\phi(\boldsymbol{r}, \mathrm{E}')}, \tag{3.8}$$

$$\nu\Sigma_{f,i}^{g}(\boldsymbol{r}) = \frac{\displaystyle\int_g \mathrm{dE} \nu\Sigma_{f,i}(\boldsymbol{r}, \mathrm{E})\phi(\boldsymbol{r}, \mathrm{E})}{\displaystyle\int_g \mathrm{dE}\phi(\boldsymbol{r}, \mathrm{E})}. \tag{3.9}$$

Finally, the multi-group problem is written as:

$$\boldsymbol{\Omega}\cdot\boldsymbol{\nabla}\psi^g(\boldsymbol{r}, \boldsymbol{\Omega}) + \Sigma_t^g(\boldsymbol{r})\psi^g(\boldsymbol{r}, \boldsymbol{\Omega}) = Q^g(\boldsymbol{r}, \boldsymbol{\Omega}), \tag{3.10}$$

with

$$Q^g(\boldsymbol{r}, \boldsymbol{\Omega}) = \mathcal{H}^{g'\to g}\psi^{g'}(\boldsymbol{r}, \boldsymbol{\Omega}) + \frac{1}{k_{\text{eff}}}\mathcal{F}^{g'\to g}\psi^{g'}(\boldsymbol{r}, \boldsymbol{\Omega}), \tag{3.11}$$

$$\mathcal{H}^{g'\to g}\psi^{g'}(\boldsymbol{r}, \boldsymbol{\Omega}) = \sum_{k=0}^{\mathrm{K}}\sum_{l=-k}^{k} A_k^l(\boldsymbol{\Omega})\sum_{g'=1}^{n_g}\Sigma_{s,k}^{g'\to g}(\boldsymbol{r})\phi_k^{g',l}(\boldsymbol{r}), \tag{3.12}$$

$$\mathcal{F}^{g'\to g}\psi^{g'}(\boldsymbol{r}, \boldsymbol{\Omega}) = \sum_{j=1}^{n_j}\chi_j^g(\boldsymbol{r})\sum_{g'=1}^{n_g}\nu_j^{g'}\Sigma_{f,j}^{g'}\phi_k^{g',l}(\boldsymbol{r}). \tag{3.13}$$

In a similar manner to the continuous problem, the multi-group problem can be formulated as a generalized eigenvalue problem. We define

$$\mathcal{L}^g\psi^g(\boldsymbol{r}, \boldsymbol{\Omega}) = \boldsymbol{\Omega}\cdot\boldsymbol{\nabla}\psi^g(\boldsymbol{r}, \boldsymbol{\Omega}) + \Sigma_t^g(\boldsymbol{r})\psi^g(\boldsymbol{r}, \boldsymbol{\Omega}),$$
$$\mathcal{B}^g\psi^g(\boldsymbol{r}, \boldsymbol{\Omega}) = \mathcal{L}^g\psi^g(\boldsymbol{r}, \boldsymbol{\Omega}) - \mathcal{H}^{g'\to g}\psi^{g'}(\boldsymbol{r}, \boldsymbol{\Omega}),$$

so that

$$\mathcal{B}^g\psi^g(\boldsymbol{r}, \boldsymbol{\Omega}) = \frac{1}{k_{\text{eff}}}\mathcal{F}^{g'\to g}\psi^{g'}(\boldsymbol{r}, \boldsymbol{\Omega}). \tag{3.14}$$

In the same manner as for the continuous energy problem (2.29), the integral forms can be adapted to the multi-group problem. By applying (3.1) to the equations (2.41) and (2.42), it follows, for infinite domain

$$\psi^g(\boldsymbol{r}, \boldsymbol{\Omega}) = \int_0^\infty \mathrm{d}t Q^g(\boldsymbol{r} - t\boldsymbol{\Omega}, \boldsymbol{\Omega}) e^{-\tau^g(t)}, \tag{3.15}$$

and for finite domain

$$\psi^g(\boldsymbol{r}, \boldsymbol{\Omega}) = \psi^g(\boldsymbol{r} - l\boldsymbol{\Omega}, \boldsymbol{\Omega}) e^{-\tau^g(l)} + \int_0^l \mathrm{d}t Q^g(\boldsymbol{r} - t\boldsymbol{\Omega}, \boldsymbol{\Omega}) e^{-\tau^g(t)}, \tag{3.16}$$

with the optical path τ, implicitly considering that the integration from 0 to t is performed over the segment from $\boldsymbol{r} - t\boldsymbol{\Omega}$ to $\boldsymbol{r}$, defined as

$$\tau^g(t) = \int_0^t \mathrm{d}t' \Sigma_t^g(t'). \tag{3.17}$$

3.1.3 . The multi-group diffusion equation

In the case where the flux and Σ_t vary weakly spatially, and where absorption is small compared to the assumed isotropic scattering, a multi-group transport approximation can be established. The starting point is to expand the angular flux in terms of the spherical harmonics up to order 1:

$$\psi^g(\boldsymbol{r}, \boldsymbol{\Omega}) \simeq \frac{1}{4\pi} \Big[\phi^g(\boldsymbol{r}) + 3\boldsymbol{\Omega} \cdot \mathrm{J}^g(\boldsymbol{r}) \Big]. \tag{3.18}$$

This is referred to as the P1 approximation. We then substitute (3.18) into the multi-group transport equation (3.10)

$$\boldsymbol{\Omega} \cdot \boldsymbol{\nabla} \Big[\phi^g(\boldsymbol{r}) + 3\boldsymbol{\Omega} \cdot \mathrm{J}^g(\boldsymbol{r}) \Big] + \Sigma_t^g(\boldsymbol{r}) \Big[\phi^g(\boldsymbol{r}) + 3\boldsymbol{\Omega} \cdot \mathrm{J}^g(\boldsymbol{r}) \Big] = 4\pi Q^g(\boldsymbol{r}, \boldsymbol{\Omega}), \tag{3.19}$$

Then we integrate the equation over the unit sphere $\mathbb{S}_2$, knowing that:

$$\int_{\mathbb{S}_2} \mathrm{d}\boldsymbol{\Omega}\, \boldsymbol{\Omega} = \mathbb{O}_3, \tag{3.20}$$

$$\int_{\mathbb{S}_2} \mathrm{d}\boldsymbol{\Omega}\, \boldsymbol{\Omega}^2 = \frac{4\pi}{3} \mathbb{I}_3, \tag{3.21}$$

where $\mathbb{O}_3$ et $\mathbb{I}_3$ are the 3×3 zero and identity matrices, respectively. After simplification, we obtain

$$\nabla \cdot \mathrm{J}^g(\boldsymbol{r}) + \Sigma_t^g(\boldsymbol{r})\phi^g(\boldsymbol{r}) = Q^g(\boldsymbol{r}). \tag{3.22}$$

Finally, to eliminate the unknowns related to the currents, we use Fick's law, which describes the tendency of neutrons to move towards regions with lower neutron density. We write:

$$\mathrm{J}^g(\boldsymbol{r}) = -\mathbb{D}(\boldsymbol{r})\boldsymbol{\nabla}\phi^g(\boldsymbol{r}), \tag{3.23}$$

where $\mathbb{D}(\boldsymbol{r})$ is the diffusion coefficient in cm. By substituting the relation (3.23) into (3.22), we obtain the multi-group diffusion equation. It writes

$$-\nabla \cdot \mathbb{D}(\boldsymbol{r})\nabla\phi^g(\boldsymbol{r}) + \Sigma_t^g(\boldsymbol{r})\phi^g(\boldsymbol{r}) = Q^g(\boldsymbol{r}). \tag{3.24}$$

Different strategies exist for calculating the diffusion coefficient [84]. The APOLLO3® code adopts the homogeneous $\mathrm{B1}$ approach as the default option. In this approach, $\mathbb{D}$ is calculated from a critical flux ($k_{eff} = 1$) derived from a leakage model to ensure the criticality of the calculation in an infinite lattice. It is possible to compare the quality of energy condensation by comparing it with continuous-energy Monte Carlo codes dedicated to this purpose [85, 86]. Moreover, it is interesting to note that the multi-group diffusion equation can be considered an asymptotic equation of the multi-group transport equation [87]. It is used for core calculations or for acceleration techniques, the most well-known of which is CMFD [88]. Numerically, the equation is solved using finite difference or finite element methods.

3.1.4 . Self-shielding

Evaluating the multi-group cross sections (3.7), (3.8), and (3.9) is necessary if one wants to solve the deterministic transport equation. More specifically, because the volumetric concentrations are known, we seek to estimate the multi-group microscopic cross sections by reaction ρ for an isotope i :

$$\sigma_{i,\rho}^g(\boldsymbol{r}) = \frac{\displaystyle\int_g \mathrm{dE}\, \sigma_{i,\rho}(\mathrm{E})\phi(\boldsymbol{r},\mathrm{E})}{\displaystyle\int_g \mathrm{dE}\, \phi(\boldsymbol{r},\mathrm{E})}. \tag{3.25}$$

Since the flux depends on space, the self-shielded cross sections also depend on space. Therefore, these sections must be calculated for each geometry and material composition.

When the nuclei are considered non-resonant, it is sufficient to weight the flux by a weighting flux $\phi_{E\text{„}}$ which reproduces the energy spectrum of the flux for the different regions.

The same approach can be applied to resonant nuclei outside the resonant region. However, within the resonant region, it is necessary to evaluate the actual flux to accurately assess the cross sections. This is the purpose of self-shielding calculations. They determine the accuracy of the solutions to the multi-group transport problem.

Self-shielding methods can be grouped into four main categories: equivalence-based methods [36] relying on homogeneous-heterogeneous equivalence, sub-group methods [89, 37], ultra-fine group methods [90], and resonance spectrum expansion (RSE) [91, 92]. The first two families of algorithm are implemented within APOLLO3® and use the collision probability method (3.4.1) as flux solver.

3.2 . Power iteration method

The solution of the multi-group problem relies on the power iteration algorithm to determine the dominant eigenvalue and eigenvector, namely k_{eff} and the angular flux. In this section, some algebraic concepts are reviewed before applying them to the solution of the multi-group problem.

3.2.1 . Brief review of iterative methods

Gauss-Seidel method: Let $\mathbb{A} \in \mathcal{M}_n(\mathbb{R})$ be a symmetric positive definite matrix or a matrix with a strictly dominant diagonal, $\boldsymbol{b} \in \mathbb{R}^n$, and $\boldsymbol{x}$ be the vector with coordinates $(x_1, x_2, \ldots, x_n)$ that is a solution to the problem

$$\mathbb{A}\boldsymbol{x} = \boldsymbol{b}. \tag{3.26}$$

Then the sequence $(\boldsymbol{x}_k)_{k\in n}$ with coordinates $(x_i)_{k+1}$ defined by

$$(x_i)_k = \frac{1}{a_{ii}} \left(b_i - \sum_{j=1}^{i-1} a_{ij}(x_j)_k - \sum_{j=i+1}^{n} a_{ij}(x_j)_{k-1} \right), \tag{3.27}$$

converges to $\boldsymbol{x}$, where a_{ij} and b_i are the coefficients of $\mathbb{A}$ and $\boldsymbol{b}$, respectively.

Eigenvalue problem: Let $\mathbb{A} \in \mathcal{M}_n(\mathbb{R})$. We seek $\lambda \in \mathbb{R}$ and $\boldsymbol{x} \in \mathbb{R}^n$, non-zero, such that

$$\mathbb{A}\boldsymbol{x} = \lambda\boldsymbol{x}. \tag{3.28}$$

Eigenvalues and eigenvectors are the scalars and vectors that are solutions, respectively.

Power iteration method: Let $\mathbb{A} \in \mathcal{M}_n(\mathbb{R})$ be a diagonalizable matrix with eigenvalues $(\lambda_k)_{k\in n}$ such that $|\lambda_1| > |\lambda_2| > \cdots > |\lambda_n|$ and $\boldsymbol{e}_i$ an eigenvector associated with λ_i. Then, by choosing a vector $\boldsymbol{x}_0$ that is not orthogonal to $\boldsymbol{e}_1$, it can be shown that the sequence $(\boldsymbol{x}_k)_{k\in\mathbb{N}}$, where $\boldsymbol{x}_k = \mathbb{A}\boldsymbol{x}_{k-1} / \|\mathbb{A}\boldsymbol{x}_{k-1}\|$, and $(\Lambda_k)_{k\in\mathbb{N}}$, where $\Lambda_k = (\mathbb{A}\boldsymbol{x}_k \cdot \boldsymbol{x}_k) / (\boldsymbol{x}_k \cdot \boldsymbol{x}_k)$), converges to the eigenvector (up to a scalar) $\boldsymbol{e}_1 / \|\boldsymbol{e}_1\|$ and the eigenvalue λ_1:

$$\lim_{k\to+\infty} \boldsymbol{x}_k = \frac{\boldsymbol{e}_1}{\|\boldsymbol{e}_1\|}, \tag{3.29}$$

$$\lim_{k\to+\infty} \Lambda_k = \lambda_1. \tag{3.30}$$

We call Λ_k the Rayleigh quotient.

3.2.2 . Application to multi-group neutron transport

The power iteration method is used to determine the angular flux, the eigenvector, and its associated eigenvalue, the effective multiplication factor k_{eff} for the generalized eigenvalue problem (2.34), which can be written as follows:

$$\mathcal{A}\psi(\boldsymbol{r}, \boldsymbol{\Omega}, \mathrm{E}) = k_{\text{eff}}\psi(\boldsymbol{r}, \boldsymbol{\Omega}, \mathrm{E}), \tag{3.31}$$

with $\mathcal{A} = \mathcal{B}^{-1}\mathcal{F}$, or as

$$\mathcal{B}\psi(\boldsymbol{r}, \boldsymbol{\Omega}, \mathrm{E}) = b, \tag{3.32}$$

with

$$b = \frac{1}{k_{\text{eff}}}\mathcal{F}\psi^g(\boldsymbol{r}, \boldsymbol{\Omega}).$$

In order to solve (2.34), an algorithm consisting of three nested loops is implemented. The algorithm begins with the initialization of the angular flux and k_{eff}, which allows the calculation of the fission source (3.13)) for all energy groups. Then, as long as the fission source has not converged, the multi-group flux is updated. Finally, if the multi-group flux has not converged, the within-group calculations are updated. Once the fluxes in each group have converged, the fission source and k_{eff} are updated until convergence. The iterations on the fission source are called external iterations, those on the multi-group flux are called thermal

iterations, and those on the within-group flux are called internal iterations. The three iteration loops are indexed by the integers o, th, and i, respectively. They can be defined as follows:

External iterations: The aim is to converge the fission source and k_{eff}. The following operations are performed:

$$\mathcal{B}\psi^{o}(\boldsymbol{r},\boldsymbol{\Omega},\mathrm{E}) = \frac{1}{k_{\text{eff}}^{o-1}}\mathcal{F}\psi^{o-1}(\boldsymbol{r},\boldsymbol{\Omega},\mathrm{E}), \tag{3.33}$$

and

$$k_{\text{eff}}^{o} = k_{\text{eff}}^{o-1}\frac{\mathcal{F}\psi^{o}(\boldsymbol{r},\boldsymbol{\Omega},\mathrm{E})}{\mathcal{F}\psi^{o-1}(\boldsymbol{r},\boldsymbol{\Omega},\mathrm{E})}. \tag{3.34}$$

Thermal iterations: The aim is to converge the multi-group flux when up-scattering is present and so the Gauss-Seidel (3.2.1) procedure does not converge immediately. Until convergence, we perform

$$Q_{ext}^{th,th-1,o-1}(\boldsymbol{r},\boldsymbol{\Omega},\mathrm{E}) = \mathcal{H}\psi^{th,th-1,o-1}(\boldsymbol{r},\boldsymbol{\Omega},\mathrm{E}) + \mathcal{F}\psi^{o-1}(\boldsymbol{r},\boldsymbol{\Omega},\mathrm{E}). \tag{3.35}$$

Internal iterations: The goal is to converge the within-group flux by

$$\mathcal{L}\psi^{i}(\boldsymbol{r},\boldsymbol{\Omega},\mathrm{E}) = \mathcal{H}\psi^{i-1}(\boldsymbol{r},\boldsymbol{\Omega},\mathrm{E}) + Q_{ext}^{th-1,o-1}(\boldsymbol{r},\boldsymbol{\Omega},\mathrm{E}). \tag{3.36}$$

The first energy groups are the fastest to converge as up-scattering is negligible for neutrons in the fast domain. Fast neutrons slow down to the thermal domain unless they are absorbed in the resonant domain (or escape through leakage).

3.3 . Angular discretization

3.3.1 . $\mathrm{S_n}$ methods

The discrete ordinates method is based on a discretization of the unit sphere. A finite number n_d of directions $\boldsymbol{\Omega}_n$ with associated weights w_n are determined using a quadrature formula (such as Gauss-Legendre, Gauss-Chebyshev, or Bickley) so that

$$\frac{1}{4\pi}\int_{\mathbb{S}_2}\mathrm{d}\boldsymbol{\Omega} f(\boldsymbol{\Omega}) \simeq \sum_{n=1}^{n_a} w_n f(\boldsymbol{\Omega}_n), \tag{3.37}$$

with

$$\sum_n w_n = 1. \tag{3.38}$$

The transport equation is evaluated for each discrete direction. Thus, n_d equations need to be solved for each energy group

$$\boldsymbol{\Omega}_n \cdot \boldsymbol{\nabla}\psi^g(\boldsymbol{r}, \boldsymbol{\Omega}_n) + \Sigma_t^g(\boldsymbol{r})\psi^g(\boldsymbol{r}, \boldsymbol{\Omega}_n) = Q^g(\boldsymbol{r}, \boldsymbol{\Omega}_n). \tag{3.39}$$

3.3.2 . $\mathrm{P_n}$ methods

The Spherical Harmonics Method relies on expanding the angular flux using a basis of spherical harmonics (10.4.2) up to a certain order K. The approximation is then inserted into equation (3.10) and projected onto the orthogonal spherical harmonics basis. The unknowns are no longer the angular fluxes but rather the $(\mathrm{K}+1)^2$ moments of the flux.

3.4 . Spatial discretization

The computational geometry is considered as a domain D with boundary $\partial\mathrm{D}$, composed of n_r homogeneous computational regions D_r with boundary ∂D_r. Then, a mesh is applied to this geometry. Each region is divided into n_i computational cells of volume V_i.

3.4.1 . Collision probabilities

The Collision Probability Method (or the P_{ij} method) is based on the multi-group integral form of the transport equation. The formalism applies to both finite and infinite domains. In this section, only the developments for infinite domains are considered. To explain the principle of the method, the integral form of the multi-group transport equation for an infinite domain is recalled:

$$\psi^g(\boldsymbol{r}, \boldsymbol{\Omega}) = \int_0^\infty \mathrm{d}t Q^g(\boldsymbol{r} - t\boldsymbol{\Omega}, \boldsymbol{\Omega}) e^{-\tau^g(t)},$$

The next step involves integrating the previous equation over the unit sphere.

$$\phi_0^{g,0}(\boldsymbol{r}) = \frac{1}{4\pi}\int_{\mathbb{S}_2} \mathrm{d}\boldsymbol{\Omega} \int_0^\infty \mathrm{d}t Q^g(\boldsymbol{r} - t\boldsymbol{\Omega}, \boldsymbol{\Omega}) e^{-\tau^g(t)}. \tag{3.40}$$

Since integrating along a line in $\mathbb{R}^3$ and then over all directions is equivalent to integrating over $\mathbb{R}^3$, we perform the change of variables $\boldsymbol{r}' = \boldsymbol{r} - t\boldsymbol{\Omega}$, with $\mathrm{d}\boldsymbol{r}' = t^2 \mathrm{d}t\mathrm{d}\boldsymbol{\Omega}$. (3.40) becomes

$$\phi_0^{g,0}(\boldsymbol{r}) = \frac{1}{4\pi} \int_{\mathbb{R}^3} \mathrm{d}\boldsymbol{r}'\, Q^g(\boldsymbol{r}', \boldsymbol{\Omega}) \frac{e^{-\tau^g(t)}}{\|\boldsymbol{r} - \boldsymbol{r}'\|^2}, \tag{3.41}$$

where $\|\cdot\|$ denotes the 2-norm. Now, in order to apply the method numerically, we consider an infinite lattice of n_i cells of volume V_i. Similar to the approach in [66], we denote by V_i^∞ the volume of all identical cells throughout the infinite lattice. The source is assumed to be isotropic, and we therefore write $\phi^g = \phi_0^{g,0}$. Finally, to determine the flux in a region $j \in [\![1, n_i]\!]$, we multiply (3.41) by Σ_t^g and integrate over the spatial domain

$$\int_{\mathrm{V}_j} \mathrm{d}\boldsymbol{r}\, \Sigma_t^g(\boldsymbol{r}) \phi^g(\boldsymbol{r}) = \frac{1}{4\pi} \int_{\mathrm{V}_j} \mathrm{d}\boldsymbol{r}\, \Sigma_t^g(\boldsymbol{r}) \sum_i \int_{\mathrm{V}_i^\infty} \mathrm{d}\boldsymbol{r}'\, Q^g(\boldsymbol{r}', \boldsymbol{\Omega}) \frac{e^{-\tau^g(t)}}{\|\boldsymbol{r} - \boldsymbol{r}'\|^2}. \tag{3.42}$$

The source and the total cross sections are now assumed to be uniform in each region. Thus, (3.42) simplifies as follows

$$\mathrm{V}_j \Sigma_{t,j}^g \phi_j^g = \sum_i \mathrm{V}_i \mathrm{P}_{ij}^g Q_i^g, \tag{3.43}$$

with

$$\phi_j^g = \frac{1}{\mathrm{V}_j} \int_{\mathrm{V}_j} \mathrm{d}\boldsymbol{r} \phi^g(\boldsymbol{r}), \tag{3.44}$$

$$\Sigma_j^g = \frac{1}{\mathrm{V}_j \phi_j^g} \int_{\mathrm{V}_j} \mathrm{d}\boldsymbol{r} \Sigma_t^g(\boldsymbol{r}) \phi^g(\boldsymbol{r}), \tag{3.45}$$

$$\mathrm{P}_{ij}^g = \frac{1}{4\pi \mathrm{V}_i} \int_{\mathrm{V}_j} \mathrm{d}\boldsymbol{r}' \int_{\mathrm{V}_i^\infty} \mathrm{d}\boldsymbol{r} \Sigma_t^g(\boldsymbol{r}) \frac{e^{-\tau}}{\|\boldsymbol{r} - \boldsymbol{r}'\|^2}. \tag{3.46}$$

It is generally preferable to divide the collision probabilities (3.46) by the total cross section $\Sigma_t^g(\boldsymbol{r})$ and define a reduced collision probability. This approach ensures improved numerical stability when handling regions with low optical path lengths.

$$\mathrm{p}_{ij}^g = \frac{1}{4\pi \mathrm{V}_i} \int \mathrm{d}\boldsymbol{r}' \int \mathrm{d}\boldsymbol{r} \frac{e^{-\tau}}{\|\boldsymbol{r} - \boldsymbol{r}'\|^2}. \tag{3.47}$$

Moreover, the equation can be further simplified by using symmetry and conservation relations. Interested readers can refer to [66]. For a given 2D geometry of n_i regions, the size

of the system to be solved is n_i^2 for each energy group. Consequently, the method is typically abandoned for handling 2D core calculations or 3D geometries.

3.4.2 . The method of characteristics

The MOC relies on the integral form of the multi-group transport equation (3.16) and the discrete ordinates method (3.3.1). The equation tells us that for a given trajectory, a straight line crossing the geometry, in the direction $\mathbf{\Omega}$, entering the domain at point r, and knowing the source in each region traversed by the trajectory, it is possible to evaluate the angular flux at any point along this trajectory. The classical approximation consists of assuming a constant source within each region. Thus, if we consider a chord, the intersection between a trajectory and a region, that traverses a region i between the points $\boldsymbol{r}_{in}$ and $\boldsymbol{r}_{out}$, we obtain:

$$\psi(\boldsymbol{r}_{out}, \mathbf{\Omega}) = \psi(\boldsymbol{r}_{in}, \mathbf{\Omega}) e^{-\Sigma_t l} + \frac{1 - e^{-\Sigma_t l}}{\Sigma_t} Q(\mathbf{\Omega}_n). \tag{3.48}$$

To evaluate the average angular flux per region, equation (3.10) is integrated over space for each computational cell

$$\int_i \mathrm{d}\boldsymbol{r}\, \mathbf{\Omega} \cdot \boldsymbol{\nabla} \psi^g(\boldsymbol{r}, \mathbf{\Omega}) + \int_i \mathrm{d}\boldsymbol{r}\, \Sigma_t^g(\boldsymbol{r}) \psi^g(\boldsymbol{r}, \mathbf{\Omega}) = \int_i \mathrm{d}\boldsymbol{r}\, Q^g(\boldsymbol{r}, \mathbf{\Omega}). \tag{3.49}$$

For simplicity, it is assumed here that the cross sections and the source are constant within each computational region. The leakage term is handled using Green's theorem, noting that $\mathbf{\Omega} \cdot \boldsymbol{\nabla} = \boldsymbol{\nabla} \cdot \mathbf{\Omega}$. Thus,

$$\int_i \mathrm{d}\boldsymbol{r}\, \boldsymbol{\nabla} \cdot (\mathbf{\Omega}\, \psi^g(\boldsymbol{r}, \mathbf{\Omega})) = \int_{\partial i} \mathrm{d}\boldsymbol{r}_s \cdot \mathbf{\Omega}\, \psi^g(\boldsymbol{r}, \mathbf{\Omega}), \tag{3.50}$$

with the term on the right side being nothing more than the integration of the multi-group angular flux over the region boundary ∂i. We separate the integral into two parts by defining an outgoing current J_+^g and an incoming current J_-^g

$$\mathrm{J}_\pm^g(\mathbf{\Omega}) = \int_{\partial i_\pm} \mathrm{d}r\, |\boldsymbol{n}(\boldsymbol{r}) \cdot \mathbf{\Omega}|\, \psi^g(\boldsymbol{r}, \mathbf{\Omega}). \tag{3.51}$$

The conservation equation (3.49) is expressed as follows:

$$\psi_i^g(\mathbf{\Omega}) = \frac{1}{\Sigma_t \mathrm{V}_i} \left[\mathrm{J}_+^g(\mathbf{\Omega}) - \mathrm{J}_-^g(\mathbf{\Omega}) \right] + \frac{1}{\Sigma_t} Q_i^g(\mathbf{\Omega}). \tag{3.52}$$

The remaining task is to numerically evaluate the current terms (3.51). For this purpose, the domain D is covered with a set of trajectories for the directions determined by the quadrature formula. Then each trajectory is swept and for all crossed regions, the transmission equation (3.48) is evaluated. APOLLO3® features the unique capability to recover angular flux over boundary surfaces between internal regions. If the trajectory crosses region i, then the boundary angular fluxes evaluated are cumulated in the currents according to the approximation

$$\mathrm{J}_{\pm}(\mathbf{\Omega}) \simeq \sum_{\substack{t||\mathbf{\Omega} \\ t\cap i}} w_{\perp,t}\psi_{\pm,t}, \tag{3.53}$$

with $\psi_{-,t}$ and $\psi_{+,t}$ representing the incoming and outgoing angular fluxes in region i along trajectory t with an integration weight of $w_{\perp,t}$. The algorithm to track 3D geometries is detailed in the next chapter (see 4.1.1).

The Method of Characteristics, like the Collision Probability Method, relies on the integral form of the transport equation. However, the source can be anisotropic and is preferably used for handling complex 2D or 3D geometries (those with typically more than 300 regions).

3.5 . Free iterations acceleration

3.5.1 . Coarse mesh finite difference accelerations

Another class of acceleration methods exists, known as nonlinear acceleration. The CMFD (Coarse-Mesh Finite Difference) acceleration belongs to this category [93, 94]. This method is based on the multi-group diffusion equation and employs the finite difference method for spatial resolution. It is also possible to define a spectral radius by linearizing the associated problem's equation around a given point. The spectral radius is generally higher than that of DP_1 acceleration, particularly in regions with high optical paths. This is disadvantageous because it hinders the goal of increasing mesh size.The method also requires stabilization [95]. Finally, it relies on homogenizing the geometry on a Cartesian grid. While this is not an issue for PWRs (Pressurized Water Reactors), challenges can arise when applying this approach to reactors with complex geometries.

3.5.2 . Synthetic accelerations

In the case of diffusive media, i.e., $\Sigma_s/\Sigma_t \approx 1$, the power iteration method converges slowly [96]. To overcome this difficulty, a synthetic problem is introduced, which is easier to solve than the transport equation and allows for a reduction in the number of iterations (external, thermal, or internal) needed to reach convergence.

The synthetic approach allows for the acceleration of both external and internal iterations. The acceleration of external iterations is achieved through the introduction of a synthetic generalized eigenvalue problem, which updates the multi-group transport flux [97]. For the acceleration of internal iterations, it updates the within-group moments of the transport. To elaborate on the principle of internal accelerations [96], we start from the definition of internal iterations, where the transport solution is denoted as $\psi^{i-1/2}$. Thus, iteration i corresponds to the accelerated transport calculation. We note:

$$\mathcal{L}\psi^{i-1/2}(\boldsymbol{r},\boldsymbol{\Omega},\mathrm{E}) = \mathcal{H}\psi^{i-1}(\boldsymbol{r},\boldsymbol{\Omega},\mathrm{E}) + Q_{ext}(\boldsymbol{r},\boldsymbol{\Omega},\mathrm{E}), \tag{3.54}$$

knowing that for the solution flux ψ^{∞}, we can write:

$$\mathcal{L}\psi^{\infty}(\boldsymbol{r},\boldsymbol{\Omega},\mathrm{E}) = \mathcal{H}\psi^{\infty}(\boldsymbol{r},\boldsymbol{\Omega},\mathrm{E}) + Q_{ext}(\boldsymbol{r},\boldsymbol{\Omega},\mathrm{E}). \tag{3.55}$$

Now, if we subtract (3.54) from (3.55), we obtain the relation:

$$\mathcal{L}\Delta\psi(\boldsymbol{r},\boldsymbol{\Omega},\mathrm{E}) = \mathcal{H}\Delta\psi(\boldsymbol{r},\boldsymbol{\Omega},\mathrm{E}) + Q_{syn}(\boldsymbol{r},\boldsymbol{\Omega},\mathrm{E}). \tag{3.56}$$

with

$$\Delta\psi(\boldsymbol{r},\boldsymbol{\Omega},\mathrm{E}) = \psi^{\infty}(\boldsymbol{r},\boldsymbol{\Omega},\mathrm{E}) - \psi^{i-1/2}(\boldsymbol{r},\boldsymbol{\Omega},\mathrm{E}), \tag{3.57}$$

$$Q_{syn}(\boldsymbol{r},\boldsymbol{\Omega},\mathrm{E}) = \mathcal{H}\left(\psi^{i-1/2}(\boldsymbol{r},\boldsymbol{\Omega},\mathrm{E}) - \psi^{i-1}(\boldsymbol{r},\boldsymbol{\Omega},\mathrm{E})\right), \tag{3.58}$$

such that

$$\psi^{\infty}(\boldsymbol{r},\boldsymbol{\Omega},\mathrm{E}) = \psi^{i-1/2}(\boldsymbol{r},\boldsymbol{\Omega},\mathrm{E}) + (\mathcal{L}-\mathcal{H})^{-1}\, Q_{syn}(\boldsymbol{r},\boldsymbol{\Omega},\mathrm{E}). \tag{3.59}$$

Solving the problem (3.59) is as complex as solving the transport problem itself, as it involves inverting the same operators. To circumvent this difficulty, approximations are introduced to replace $(\mathcal{L}-\mathcal{H})^{-1}$ with a simplified operator $\mathcal{O}$, so that:

$$\psi^{i}(\boldsymbol{r},\boldsymbol{\Omega},\mathrm{E}) = \psi^{i-1/2}(\boldsymbol{r},\boldsymbol{\Omega},\mathrm{E}) + \mathcal{O}Q_{syn}(\boldsymbol{r},\boldsymbol{\Omega},\mathrm{E}). \tag{3.60}$$

Different sets of approximations lead to different operators $\mathcal{O}$ and various synthetic accelerations. DSA (Diffusion Synthetic Acceleration) [98], ACA (Algebraic Collapsing Acceleration) [99, 100] and DP_n (Double P_n Acceleration) [59] are examples of such accelerations.

3.5.3 . Accelerations properties

Synthetic accelerations can be regarded as a preconditioning of the Richardson problem. Consequently, the effectiveness of the acceleration can be assessed by examining the spectral radius ρ of the synthetic operator. The closer ρ is to 0 (and further from 1), the fewer iterations are required to achieve convergence [96]. Traditionally, this analysis is performed by applying the Fourier transform to the synthetic problem. In general, such analyses are typically restricted to one-dimensional slab geometries with isotropic scattering.

The Fourier analysis of transport reveals that $\rho = c$, where $c = \Sigma_s/\Sigma_t$ represents the scattering ratio. Consequently, the method becomes less effective and prone to issues of false convergence [96].

The Fourier analysis of DSA acceleration shows that $\rho = 0.22c$ [96]. Therefore, even in diffusive media where $c \simeq 1$, this approach effectively reduces the number of iterations. However, DSA relies on the diffusion approximation. As stated in the reference [101], "DSA loses effectiveness for transport problems that have strongly anisotropic scattering".

The Fourier analysis of DP_1 acceleration demonstrates that $\rho \leqslant 0.07$, regardless of the optical mesh size. However, this analysis is limited to isotropic scattering [55, 59].

The Fourier analysis of CMFD acceleration is not straightforward because the method is nonlinear. To perform such analyses, it is necessary to linearize the equations. The findings indicate that without stabilization techniques, the acceleration diverges in highly diffusive regimes ($c \leqslant 0.99$ in the study [102]). It is also noteworthy that this acceleration behaves similarly to DSA acceleration when the low-order diffusion operator is discretized on a coarser grid [102]. Stabilization techniques have led to the development of other methods that remain stable for large optical thicknesses and diffusive media. Examples include partial current-based CMFD (pCMFD) [103] and linear prolongation CMFD (lpCMFD) [104]. A Fourier analysis of these two approaches is detailed in the literature. The conclusion is that as the optical mesh size approaches zero, the spectral radius decreases. For small optical paths, the spectral radius tends toward 0.2 or even 0.1 in certain cases with the lpCMFD approach. However, for large optical paths, the spectral radius tends to 1 [105].

3.6 . Worldwide inventory of MOC-based solvers to treat 3D geometries

In this section, a review of MOC solvers capable of solving the transport equation in 3D geometry is provided. The solvers can be categorized into two families: 2D/1D codes on one side, and 3D codes on the other. The codes are compared based on the levels of approximation available for the source, the approximation of the diffusion operator, the level of parallelization, the acceleration methods, and the numerical stability of the schemes. Finally, we will discuss solvers that rely on random ray tracking.

3.6.1 . 2D/1D MOC solvers

DeCART is a code developed by the Korea Atomic Energy Research Institute (KAERI). The source is assumed to be constant and the scattering isotropic [106, 107]. Specifically, the Method of Characteristics (MOC) is used to solve the transport problem in 2D planes, and it feeds an axial 1D model with axial transverse leakage. The axial model uses the Nodal Expansion Method (NEM), which relies on the diffusion approximation. CMFD acceleration is implemented [94].

nTRACER is developed by the Department of Nuclear Engineering at Seoul National University. The source is assumed constant by region. The scattering can be assumed to be anisotropic [108]. The Method of Characteristics (MOC) is used on 2D radial planes, and an SP_3 nodal model is embedded in the 3D CMFD formulation [27, 109]. Parallelization using MPI and GPU are available [110].

MPACT has been supported by the University of Michigan, Oak Ridge National Laboratory, and the Consortium for Advanced Simulation of Light Water Reactors. The source can be assumed to be constant or linear by region [111]. As with DeCART, the Method of Characteristics (MOC) is only used at the 2D level and is coupled with 1D models based on P_1 or P_3 nodal method [112, 113]. Three transport-correction methods for its transport-corrected P_0 cross-sections are available [114]. CMFD acceleration is implemented.

3.6.2 . Full 3D MOC solvers

OpenMOC is a code developed at MIT for high fidelity whole core calculations [22, 23]. The source can be assumed to be constant or linear by region. The scattering is assumed to be isotropic, but transport correction for cross sections is available, and it is accompanied by a stabilization technique to address convergence issues [115]. CMFD acceleration is implemented [88]. Parallelizations using OpenMP, MPI, and GPU are available.

MOCkingbird is a code developed by the Idaho National Laboratory [28]. It is based on the MOOSE platform, an open-source, parallel finite element framework that makes the

transport solver suitable for coupled multi-physics simulations [116]. For this purpose, the solver works with unstructured meshes. The source is constant within each region with transport-corrected P0 scattering cross sections. A DSA-type acceleration is planned to be implemented. The code relies on OpenMP and MPI parallelization.

TDT is a code developed at CEA for two-step calculations, specifically for lattice calculations. The source can be expanded in a polynomial basis in the axial direction, and the cross sections can also be treated similarly for depletion calculations. The scattering can be assumed to be anisotropic. The DP_0 and DP_1 acceleration techniques are implemented. OpenMP parallelization is implemented. Chapter 4 provides a summary of all available approximations.

3.6.3 . Random ray tracking

ARRC is a random ray neutron transport code developed in collaboration between MIT and Argonne National Laboratory. The code is designed for high-fidelity 3D reactor simulations. Regarding the physical approximations: the source is assumed to be constant within each computational region. The scattering is anisotropic. Currently, no acceleration techniques are implemented, but there are plans to develop a CMFD (Coarse Mesh Finite Difference) type acceleration. Parallelization using SIMD vectorization, OpenMP, and MPI is available [117, 118].

Unlike deterministic solvers, the ray tracking is not stored before the sweep but is performed on-the-fly using a uniform random distribution in space and angle. As a result, the sweep requires more floating-point operations, but there is no need for read/write operations associated with storing the ray tracking.

ARRC demonstrates excellent performance in terms of computation time [117]. On the 2D C5G7 benchmark, for a k_{eff} value within 20 pcm from the reference solution, OpenMOC (with CMFD) takes 0.69 core-hours, while ARRC requires 0.74 core-hours without acceleration [118]. These results are very promising. However, the Random Ray Method (RRM) has been implemented in the multi-group Monte Carlo (MGMC) solvers OpenMC [2] and SCONE [119], and compared on the same benchmark, the 2D C5G7, showing that the random ray approach has shorter computation times than the MGMC approach [120]. Thus, it would be interesting to compare how loop structures and vectorization strategies have been implemented.

4 - TDT-MOC solver within APOLLO3® code

Chapter 4 summarizes the key features of the TDT flux solver for neutron transport in extruded 3D geometries. It begins by outlining the strategy employed to construct 3D trajectories and reduce their memory footprint. The second and third sections detail the available approximations for the source and cross sections. Literature results are also reviewed.

Contents

4.1 . Treatment of 3D geometries

4.1.1 . Trajectories construction

First, let's recall that a trajectory refers to straight lines that pass through the geometry, and a chord is the set of intersection points between a trajectory and the computational region under consideration. The TDT solver handles extruded 3D geometries, with either structured or unstructured meshes, which can be described as the Cartesian product of a 2D geometry $\mathcal{R}_{2D}$ and a 1D axial geometry $\mathcal{R}_z$. The geometry is covered by trajectories as follows: for each azimuthal angle φ belonging to an optimal quadrature formula, the boundaries of the geometry are projected in the direction perpendicular to φ. The resulting segment is subdivided into sub-intervals of user-defined length Δr, known as transverse integration step. Finally, for each segment of length Δr, a trajectory with direction $(\varphi, \theta = 0)$, (where θ is the polar angle) passing through the midpoint of the segment is traced. Figure 4.1 (b) illustrates this step. Thus, each "2D" trajectory traverses a set of 2D regions denoted by $\mathcal{R}_s$.

4.1.2 . 3D trajectories construction

The 3D trajectories are then traced from the 2D trajectories as follows: the Cartesian product $\mathcal{R}_{sz} = \mathcal{R}_s \times \mathcal{R}_z$ is performed. This defines an sz-plane to which the trajectories will belong. To achieve this, the boundary of the $\mathcal{R}_{sz}$ plane is projected in the direction perpendicular to one of the angles θ from the quadrature formula. The resulting segment is subdivided into sub-intervals of user-defined length Δs, known as transverse integration paths. Finally, for each segment of length Δs, a trajectory with direction (φ, θ) passing through the midpoint of the segment is traced. Figure 4.1 (c) illustrates this step, where one of the sz-planes is represented.

If the algorithm is repeated for each angle φ and θ, then the 3D geometry is fully covered by trajectories. However, 3D tracking is memory-demanding; for instance, reference such as [23] provides an example of this: "Explicit storage of 3D segments in OpenMOC for a single assembly of the C5G7 benchmark with coarse MOC parameters required 79 GB of memory." To reduce the memory footprint of the tracking, two techniques have been implemented: the classification of chords and the hit surface sequence.

In 3D, the lengths of the chords are not normalized. Typically, the lengths are normalized so that the numerical volume equals the analytical volume, which ensures that the analytical particle balance is respected in the case of isotropic scattering [121].

4.1.3 . Cyclic trajectories

The solution of the transport equation in infinite media relies on cyclic trajectories, i.e. trajectories for which the exiting point $\boldsymbol{r}_{out}$ is equal to the entering point $\boldsymbol{r}_{in}$. Such trajectories

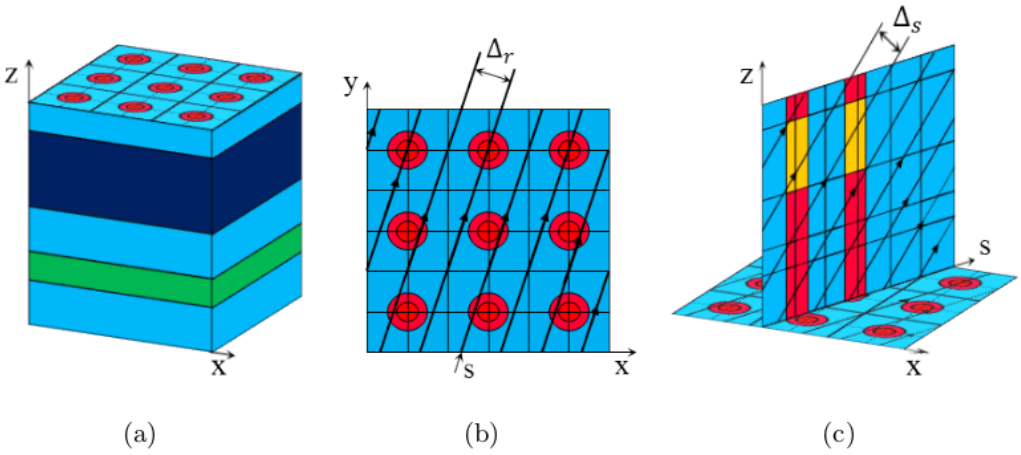

Figure 4.1 – TDT tracking strategy for 3D extruded geometries [5].

are obtained for rectangular or hexagonal geometries. Their tracking is based on the determination of cyclic directions $\mathbf{\Omega}_c = (\varphi_c, \theta_c)$, where φ_c and θ_c are the cyclic azimuthal and polar angles, respectively. The analysis carried out in the reference [122, 51] allows these angles to be determined from the geometric data of the problem: lengths, widths, heights...

These trajectories are used to evaluate the incoming flux into the domain in the case of closed boundary conditions. Indeed, if we consider a cyclic trajectory of length l, which traverses the geometry between $\boldsymbol{r}_{in}$ and $\boldsymbol{r}_{out}$, with $\boldsymbol{r}_{out} = \boldsymbol{r}_{in}$, then $\psi(\boldsymbol{r}_{out}, \mathbf{\Omega}) = \psi(\boldsymbol{r}_{in}, \mathbf{\Omega})$. Consequently, if we express the exiting angular flux using the transmission equation (3.16), we obtain:

$$\psi(\boldsymbol{r}_{in}, \mathbf{\Omega}) = \frac{\displaystyle\int_0^l \mathrm{d}t\, Q(\boldsymbol{r}_{out} - t\mathbf{\Omega})\, e^{-\tau(t)}}{1 - e^{-\tau(l)}}. \tag{4.1}$$

4.1.4 . Classification of chords

The chords can be categorized into four families: VV, HV, VH, and HH. These are illustrated in figure 4.2. The VV family consists of chords that enter and exit a region through vertical surfaces. The HV family includes chords that enter a region through a horizontal surface and exit through a vertical surface. The definitions of the VH- and HH-chords follow the same logic.

This classification is useful because it reduces the memory footprint of the tracking process. Indeed, all VV chords in the directions $\mathbf{\Omega}$, $-\mathbf{\Omega}$, $g_{\pi|z}(\mathbf{\Omega})$, and $-g_{\pi|z}(\mathbf{\Omega})$ that traverse any of

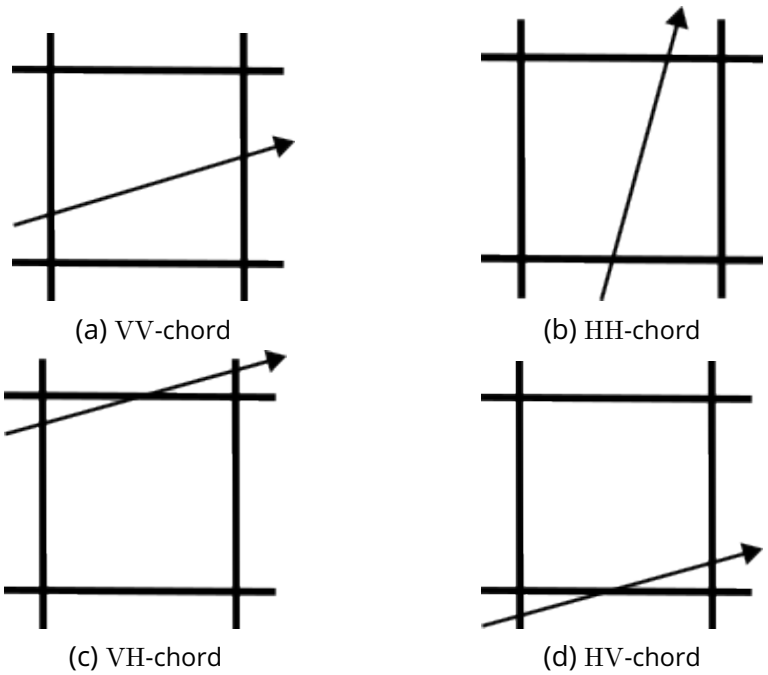

(a) VV-chord (b) HH-chord

(c) VH-chord (d) HV-chord

Figure 4.2 – Classification of chords crossing a region belonging to a sz-plane.

the regions belonging to a sz-plane $\mathcal{R}_{sz}$ are of the same length l. The notation $g_{\pi|z}$ designates the π rotation around the z-axis. Therefore, TDT only stores the 2D chord length associated with the angle θ. All data calculable from the length l, such as escape factors, are computed before sweeping each 3D trajectory, using the 2D length l_2 and the angle θ:

$$l = \frac{l_2}{sin(\theta)}. \tag{4.2}$$

A similar procedure is applied to HH-chords: all chords in the directions $\mathbf{\Omega}$, $-\mathbf{\Omega}$, $g_{\pi|z}(\mathbf{\Omega})$, and $-g_{\pi|z}(\mathbf{\Omega})$ that traverse any of the regions belonging to $r_z \times \mathcal{R}_{2D}$ have the same length l.

$$l = \frac{\Delta z}{cos(\theta)}, \tag{4.3}$$

with Δz representing the height of the 2D regions and θ the polar angle associated with the direction $\mathbf{\Omega}$. The HV- and VH-chords, known as mixed chords, are not classified.

Note that the distribution of chords type depends on the ratio of height to width of the calculation regions. Figure 4.3 provides an example, showing the distribution of the chord population for different values of the ratio between the axial node height and the average 2D chord length, based on geometry 4.4. For the reasons mentioned earlier, it is most advanta-

geous to achieve a high rate of classifications of type VV or HH. This is one of the arguments for developing the angular flux on a spatial basis in the axial direction. If precision can be maintained while reducing the number of axial meshes, the percentage of VV-chords for a given calculation region increases, thereby decreasing the memory footprint of the tracking.

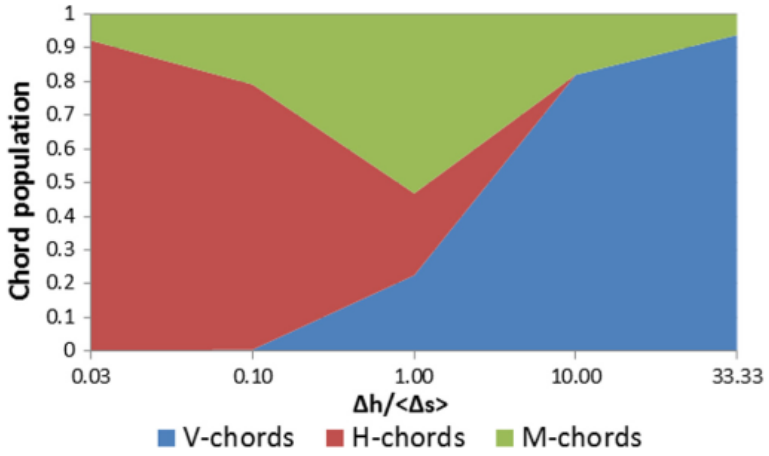

Figure 4.3 – Distribution of the chord population for different values of the ratio between the axial node height δh, and the average 2D chord length for a given 3D region [5]. V-chords (H-chords) designs VV-chords (HH-chords) and M-chords, HV- or VH-chords.

4.1.5 . Hit Surface Sequence

A complementary technique for reducing the memory footprint of trajectories tracking relies on data compression. A standard MOC trajectories tracking without optimizations requires storing in memory all the regions traversed by a 3D trajectory $\mathcal{R}_t$, defined as:

$$\mathcal{R}_t = \left\{ r_i,\, i \in [\![1, n_i^t]\!] \right\},$$

where n_i^t represents the number of regions traversed by trajectory t. However, the sequence of traversed regions can be reconstructed during the sweep, eliminating the need to store n_i^t for each trajectory. To achieve this, let's start with the following observation: If a trajectory t intersects a vertical surface, either it transitions to a different 2D region, or it encounters a vertical boundary of the domain. Conversely, if the trajectory intersects a horizontal surface, it either transitions to a different axial region or reaches a horizontal boundary of the domain.

Thus, if the first region traversed by trajectory t and the set of intersected surfaces are known, the regions in the set $\mathcal{R}_t$ can be reconstructed during the sweep. Additionally, it is unnecessary to store the type of surface crossed one after another; instead, it suffices to

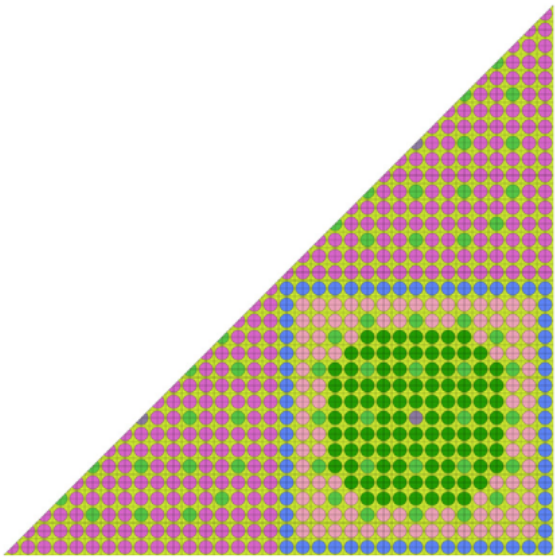

Figure 4.4 – Two-dimensional section of the basic domain with mesh details. The geometry is composed by one complete assembly with Uox composition, and two identical diagonal assemblies with Mox fuel. Each color represents a material composition [5].

record the number of consecutive surfaces of the same type, along with a $-$ or $+$ sign to indicate whether the trajectory crosses a vertical or horizontal surface.

To give you an example, consider a trajectory that traverses 100 regions ($n_i^t = 100$) but only through vertical surfaces. In this case, it is sufficient to store in memory $\mathcal{R}_t^{hss}$, defined as

$$\mathcal{R}_t^{hss} = \{r_1, -100\}\,,$$

where r_1 denotes the first 3D region traversed by the trajectory t, and the minus sign $-$ indicates that the surfaces crossed are vertical. In this way, the memory required to store the 3D part of the tracking is reduced. It is possible to determine the compression ratio of 3D tracking by calculating the ratio

$$\eta_{\text{trk}} = \frac{\sum_t \text{Card}(\mathcal{R}_t)}{\sum_t \text{Card}(\mathcal{R}_t^{hss})}.$$

4.2 . Polynomial expansion of the angular flux

In this section, the numerical expressions of the transmission and conservation equations related to the development of the angular flux (and consequently the source) are reviewed. For further details, see [6].

4.2.1 . Approximations

The axial polynomial method [56] relies on the hypothesis that the angular flux varies sufficiently smoothly to be described by a polynomial function and that cross sections are constant per region. The choice has been made to define a basis $\mathbf{P}$ for each spatial region i. For a point $\boldsymbol{r}$ in i of coordinate (x, y, z) one may evaluate the basis as

$$\mathbf{P}(z) = \left\{ \mathrm{P}_p(z) = \left(\frac{z - \bar{z}}{\Delta z/2} \right)^p,\ p \in [\![0, n_p]\!] \right\}, \tag{4.4}$$

where Δz is the height of the region crossed by the trajectory t, $\bar{z}$ is the value of the axial coordinate at the region center, and n_p is the maximum degree of the basis. This basis is only a function of the axial coordinate and geometrical parameters. As a consequence, the value of P_p varies between -1 and 1. This reduces the number of operations when a trajectory crosses horizontal surfaces and changes region [56]. In such case, the sign of P_p changes (from -1 to 1 or from 1 to -1) depending on whether the surface is the upper or the bottom one and if p is odd. Thus, one has to change the sign of the basis only for odd powers to evaluate the basis when switching regions. A graphical representation of the base for $n_p = 4$ is given in figure 4.5. Then, for any spatial region, the angular flux $\psi_i^g(\boldsymbol{r}, \boldsymbol{\Omega})$ is expanded on the polynomial basis and thus depends only on the axial coordinate. Mathematically, the hypothesis can be written as:

$$\psi_i^g(\boldsymbol{r}, \boldsymbol{\Omega}) = \sum_{p=0}^{n_p} \mathrm{P}_p(z)\, \psi_i^{g,p}(\boldsymbol{\Omega}). \tag{4.5}$$

Accordingly, the scattering and fission source, equation (3.12) and equation (3.13), are rewritten

$$\mathcal{H}^{g' \to g} \psi_i^{g'}(\boldsymbol{r}, \boldsymbol{\Omega}) = \sum_{n=1}^{n_m} A_n(\boldsymbol{\Omega}) \sum_{p=0}^{n_p} \mathrm{P}_p(z) \sum_{g'=1}^{n_g} \Sigma_{s,n}^{g' \to g} \phi_i^{g',n,p}, \tag{4.6}$$

$$\mathcal{F}^{g' \to g} \psi_i^{g'}(\boldsymbol{r}, \boldsymbol{\Omega}) = \sum_{j=1}^{n_j} \chi_j^g \sum_{p=0}^{n_p} \mathrm{P}_p(z) \sum_{g'=1}^{n_g} \nu_j^{g'} \Sigma_{f,j}^{g'} \phi_i^{g',0,p}, \tag{4.7}$$

with $\phi_i^{g,n,p}$ being the angular moments of each polynomial component:

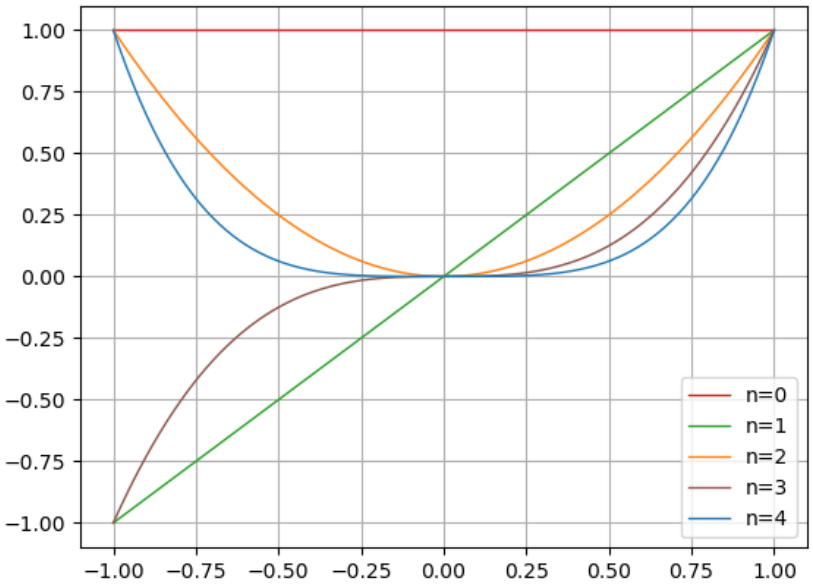

Figure 4.5 – Graphical representation of the polynomials of the base $\mathbf{P}$ (4.4) up to $n_p = 4$.

$$\phi_i^{g,n,p} = \frac{1}{4\pi} \int_{\mathbb{S}_2} \mathrm{d}\mathbf{\Omega} A_n(\mathbf{\Omega})\, \psi_i^{g,p}(\mathbf{\Omega}), \tag{4.8}$$

where $A_n(\mathbf{\Omega})$ designates the harmonic of order $n \in [\![1, n_m]\!]$, with $n_m = (\mathrm{K}+1)^2$, where K is the scattering order, and such that

$$\sum_{n=1}^{n_m} A_n(\mathbf{\Omega}) = \sum_{k=0}^{\mathrm{K}} \sum_{l=-k}^{k} A_k^l(\mathbf{\Omega}). \tag{4.9}$$

This notation is retained in the rest of the manuscript. The source is reformulated in an expression to suit the structure of the power iteration algorithm. Practically, the self-scattering term $\Sigma_{s,n}^{g\to g}(\boldsymbol{r})\phi_i^{g,n,p}$ of (4.6) is isolated from other energy groups and up- or down-scattering terms are gathered with the fission source contribution. From the point of view of self-scattering, fission and scattering from other energy groups may be seen as an external source. The emission density is now written as

$$Q_i^g(\boldsymbol{r}, \mathbf{\Omega}) = \sum_{n=1}^{n_m} A_n(\mathbf{\Omega}) \sum_{p=0}^{n_p} \mathrm{P}_p(z)\, Q_i^{g,n,p}, \tag{4.10}$$

where the component $Q_i^{g,n,p}$ is made of the self-scattering and external source contribution, $Q_{\text{self}}^{g,n,p}$ and $Q_{\text{ext}}^{g,n,p}$, respectively, such that

$$Q_i^{g,n,p} = Q_{\text{self}}^{g,n,p} + Q_{\text{ext}}^{g,n,p}, \tag{4.11}$$

where,

$$Q_{\text{self}}^{g,n,p} = \Sigma_{s,n}^{g\to g}\phi_i^{g,n,p}, \tag{4.12}$$

$$Q_{\text{ext}}^{g,n,p} = \sum_{g'\neq g}\Sigma_{s,n}^{g'\to g}\phi_i^{g',n,p} + \frac{\delta_{n,0}}{k_{\text{eff}}}\sum_{j=1}^{n_j}\chi_j^g\sum_{g'=1}^{n_g}\nu_j^{g'}\Sigma_{f,j}^{g'}\phi_i^{g',0,p}. \tag{4.13}$$

We also define $Q_i^{g,p}(\mathbf{\Omega})$ as

$$Q_i^{g,p}(\mathbf{\Omega}) = \sum_{n=1}^{n_m} A_n(\mathbf{\Omega})Q_i^{g,n,p}. \tag{4.14}$$

4.2.2 . Transmission equation

An iterative algorithm on the self-scattering source makes it possible to solve (3.10) until its convergence. At each iteration, the MOC scheme sweeps the geometry with trajectories to compute the angular flux along them. If one considers the trajectory crossing the region i between points $\boldsymbol{r}_{\text{in}}$ and $\boldsymbol{r}_{\text{out}}$, such that $l = ||\boldsymbol{r}_{\text{out}} - \boldsymbol{r}_{\text{in}}||$, the evaluation is made thanks to the transmission equation

$$\psi(\boldsymbol{r}_{out}, \mathbf{\Omega}) = \psi(\boldsymbol{r}_{in}, \mathbf{\Omega})e^{-\tau(l)} + \int_0^l \mathrm{d}t\, Q(\boldsymbol{r}_{in} + t\mathbf{\Omega})\, e^{-[\tau(l)-\tau(t)]}, \tag{4.15}$$

where τ is the optical path length defined as

$$\tau(t) = \int_0^t \mathrm{d}t'\Sigma_t(t') = \Sigma_t t. \tag{4.16}$$

To integrate the source term in Equation (4.15), a previous work [56] developed the source thanks to Newton's binomial coefficients to isolate the integration along the local coordinate t. The transmission is simplified as

$$\psi(\boldsymbol{r}_{out}, \boldsymbol{\Omega}) = \psi(\boldsymbol{r}_{in}, \boldsymbol{\Omega}) e^{-\tau(l)} + \mathbf{P}(\boldsymbol{r}_{in}) \cdot \mathbf{T}, \tag{4.17}$$

with $\mathbf{T}$ being the vector of components T_k defined as

$$\mathrm{T}_k = \sum_{p=k}^{n_p} \binom{p}{k} \left(\frac{2\mu}{\Delta z_r} \right)^{p-k} \frac{Q_p}{\Sigma_t}(\boldsymbol{\Omega})\, \mathrm{E}_{p-k}(\tau),$$

and where,

$$\mathrm{E}_p(\tau) = \frac{1}{\Sigma_t^p} \int_0^\tau \mathrm{d}\tau'\, \tau'^{,p}\, e^{-[\tau-\tau']}. \tag{4.18}$$

The integral part is retrieved from tabulated values to compute $\mathrm{E}_p(\tau)$. More information is detailed in [56].

4.2.3 . Conservation equation

The update of the source relies on the update of $\psi_i^{g,p}(\boldsymbol{\Omega})$ used to compute the angular moments of the flux defined in (5.8). To do so, one can obtain a balance equation per region i by projecting the multi-group transport equation (3.10) by means of the operator

$$\frac{1}{\mathrm{V}_i(\boldsymbol{\Omega})} \int \mathrm{d}\boldsymbol{r} \mathbf{P}(z)\,. \tag{4.19}$$

The projection leads to an angular balance equation. Details concerning its derivation are found in [56]. The conservation writes

$$\Sigma_t\, {}'\boldsymbol{\psi}_i(\boldsymbol{\Omega}) = -\Delta \mathbf{J}_i(\boldsymbol{\Omega}) + \mathbb{PP}(\boldsymbol{\Omega}) \cdot \boldsymbol{Q}(\boldsymbol{\Omega}) + \mu \mathbb{C}\, {}'\boldsymbol{\psi}_i(\boldsymbol{\Omega}). \tag{4.20}$$

${}'\boldsymbol{\psi}_i$ is the unknown defined as

$${}'\boldsymbol{\psi}_i(\boldsymbol{\Omega}) = \frac{1}{\mathrm{V}_i(\boldsymbol{\Omega})} \int_i \mathrm{d}\boldsymbol{r} \mathbf{P}(z) \psi(\boldsymbol{r}, \boldsymbol{\Omega}). \tag{4.21}$$

V_i is the volume of the region i, μ is the cosine of the polar angle θ of the direction $\boldsymbol{\Omega}$ and $\mathbb{C}$ is a triangular matrix that makes the resolution of Equation (4.20) hierarchic:

$$\mathbb{C} = \frac{2}{\Delta z} \begin{pmatrix} 0 & & & & \\ 1 & 0 & & & \\ 0 & 2 & 0 & & \\ \vdots & \ddots & \ddots & \ddots & \\ 0 & 0 & \dots & n_p & 0 \end{pmatrix}.$$

$\boldsymbol{Q}(\boldsymbol{\Omega})$ is the vector of the angular source components $Q^p(\boldsymbol{\Omega})$. $\mathbb{PP}(\boldsymbol{\Omega})$ is a $(n_p+1)\times(n_p+1)$ matrix computed thanks to a preliminary tracking-based integration and stored before the trajectory sweep. The matrix is defined as

$$\mathbb{PP}(\boldsymbol{\Omega}) = \frac{1}{\mathrm{V}_i(\boldsymbol{\Omega})} \int_i \mathrm{d}\boldsymbol{r} \mathbf{P}(z) \otimes \mathbf{P}(z), \tag{4.22}$$

where the component $\mathbb{PP}_{(n,m)}(\boldsymbol{\Omega})$ is computed as

$$\mathbb{PP}_{(n,m)}(\boldsymbol{\Omega}) = \frac{1}{\mathrm{V}_i(\boldsymbol{\Omega})} \sum_{\substack{t||\boldsymbol{\Omega} \\ t\cap i}} w_{\perp,t} \left\langle \mathrm{P}_n, \mathrm{P}_m \right\rangle, \tag{4.23}$$

where $w_{\perp,t}$ is the spatial integration weight of the trajectory t, and

$$\left\langle \mathrm{P}_n, \mathrm{P}_m \right\rangle = \int_0^l \mathrm{d}t \left[\frac{z_{in} + \mu t - \bar{z}}{\Delta z/2} \right]^{n+m}. \tag{4.24}$$

By introducing the function $\tilde{z}$ defined as

$$\tilde{z}(t) = \frac{z_{in} + \mu t - \bar{z}}{\Delta z/2}, \tag{4.25}$$

we can write the scalar product as

$$\left\langle \mathrm{P}_n, \mathrm{P}_m \right\rangle = \frac{\Delta z/2}{\mu} \int_{\tilde{z}(0)}^{\tilde{z}(l)} \mathrm{d}\tilde{z}\, \tilde{z}^{n+m},$$

and after integration:

$$\left\langle \mathrm{P}_n, \mathrm{P}_m \right\rangle = \frac{\Delta z/2}{\mu(p+1)} \left[\tilde{z}(l)^{n+m+1} - \tilde{z}(0)^{n+m+1} \right]. \tag{4.26}$$

Note that in (4.23), the volume is angle-dependent. The strategy gives better results regarding conservation (compared to angle-independent volume) since the volume and the integral are computed from the same tracking discretization. Then, one can remark that an analytical expression of $\mathbb{PP}(\mathbf{\Omega})$ is retrievable. The matrix will be noted $\mathbb{PP}^{\text{an}}$ and does not depend on angle. Its elements $\mathbb{PP}^{\text{an}}_{(n,m)}$ are defined as:

$$\begin{aligned}\mathbb{PP}^{\text{an}}_{(n,m)} &= \frac{1}{\mathrm{V}_i}\int \mathrm{d}\boldsymbol{r}\mathrm{P}_n(z)\otimes\mathrm{P}_m(z),\\ &= \frac{1}{\Delta z}\int_{\bar{z}-\Delta z/2}^{\bar{z}+\Delta z/2} dz\left[\frac{z-\bar{z}}{\Delta z/2}\right]^p,\\ &= \begin{cases}\frac{1}{n+m+1} & \text{if n+m even,}\\ 0 & \text{otherwise.}\end{cases}\end{aligned} \tag{4.27}$$

For simplicity, index n and m will be omitted. The volume normalization is angle-dependent in Equation (4.23). The reason behind the integration is that this way the first element of the matrix is one, no matter how accurate the tracking is, and due to this, the solver behaves better. The last term is the current $\Delta\mathbf{J}_i(\mathbf{\Omega})$, whose expression is

$$\Delta\mathbf{J}_i(\mathbf{\Omega}) = \frac{1}{\mathrm{V}_i(\mathbf{\Omega})}\int_{\partial i}\mathrm{d}\boldsymbol{r}\,\mathbf{\Omega}\cdot\boldsymbol{n}\,\mathbf{P}(z)\psi(\boldsymbol{r},\mathbf{\Omega}), \tag{4.28}$$

with $\boldsymbol{n}$ the normal to the surface at point $\boldsymbol{r}$. To determine its numerical equivalent the boundary ∂i is split in two borders ∂i^+ and ∂i^- such that, $\mathbf{\Omega}\cdot\boldsymbol{n} > 0$ on ∂i^+ and $\mathbf{\Omega}\cdot\boldsymbol{n} < 0$ on ∂i^-. The final expression is

$$\Delta\mathbf{J}_i(\mathbf{\Omega}) \sim \frac{1}{\mathrm{V}_i(\mathbf{\Omega})}\sum_{\substack{t||\Omega\\ t\cap i}} w_{\perp,t}\left[\mathbf{P}(z_{out})\psi(\boldsymbol{r}_{out},\mathbf{\Omega}) - \mathbf{P}(z_{in})\psi(\boldsymbol{r}_{in},\mathbf{\Omega})\right], \tag{4.29}$$

with $\boldsymbol{r}_{out}$ being the exiting point of coordinate $(x_{out}, y_{out}, z_{out})$ for trajectory t in region i. $\boldsymbol{r}_{in}$ the entering point is defined similarly.

4.2.4 . Results

Here, we recall some results related to the equations in the section 4.2, obtained during previous work [6]. These results are mentioned to justify the quality of the approximations made on the flux and their re-use in the developments of this thesis.

Verification calculations were performed on a portion of the ASTRID reactor, a sodium-cooled fast neutron reactor. Such a reactor offers several advantages: it better exploits from

uranium-238, the recycling of plutonium, and the transmutation of minor actinides. The reactor geometry is depicted in figure 4.6. Here, we focus solely on the reflected sub-assembly, which consists of a fissile layer and a fertile layer.

Table 4.1 summarizes the comparison between a calculation where, for a given accuracy, the flux was constant in the axial direction and a calculation where the flux was parabolic in the axial direction, i.e., of degree 2. The results were as follows: developing the flux axially allowed for a reduction in the number of axial meshes by a factor of 15 while maintaining the same accuracy (around -40 pcm) on the effective multiplication factor k_{eff} compared to the reference Monte Carlo calculation $k_{\text{eff}}^{\text{ref}} = 1.16103$. Additionally, the calculation showed gains in both memory usage and computation time. Specifically, the memory usage was reduced by a factor of 3.4, reaching 5.3 GB for the DP_1 accelerated calculation. The computation time was reduced by a factor of 2.11, with a total duration of 788 seconds.

Results performed on the half-column fuel sub-assembly and the full-column fuel sub-assembly, see figure 4.6, are provided in the thesis manuscript [6]. For instance, the depletion of the k_{eff} discrepancy compared to Monte Carlo code TRIPOLI-4® for polynomial degrees ranging from 0 to 3 is detailed. Results concerning a non-linear fitting technique that have been introduced in order to reduce the memory cost of DP_n matrices storage are also described.

Table 4.1 – Comparison of k_{eff}, time and memory requirement for a k-eigenvalue calculation with and without DP_1 acceleration. The k_{eff} is compared relatively to the one obtained with the Monte Carlo code TRIPOLI-4® to assess physical accuracy.

		Free iterations		**Acceleration**		**Δk_{eff} (pcm)**
Degree	Axial meshes	Memory (GB)	Time (s)	Memory (GB)	Time (s)	1.16103
0	30	2.2	18 891	17.9	1 719	-44
2	2	1.7	15 637	5.3	788	-41

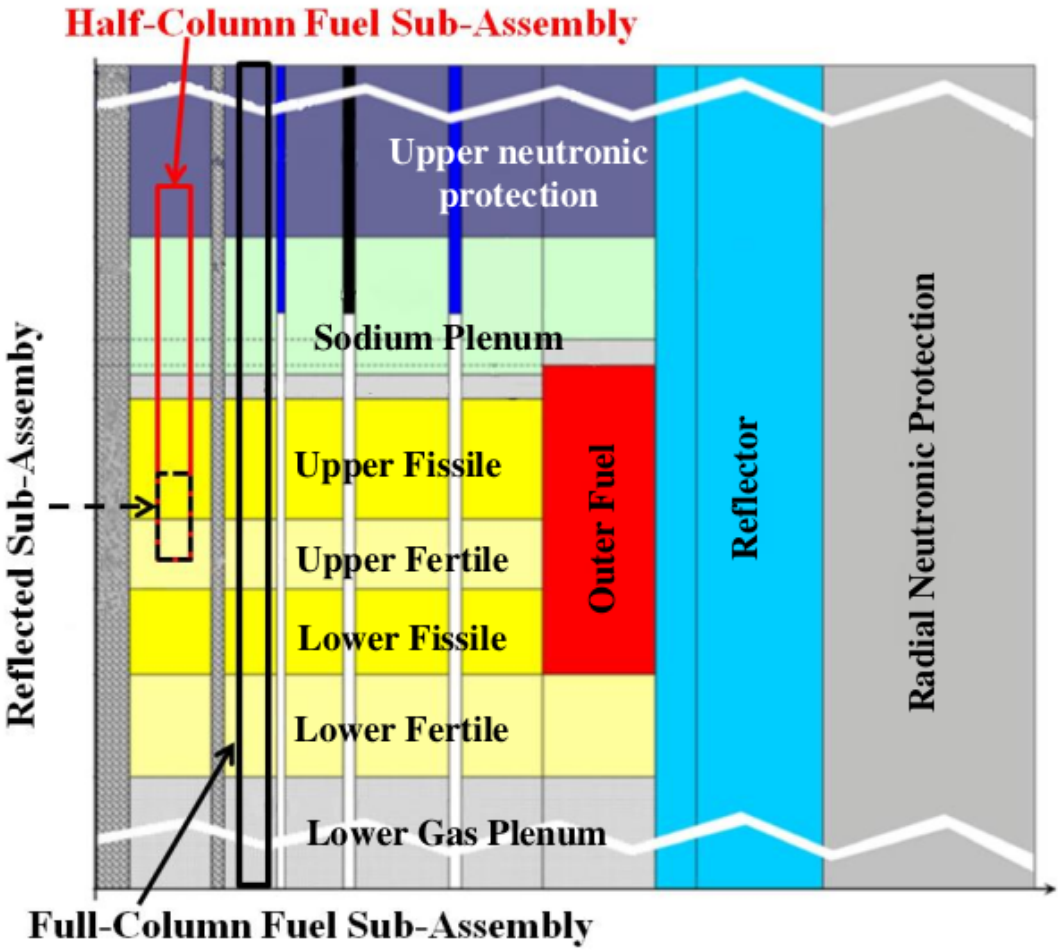

Figure 4.6 – Representation of ASTRID axial layout and of the three computational sub-assemblies [6].

4.3 . Polynomial expansion of the cross sections

In this section, the numerical expressions for the transmission and conservation equations relevant to the development of the angular flux and cross sections (and thus the source) are reminded. Indeed, if the user intends to perform a depletion calculation with a polynomial flux in the axial direction, then the cross sections will no longer be homogeneous for a computational cell. However, it is possible to assume that the cross sections vary in the same manner as the flux in the axial direction, thereby accounting for the influence of the spatial dependence of the flux on the depletion of the macroscopic spatial cross sections. For further details, see [7].

4.3.1 . Approximations

In the spatial regions where macroscopic cross sections are spatially expanded on the polynomial basis, a new approach to evaluate the transmission equation was implemented [57]. The choice of the basis is the same as the one used to develop the angular flux. For a nuclear reaction ρ, at position $\boldsymbol{r}$ and within region i, we write:

$$\Sigma_\rho(\boldsymbol{r}) = \sum_{p=0}^{n_p} \mathrm{P}_p(z)\Sigma_{\rho,p}. \tag{4.30}$$

This hypothesis has consequences on the expression of the optical thickness τ and the emission density $Q(\boldsymbol{\Omega})$. Concerning the optical thickness, if we consider a point $\boldsymbol{r}_{out}$ at a distance t from an origin $\boldsymbol{r}_{in} = (x_{in}, y_{in}, z_{in})$, and we plug (4.30) in the definition of τ, we obtain:

$$\begin{aligned} \tau(t) &= \int_0^t \mathrm{d}t' \Sigma_t(\boldsymbol{r}_{t'}), \\ &= \sum_{p=0}^{n_p} \Lambda_{p,0} t + \sum_{p=0}^{n_p-1} \Lambda_{p,1} t^2 + \ldots + \Lambda_{0,n_p} t^{n_p+1}, \end{aligned} \tag{4.31}$$

where:

$$\Lambda_{p,q} = \mathrm{P}_p(\boldsymbol{r}_{in})\Sigma_{t,p+q} \left(\frac{2\mu}{\Delta z}\right)^q \frac{1}{q+1} \binom{p+q}{p}. \tag{4.32}$$

The expression for the source also changes. The scattering and fission terms can be written as

$$\mathcal{H}^{g'\to g}\psi^{g'}(\boldsymbol{r},\boldsymbol{\Omega}) = \sum_{n=1}^{n_m} A_n(\boldsymbol{\Omega}) \sum_{k=0}^{2n_p} \sum_{p+q=k} \mathrm{P}_k(z) \sum_{g'=1}^{n_g} \Sigma_{s,n,q}^{g'\to g} \phi_i^{g',n,p}, \tag{4.33}$$

$$\mathcal{F}^{g'\to g}\psi^{g'}(\boldsymbol{r},\boldsymbol{\Omega}) = \sum_{j=1}^{n_j} \chi_j^g \sum_{k=0}^{2n_p} \sum_{p+q=k} \mathrm{P}_k(z) \sum_{g'=1}^{n_g} \nu_j^{g'} \Sigma_{f,j,q}^{g'} \phi_i^{g',0,p}. \tag{4.34}$$

The emission density is now written as

$$Q_i^g(\boldsymbol{r},\boldsymbol{\Omega}) = \sum_{n=1}^{n_m} A_n(\boldsymbol{\Omega}) \sum_{k=0}^{2n_p} \mathrm{P}_k(z)\, Q_i^{g,n,k}, \tag{4.35}$$

where the component $Q_i^{g,n,k}$ is made of the self-scattering and external source contribution, $Q_{\mathsf{self}}^{g,n,k}$ and $Q_{\mathsf{ext}}^{g,n,k}$, respectively, such that

$$Q_i^{g,n,k} = Q_{\mathsf{self}}^{g,n,k} + Q_{\mathsf{ext}}^{g,n,k}, \tag{4.36}$$

where

$$Q_{\mathsf{self}}^{g,n,k} = \sum_{p+q=k} \Sigma_{s,n,q}^{g\to g} \phi_i^{g,n,p}, \tag{4.37}$$

$$Q_{\mathsf{ext}}^{g,n,k} = \sum_{p+q=k} \left(\sum_{g'\neq g} \Sigma_{s,n,q}^{g'\to g} \phi_i^{g',n,p} + \frac{\delta_{n,0}}{k_{\mathsf{eff}}} \sum_{j=1}^{n_j} \chi_j^g \sum_{g'=1}^{n_g} \nu_j^{g'} \Sigma_{f,j,q}^{g'} \phi_i^{g',0,p} \right). \tag{4.38}$$

4.3.2 . Transmission equation

From (4.30) and (4.35), a specific transmission equation was introduced, which reads, for a chord of length l comprised between an entering point $\boldsymbol{r}_{in}$ and an exiting point $\boldsymbol{r}_{out}$,

$$\psi(\boldsymbol{r}_{out},\boldsymbol{\Omega}) = \psi(\boldsymbol{r}_{in},\boldsymbol{\Omega}) e^{-\tau(l)} + \mathbf{P}(\boldsymbol{r}_{in}) \cdot \mathbf{T}, \tag{4.39}$$

with $\mathbf{T}$ the vector of components T_k defined as

$$\mathrm{T}_k = \sum_{p=k}^{2n_p} \binom{p}{k} \left(\frac{2\mu}{\Delta z_r}\right)^{p-k} Q_p(\mathbf{\Omega})\, \mathrm{E}_{p-k},$$

and where,

$$\mathrm{E}_p = \int_0^l \mathrm{d}t\, t^p\, e^{-[\tau(l)-\tau(t)]}. \tag{4.40}$$

Here, it is not possible to modify the (4.40) to obtain a function of the optical path τ that could be tabulated as it is done for the case where cross sections are spatially constant (see (4.18)). Consequently, integrals E_p were computed thanks to a Gauss-Legendre quadrature when cross sections are expanded polynomially [57]. The new strategy modifies the transmission equation but also relies on a Gauss-Legendre quadrature. We write:

$$\psi(\boldsymbol{r}_{out}, \mathbf{\Omega}) = \psi(\boldsymbol{r}_{in}, \mathbf{\Omega}) e^{-\tau(l)} + \boldsymbol{Q}(\mathbf{\Omega}) \cdot \underbrace{\int_0^l \mathrm{d}t\, \mathbf{P}(z_{in} + \mu t)\, e^{-[\tau(l)-\tau(t)]}}_{\tilde{\mathbf{E}}}, \tag{4.41}$$

with $\tilde{\mathbf{E}}$ the vector of components $\tilde{\mathrm{E}}_p$:

$$\tilde{\mathrm{E}}_p = \int_0^l \mathrm{d}t\, \left[\frac{z_{in} + \mu t - \tilde{z}}{\Delta z/2}\right]^p e^{-[\tau(l)-\tau(t)]}. \tag{4.42}$$

All the $\tilde{\mathrm{E}}_p$ are now computed through a Gauss-Legendre quadrature, instead of the integral E_p defined in Equation (4.40). The integration limits are set between -1 and 1 thanks to the change of variable $t(x) = \frac{l}{2}(1+x)$. It leads to the approximation

$$\tilde{\mathrm{E}}_p \approx \frac{l}{2} \sum_{j=1}^{m} w_j \left[\mathrm{P}_1(\boldsymbol{r}_{in}) + \frac{2\mu}{\Delta z_r}\, t(x_j)\right]^p e^{\tau(t(x_j))-\tau(l)}, \tag{4.43}$$

with x_j the roots of the m^{th}-degree Legendre polynomial, w_j the weights associated to the chosen quadrature order and $t(x_j) = \frac{l}{2}(1+x_j)$ and P_1 the polynomial component of order one of the basis introduced in Equation (4.4). A first sweep is performed before the transport one to determine the integer m. For each chord and energy group, $\tilde{\mathrm{E}}_p$ estimations are performed with m increasing until falling below a certain tolerance. After that, m is stored in memory. If m exceeds a certain limit m_{max}, the integration interval is divided into smaller intervals. However, it has been shown that $m = 5$ is enough for 90% of chords [7]. In terms of memory, the new strategy employed constitutes an advantage compared to the former

strategy as it only saves the scalar $\boldsymbol{Q}(\boldsymbol{\Omega}) \cdot \tilde{\mathbf{E}}$ in memory instead of the vectors $\mathbf{P}(\boldsymbol{r}_{in})$ and $\mathbf{T}$ [123].

4.3.3 . Conservation equation

The update of the source relies on the update of $\psi_p(\boldsymbol{\Omega})$ used to compute the angular moments of the flux defined in (5.8). To do so, one can obtain a balance equation per region i by projecting the multi-group transport equation (3.10) by means of the operator (4.19)

$$\sum_{k=0}^{n_p} \Sigma_{t,k} \sum_{q=0}^{n_p} \mathrm{P}_{p+k,q} \psi_i^q(\boldsymbol{\Omega}) - p\frac{2}{\Delta z} \sum_{q=0}^{n_p} \mathrm{P}_{p-1,j} \psi_i^q(\boldsymbol{\Omega}) \\ - \Delta \mathrm{J}_{i,p}(\boldsymbol{\Omega}) + \left(\mathbb{PP}^{2n_p}(\boldsymbol{\Omega}) \cdot \boldsymbol{Q}(\boldsymbol{\Omega})\right)_p, \quad (4.44)$$

where,

$$\Delta \mathrm{J}_{i,p}(\boldsymbol{\Omega}) = \frac{1}{\mathrm{V}_i(\boldsymbol{\Omega})} \int_{\partial i} \mathrm{d}\boldsymbol{r}\, \boldsymbol{\Omega} \cdot \boldsymbol{n}\, \mathrm{P}_p(z) \psi(\boldsymbol{r}, \boldsymbol{\Omega}), \quad (4.45)$$

and,

$$\mathbb{PP}^{2n_p}(\boldsymbol{\Omega}) = \frac{1}{\mathrm{V}_i(\boldsymbol{\Omega})} \int_i \mathrm{d}\boldsymbol{r} \mathbf{P}(z) \otimes \mathbf{P}^{2n_p}(z), \quad (4.46)$$

with,

$$\mathbf{P}^{2n_p}(z) = \left\{ \mathrm{P}_p(z) = \left(\frac{z - \bar{z}}{\Delta z/2} \right)^p,\ p \in [\![0, 2n_p]\!] \right\}. \quad (4.47)$$

The equation (4.44) is a balance equation on the $n_p + 1$ angular coefficients of the flux. The resolution of the system for every spatial component and every direction belonging to the angular quadrature allows to update the emission density through (4.33) and (4.34).

4.3.4 . Information transfer between flux and depletion solvers

It is important to recall that the cross sections are expanded on a polynomial basis within the depletion calculations so that the isotopic inventory can track the spatial variations in the flux. To achieve this, we discuss how the cross sections values are communicated to the self-shielding and depletion solvers. The data exchange is not straightforward since the

cross sections are treated as polynomial in the axial direction for the flux solver, while they are uniform for the self-shielding and depletion calculations.

To facilitate data exchange, we consider a "polynomial" mesh consisting of a single region i_{pol} and a step mesh composed of n_{sc} regions. At the end of a depletion step, we have a set of depleted and self-shielded cross sections for each region within the step mesh. Then, for each reaction ρ, the cross sections for the polynomial mesh are determined by conserving the moments $\Sigma'_{\rho,p}$

$$'\Sigma_{\rho,p} = \frac{1}{\mathrm{V}_{i_{pol}}} \int_{i_{pol}} \mathrm{d}\boldsymbol{r} \mathrm{P}_p(z) \Sigma_\rho(\boldsymbol{r}). \tag{4.48}$$

The integration is then decomposed over each region $i \in [\![1, n_{sc}]\!]$

$$'\Sigma_{\rho,p} = \frac{1}{\Delta z_{i_{pol}}} \sum_{i=1}^{n_{sc}} \Sigma_{\rho,i} \int_{z_{min}}^{z_{max}} \mathrm{d}z \mathrm{P}_p(z), \tag{4.49}$$

with $\Delta z_{i_{\text{pol}}}$ representing the height of region i_{pol}, and z_{min} and z_{max} denoting the axial coordinates of each region in the step mesh. However, to reduce the size of the library required to store the cross sections for the n_{sc} regions, a mesh with n_{gs} axial cells associated with a Gauss-Legendre quadrature is used instead. Such a mesh is referred to as Gaussian mesh. Therefore, to evaluate (4.48), an n_{gs}-point quadrature is employed:

$$'\Sigma_{\rho,p} = \frac{1}{2} \sum_{i=1}^{n_{gs}} w_i (x_i)^p \Sigma_{i,\rho}, \tag{4.50}$$

with x_i and w_i being the roots of the Legendre polynomial of order n_{gs} and the corresponding Gaussian weights proportional to the height of each region $\Delta z_{i_{pol}}$, where $i \in [\![1, n_{gs}]\!]$, respectively. The only requirement for the selection of n_{gs} is that it must be able to integrate a polynomial of degree $2n_p$. Therefore, n_{gs} must satisfy the condition $2n_{gs} - 1 \geq 2n_p$. According to the results provided in [57], the use of a Gaussian mesh for depletion and self-shielding solvers in a 17x17 PWR assembly enabled a reduction in memory footprint by 55% compared to a 87 axial layers step mesh.

4.3.5 . Results

Here, we recall some results related to the equations in the section 4.3, obtained during previous work [7]. These results are mentioned to justify the quality of the approximations made on both the flux and cross-sections, and their re-use in the developments of this thesis.

Depletion calculations with spatially dependent cross sections were verified by comparison with uniform cross-section and source per region, on a 17x17 PWR assembly, with the radial and axial meshes displayed in figure 4.7 and in figure 4.8, respectively. It is worth noting that the calculation was performed on the lower half of the assembly and on 1/8 of the radial section. For details on the isotopic compositions of the various materials at the beginning of the cycle, as well as the calculation parameters (angular quadrature, spatial integration, convergence criteria for the power iteration method, etc.), the reader is referred to [7]. The fuel was depleted up to a burn-up of 60 GWd/t. The effective multiplication factor k_{eff} was compared with a depletion calculation where the flux and cross sections are uniform in each calculation region; i.e., axially, this calculation uses the mesh from figure 4.8 (c). The transport was accelerated using synthetic acceleration DP_1. The two calculations are referenced as FPX and FSC, FPX designating the case with polynomial cross sections, or as FPX_fit and FSC_fit if a fitting technique is applied to reduce the memory cost of the acceleration.

Two results are highlighted here: a comparison of the depletion of the effective multiplication factor k_{eff} between the FPX and FSC calculations, and the spatial profile of the total macroscopic cross section Σ_t for selected energy groups, including group 167, which contains the lowest-energy resonance of uranium-238.

Regarding k_{eff}, the relative error between the FPX and FSC calculations (with FSC taken as the reference) does not exceed 120 pcm, as shown in figure 4.9. Additionally, as mentioned in [7], at the beginning of the cycle, the FPX calculation is at -39 pcm compared to the Monte Carlo solution obtained with TRIPOLI-4®, while the FSC calculation is at -126 pcm. More specifically, the largest errors (between 100 and 120 pcm) occur between 0 and 20 $\mathrm{GWd/t}$. Beyond 20 $\mathrm{GWd/t}$, the relative error decreases, reaching 60 pcm at 60 $\mathrm{GWd/t}$. Furthermore, the fitting technique used to reduce the memory cost of the DP_n acceleration does not alter the depletion of the relative error between the two calculations. Finally, the FPX calculation took 105 hours, compared to 259 hours for the calculation with uniform flux and cross sections. These results were obtained on a machine with two EPYC 7352 CPUs @ 2.3 GHz using 48 OpenMP threads.

Regarding the cross sections spatial profile, figure 4.10 shows that the spatial variation is mainly located near the reflector for each chosen energy group.

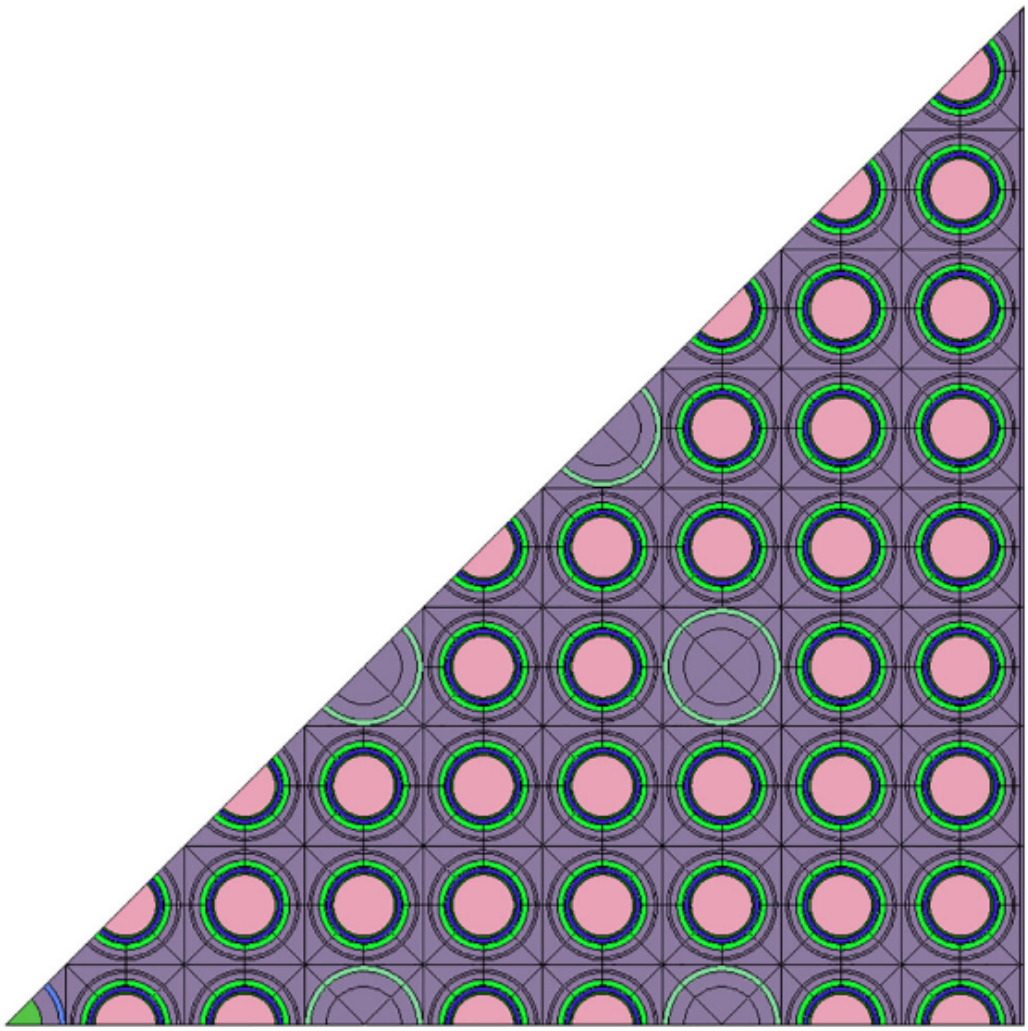

Figure 4.7 – Two-dimensional radial section of the 17x17 PWR assembly [7].

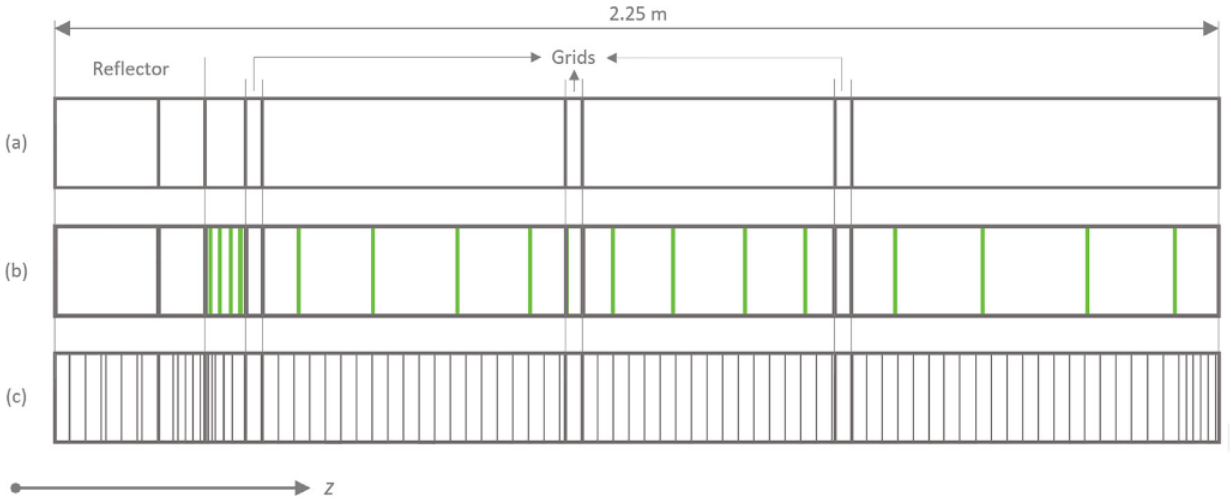

Figure 4.8 – Half axial meshes of the 17x17 PWR assembly composed of a bottom reflector, grids, and fuel: (a) is the polynomial mesh which corresponds to the material mesh, (b) is the gaussian mesh, and (c) is the step one used for comparison with uniform flux and cross sections approximations [7].

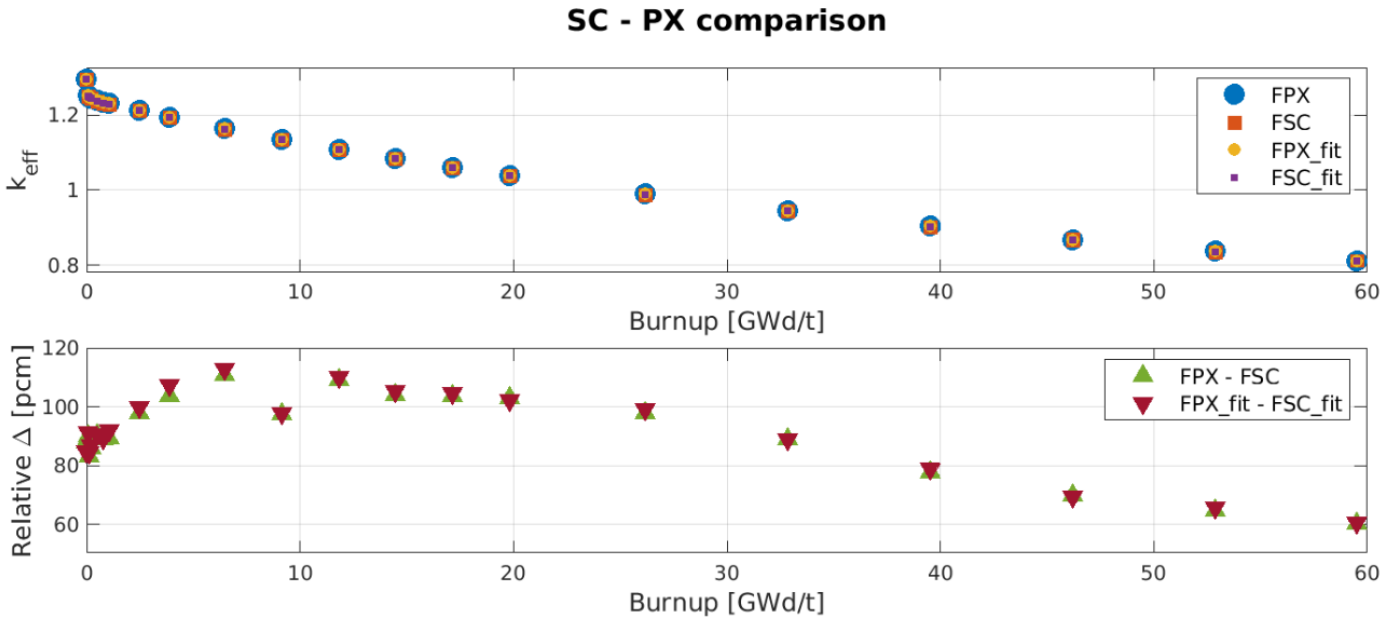

Figure 4.9 – Evolution of k_{eff} up to a burn-up of $60\ \text{GWd/t}$ and the relative error between the FPX and FSC calculations, with and without the fitting technique that reduces the memory cost of storing matrices required for DP_1 acceleration [7].

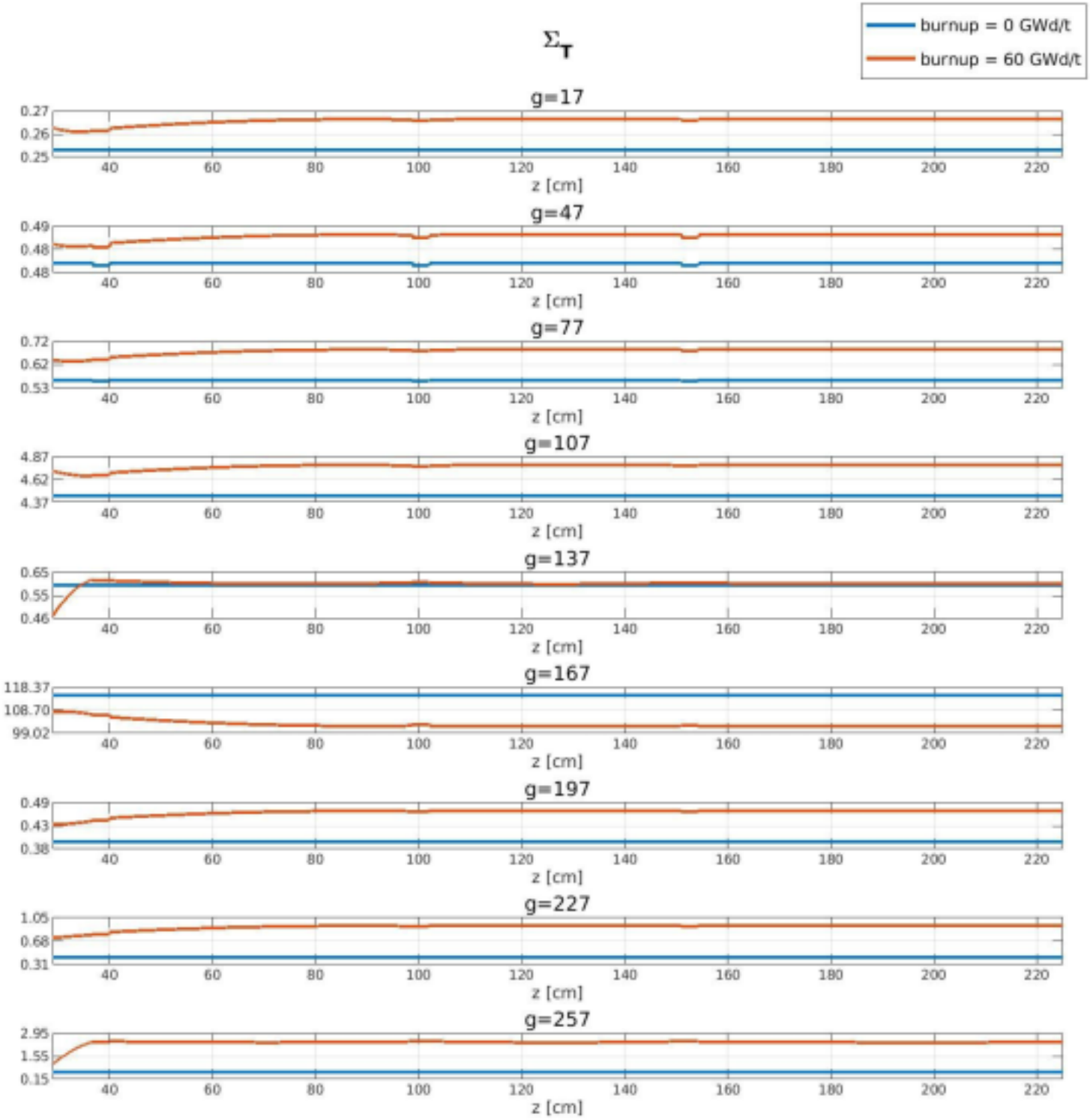

Figure 4.10 – Spatial profile of the total macroscopic cross sections at 0 and 60 $\mathrm{GWd/t}$ for various energy groups, including group 167 corresponding to the lowest-energy resonance of uranium-238. The values have been plotted for the two-dimensional region exhibiting the maximum axial gradient of the system [7].

5 - Surface characteristics scheme

The chapter starts presenting new developments implemented in the TDT solver during the PhD for the treatment of extruded 3D geometries, incorporating polynomial variations of flux in the axial direction. After introducing the method of handling surfaces using TDT, the surface linear approximation is discussed. Finally, the associated transmission and conservation equations are derived.

Contents

5.1 . Surface representation

5.1.1 . Geometry discretization

Before discussing the choice of interpolation, it is important to note that the quantities of interest introduced in Chapter 2 are developed on the surfaces of the geometry. Thus, as depicted in figure 5.1, each computational region i, with boundary ∂i, is divided into n_s surfaces α_k such that

$$\partial i = \bigcup_{k=1}^{n_s} \alpha_k. \tag{5.1}$$

In three dimensions, TDT recognizes the extruded surfaces along z that can be derived from segments, arcs and circles, for given finite heights, and the interface surfaces parallel to the xy plane that separate the 3D regions. These last are not simply rectangle or rectangle-circle, but an arbitrary 2D form that can be obtained by a sequence of segments, arcs or (isolated) circles, as shown with the BWR assembly discretization in figure 5.2. From now on, vertical surfaces will refer to the surfaces where the coordinate along the z-axis varies. The set of vertical surfaces in a region is denoted ∂i_v. Horizontal surfaces will be those where the z-coordinate remains constant at every point on the surface.

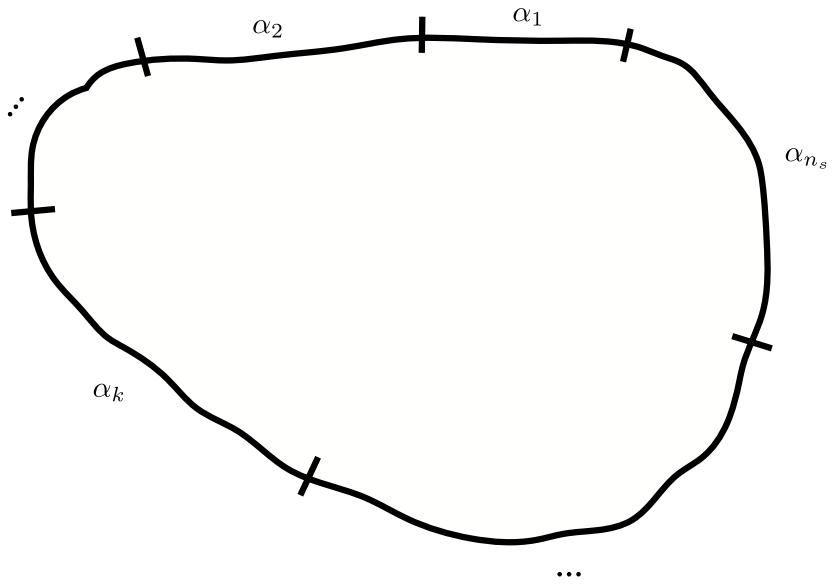

Figure 5.1 – Representation of the decomposition of the boundary ∂i of a given spatial region i in n_s surfaces.

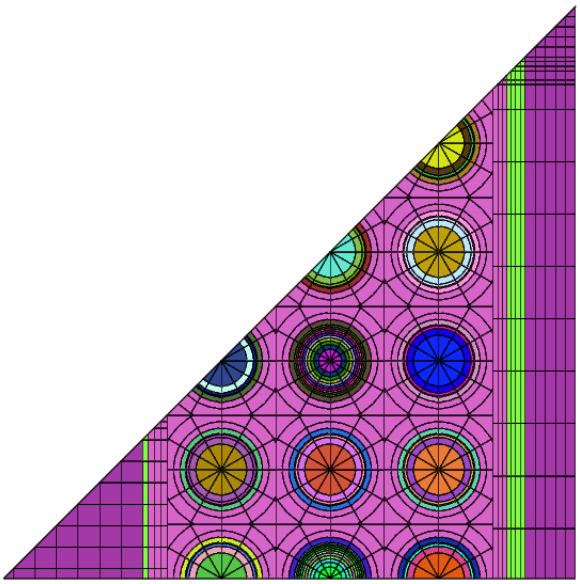

Figure 5.2 – Two-dimensional section of the BWR lattice defined as a part of the Burn-up Credit Criticality Safety Benchmark coordinated by NEA/OECD [8].

5.1.2 . Tracking-based integration of surfaces

We consider a surface α and call S_α^{ana} the analytical value of its area, defined as

$$S_\alpha^{\text{ana}} = \int_\alpha \mathrm{d}\boldsymbol{r}. \tag{5.2}$$

The numerical areas are calculated from a tracking-based integration. Their accuracy depends on the number of directions and chords per direction. They are defined as

$$S_\alpha^{\text{num}} = \sum_{\boldsymbol{\Omega}_n \in S_n} w_n \sum_{\substack{t || \boldsymbol{\Omega}_n \\ t \cap \alpha}} w_{\perp,t}(\boldsymbol{\Omega}_n), \tag{5.3}$$

with $w_{\perp,t}(\boldsymbol{\Omega}_n)$, the integration weight associated with each trajectory, calculated as

$$w_{\perp,t}(\boldsymbol{\Omega}_n) = \frac{\Delta r \Delta s}{|\boldsymbol{n} \cdot \boldsymbol{\Omega}_n|}, \tag{5.4}$$

where $\boldsymbol{n}$ is the normal to the surface α_k intersected by the trajectory t at a certain point. The comparison between analytical and numerical values is important because it provides information about the quality of surface integration. Poor surface integration can hinder the

convergence of internal iterations.

In two dimensions, an adaptive tracking method is implemented, allowing for the addition of trajectories locally [124]. This technique has not been implemented for the treatment of 3D geometries. Thus, the accuracy of the tracking, i.e., the values imposed on Δr and Δs, is conditioned by the precision required to integrate the smallest surface in the geometry.

5.1.3 . Definition of surface quantities

For any surface α on ∂i, the angular flux $\psi_\alpha^g(\boldsymbol{r}, \boldsymbol{\Omega})$ is expanded on the polynomial basis (4.4). Mathematically, the hypothesis can be written as:

$$\psi_\alpha^g(\boldsymbol{r}, \boldsymbol{\Omega}) = \sum_{p=0}^{n_p} \mathrm{P}_p(z)\, \psi_\alpha^{g,p}(\boldsymbol{\Omega}). \tag{5.5}$$

Accordingly, the scattering and fission source are rewritten as:

$$\mathcal{H}^{g'\to g}\psi_\alpha^{g'}(\boldsymbol{r}, \boldsymbol{\Omega}) = \sum_{n=1}^{n_m} A_n(\boldsymbol{\Omega}) \sum_{p=0}^{n_p} \mathrm{P}_p(z) \sum_{g'=1}^{n_g} \Sigma_{s,n}^{g'\to g} \phi_\alpha^{g',n,p}, \tag{5.6}$$

$$\mathcal{F}^{g'\to g}\psi_\alpha^{g'}(\boldsymbol{r}, \boldsymbol{\Omega}) = \sum_{j=1}^{n_j} \chi_j^g \sum_{p=0}^{n_p} \mathrm{P}_p(z) \sum_{g'=1}^{n_g} \nu_j^{g'} \Sigma_{f,j}^{g'} \phi_\alpha^{g',0,p}, \tag{5.7}$$

with $\phi_\alpha^{g,n,p}$ being the surface angular moments of each polynomial component:

$$\phi_\alpha^{g,n,p} = \frac{1}{4\pi} \int_{\mathbb{S}_2} \mathrm{d}\boldsymbol{\Omega} A_n(\boldsymbol{\Omega})\, \psi_\alpha^{g,p}(\boldsymbol{\Omega}). \tag{5.8}$$

The surface source is now written as

$$Q_\alpha^g(\boldsymbol{r}, \boldsymbol{\Omega}) = \sum_{n=1}^{n_m} A_n(\boldsymbol{\Omega}) \sum_{p=0}^{n_p} \mathrm{P}_p(z)\, Q_\alpha^{g,n,p}, \tag{5.9}$$

where the component $Q_\alpha^{g,n,p}$ is made of the self-scattering and external source contribution, $Q_{\mathsf{self}}^{g,n,p}$ and $Q_{\mathsf{ext}}^{g,n,p}$, respectively, such that

$$Q_\alpha^{g,n,p} = Q_{\mathsf{self}}^{g,n,p} + Q_{\mathsf{ext}}^{g,n,p}, \tag{5.10}$$

where,

$$Q_{\text{self}}^{g,n,p} = \Sigma_{s,n}^{g\to g}\phi_{\alpha}^{g,n,p}, \tag{5.11}$$

$$Q_{\text{ext}}^{g,n,p} = \sum_{g'\neq g}\Sigma_{s,n}^{g'\to g}\phi_{\alpha}^{g',n,p} + \frac{\delta_{n,0}}{k_{\text{eff}}}\sum_{j=1}^{n_j}\chi_j^g\sum_{g'=1}^{n_g}\nu_j^{g'}\Sigma_{f,j}^{g'}\phi_{\alpha}^{g',0,p}. \tag{5.12}$$

We also define $Q_{\alpha}^{g,p}(\mathbf{\Omega})$ as

$$Q_{\alpha}^{g,p}(\mathbf{\Omega}) = \sum_{n=1}^{n_m} A_n(\mathbf{\Omega})Q_{\alpha}^{g,n,p}. \tag{5.13}$$

The surface moments are only evaluated for the vertical surfaces $\alpha \in \partial i_v$. Their analytical expression is

$${}'\Phi_{\alpha}^{n,p} = \frac{1}{4\pi S_{\alpha}}\int_{\mathbb{S}_2}\mathrm{d}\mathbf{\Omega}A_n(\mathbf{\Omega})\int_{\alpha}\mathrm{d}\boldsymbol{r}\mathrm{P}_p(\boldsymbol{r})\psi(\boldsymbol{r},\mathbf{\Omega}). \tag{5.14}$$

Numerically, the moments are evaluated as

$${}'\Phi_{\alpha}^{n,p} = \frac{1}{4\pi S_{\alpha}}\sum_{\mathbf{\Omega}_n\in S_n} w_n A_n(\mathbf{\Omega}_n)\sum_{\substack{t||\Omega\\ t\cap\alpha}} w_{\perp,t}(\mathbf{\Omega}_n)\mathrm{P}_p(z_t)\psi_{\alpha,t}(\mathbf{\Omega}). \tag{5.15}$$

From a computational point of view, the moments are organized into a vector in the following manner:

$${}'\mathbf{\Phi}_{\alpha} = \left\{ {}'\Phi_{\alpha}^{1,0}, {}'\Phi_{\alpha}^{2,0}, \ldots, {}'\Phi_{\alpha}^{n,p}, \ldots, {}'\Phi_{\alpha}^{n_m-1,n_p}, {}'\Phi_{\alpha}^{n_m,n_p}\right\}. \tag{5.16}$$

5.2 . Choice of the linear interpolation

This section details the choice of linear approximation implemented in the TDT solver. To this end, two strategies are compared. The first strategy is based on the linear interpolation of the source between surface values that vary polynomially in the axial direction (see (5.9)). The second strategy is based on the development of the source at a point on a trajectory, followed by the linear interpolation of each of its components. The transmission equations

associated with these two approaches are derived.

To introduce the subsequent discussion, we consider a point $\boldsymbol{r}_t$ with coordinates (x_t, y_t, z_t) on a chord of length l and direction $\boldsymbol{\Omega}$ that traverses region i entering through surface β at point $\boldsymbol{r}_{in}$ and exiting through surface α at point $\boldsymbol{r}_{out}$. Let t denote the distance between point $\boldsymbol{r}_{in}$ and $\boldsymbol{r}_t$, $t = [|\boldsymbol{r}_t - \boldsymbol{r}_{in}|]$, such that $\boldsymbol{r}_t = \boldsymbol{r}_{in} + t\boldsymbol{\Omega}$. A graphical representation of the chord where the notation are included is shown in figure in 5.3. The macroscopic cross sections are constant per region. For simplicity, the transmission equation for a finite domain is rewritten as

$$\psi(\boldsymbol{r}_{out}, \boldsymbol{\Omega}) = \psi(\boldsymbol{r}_{in}, \boldsymbol{\Omega}) e^{-\tau(l)} + \int_0^l \mathrm{d}t\, Q(\boldsymbol{r}_{in} + t\boldsymbol{\Omega})\, e^{-[\tau(l)-\tau(t)]}. \tag{5.17}$$

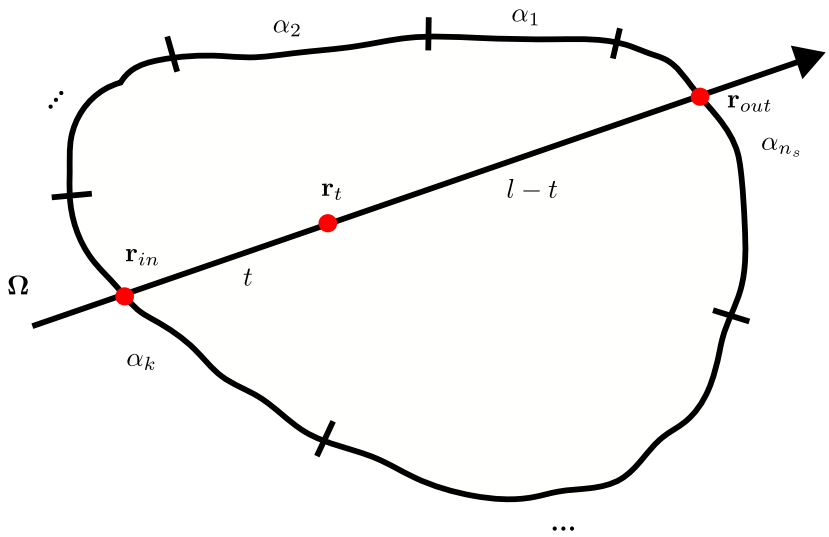

Figure 5.3 – Representation of a chord of length l crossing region i between surfaces α_k and α_{n_s} through $\boldsymbol{r}_{in}$ and $\boldsymbol{r}_{out}$, respectively.

5.2.1 . Source interpolation between surfaces

We assume that the source at point $\boldsymbol{r}_t$ varies linearly between the values of the surface source, and that the vertical surface source varies according to the basis $\mathbf{P}$ (4.4). Practically, we recall that each 3D trajectory belongs to a sz-plane. Keeping this in mind, a graphical representation of the interpolation strategy is shown in figure in 5.4: the source is simply interpolated between the entering and exiting source, on β and α, respectively. Thus, we write

$$Q(\boldsymbol{r}_t, \boldsymbol{\Omega}) = Q_\beta(z_{in}, \boldsymbol{\Omega}) \left(1 - \frac{t}{l}\right) + Q_\alpha(z_{out}, \boldsymbol{\Omega}) \frac{t}{l}. \tag{5.18}$$

To obtain the associated transmission equation, it is sufficient to substitute (5.18) into (5.17)

$$\psi(\boldsymbol{r}_{out}, \boldsymbol{\Omega}) = \psi(\boldsymbol{r}_{in}, \boldsymbol{\Omega}) e^{-\tau(l)} + \frac{Q_\beta(z_{in}, \boldsymbol{\Omega})}{\Sigma_t} \mathrm{E}_0(\tau) + \frac{Q_\alpha(z_{out}, \boldsymbol{\Omega}) - Q_\beta(z_{in}, \boldsymbol{\Omega})}{\Sigma_t} \frac{1}{l} \mathrm{E}_1(\tau), \tag{5.19}$$

with,

$$Q_\beta(z_{in}, \boldsymbol{\Omega}) = \sum_{p=0}^{n_p} \mathrm{P}_p(z_{in}) Q_\beta^p(\boldsymbol{\Omega}), \tag{5.20}$$

$$Q_\alpha(z_{out}, \boldsymbol{\Omega}) = \sum_{p=0}^{n_p} \mathrm{P}_p(z_{out}) Q_\alpha^p(\boldsymbol{\Omega}), \tag{5.21}$$

and with,

$$\mathrm{E}_0(\tau) = 1 - e^{-\tau}, \tag{5.22}$$

$$\mathrm{E}_1(\tau) = l - \frac{1}{\Sigma_t}(1 - e^{-\tau}). \tag{5.23}$$

Some comments now. Note that surface sources are normalized, including horizontal sources defined on horizontal surfaces. Unfortunately, it is generally challenging to integrate horizontal surfaces from tracking. Indeed, for an industrial scale mesh with given tracking parameters, the fraction of chords that intersect the horizontal surfaces of a region i is at least an order of magnitude smaller than that of chords that intersect the vertical surfaces of region i. Figure 4.3 provides an initial impression of this phenomenon. This effect becomes even more significant as it is now possible to expand the flux on a polynomial basis in the axial direction, which increases the ratio $\Delta \mathrm{h} / \Delta \langle s \rangle$. This specific characteristic of tracking in 3D geometries will be discussed in greater detail in Chapter 6. Of course, it would be possible to use analytical values for horizontal surfaces and numerical values for vertical surfaces, but this would likely introduce errors in particle conservation during the balance assessment [49]. The same observation applies if values for any type of surface were used,

since the quantities calculated are derived from tracking-based integration. Thus, approximation (5.18) has not been implemented.

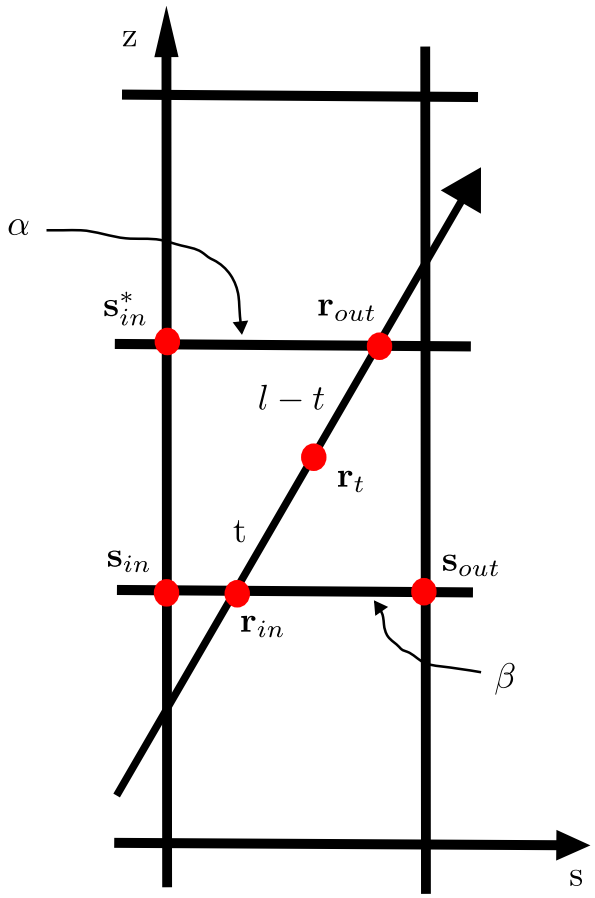

Figure 5.4 – First source interpolation strategy. For a given direction $\mathbf{\Omega}$, the source in $\boldsymbol{r}_t$ is interpolated from the source on β and α.

5.2.2 . Interpolation of source components

We assume that the source at point r_t can be expanded in the basis $\mathbf{P}$ (4.4) for the axial direction, and that each spatial component varies linearly between the surface spatial components. Thus, we write

$$Q(\boldsymbol{r}_t, \mathbf{\Omega}) = \sum_{p=0}^{n_p} \mathrm{P}_p(z_t) Q^p(\mathbf{\Omega}), \tag{5.24}$$

$$Q^p(\mathbf{\Omega}) = Q^p_\beta(\mathbf{\Omega}) \left(1 - \frac{t}{l}\right) + Q^p_\alpha(\mathbf{\Omega}) \frac{t}{l}. \tag{5.25}$$

Note that for a VV-type chord, this amounts to performing radial interpolation of the surface components. According to section (4.1.1), the chord is known to belong to a region of the sz-plane. Let t_2 and l_2 denote the projections of t and l onto the s-axis, respectively. Thus,

$$Q^p(\mathbf{\Omega}) = Q^p_\beta(\mathbf{\Omega})\left(1 - \frac{t_2}{l_2}\right) + Q^p_\alpha(\mathbf{\Omega})\frac{t_2}{l_2}. \tag{5.26}$$

Then, if we substitute (5.26) into (5.17), we obtain a transmission equation similar to (4.17), which is detailed in 4.2.2. That is, just as in the case where the source is volumetric, the escape factors are considered up to the n_p order. However, for HH-type chords, the source is assumed to be spatially constant on a horizontal surface as there is no variation in the axial coordinate. Consequently, the interpolation (5.24) simplifies to

$$Q(\boldsymbol{r}_t, \mathbf{\Omega}) = Q^0_\beta(\mathbf{\Omega})\left(1 - \frac{t}{l}\right) + Q^0_\alpha(\mathbf{\Omega})\frac{t}{l}. \tag{5.27}$$

The transmission equation then reads

$$\psi(\boldsymbol{r}_{out}, \mathbf{\Omega}) = \psi(\boldsymbol{r}_{in}, \mathbf{\Omega})e^{-\tau(l)} + \frac{Q^0_\beta(z_{in}, \mathbf{\Omega})}{\Sigma_t}\mathrm{E}_0(\tau) + \frac{Q^0_\alpha(z_{out}, \mathbf{\Omega}) - Q^0_\beta(z_{in}, \mathbf{\Omega})}{\Sigma_t}\frac{1}{l}\mathrm{E}_1(\tau), \tag{5.28}$$

with $\mathrm{E}_0(\tau)$ and $\mathrm{E}_1(\tau)$ defined by (5.22) and (5.23), respectively. This places us in the same situation as with the first approximation of the source, with the same disadvantages. However, it should be noted that expression (5.28) only applies to HH-type chords, which are particularly present in computational regions where the height is small relative to the 2D length of the region, as shown in figure (4.3). Therefore, it is possible that (5.28) provides a reasonably good approximation of $\psi(\boldsymbol{r}_{out}, \mathbf{\Omega})$. Nonetheless, the difficulty in integrating horizontal surfaces compared to vertical ones remains. A solution to address this issue is presented in the following section.

5.2.3 . On-the-fly horizontal source computation

As explained in the two preceding sections, two radial interpolations can be defined. In this thesis, the choice was made to implement equation (5.25) to obtain an evaluable expression of the transmission equation. The reasoning used is to note that, with this approximation, the source is assumed to be polynomial in the axial direction at each point along the

chord, unlike the first approximation, which assumes the source to be polynomial only on the vertical surfaces. Thus, it can be expected that the error on the outgoing angular flux will be lower with this approximation compared to the first approximation introduced. Quantitatively, this results in a transmission equation with more floating-point operations. (See (5.40) and (5.19)). However, it would be reasonable to implement the first approximation in order to perform a numerical comparison (physical accuracy, computation time) of the two approaches.

Then, to bypass the issue of integrating horizontal surfaces, horizontal sources are computed on-the-fly based on the source defined on vertical surfaces. Below, we explain how the interpolation is performed after introducing some useful definitions.

Consider a chord of length l in a region of the sz-plane with polar angle θ. This chord is of type $\mathrm{VV}, \mathrm{HV}, \mathrm{VH}$, or HH. It is noted that this chord is part of a set of chords of size n_c located between an incoming vertical surface γ and an outgoing vertical surface $\gamma^\star$. If the chord is of type VV, then the set of chords size is one, ($n_c = 1$). If the chord is of type VH and is followed by a chord of type HV, then the set of chords size is two, ($n_c = 2$).

Furthermore, a VH chord is always followed by an HV chord or a sequence of HH chords followed by an HV chord. The same reasoning applies to HV chords, but in the opposite direction. Finally, HH chords are part of a sequence of HH chords bounded by a VH chord and an HV chord. Each length thus belongs to a set of n_c lengths with a total length L_{tot}, defined as

$$\mathrm{L}_{tot} = \sum_{k=1}^{n_c} l_k. \tag{5.29}$$

The cumulative length L_k is also defined as:

$$\mathrm{L}_k = \sum_{i=1}^{k} l_i. \tag{5.30}$$

With these definitions in place, we can now construct the sources on the horizontal surfaces. If the chord is the k^{th} of the set, we define:

$$Q^p_\beta(\mathbf{\Omega}) = Q^p_\gamma(\mathbf{\Omega}) \left(1 - \frac{\mathrm{L}_{k-1}}{\mathrm{L}_{tot}}\right) + Q^p_{\gamma^\star}(\mathbf{\Omega}) \frac{\mathrm{L}_{k-1}}{\mathrm{L}_{tot}}, \tag{5.31}$$

$$Q^p_\alpha(\mathbf{\Omega}) = Q^p_\gamma(\mathbf{\Omega}) \left(1 - \frac{\mathrm{L}_{k}}{\mathrm{L}_{tot}}\right) + Q^p_{\gamma^\star}(\mathbf{\Omega}) \frac{\mathrm{L}_{k}}{\mathrm{L}_{tot}}. \tag{5.32}$$

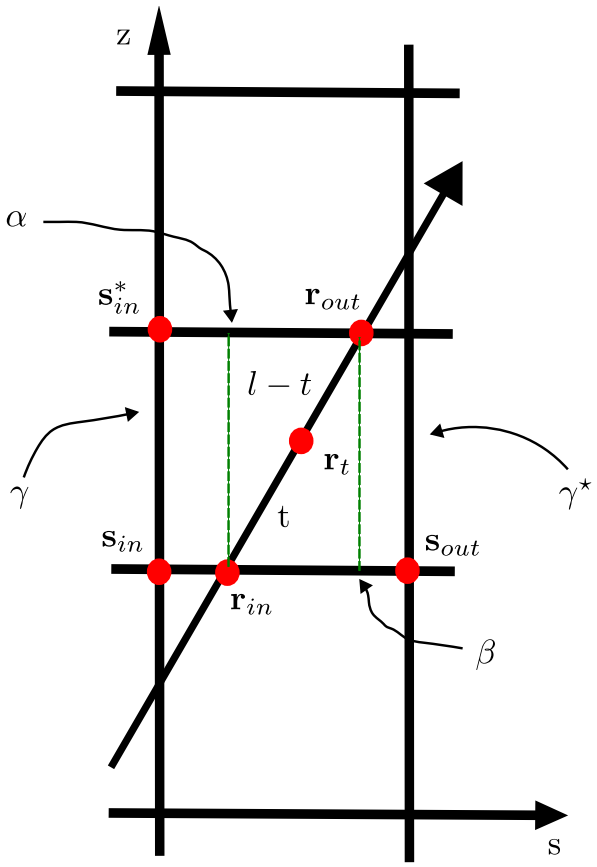

Figure 5.5 – On-the-fly horizontal source interpolation strategy. The source in $\boldsymbol{r}_t$ is interpolated from the source on β and α constructed from source on γ and $\gamma^\star$.

Note that if the incoming surface is vertical, then $\mathrm{L}_{k-1} = 0$ and $Q^p_\beta = Q^p_\gamma$. Similarly, if the outgoing surface is vertical, $\mathrm{L}_k = \mathrm{L}_{tot}$ and $Q^p_\alpha = Q^p_{\gamma^\star}$. Additionally, along the tracking sweep, if the chord considered is of type HH one can use (5.31) and (5.32), analogous to the on-the-fly construction of vertical surfaces. In practice, we do not store in memory L_k and L_{tot} for each chord during the tracking phase. Instead, the projection onto the s-axis is applied by using the fact that $\mathrm{L}_{2,tot} = cos(\theta)\mathrm{L}_{tot}$ and $\mathrm{L}_{2,k} = cos(\theta)\mathrm{L}_k$, such that

$$Q^p_\beta(\boldsymbol{\Omega}) = Q^p_\gamma(\boldsymbol{\Omega})\left(1 - \frac{\mathrm{L}_{2,k-1}}{\mathrm{L}_{2,tot}}\right) + Q^p_{\gamma^\star}(\boldsymbol{\Omega})\frac{\mathrm{L}_{2,k-1}}{\mathrm{L}_{2,tot}}, \tag{5.33}$$

$$Q^p_\alpha(\boldsymbol{\Omega}) = Q^p_\gamma(\boldsymbol{\Omega})\left(1 - \frac{\mathrm{L}_{2,k}}{\mathrm{L}_{2,tot}}\right) + Q^p_{\gamma^\star}(\boldsymbol{\Omega})\frac{\mathrm{L}_{2,k}}{\mathrm{L}_{2,tot}}, \tag{5.34}$$

with $\mathrm{L}_{2,k}$ and $\mathrm{L}_{2,tot}$ that are computed on-the-fly during each 3D trajectory reconstruction that precedes the sweep. During the reconstruction (5.33) and (5.34) are also evaluated to store $Q^p_\beta(\boldsymbol{\Omega})$ and $Q^p_\alpha(\boldsymbol{\Omega})$ before the sweep for each type of chords except for the VV chords.

The last point is that trajectories do not always begin by crossing a vertical surface. Thus, one cannot assume that $\mathrm{L}_1 = l_1$. It is necessary to account for the contribution of the 2D chord segment from which the local 3D one starts from, as shown in figure 5.6. For such trajectories, we introduce the length l_{ini}, represented in figure 5.6, and such that $\mathrm{L}_1 = l_{ini} + l_1$. The value of l_{ini} is obtained by the tracking algorithm.

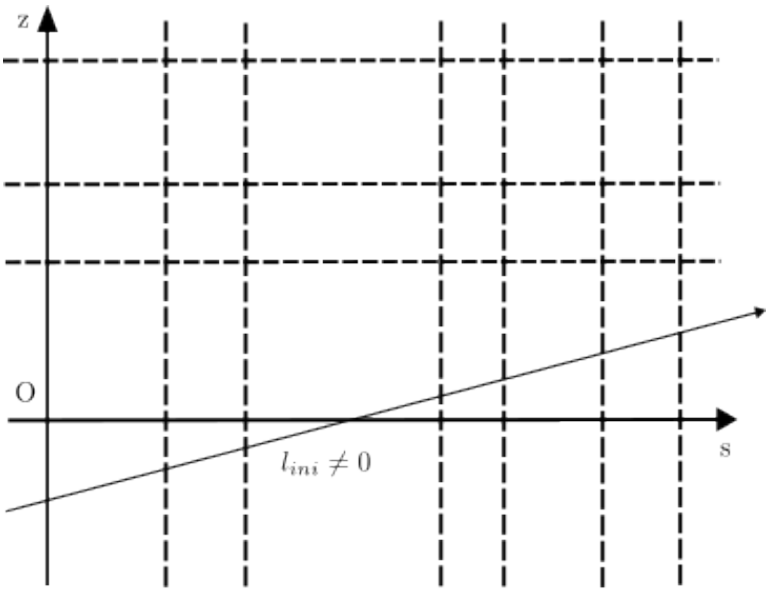

Figure 5.6 – 3D trajectory entering a sz-plane by crossing a horizontal surface.

On the contrary, if trajectories begin by entering the sz-plane by crossing a vertical surface, then $l_{ini} = 0$, as shown in figure 5.7.

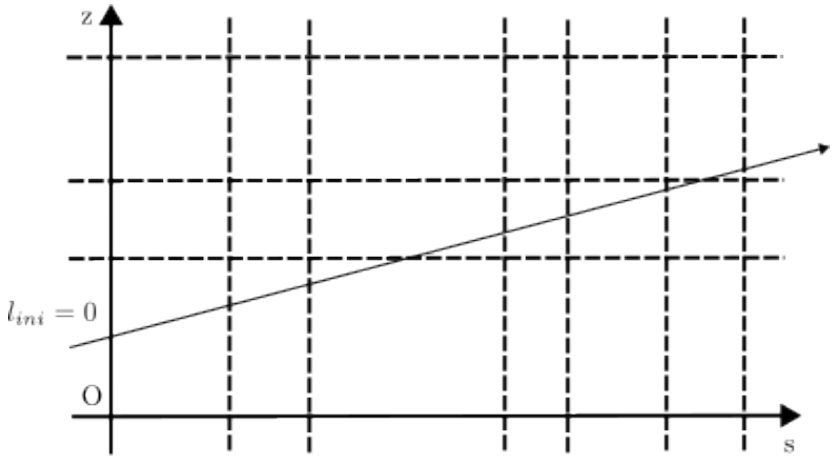

Figure 5.7 – 3D trajectory entering a sz-plane by crossing a vertical surface.

5.3 . Transmission equation

The approximation of the surface linear scheme is established; it is now possible to numerically evaluate the transmission equation. Similarly to the previous section, let us consider a chord t of length l that traverses region i entering through surface β at point $\boldsymbol{r}_{in}$ and exiting through surface α at point $\boldsymbol{r}_{out}$. Let t denote the distance between point $\boldsymbol{r}_{in}$ and $\boldsymbol{r}_t$, where $t = [|\boldsymbol{r}_t - \boldsymbol{r}_{in}|]$, so that $\boldsymbol{r}_t = \boldsymbol{r}_{in} + t\boldsymbol{\Omega}$. Next, we substitute (5.25) into (5.17). This yields:

$$\psi(\boldsymbol{r}_{out}, \boldsymbol{\Omega}) = \psi(\boldsymbol{r}_{in}, \boldsymbol{\Omega}) e^{-\tau(l)} + \int_0^l \mathrm{d}t \mathbf{P}(z) \cdot \left[\boldsymbol{Q}_\beta(\boldsymbol{\Omega})(1 - \frac{t}{l}) + \boldsymbol{Q}_\alpha(\boldsymbol{\Omega}) \frac{t}{l} \right] e^{-(\tau(l)-\tau(t))}, \quad (5.35)$$

Then, we develop $\mathbf{P}$ (4.4) to take out the integral constant. This gives:

$$\begin{aligned} &\int_0^l \mathrm{d}t (1 - \frac{t}{l}) \mathbf{P}(z) \cdot \boldsymbol{Q}_\beta(\boldsymbol{\Omega}) e^{-(\tau(l)-\tau(t))} \\ &= \sum_{p=0}^{n_p} \sum_{k=0}^{p} \binom{p}{k} \left[\frac{z_0 - \tilde{z}}{\Delta z/2} \right]^k \left(\frac{2\mu}{\Delta z} \right)^{p-k} Q_\beta^p(\boldsymbol{\Omega}) \mathrm{E}_{p-k}^-(l), \\ &= \sum_{k=0}^{n_p} \sum_{p=k}^{n_p} \binom{p}{k} \left[\frac{z_0 - \tilde{z}}{\Delta z/2} \right]^k \left(\frac{2\mu}{\Delta z} \right)^{p-k} Q_\beta^p(\boldsymbol{\Omega}) \mathrm{E}_{p-k}^-(l), \end{aligned} \quad (5.36)$$

where

$$\mathrm{E}_{p-k}^-(l) = \int_0^l \mathrm{d}t (1 - \frac{t}{l}) t^{p-k} e^{-(\tau(l)-\tau(t))}. \quad (5.37)$$

In E_{p-k}^-, the symbol "$-$" means that we multiply the power of t and the integral by the factor $(1 - \frac{t}{l})$. We can similarly define E_{p-k}^+ with a multiplication by $\frac{t}{l}$. Then, we can write

$$\begin{aligned} \int_0^l \mathrm{d}t' (1 - \frac{t}{l}) \mathbf{P}(z) \cdot \boldsymbol{Q}_\beta(\boldsymbol{\Omega}) e^{-(\tau(t)-\tau(t'))} &= \sum_{k=0}^{n_p} \mathrm{P}_k(z_{in}) \mathrm{T}_k^-(\boldsymbol{\Omega}), \\ &= \mathbf{P}(z_{in}) \cdot \mathbf{T}^-(\boldsymbol{\Omega}), \end{aligned}$$

with:

$$\mathbf{T}^{-}(\mathbf{\Omega}) = \left\{ \sum_{p=k}^{n_p} \binom{p}{k} \left(\frac{2\mu}{\Delta z}\right)^{p-k} Q_{\beta}^{p}(\mathbf{\Omega}) \mathrm{E}_{p-k}^{-}(l), \quad k \in [|0, n_p|] \right\}, \tag{5.38}$$

$$\mathbf{T}^{+}(\mathbf{\Omega}) = \left\{ \sum_{p=k}^{n_p} \binom{p}{k} \left(\frac{2\mu}{\Delta z}\right)^{p-k} Q_{\alpha}^{p}(\mathbf{\Omega}) \mathrm{E}_{p-k}^{+}(l), \quad k \in [|0, n_p|] \right\}. \tag{5.39}$$

Finally, we get the transmission equation expression. It writes

$$\psi(\boldsymbol{r}_{out}, \mathbf{\Omega}) = \psi(\boldsymbol{r}_{in}, \mathbf{\Omega}) e^{-\tau(l)} + \mathbf{P}(z_{in}) \cdot \left[\mathbf{T}^{-}(\mathbf{\Omega}) + \mathbf{T}^{+}(\mathbf{\Omega}) \right]. \tag{5.40}$$

One may note the difference between expression (5.19) and expression (5.40) obtained in the case where the source is expanded on the polynomial basis for each point along the chord. In the first case, the leakage factor is accounted for up to the first order, whereas it is accounted for up to the n_p^{th} order in the second expression. One might therefore conjecture that (5.19) represents the spatial variation of the source less accurately compared to (5.40) since it is only considered on the surfaces of the region.

5.3.1 . Numerical evaluation of spectral factors

In this section, we detail the algorithm behind the computation of the spectral factors E_k^- and E_k^+. Two cases will be considered according to the type of cross sections; spatially uniform or following a polynomial variation along the axial direction. If the cross sections are polynomial, the evaluation of E_k^- and E_k^+ will follow a different algorithm than the one used in the step constant hypothesis. To begin let's start with the definitions:

$$\mathrm{E}_k^+(l) = \frac{1}{l} \int_0^l \mathrm{d}t t^{k+1} e^{-(\tau(l)-\tau(t))}, \tag{5.41}$$

$$\mathrm{E}_k^-(l) = \int_0^l \mathrm{d}t (1 - \frac{t}{l}) t^k e^{-(\tau(l)-\tau(t))}. \tag{5.42}$$

Now, it is useful to note that E_k^- can be expressed in terms of l and E_k^+. Indeed, by expanding the factor $1 - \frac{t}{l}$, we obtain

$$\begin{aligned}
\mathrm{E}_k^-(l) &= \int_0^l \mathrm{d}t \left(1 - \frac{t}{l}\right) t^k e^{-(\tau(l)-\tau(t))}, \\
&= \int_0^l \mathrm{d}t t^k e^{-(\tau(l)-\tau(t))} - \frac{1}{l}\int_0^l \mathrm{d}t t^{k+1} e^{-(\tau(l)-\tau(t))}, \\
&= l\mathrm{E}_{k-1}^+(l) - \mathrm{E}_k^+(l).
\end{aligned}$$

Consequently, only the calculation of the functions E_k^+ is detailed in the remainder of the section.

5.3.2 . Constant cross sections case

If one considers the cross section Σ_t spatially constant wihtin a region i, the optical path (3.17) writes:

$$\tau(t) = \Sigma_t t. \tag{5.43}$$

Then for every value of k, E_k^+ factors become:

$$\begin{aligned}
\mathrm{E}_k^+(l) &= \frac{1}{l}\int_0^l \mathrm{d}t t^{k+1} e^{-\Sigma_t(l-t)}, \\
&= \frac{1}{\Sigma_t l}\frac{1}{\Sigma_t^{k+1}}\int_0^{\tau(l)} \mathrm{d}\tau' \tau'^{,k+1} e^{-(\tau'-\tau(l))}, \\
&= \frac{1}{\Sigma_t l}\mathrm{E}_{k+1}(\tau),
\end{aligned}$$

with

$$\mathrm{E}_k(\tau) = \frac{1}{\Sigma_t^k}\int_0^\tau \mathrm{d}\tau' \tau'^k e^{-(\tau-\tau')}. \tag{5.44}$$

So that,

$$\begin{aligned}
\mathrm{E}_k^- &= l\mathrm{E}_{k-1}^+(l) - \mathrm{E}_k^+(l), \\
&= \frac{1}{\Sigma_t}\left[\mathrm{E}_k(\tau) - \frac{1}{l}\mathrm{E}_{k+1}(\tau)\right].
\end{aligned}$$

For instance, in the particular case of $k = 0$, it is possible to obtain an analytical expression of E_0^+ thanks to an integration by part.

$$\mathrm{E}_0^+(\tau) = \frac{1}{\Sigma_t}\left[1 - (1 - e^{-\tau})/\tau)\right]. \tag{5.45}$$

Demonstration:

$$\begin{aligned}
\mathrm{E}_0^+(t) &= \frac{1}{l}\int_0^l \mathrm{d}t t e^{-\Sigma_t(l-t)}, \\
&= \frac{1}{\Sigma_t l}\left[te^{-\Sigma_t(l-t)}\right]_0^l - \frac{1}{\Sigma_t l}\mathrm{d}t e^{-\Sigma(l-t)}, \\
&= \frac{1}{\Sigma_t} - \frac{1}{\Sigma_t^2 l}\left[e^{-\Sigma_t(l-t)}\right]_0^l, \\
&= \frac{1}{\Sigma_t}\left[1 - (1 - e^{-\tau})/\tau)\right].
\end{aligned}$$

Finally, we introduce E_k^T for the next discussion:

$$\mathrm{E}_k^T(\tau) = \frac{1}{l^k}\mathrm{E}_k(\tau), \tag{5.46}$$

$$\mathrm{E}_k^T(\tau) = \frac{1}{\tau^k}\int_0^\tau \mathrm{d}\tau' \tau'^k e^{-(\tau-\tau')}. \tag{5.47}$$

Numerically, $\mathrm{E}_k^-(\tau)$ and $\mathrm{E}_k^+(\tau)$ are computed from the tabulated $\mathrm{E}_k^T(\tau)$ (5.47) to avoid numerical instability issues for small values of τ. Specifically, for $\tau \gg \tau_c$, a recurrence relation is used to calculate all orders starting from order 0, whose analytical expression is $\mathrm{E}_0^T(\tau) = 1 - e^{-\tau}$. In the case where $\tau \ll \tau_c$, E_k^T is computed up to the highest order using a series expansion, before calculating the lower orders using a recurrence formula [56].

5.3.3 . Polynomial cross sections case

As for the scalar product defined in Equation (4.26), the optical path may be computed thanks to the same change of variable in order to save floating point operations. The expression writes

$$\tau(t) = \frac{\Delta z/2}{\mu}\sum_{p=0}^{n_p}\frac{1}{p+1}\left[\tilde{z}(t)^{p+1} - \tilde{z}(0)^{p+1}\right]\Sigma_{t,p}. \tag{5.48}$$

When the cross sections are spatially dependent, tabulations can no longer be used to evaluate the spectral factors. Instead, a Gauss-Legendre quadrature is employed, which, as

demonstrated in [125], helps save memory and computational time. To this end, let us start from the transmission equation (5.35) and rewrite it in the form:

$$\psi(\boldsymbol{r}_{out}, \boldsymbol{\Omega}) = \psi(\boldsymbol{r}_{in}, \boldsymbol{\Omega}) e^{-\tau(l)} + \int_0^l \mathrm{d}t \mathbf{P}(z) \cdot \boldsymbol{Q}_\beta(\boldsymbol{\Omega}) e^{-(\tau(l)-\tau(t))} + \frac{1}{l} \int_0^l \mathrm{d}t \mathbf{P}(z) t \cdot \left[\boldsymbol{Q}_\alpha(\boldsymbol{\Omega}) - \boldsymbol{Q}_\beta(\boldsymbol{\Omega})\right] e^{-(\tau(l)-\tau(t))}, \quad (5.49)$$

with the components of the source that can be factored out of the integral:

$$\psi(\boldsymbol{r}_{out}, \boldsymbol{\Omega}) = \psi(\boldsymbol{r}_{in}, \boldsymbol{\Omega}) e^{-\tau(l)} + \boldsymbol{Q}_\beta(\boldsymbol{\Omega}) \cdot \underbrace{\int_0^l \mathrm{d}t \mathbf{P}(z) e^{-(\tau(l)-\tau(t))}}_{\mathbf{E}_0} + \frac{1}{l} \left[\boldsymbol{Q}_\alpha(\boldsymbol{\Omega}) - \boldsymbol{Q}_\beta(\boldsymbol{\Omega})\right] \cdot \underbrace{\int_0^l \mathrm{d}t \mathbf{P}(z) t e^{-(\tau(l)-\tau(t))}}_{\mathbf{E}_1}. \quad (5.50)$$

Thus, the transmission, under these assumptions, is implemented in the following form:

$$\psi(\boldsymbol{r}_{out}, \boldsymbol{\Omega}) = \psi(\boldsymbol{r}_{in}, \boldsymbol{\Omega}) e^{-\tau(l)} + \boldsymbol{Q}_\beta(\boldsymbol{\Omega}) \cdot \mathbf{E}_0 + \frac{1}{l} \left[\boldsymbol{Q}_\alpha(\boldsymbol{\Omega}) - \boldsymbol{Q}_\beta(\boldsymbol{\Omega})\right] \cdot \mathbf{E}_1. \quad (5.51)$$

The vectors $\mathbf{E}_0$ and $\mathbf{E}_1$ need to be calculated, with dimensions ranging from 0 to n_p. In this section, we will detail only the calculation of $\mathbf{E}_1$ and provide the formula for $\mathbf{E}_0$ directly. As a starting point, consider the k^{th} component $\mathrm{E}_{1,k}$:

$$\mathrm{E}_{1,k} = \int_0^l \mathrm{d}t t \mathrm{P}_k(z_t) e^{-(\tau(l)-\tau(t))}. \quad (5.52)$$

First, we perform the change of variable $x = \frac{2}{l}t - 1$ to transform the integration interval to $[-1, 1]$. The previous integral can then be rewritten as:

$$\mathrm{E}_{1,k} = \left(\frac{l}{2}\right)^2 \int_{-1}^1 \mathrm{d}x \, (x+1) \left(\mathrm{P}_1(z_{in}) + \mu \frac{l/2(1+x)}{\Delta z/2}\right)^k e^{-(\tau(l)-\tau(t(x)))}. \quad (5.53)$$

In this case E_k integrals cannot be expressed in terms of elementary functions as in the constant case. Instead, they are computed thanks to a Gauss-Legendre quadrature rule.

$$\mathrm{E}_{1,k} \simeq \left(\frac{l}{2}\right)^2 \sum_{j=1}^{m} w_j \left(1+x_j\right) \left(\mathrm{P}_1(z_{in}) + \mu \frac{l/2(1+x_j)}{\Delta z/2}\right)^k e^{\tau[t(x_j)]-\tau(l)}, \tag{5.54}$$

x_j being the roots of the m^{th}-degree Legendre polynomial, w_j the weights associated to the chosen quadrature order and $t(x_j) = \frac{l}{2}(x_j+1)$. In the same manner:

$$\mathrm{E}_{0,k} \simeq \frac{l}{2} \sum_{j=1}^{m} w_j \left(\mathrm{P}_1(z_{in}) + \mu \frac{l/2(1+x_j)}{\Delta z/2}\right)^k e^{\tau[t(x_j)]-\tau(l)}. \tag{5.55}$$

5.4 . Conservation equation

In this section, the conservation equation is derived only for uniform cross sections. To ensure convergence of the internal iterations, the (surface) moments of the flux are updated. At each sweep, the surface moments are updated based on the current term and the sources of fission, down-scattering, and up-scattering. To ensure particle conservation, a particle balance is performed at the end of each iteration, where the volumetric source is replaced by a geometric source calculated from the surface moments, and where these moments are corrected to ensure equality between surface and geometric moments.

Particle conservation relies on the angular balance equation (4.20) derived in the previous chapter, where the angular flux is assumed to vary polynomially in the axial direction (4.4). This angular flux is projected onto the spherical harmonics basis to obtain an equation for the moments. The resulting equation is:

$$\Sigma_t {}'\mathbf{\Phi}_i = -\Delta \mathbf{J}_i + {}'\boldsymbol{Q}_i + \mathbb{D}{}'\mathbf{\Phi}_i, \tag{5.56}$$

with

$$\Delta \mathbf{J}_i = \frac{1}{4\pi} \int_{\mathbb{S}_2} \mathrm{d}\mathbf{\Omega} \boldsymbol{A}(\mathbf{\Omega}) \otimes \Delta \mathbf{J}_i(\mathbf{\Omega}), \tag{5.57}$$

$${}'\boldsymbol{Q}_i = \frac{1}{4\pi \mathrm{V}_i} \int_i \boldsymbol{Z}(\boldsymbol{r}, \mathbf{\Omega}) \otimes \boldsymbol{Z}(\boldsymbol{r}, \mathbf{\Omega}) \cdot \boldsymbol{Q}_i, \tag{5.58}$$

$$\mathbb{D}{}'\mathbf{\Phi}_i = \frac{1}{4\pi} \int_{\mathbb{S}_2} \mathrm{d}\mathbf{\Omega} \mu \boldsymbol{A}(\mathbf{\Omega}) \otimes \mathbb{C}{}'\boldsymbol{\psi}_i(\mathbf{\Omega}). \tag{5.59}$$

Then, knowing that

$$\mu A_k^l(\mathbf{\Omega}) = \alpha_{k+1}^l A_{k+1}^l(\mathbf{\Omega}) + \beta_{k-1}^l A_{k-1}^l(\mathbf{\Omega}), \tag{5.60}$$

with, α_{k+1}^l and β_{k-1}^l defined in [56], one may remark that the matrix $\mathbb{D}$ couples each polynomial component p with the polynomial component $p-1$. This coupling necessitates the calculation of additional angular moments to ensure that the interactions between different polynomial components are accurately accounted for. To do so, (5.56) is obtained by projecting the angular balance equation onto the spherical harmonics vector, using a higher anisotropy order to account for the additional moments that must be computed. To stress this difference the subscript D is added to the vectors of (5.56). It gives

$$\Sigma_t {}'\mathbf{\Phi}_{i,D} = -\Delta\mathbf{J}_{i,D} + {}'\boldsymbol{Q}_{i,D} + \mathbb{D}\,{}'\mathbf{\Phi}_{i,D}, \tag{5.61}$$

with

$$\Delta\mathbf{J}_{i,D} = \frac{1}{4\pi}\int_{\mathbb{S}_2} \mathrm{d}\mathbf{\Omega}\boldsymbol{A}_D(\mathbf{\Omega}) \otimes \Delta\mathbf{J}_i(\mathbf{\Omega}), \tag{5.62}$$

$${}'\boldsymbol{Q}_{i,D} = \frac{1}{4\pi \mathrm{V}_i}\int_i \boldsymbol{Z}_D(\boldsymbol{r},\mathbf{\Omega}) \otimes \boldsymbol{Z}(\boldsymbol{r},\mathbf{\Omega}) \cdot \boldsymbol{Q}_i, \tag{5.63}$$

$$\mathbb{D}\,{}'\mathbf{\Phi}_{i,D} = \frac{1}{4\pi}\int_{\mathbb{S}_2} \mathrm{d}\mathbf{\Omega}\mu\boldsymbol{A}_D(\mathbf{\Omega}) \otimes \mathbb{C}\,{}'\boldsymbol{\psi}_i(\mathbf{\Omega}). \tag{5.64}$$

Once (5.61) is evaluated, only the moments belonging to the scattering dimensions are kept to iterate. Nonetheless, (5.56) involves a volumetric source term, which is not defined within the linear surface scheme. Therefore, a geometric operator is introduced to construct this volumetric source term, ensuring particle conservation within each computational region.

5.4.1 . Definition of a geometrical operator

The principle of the geometric operator involves constructing a volumetric source from vertical sources that ensures conservation within the calculation region. The idea is to project the angular moments of the flux onto the spatial basis before using the linear approximation along a chord. Numerically, the spatial integration depends on the direction because the MOC relies on the discrete ordinates method. Therefore, angular integration is performed on top of the spatial integration. For any angular and spatial moments of order (n,p), the geometrical moment ${}'\Phi_{\mathrm{G}}^{n,p}$ is defined as

$$'\Phi_{\mathrm{G}}^{n,p} = \frac{1}{4\pi \mathrm{V}_i} \int_{\mathbb{S}_2} \mathrm{d}\boldsymbol{\Omega} \int_i \mathrm{d}\boldsymbol{r} \mathrm{P}_p(\boldsymbol{r}) \Phi^n(\boldsymbol{r}), \tag{5.65}$$

which can be numerically written as

$$'\Phi_{\mathrm{G}}^{n,p} = \frac{1}{4\pi \mathrm{V}_i} \sum_{\boldsymbol{\Omega}_n \in S_n} w_n \sum_{\substack{t || \Omega_n \\ t \cap i}} w_{\perp,t} \int_0^l \mathrm{dt} \mathrm{P}_p(t) \Phi^n(t), \tag{5.66}$$

with Φ^n being the angular moment of order n. Now, according to the approximations on the spatial variations of the flux, it writes along a chord :

$$\Phi^n(t) = \sum_{p=0}^{n_p} \mathrm{P}_p(z_t) \cdot \left[\Phi_\beta^{n,p} (1 - \frac{t}{l}) + \Phi_\alpha^{n,p} \frac{t}{l} \right], \tag{5.67}$$

where α is the exiting surface associated to the considered chord and β to the entering one. Injecting (5.67) in (5.66) one gets the following expression that can be written as:

$$'\Phi_{\mathrm{G}}^{n,p} = \frac{1}{4\pi \mathrm{V}_i} \sum_{\boldsymbol{\Omega}_n \in S_n} w_n \sum_{\substack{t || \Omega \\ t \cap i}} w_{\perp,t} \int_0^l \mathrm{dt} \sum_{p'=0}^{n_p} \mathrm{P}_{p+p'}(z_t) \left[\Phi_\beta^{n,p'} (1 - \frac{t}{l}) + \Phi_\alpha^{n,p'} \frac{t}{l} \right]. \tag{5.68}$$

Note that the geometric factor needs to be applied only to the vertical surfaces of the region, whereas the previous equation involves the surfaces encountered by trajectories passing through the region, which can be either vertical or horizontal. To eliminate the latter, the system of equations (5.31), (5.32) is substituted into (5.68). This yields:

$$\begin{aligned}
\Phi_\beta^{n,p'} (1 - \frac{t}{l}) + \Phi_\alpha^{n,p'} \frac{t}{l} &= \Phi_\gamma^{n,p'} \left(1 - \frac{\mathrm{L}_{k-1}}{\mathrm{L}_{tot}} \right) (1 - \frac{t}{l}) + \Phi_{\gamma^\star}^{n,p'} \frac{\mathrm{L}_{k-1}}{\mathrm{L}_{tot}} (1 - \frac{t}{l}) \\
&+ \Phi_\gamma^{n,p'} \left(1 - \frac{\mathrm{L}_k}{\mathrm{L}_{tot}} \right) \frac{t}{l} + \Phi_{\gamma^\star}^{n,p'} \frac{\mathrm{L}_k}{\mathrm{L}_{tot}} \frac{t}{l}, \\
&= \Phi_\gamma^{n,p'} \left[\left(1 - \frac{\mathrm{L}_{k-1}}{\mathrm{L}_{tot}} \right) (1 - \frac{t}{l}) + \left(1 - \frac{\mathrm{L}_k}{\mathrm{L}_{tot}} \right) \frac{t}{l} \right], \\
&+ \Phi_{\gamma^\star}^{n,p'} \left[\frac{\mathrm{L}_{k-1}}{\mathrm{L}_{tot}} (1 - \frac{t}{l}) + \frac{\mathrm{L}_k}{\mathrm{L}_{tot}} \frac{t}{l} \right].
\end{aligned}$$

Recalling that $\mathrm{L}_k - \mathrm{L}_{k-1} = l$, one obtains:

$$\Phi_{\beta}^{n,p'}(1 - \frac{t}{l}) + \Phi_{\alpha}^{n,p'}\frac{t}{l} = \Phi_{\gamma}^{n,p'}\left(1 - \frac{\mathrm{L}_{k-1} + t}{\mathrm{L}_{tot}}\right) + \Phi_{\gamma^\star}^{n,p'}\frac{\mathrm{L}_{k-1} + t}{\mathrm{L}_{tot}}. \tag{5.69}$$

To remove the dependence on the coordinate t in the expression (5.69), we add to this expression the contribution from the trajectory in the direction $-\mathbf{\Omega}_n$. The expression for the linear interpolation as a function of the moments defined on the vertical surfaces of the geometry is given by:

$$\Phi_{\alpha}^{n,p'}(1 - \frac{t}{l}) + \Phi_{\beta}^{n,p'}\frac{t}{l} = \Phi_{\gamma}^{n,p'}\left(1 - \frac{\mathrm{L}_{k} - t}{\mathrm{L}_{tot}}\right) + \Phi_{\gamma^\star}^{n,p'}\frac{\mathrm{L}_{k} - t}{\mathrm{L}_{tot}}. \tag{5.70}$$

Then, by adding (5.70) to (5.69) in the geometric factor (5.68), we obtain:

$$\begin{aligned} {}'\Phi_{\mathrm{G}}^{n,p} = \frac{1}{4\pi \mathrm{V}_i} \sum_{\mathbf{\Omega}_n \in S_n^+} \mathrm{d}\mathbf{\Omega} \sum_{\substack{t||\Omega \\ t\cap i}} w_{\perp,t} \sum_{p'=0}^{n_p} \int_0^l \mathrm{d}t \\ \mathrm{P}_{p+p'}(z_t) \cdot \left[\left(2 - \frac{\mathrm{L}_{k-1} + \mathrm{L}_k}{\mathrm{L}_{tot}}\right)\Phi_{\gamma}^{n,p'} + \frac{\mathrm{L}_{k-1} + \mathrm{L}_k}{\mathrm{L}_{tot}}\Phi_{\gamma^\star}^{n,p'}\right]. \end{aligned} \tag{5.71}$$

We now define

$$A_{t,p} = \int_0^l \mathrm{d}t \mathrm{P}_p(z_t), \tag{5.72}$$

$$A_{t,p}^{\gamma} = \left(2 - \frac{\mathrm{L}_{k-1} + \mathrm{L}_k}{\mathrm{L}_{tot}}\right) A_{t,p}, \tag{5.73}$$

$$A_{t,p}^{\gamma^\star} = \frac{\mathrm{L}_{k-1} + \mathrm{L}_k}{\mathrm{L}_{tot}} A_{t,p}, \tag{5.74}$$

where $A_{t,p}$ is computed thanks to the change of variable (4.25). It analytical expression is

$$A_{t,p} = \frac{\Delta z/2}{\mu(p+1)}\left[\tilde{z}(l)^{p+1} - \tilde{z}(0)^{p+1}\right]. \tag{5.75}$$

Finally, the sum over all trajectories traversing region i in the direction $\mathbf{\Omega}_n$ is decomposed over the vertical surfaces γ:

$$
\begin{aligned}
{}'\Phi_{\mathrm{G}}^{n,p} &= \frac{1}{4\pi \mathrm{V}_i} \sum_{\mathbf{\Omega}_n \in S_n^+} w_n \sum_{\substack{t||\Omega \\ t\cap i}} w_{\perp,t} \sum_{p'=0}^{n_p} \left(A_{t,p+p'}^{\gamma} \Phi_{\gamma}^{n,p'} + A_{t,p+p'}^{\gamma^\star} \Phi_{\gamma^\star}^{n,p'} \right), \\
&= \frac{1}{4\pi \mathrm{V}_i} \sum_{\mathbf{\Omega}_n \in S_n^+} w_n \sum_{\gamma \in \partial i_v} \sum_{\substack{t||\Omega \\ t\cap \gamma}} w_{\perp,t} \sum_{p'=0}^{n_p} \left(A_{t,p+p'}^{\gamma} \Phi_{\gamma}^{n,p'} + A_{t,p+p'}^{\gamma^\star} \Phi_{\gamma^\star}^{n,p'} \right).
\end{aligned}
$$

Such that,

$$
{}'\Phi_{\mathrm{G}}^{n,p} = \sum_{\gamma \in \partial i_v} \sum_{p'=0}^{n_p} \frac{1}{4\pi \mathrm{V}_i} \sum_{\mathbf{\Omega}_n \in S_n^+} w_n \sum_{\substack{t||\Omega \\ t\cap \gamma}} w_{\perp,t} \left(A_{t,p+p'}^{\gamma} \Phi_{\gamma}^{n,p'} + A_{t,p+p'}^{\gamma^\star} \Phi_{\gamma^\star}^{n,p'} \right) \tag{5.76}
$$

This way, we implicitly define the geometrical factor $\mathbb{M}_{\mathrm{G},\gamma}^{p,p'}$ for any vertical surface γ as:

$$
{}'\Phi_{G}^{n,p} = \sum_{\gamma \in \partial i_v} \sum_{q=0}^{n_p} \mathbb{M}_{\mathrm{G},\gamma}^{p,q} \Phi_{\gamma}^{n,q}. \tag{5.77}
$$

From relation (5.76), it is understood that each trajectory, swept in the direction $\mathbf{\Omega}n$ and $-\mathbf{\Omega}n$, contributes two terms to the geometric operator $\mathbb{M}_{\mathrm{G},\gamma}^{p,q} : A_{t,p+p'}^{\gamma}$ for the surface intersected by the trajectory when entering region i through surface β, and $A_{t,p+p'}^{\gamma^\star}$ for the surface intersected when exiting the region through surface α. Now, note that if the trajectory crosses the region through two vertical surfaces, then $\beta = \gamma$, $\alpha = \gamma^\star$, and $A_{t,p+p'}^{\gamma} = A_{t,p+p'}^{\gamma^\star} = At, p + p'$; that is, the two contributions of the trajectory to the operator are identical. In contrast, for other types of chords, $A_{t,p+p'}^{\gamma} \neq A_{t,p+p'}^{\gamma^\star}$. For example, for an HV-type chord:

$$
\begin{aligned}
0 < A_{t,p+p'}^{\gamma} &= \left(1 - \frac{\mathrm{L}_{k-1}}{\mathrm{L}_{tot}} \right) A_{t,p+p'} < 1, \\
1 < A_{t,p+p'}^{\gamma^\star} &= \left(\frac{\mathrm{L}_{k-1}}{\mathrm{L}_{tot}} + 1 \right) A_{t,p+p'} < 2.
\end{aligned}
$$

Thus, $A_{t,p+p'}^{\gamma^\star} > A_{t,p+p'}^{\gamma}$. Consequently, the contribution of the flux on the vertical surface $\gamma^\star$ will have a greater impact on the geometric moments than the flux on γ for this HV-type trajectory.

5.4.2 . Moments of the flux correction

It remains to correct the surface moments of the flux (5.15) to ensure equality between the geometric and conservative moments, so that conservation of the balance is guaranteed for each calculation region, and convergence of the internal iterations is assured. In order to do so, a corrective factor per region $\delta_i^{n,q}$ is introduced such that:

$$'\Phi_i^{n,p} = \sum_{\gamma \in \partial i_v} \sum_{q=0}^{n_p} \mathbb{M}_{\mathrm{G},\gamma}^{p,q} (\Phi_\gamma^{n,q} + \delta_i^{n,q}). \tag{5.78}$$

Then, we define

$$\mathrm{S}^{n,p} = '\Phi_i^{n,p} - \sum_{\gamma \in \partial i_v} \sum_{q=0}^{n_p} \mathbb{M}_{\mathrm{G},\gamma}^{p,q} \Phi_\gamma^{n,q}, \tag{5.79}$$

$$\mathbb{M}_{\mathrm{G}}^{p,q} = \sum_{\gamma \in \partial i_v} \mathbb{M}_{\mathrm{G},\gamma}^{p,q}, \tag{5.80}$$

such that the final system obtained is:

$$\sum_{q=0}^{n_p} \mathbb{M}_{\mathrm{G}}^{p,q} \delta^{n,q} = \mathrm{S}^{n,p}. \tag{5.81}$$

The linear system (5.81) has a unique solution if and only if the matrix $\mathbb{M}_{\mathrm{G}}$ is invertible. Since $\mathbb{M}_{\mathrm{G}}^{0,0} = 1$, this is always true at least when the flux is constant axially. If the matrix is non-invertible, the degree of the polynomial basis, in the region, is reduced until it can be inverted. Furthermore, it is noteworthy that the matrix is symmetric; this avoids the need to store all the elements of the matrix. Finally, we define the scaled surface moments as,

$$'\Phi_{\gamma^\star}^{s,n,p} = '\Phi_{\gamma^\star}^{n,p} + \mathrm{S}^{n,p}, \tag{5.82}$$

such that the geometrical factor applied to the scaled coefficients of the scaled moments gives the volume moments $'\Phi_i^{n,p}$.

5.4.3 . Volume conservation

In the last two sections, a geometric operator was constructed to ensure the conservation of flux moments within each region. We now seek to understand if it is possible to construct a geometric source whose moments are equal to those of the volumetric source defined as:

$$'Q_i^{n,p} = \frac{1}{4\pi \mathrm{V}_i} \int_{\mathbb{S}_2} \mathrm{d}\mathbf{\Omega} A_n(\mathbf{\Omega}) \int_i \mathrm{d}\boldsymbol{r} \mathrm{P}_p(\boldsymbol{r}) Q(\boldsymbol{r}, \mathbf{\Omega}). \tag{5.83}$$

We define

$$'Q_G^{n,p} = \sum_{\gamma \in \partial i_v} \sum_{q=0}^{n_p} \mathbb{M}_{\mathrm{G},\gamma}^{p,q} Q_\gamma^{n,q}, \tag{5.84}$$

which can be viewed as a geometric average of the surface components. We now seek to determine whether there is equality between (5.83) and (5.84). To address this question, (5.83) is expanded according to spatial and directional approximations, with polynomial expansion in the axial direction and spherical harmonics for the angular variable, respectively. Thus, we can write:

$$'Q_i^{n,p} = \frac{1}{4\pi \mathrm{V}_i} \sum_{n',q} \int_{\mathbb{S}_2} \mathrm{d}\mathbf{\Omega} A_n(\mathbf{\Omega}) A_{n'}(\mathbf{\Omega}) \int_i \mathrm{d}\boldsymbol{r} \mathrm{P}_{p+q}(\boldsymbol{r}) Q_i^{n',q}. \tag{5.85}$$

Now, knowing that $Q_i^{n',q} = \Sigma_s^n \phi_i^{n',q} + Q_{ext}^{n',q}$ and also knowing that

$$\frac{1}{4\pi} \int_{\mathbb{S}_2} \mathrm{d}\mathbf{\Omega} A_n(\mathbf{\Omega}) A_{n'}(\mathbf{\Omega}) = \frac{1}{2k(n)+1} \delta^{n,n'}, \tag{5.86}$$

where $k(n)$ is the harmonic order associated to n according to the mono-index formulation (4.9). Then, we write

$$\begin{aligned} 'Q_i^{n,p} &= \frac{1}{2k(n)+1} \sum_q \frac{1}{\mathrm{V}_i} \int_i \mathrm{d}\boldsymbol{r} \mathrm{P}_{p+q}(\boldsymbol{r}) \left[\Sigma_s \phi_i^{n,q} + Q_{ext}^{n,q}\right], \\ &= \frac{1}{2k(n)+1} \frac{1}{\mathrm{V}_i} \int_i \mathrm{d}\boldsymbol{r} \sum_q \mathrm{P}_{p+q}(\boldsymbol{r}) \left[\Sigma_s \phi_i^{n,q} + Q_{ext}^{n,q}\right]. \end{aligned}$$

And thus,

$$'Q_i^{n,p} = \frac{1}{2k(n)+1} \left[\Sigma_s \, '\phi_i^{n,p} + \, 'Q_{ext}^{n,p}\right]. \tag{5.87}$$

On the other hand, if we define the geometric source from (5.84) and recall that $Q_\gamma^{n,q} = \Sigma_s^n \phi_\gamma^{n,q} + Q_{\gamma,ext}^{n,q}$, we obtain

$$
\begin{aligned}
{}'Q_G^{n,p} &= \sum_{\gamma \in \partial i_v} \sum_{q=0}^{n_p} \mathbb{M}_{\mathrm{G},\gamma}^{p,q} \left[\Sigma_s^n \phi_\gamma^{n,q} + Q_{\gamma,ext}^{n,q} \right], \\
&= \Sigma_s^n \sum_{\gamma \in \partial i_v} \sum_{q=0}^{n_p} \mathbb{M}_{\mathrm{G},\gamma}^{p,q} \phi_\gamma^{n,q} + \sum_{\gamma \in \partial i_v} \sum_{q=0}^{n_p} \mathbb{M}_{\mathrm{G},\gamma}^{p,q} Q_{\gamma,ext}^{n,q},
\end{aligned}
$$

which, by definition of the geometric moments, can be written as:

$$
{}'Q_G^{n,p} = \Sigma_s^n \, {}'\phi_G^{n,p} + {}'Q_{G,ext}^{n,p}. \tag{5.88}
$$

Knowing that by construction ${}'\phi_G^{n,p} = {}'\phi_i^{n,p}$, it follows that

$$
{}'Q_i^{n,p} = \frac{1}{2k(n)+1} \left[\Sigma_s^n \, {}'\phi_G^{n,p} + {}'Q_{G,ext}^{n,p} \right]. \tag{5.89}
$$

We define $\mathbb{S}$ as the diagonal matrix of size $(n_m \times n_p) \times (n_m \times n_p)$, where the component $\mathbb{S}_{ii}$, with $i = n + p \times n_m$, is defined as follows:

$$
\mathbb{S}_{ii} = \frac{1}{2k(n)+1}. \tag{5.90}
$$

This leads to rewrite (5.61) as:

$$
\Sigma_t \, {}'\boldsymbol{\Phi}_{i,D} = -\Delta \mathbf{J}_{i,D} + \mathbb{S} \, {}'\boldsymbol{Q}_G + \mathbb{D} \, {}'\boldsymbol{\Phi}_{i,D}. \tag{5.91}
$$

Thus, the scheme is complete. At each iteration, the sweep evaluates the current term (5.57) and the surface moments of the flux (5.15). Then, the conservation equation (5.91) is used to correct the surface moments of the flux through (5.81). This process is repeated until the volumetric moments converge.

5.5 . Shared memory parallelism

The trajectory sweep is parallelized in shared memory using OpenMP. The strategy follows the one implemented in the initial work on applying the TDT solver to 3D geometries [51].

The difference lies in integrating the computation of angular surface fluxes into the parallelization.

The general idea is to associate a direction Ω with each thread so that it can sweep all trajectories in the Ω direction to add their contribution to the angular current term for each region (4.28). However, this idea is not practically applicable when the geometry boundaries have closed boundary conditions, such as reflective boundary conditions. With such conditions, the trajectory direction changes during the sweep. Thus, two distinct threads could sweep two different trajectories passing through a region with the same direction. As a result, both threads would add their contributions to the same angular current term, which could lead to race condition errors.

To circumvent this issue, the smallest set of angles is determined, allowing the others to be recovered during the sweep by applying the boundary conditions. These angles are referred to as basic angles. Finally, the degree of parallelism is increased by allowing two distinct threads to sweep trajectories sharing the same basic angle but providing each thread with a private copy of the angular current and performing reduction operations during the sweep.

6 - Surface DP_n synthetic acceleration of free iterations

Chapter 6 begins by justifying the choice of the DP_n-type synthetic acceleration. Following this, the equations specific to the acceleration method, consistent with the linear surface transport scheme, are detailed.

Contents

6.1 . DP$_n$ approximation and derivation of the transport equation

Before deriving the equations specific to acceleration, it is important to recall that, similar to the Method of Characteristics (MOC), the DPn acceleration relies on the integral form of the transport equation and that the linear system is constructed based on a tracking-based integration of the problem matrices. Such an approach allows the use of the same spatial mesh for both transport and acceleration, including unstructured meshes, which are particularly used for handling complex geometries such as the RJH reactor or TRISO particle reactors. Moreover, the synthetic approach adopted enables adding the DPn solution to the transport solution, that is, the synthetic multi-group flux in the case of outer iterations, and the within-group moments in the case of inner iterations. (see 3.5.2).

The DP$_n$ acceleration relies on expanding the angular variable using spherical harmonics at the angular flux boundaries $\Gamma_{i,-}$ and $\Gamma_{i,+}$, as shown in figure 6.1. The spatial variable is treated similarly to the transport method. Macroscopic cross sections are assumed to be constant within each region. We recall that α and β denotes vertical or horizontal surfaces, and that the symbols γ and $\gamma^\star$ are used to refer to vertical surfaces. Let us begin by expanding the angular flux on the vertical surface γ

$$\psi_\gamma(\boldsymbol{r},\boldsymbol{\Omega}) = \begin{cases} \mathbf{Z}(\boldsymbol{r},\boldsymbol{\Omega})\cdot\boldsymbol{\psi}_{\gamma,-} & |\boldsymbol{n}(\boldsymbol{r})\cdot\boldsymbol{\Omega}| < 0 \\ \mathbf{Z}(\boldsymbol{r},\boldsymbol{\Omega})\cdot\boldsymbol{\psi}_{\gamma,+} & |\boldsymbol{n}(\boldsymbol{r})\cdot\boldsymbol{\Omega}| > 0. \end{cases} \tag{6.1}$$

with the vector $\mathbf{Z}$ of dimension $(n_m \times n_p)$, whose components of order (n,p) are given by the product $A_n(\boldsymbol{\Omega})\mathrm{P}_p(\boldsymbol{r})$. The surface moments of the flux can then be expressed in terms of the DP$_n$ coefficients. Starting from the definition of the moments (5.14), we then write

$$\begin{aligned} {}'\boldsymbol{\Phi}_\gamma &= \frac{1}{4\pi S_\gamma}\int_{\mathbb{S}_{2+}} \mathrm{d}\boldsymbol{\Omega}\int_\gamma \mathrm{d}\boldsymbol{r}\,\mathbf{Z}(\boldsymbol{r},\boldsymbol{\Omega})\psi(\boldsymbol{r},\boldsymbol{\Omega}) \\ &\quad + \frac{1}{4\pi S_\gamma}\int_{\mathbb{S}_{2-}} \mathrm{d}\boldsymbol{\Omega}\int_\gamma \mathrm{d}\boldsymbol{r}\,\mathbf{Z}(\boldsymbol{r},\boldsymbol{\Omega})\psi(\boldsymbol{r},\boldsymbol{\Omega}), \\ &= \frac{1}{4\pi S_\gamma}\int_{\mathbb{S}_{2+}} \mathrm{d}\boldsymbol{\Omega}\int_\gamma \mathrm{d}\boldsymbol{r}\,\mathbf{Z}(\boldsymbol{r},\boldsymbol{\Omega})\otimes\mathbf{Z}(\boldsymbol{r},\boldsymbol{\Omega})\cdot\boldsymbol{\psi}_{\gamma,+} \\ &\quad + \frac{1}{4\pi S_\gamma}\int_{\mathbb{S}_{2-}} \mathrm{d}\boldsymbol{\Omega}\int_\gamma \mathrm{d}\boldsymbol{r}\,\mathbf{Z}(\boldsymbol{r},\boldsymbol{\Omega})\otimes\mathbf{Z}(\boldsymbol{r},\boldsymbol{\Omega})\cdot\boldsymbol{\psi}_{\gamma,-}. \end{aligned}$$

Then, we set

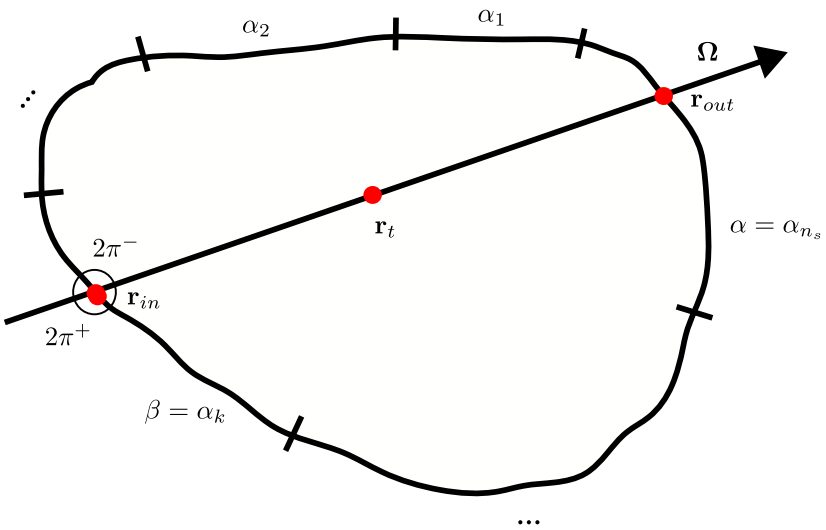

Figure 6.1 – Representation of a chord crossing region i between surfaces β and α through $\boldsymbol{r}_{in}$ and $\boldsymbol{r}_{out}$, respectively. On each surface α_k the angular flux is developed according to a double P_n expansion, on $2\pi^-$ and $2\pi^+$.

$$\mathbb{A}_{\gamma,+} = \frac{1}{4\pi S_\gamma} \int_{\mathbb{S}_{2+}} \mathrm{d}\boldsymbol{\Omega} \int_\gamma \mathrm{d}\boldsymbol{r}\, \mathbf{Z}(\boldsymbol{r},\boldsymbol{\Omega}) \otimes \mathbf{Z}(\boldsymbol{r},\boldsymbol{\Omega}), \tag{6.2}$$

$$\mathbb{A}_{\gamma,-} = \frac{1}{4\pi S_\gamma} \int_{\mathbb{S}_{2-}} \mathrm{d}\boldsymbol{\Omega} \int_\gamma \mathrm{d}\boldsymbol{r}\, \mathbf{Z}(\boldsymbol{r},\boldsymbol{\Omega}) \otimes \mathbf{Z}(\boldsymbol{r},\boldsymbol{\Omega}). \tag{6.3}$$

We can thus write

$$'\boldsymbol{\Phi}_\gamma = \mathbb{A}_{\gamma,+}\boldsymbol{\psi}_{\gamma,+} + \mathbb{A}_{\gamma,+}\boldsymbol{\psi}_{\gamma,-}. \tag{6.4}$$

where $\mathbb{A}_{\gamma,+}$ and $\mathbb{A}_{\gamma,-}$ are two square matrices of dimension $(n_m \times n_p) \times (n_m \times n_p)$. Similarly to the transport method, a conservation equation must be established. To this end, we start again from (5.91), then isolate the flux moments on the left side:

$$(\Sigma_t - \mathbb{D})\, '\boldsymbol{\Phi}_{i,D} = -\Delta \mathbf{J}_{i,D} + \mathbb{S}\, '\boldsymbol{Q}_G. \tag{6.5}$$

Then, we set

$$\mathbb{X}_D = (\Sigma_t - \mathbb{D})^{-1}. \tag{6.6}$$

Eq (6.5) becomes

$$
{}'\mathbf{\Phi}_{i,D} = -\mathbb{X}_D \Delta \mathbf{J}_{i,D} + \mathbb{X}_D \mathbb{S}' \boldsymbol{Q}_G. \tag{6.7}
$$

We now expand the current term on the surfaces of the region:

$$
\begin{aligned}
\Delta \mathbf{J}_i &= \frac{1}{4\pi \mathrm{V}_i} \int_{\mathbb{S}_2} \mathrm{d}\boldsymbol{\Omega} \int_{\partial i} \mathrm{d}\boldsymbol{r} (\boldsymbol{\Omega} \cdot n) \mathbf{Z}_D(\boldsymbol{r}, \boldsymbol{\Omega}) \psi(\boldsymbol{r}, \boldsymbol{\Omega}), \\
&= \frac{1}{\mathrm{V}_i} \sum_{\alpha \in \partial i} \int_\alpha \mathrm{d}\boldsymbol{r} \left[\int_{\mathbb{S}_{2+}} \frac{\mathrm{d}\boldsymbol{\Omega}}{4\pi} |\boldsymbol{\Omega} \cdot n| \mathbf{Z}_D(\boldsymbol{r}, \boldsymbol{\Omega}) \psi(\boldsymbol{r}, \boldsymbol{\Omega}) - \int_{\mathbb{S}_{2-}} \frac{\mathrm{d}\boldsymbol{\Omega}}{4\pi} |\boldsymbol{\Omega} \cdot n| \mathbf{Z}_D(\boldsymbol{r}, \boldsymbol{\Omega}) \psi(\boldsymbol{r}, \boldsymbol{\Omega}) \right], \\
&= \frac{1}{\mathrm{V}_i} \sum_{\alpha \in \partial i} \left[\mathbf{J}_{\alpha,+} - \mathbf{J}_{\alpha,-} \right].
\end{aligned}
$$

In summary, we write

$$
{}'\mathbf{\Phi}_i = -\frac{1}{\mathrm{V}_i} \mathbb{X}_D \sum_{\alpha \in \partial i} \left(\mathbf{J}_{\alpha,+} - \mathbf{J}_{\alpha,-} \right) + \mathbb{X}_D \mathbb{S}' \boldsymbol{Q}_G, \tag{6.8}
$$

with, for the vertical surfaces

$$
\begin{aligned}
\mathbf{J}_{\gamma,+} &= \int_\gamma \mathrm{d}\boldsymbol{r} \int_{\mathbb{S}_{2+}} \frac{\mathrm{d}\boldsymbol{\Omega}}{4\pi} |\boldsymbol{\Omega} \cdot n| \mathbf{Z}_D(\boldsymbol{r}, \boldsymbol{\Omega}) \otimes \mathbf{Z}(\boldsymbol{r}, \boldsymbol{\Omega}) \cdot \boldsymbol{\psi}_{\gamma,+}, && (6.9) \\
&= \mathbb{B}^v_{\gamma,+} \boldsymbol{\psi}_{\gamma,+}, && (6.10)
\end{aligned}
$$

and, for the horizontal surfaces, where the flux is spatially constant

$$
\begin{aligned}
\mathbf{J}_{\alpha,+} &= \int_\alpha \mathrm{d}\boldsymbol{r} \int_{\mathbb{S}_{2+}} \frac{\mathrm{d}\boldsymbol{\Omega}}{4\pi} |\boldsymbol{\Omega} \cdot n| \mathbf{A}_D(\boldsymbol{r}, \boldsymbol{\Omega}) \otimes \mathbf{A}(\boldsymbol{r}, \boldsymbol{\Omega}) \cdot \boldsymbol{\psi}_{\alpha,+}, && (6.11) \\
&= \mathbb{B}^h_{\alpha,+} \boldsymbol{\psi}_{\alpha,+}. && (6.12)
\end{aligned}
$$

We recall here that the index D denotes the coupling of the polynomial components, which requires the computation of additional angular moments (see 5.4). Thus $\mathbb{B}^v_{\alpha,+}$ and $\mathbb{B}^h_{\alpha,+}$ are rectangular and non-invertible. In the following the index D will be omitted for simplicity.

From the relations Eq (6.4), Eq (6.9), and Eq (6.11), it is possible to determine a relationship between the currents and the vertical moments. We begin by setting

$$\mathbb{F}_{\gamma,+} = \mathbb{A}_{\gamma,+}\mathbb{B}_{\gamma,+}^{-1}, \tag{6.13}$$

with $\mathbb{B}_{\gamma,+}^{-1}$ of dimension $(n_m \times n_p) \times (n_m \times n_p)$ as we only consider the principal sub-block of $\mathbb{B}_{\gamma,+}$ to make its inversion. $\mathbb{A}_{\gamma,+}$ is of dimension $(n_m \times n_p) \times (n_m \times n_p)$, the matrix $\mathbb{F}_{\gamma,+}$ has a dimension of $(n_m \times n_p) \times (n_m \times n_p)$. By combining (6.4) and (6.9), we obtain

$$'\mathbf{\Phi}_\gamma = \mathbb{F}_{\gamma,+}\mathbf{J}_{\gamma,+} + \mathbb{F}_{\gamma,-}\mathbf{J}_{\gamma,-}. \tag{6.14}$$

6.2 . DP$_n$ transmission equation

In this section, we derive an expression for the outgoing current as a function of the incoming current and the source, starting from the transport equation. To this end, we first write the transport equation for a chord of length l that traverses the region, entering through surface β at point $\boldsymbol{r}_{in}$ and exiting through surface α at point $\boldsymbol{r}_{out}$:

$$\psi_\alpha(\boldsymbol{r}_{out}, \mathbf{\Omega}) = \psi_\beta(\boldsymbol{r}_{in}, \mathbf{\Omega})e^{-\tau(l)} + \mathbf{P}(\boldsymbol{r}_{in}) \cdot \left[\mathbf{T}^-(\mathbf{\Omega}) + \mathbf{T}^+(\mathbf{\Omega})\right], \tag{6.15}$$

with

$$\begin{aligned}
\mathbf{P}(\boldsymbol{r}_{in}) \cdot \mathbf{T}^- &= \int_0^l \mathrm{d}t(1 - \frac{t}{l})\, Q(\boldsymbol{r}_{in} + t\mathbf{\Omega})e^{-(\tau(t)-\tau(t'))}, \\
&= \sum_{k=0}^{n_p} \left[\frac{z_{in} - \tilde{z}}{\Delta z/2}\right]^k \sum_{p=k}^{n_p} \binom{p}{k} \left(\frac{2\mu}{\Delta z}\right)^{p-k} Q_\beta^p(\mathbf{\Omega})\mathrm{E}_{p-k}^-, \\
&= \sum_{p=0}^{n_p} \left(\sum_{k=0}^{p} \binom{p}{k} \left[\frac{z_{in} - \tilde{z}}{\Delta z/2}\right]^k \left(\frac{2\mu}{\Delta z}\right)^{p-k} \mathrm{E}_{p-k}^- \right) Q_\beta^p(\mathbf{\Omega}), \\
&= \sum_{n=1}^{n_m} \sum_{p=0}^{n_p} A_n(\mathbf{\Omega}) \left(\sum_{k=0}^{p} \binom{p}{k} \left[\frac{z_{in} - \tilde{z}}{\Delta z/2}\right]^k \left(\frac{2\mu}{\Delta z}\right)^{p-k} \mathrm{E}_{p-k}^- \right) Q_\beta^{p\,n}, \\
&= \mathbf{W}^-(\boldsymbol{r_{in}}, \mathbf{\Omega}) \cdot \boldsymbol{Q}_\beta.
\end{aligned}$$

In a similar manner,

$$\mathbf{P}(\boldsymbol{r}_{in}) \cdot \mathbf{T}^{+} = \mathbf{W}^{+}(\boldsymbol{r_{in}}, \boldsymbol{\Omega}) \cdot \boldsymbol{Q}_{\alpha}.$$

Eq (6.15) can thus be written as

$$\psi_{\alpha}(\boldsymbol{r}_{out}, \boldsymbol{\Omega}) = \psi_{\beta}(\boldsymbol{r}_{in}, \boldsymbol{\Omega}) e^{-\tau(l)} + \mathbf{W}^{-}(\boldsymbol{r_{in}}, \boldsymbol{\Omega}) \cdot \boldsymbol{Q}_{\beta} + \mathbf{W}^{+}(\boldsymbol{r_{in}}, \boldsymbol{\Omega}) \cdot \boldsymbol{Q}_{\alpha}. \tag{6.16}$$

Equation (6.16) is valid for a single chord but can be integrated over all chords entering through β and exiting through α. This is followed by summing over all surfaces where a chord exits the region through surface α at point $\boldsymbol{r}_{\text{out}}$:

$$\begin{aligned}
\mathbf{J}_{\alpha,+}(\boldsymbol{r}) = & \sum_{\beta \in \partial i} \int_{\beta \to \alpha} \frac{\mathrm{d}\boldsymbol{\Omega}}{4\pi} |\boldsymbol{\Omega} \cdot n| \boldsymbol{Z}_D(\boldsymbol{r_{out}}, \boldsymbol{\Omega}) e^{-\tau(l)} \psi_{\beta}(\boldsymbol{r_{in}}, \boldsymbol{\Omega}) \\
& + \sum_{\beta \in \partial i} \int_{\beta \to \alpha} \frac{\mathrm{d}\boldsymbol{\Omega}}{4\pi} |\boldsymbol{\Omega} \cdot n| \boldsymbol{Z}_D(\boldsymbol{r_{out}}, \boldsymbol{\Omega}) \otimes \mathbf{W}^{-}(\boldsymbol{r_{in}}, \boldsymbol{\Omega}) \cdot \boldsymbol{Q}_{\beta} \\
& + \int_{\mathbb{S}_{2+}} \frac{\mathrm{d}\boldsymbol{\Omega}}{4\pi} |\boldsymbol{\Omega} \cdot n| \boldsymbol{Z}_D(\boldsymbol{r_{out}}, \boldsymbol{\Omega}) \otimes \mathbf{W}^{+}(\boldsymbol{r_{in}}, \boldsymbol{\Omega}) \cdot \boldsymbol{Q}_{\alpha}.
\end{aligned} \tag{6.17}$$

We now use (6.1) to expand the angular surface flux

$$\begin{aligned}
\mathbf{J}_{\alpha,+}(\boldsymbol{r}) = & \sum_{\beta \in \partial i} \int_{\beta \to \alpha} \frac{\mathrm{d}\boldsymbol{\Omega}}{4\pi} |\boldsymbol{\Omega} \cdot n| \boldsymbol{Z}_D(\boldsymbol{r_{out}}, \boldsymbol{\Omega}) \otimes \boldsymbol{Z}(\boldsymbol{r_{in}}, \boldsymbol{\Omega}) e^{-\tau(l)} \cdot \boldsymbol{\psi}_{\beta,-} \\
& + \sum_{\beta \in \partial i} \int_{\beta \to \alpha} \frac{\mathrm{d}\boldsymbol{\Omega}}{4\pi} |\boldsymbol{\Omega} \cdot n| \boldsymbol{Z}_D(\boldsymbol{r_{out}}, \boldsymbol{\Omega}) \otimes \mathbf{W}^{-}(\boldsymbol{r_{in}}, \boldsymbol{\Omega}) \cdot \boldsymbol{Q}_{\beta} \\
& + \int_{\mathbb{S}_{2+}} \frac{\mathrm{d}\boldsymbol{\Omega}}{4\pi} |\boldsymbol{\Omega} \cdot n| \boldsymbol{Z}_D(\boldsymbol{r_{out}}, \boldsymbol{\Omega}) \otimes \mathbf{W}^{+}(\boldsymbol{r_{in}}, \boldsymbol{\Omega}) \cdot \boldsymbol{Q}_{\alpha}.
\end{aligned} \tag{6.18}$$

Then, noting that

$$\int_{\mathbb{S}_{2+}} \mathrm{d}\boldsymbol{\Omega} = \sum_{\beta \in \partial i} \int_{\beta \to \alpha} \mathrm{d}\boldsymbol{\Omega},$$

and that integrating over the surface α in equation (6.18) gives the outgoing current $\mathbf{J}_{\alpha,+}$ on the left side, we obtain:

$$\begin{aligned}\mathbf{J}_{\alpha,+} = &\int_{\alpha} \mathrm{d}\boldsymbol{r} \sum_{\beta\in\partial i} \int_{\beta\to\alpha} \frac{\mathrm{d}\boldsymbol{\Omega}}{4\pi} |\boldsymbol{\Omega}\cdot n| \boldsymbol{Z}_D(\boldsymbol{r_{out}},\boldsymbol{\Omega}) \otimes \boldsymbol{Z}(\boldsymbol{r_{in}},\boldsymbol{\Omega}) e^{-\tau(l)} \cdot \boldsymbol{\psi}_{\beta,-} \\ &+ \int_{\alpha} \mathrm{d}\boldsymbol{r} \sum_{\beta\in\partial i} \int_{\beta\to\alpha} \frac{\mathrm{d}\boldsymbol{\Omega}}{4\pi} |\boldsymbol{\Omega}\cdot n| \boldsymbol{Z}_D(\boldsymbol{r_{out}},\boldsymbol{\Omega}) \otimes \mathbf{W}^{-}(\boldsymbol{r_{in}},\boldsymbol{\Omega}) \cdot \boldsymbol{Q}_{\beta} \\ &+ \int_{\alpha} \mathrm{d}\boldsymbol{r} \int_{\mathbb{S}_{2+}} \frac{\mathrm{d}\boldsymbol{\Omega}}{4\pi} |\boldsymbol{\Omega}\cdot n| \boldsymbol{Z}_D(\boldsymbol{r_{out}},\boldsymbol{\Omega}) \otimes \mathbf{W}^{+}(\boldsymbol{r_{in}},\boldsymbol{\Omega}) \cdot \boldsymbol{Q}_{\alpha}.\end{aligned}$$

However, since we do not have horizontal sources, we proceed as in transport: horizontal sources are constructed through linear interpolation of the vertical sources. By substituting the relations (5.31) and (5.32) into (6.16), we obtain

$$\psi_{\alpha}(\boldsymbol{r}_{out},\boldsymbol{\Omega}) = \psi_{\beta}(\boldsymbol{r}_{in},\boldsymbol{\Omega}) e^{-\tau(l)} + \mathbf{W}_{\gamma}(\boldsymbol{r_{in}},\boldsymbol{\Omega}) \cdot \boldsymbol{Q}_{\beta} + \mathbf{W}_{\gamma}(\boldsymbol{r_{in}},\boldsymbol{\Omega}) \cdot \boldsymbol{Q}_{\gamma^{\star}}, \tag{6.19}$$

with

$$\mathbf{W}_{\gamma}(\boldsymbol{r_{in}},\boldsymbol{\Omega}) = \mathbf{W}^{-}(\boldsymbol{r_{in}},\boldsymbol{\Omega}) \left(1 - \frac{\mathrm{L}_{k-1}}{\mathrm{L}_{tot}}\right) + \mathbf{W}^{+}(\boldsymbol{r_{in}},\boldsymbol{\Omega}) \left(1 - \frac{\mathrm{L}_{k}}{\mathrm{L}_{tot}}\right), \tag{6.20}$$

$$\mathbf{W}_{\gamma^{\star}}(\boldsymbol{r_{in}},\boldsymbol{\Omega}) = \mathbf{W}^{-}(\boldsymbol{r_{in}},\boldsymbol{\Omega}) \frac{\mathrm{L}_{k-1}}{\mathrm{L}_{tot}} + \mathbf{W}^{+}(\boldsymbol{r_{in}},\boldsymbol{\Omega}) \frac{\mathrm{L}_{k}}{\mathrm{L}_{tot}}. \tag{6.21}$$

It should be understood that what equation (6.19) implicitly highlights is that, even if α or β are horizontal surfaces, the source term is driven by sources defined on the vertical surfaces. The $\mathrm{DP_n}$ transmission equation can thus be rewritten as

$$\begin{aligned}\mathbf{J}_{\alpha,+} = &\int_{\alpha} \mathrm{d}\boldsymbol{r} \sum_{\beta\in\partial i} \int_{\beta\to\alpha} \frac{\mathrm{d}\boldsymbol{\Omega}}{4\pi} |\boldsymbol{\Omega}\cdot n| \boldsymbol{Z}_D(\boldsymbol{r_{out}},\boldsymbol{\Omega}) \otimes \boldsymbol{Z}(\boldsymbol{r_{in}},\boldsymbol{\Omega}) e^{-\tau(l)} \cdot \boldsymbol{\psi}_{\beta,-} \\ &+ \int_{\alpha} \mathrm{d}\boldsymbol{r} \sum_{\beta\in\partial i} \int_{\beta\to\alpha} \frac{\mathrm{d}\boldsymbol{\Omega}}{4\pi} |\boldsymbol{\Omega}\cdot n| \boldsymbol{Z}_D(\boldsymbol{r_{out}},\boldsymbol{\Omega}) \otimes \mathbf{W}_{\gamma}(\boldsymbol{r_{in}},\boldsymbol{\Omega}) \cdot \boldsymbol{Q}_{\gamma} \\ &+ \int_{\alpha} \mathrm{d}\boldsymbol{r} \int_{\mathbb{S}_{2+}} \frac{\mathrm{d}\boldsymbol{\Omega}}{4\pi} |\boldsymbol{\Omega}\cdot n| \boldsymbol{Z}_D(\boldsymbol{r_{out}},\boldsymbol{\Omega}) \otimes \mathbf{W}_{\gamma^{\star}}(\boldsymbol{r_{in}},\boldsymbol{\Omega}) \cdot \boldsymbol{Q}_{\gamma^{\star}}.\end{aligned}$$

Let us specify that each outgoing surface α is associated with the vertical surface $\gamma^{\star}$, and each incoming surface β can be associated with the surface γ. We now simplify the previous equation by introducing some notations:

$$\tilde{\mathbb{T}}_{\alpha\beta} = \int_{\alpha} \mathrm{d}\boldsymbol{r} \int_{\beta\to\alpha} \frac{\mathrm{d}\boldsymbol{\Omega}}{4\pi} |\boldsymbol{\Omega}\cdot n| \boldsymbol{Z}_D(\boldsymbol{r_{out}},\boldsymbol{\Omega}) \otimes \boldsymbol{Z}(\boldsymbol{r_{in}},\boldsymbol{\Omega}) e^{-\tau(l)}, \tag{6.22}$$

$$\mathbb{E}^{-}_{\alpha\gamma} = \sum_{\beta\in(\partial i,\gamma)} \int_{\alpha} \mathrm{d}\boldsymbol{r} \int_{\beta\to\alpha} \frac{\mathrm{d}\boldsymbol{\Omega}}{4\pi} |\boldsymbol{\Omega}\cdot n| \boldsymbol{Z}_D(\boldsymbol{r_{out}},\boldsymbol{\Omega}) \otimes \mathbf{W}_{\gamma}(\boldsymbol{r_{in}},\boldsymbol{\Omega}), \tag{6.23}$$

$$\mathbb{E}^{+}_{\alpha\gamma^\star} = \int_{\alpha} \mathrm{d}\boldsymbol{r} \int_{\mathbb{S}_{2+}} \frac{\mathrm{d}\boldsymbol{\Omega}}{4\pi} |\boldsymbol{\Omega}\cdot n| \boldsymbol{Z}_D(\boldsymbol{r_{out}},\boldsymbol{\Omega}) \otimes \mathbf{W}_{\gamma^\star}(\boldsymbol{r_{in}},\boldsymbol{\Omega}). \tag{6.24}$$

where $(\partial i,\gamma)$ denotes the set of chords entering through β, and thus the surface β is associated through interpolation with the incoming vertical surface γ:

$$\sum_{\beta\in\partial i} = \sum_{\gamma\in\partial i_v} \sum_{\beta\in(\partial i,\gamma)} \tag{6.25}$$

We can thus summarize by writing:

$$\mathbf{J}_{\alpha,+} = \sum_{\beta\in\partial i} \tilde{\mathbb{T}}_{\alpha\beta} \boldsymbol{\psi}_{\beta,-} + \sum_{\gamma\in\partial i_v} \mathbb{E}^{-}_{\alpha\gamma} \boldsymbol{Q}_{\gamma} + \mathbb{E}^{+}_{\alpha\gamma^\star} \boldsymbol{Q}_{\gamma^\star}. \tag{6.26}$$

Then, to express this last equation in terms of the incoming vertical surfaces γ, it is sufficient to write:

$$\mathbb{E}^{+}_{\alpha\gamma^\star} \boldsymbol{Q}_{\gamma^\star} = \delta_{\gamma^\star\gamma} \mathbb{E}^{+}_{\alpha\gamma} \boldsymbol{Q}_{\gamma}, \tag{6.27}$$

then

$$\mathbb{E}_{\alpha\gamma} = \mathbb{E}^{-}_{\alpha\gamma} + \delta_{\gamma^\star\gamma} \mathbb{E}^{+}_{\alpha\gamma}. \tag{6.28}$$

Finally, we obtain

$$\mathbf{J}_{\alpha,+} = \sum_{\beta\in\partial i} \tilde{\mathbb{T}}_{\alpha\beta} \boldsymbol{\psi}_{\beta,-} + \sum_{\gamma\in\partial i_v} \mathbb{E}_{\alpha\gamma} \boldsymbol{Q}_{\gamma}. \tag{6.29}$$

However, rather than expressing the transmission using the $\mathrm{DP_n}$ coefficients, it has been shown that a formulation based on currents converges more quickly [126]. The reason is as follows: unlike current, flux is an intensive quantity. Thus, the size of the geometry's surfaces

- whether small or large - does not influence the value of the flux. Given that a Krylov method is used to solve this system and that the convergence rate is conditioned by the norm of the residual, it is preferable not to use the flux formulation, which converges more slowly. We define:

$$\mathbb{T}_{\alpha\beta} = \tilde{\mathbb{T}}_{\alpha\beta}\mathbb{B}_{\beta,-}. \tag{6.30}$$

Thus

$$\mathbf{J}_{\alpha,+} = \sum_{\beta\in\partial i} \mathbb{T}_{\alpha\beta}\mathbf{J}_{\beta,-} + \sum_{\gamma\in\partial i_v} \mathbb{E}_{\alpha\gamma}\boldsymbol{Q}_{\gamma}. \tag{6.31}$$

The system (6.31) can also be written for a region i. To this end, we define $\mathbf{J}_{bd,+} = (\mathbf{J}_{\alpha_1,+}, \mathbf{J}_{\alpha_2,+}, \ldots, \mathbf{J}_{\alpha_{n_s},+})$, where n_s is the number of surfaces in region i, and $\boldsymbol{Q}_{bd} = (\boldsymbol{Q}\alpha_1, \boldsymbol{Q}\alpha_2, \ldots, \boldsymbol{Q}\alpha_{n_s-2}, 0, 0)$ that represents the surface source defined on the vertical surfaces. Thus, we obtain

$$\mathbf{J}_{bd,+} = \mathbb{T}\mathbf{J}_{bd,-} + \mathbb{E}\boldsymbol{Q}_{bd}, \tag{6.32}$$

with

$$\mathbb{T} = \begin{pmatrix} \mathbb{T}_{\alpha_1\alpha_1} & & & \\ \mathbb{T}_{\alpha_2\alpha_2} & \mathbb{T}_{\alpha_2\alpha_2} & & \\ \vdots & \ddots & \ddots & \\ \mathbb{T}_{\alpha_{n_s}\alpha_1} & \mathbb{T}_{\alpha_{n_s}\alpha_2} & \cdots & \mathbb{T}_{\alpha_{n_s}\alpha_{n_s}} \end{pmatrix}, \tag{6.33}$$

$$\mathbb{E} = \begin{pmatrix} \mathbb{E}_{\alpha_1\alpha_1} & & & & & \\ \mathbb{E}_{\alpha_2\alpha_2} & \mathbb{E}_{\alpha_2\alpha_2} & & & & \\ \vdots & \ddots & \ddots & & & \\ \mathbb{E}_{\alpha_{n_s-2}\alpha_1} & \mathbb{E}_{\alpha_{n_s-2}\alpha_2} & \cdots & \mathbb{E}_{\alpha_{n_s-2}\alpha_{n_s-2}} & 0 & 0 \\ \mathbb{E}_{\alpha_{n_s-1}\alpha_1} & \mathbb{E}_{\alpha_{n_s-1}\alpha_2} & \cdots & \mathbb{E}_{\alpha_{n_s-1}\alpha_{n_s-2}} & 0 & 0 \\ \mathbb{E}_{\alpha_{n_s}\alpha_1} & \mathbb{E}_{\alpha_{n_s}\alpha_2} & \cdots & \mathbb{E}_{\alpha_{n_s}\alpha_{n_s-2}} & 0 & 0 \end{pmatrix}. \tag{6.34}$$

It is noteworthy that $\mathbb{E}$ and $\mathbb{T}$ can be decomposed into four blocks corresponding to each pair (incoming surface, outgoing surface).

6.3 . Equation relating moments, currents, and external source

In this section, we aim to establish an equation that allows us to calculate the flux moments (6.4) from the currents and the external source. We begin by using the transmission equation (6.31) to express $\mathbf{J}_{\alpha,+}$ in terms of $\mathbf{J}_{\alpha,-}$ and the surface source $\boldsymbol{Q}_\gamma$:

$$\begin{aligned}\sum_{\alpha\in\partial i}\mathbf{J}_{\alpha,+} &= \sum_{\alpha\in\partial i}\left(\sum_{\beta\in\partial i}\mathbb{T}_{\alpha\beta}\mathbf{J}_{\beta,-}+\sum_{\gamma\in\partial i_v}\mathbb{E}_{\alpha\gamma}\boldsymbol{Q}_\gamma\right),\\ &= \sum_{\beta\in\partial i}\sum_{\alpha\in\partial i}\mathbb{T}_{\alpha\beta}\mathbf{J}_{\beta,-}+\sum_{\gamma\in\partial i_v}\sum_{\alpha\in\partial i}\mathbb{E}_{\alpha\gamma}\boldsymbol{Q}_\gamma,\\ &= \sum_{\beta\in\partial i}\mathbb{T}_{\beta}\mathbf{J}_{\beta,-}+\sum_{\gamma\in\partial i_v}\mathbb{E}_{\gamma}\boldsymbol{Q}_\gamma.\end{aligned}$$

Finally, we write

$$\sum_{\alpha\in\partial i}\mathbf{J}_{\alpha,+} = \sum_{\alpha\in\partial i}\mathbb{T}_{\beta}\mathbf{J}_{\alpha,-}+\sum_{\gamma\in\partial i_v}\mathbb{E}_{\gamma}\boldsymbol{Q}_\gamma. \tag{6.35}$$

The next step is to use the definition of the scaled moments (bi5.82) to find an expression that depends on the currents and the external source.

$${}'\boldsymbol{\Phi}^s_{\gamma^\star} = {}'\boldsymbol{\Phi}_{\gamma^\star} - {}'\boldsymbol{\Phi}_G + {}'\boldsymbol{\Phi}_i. \tag{6.36}$$

We then substitute the synthetic balance equation (6.8) into equation (6.36).

$$\begin{aligned}{}'\boldsymbol{\Phi}^s_{\gamma^\star} &= {}'\boldsymbol{\Phi}_{\gamma^\star} - {}'\boldsymbol{\Phi}_G + \frac{1}{\mathrm{V}_i}\mathbb{X}_D\sum_{\alpha\in\partial i}\left[\mathbf{J}_{\alpha,-}-\mathbf{J}_{\alpha,+}\right]+\mathbb{X}_D\mathbb{S}\sum_{\gamma\in\partial i_v}\mathbb{M}_{G,\gamma}\boldsymbol{Q}_\gamma,\\ &= {}'\boldsymbol{\Phi}_{\gamma^\star} - {}'\boldsymbol{\Phi}_G + \frac{1}{\mathrm{V}_i}\mathbb{X}_D\sum_{\alpha\in\partial i}\left[\mathbb{I}\mathrm{d}-\mathbb{T}_\alpha\right]\mathbf{J}_{\alpha,-}+\mathbb{X}_D\sum_{\gamma\in\partial i_v}\left(\mathbb{S}\mathbb{M}_{G,\gamma}-\frac{1}{\mathrm{V}_i}\mathbb{E}_\gamma\right)\boldsymbol{Q}_\gamma.\end{aligned}$$

Then, we set

$$
\begin{aligned}
\mathbb{N}_\gamma &= \mathbb{SM}_{G,\gamma} - \frac{1}{\mathrm{V}_i}\mathbb{E}_\gamma, \\
\mathbb{N}c &= \mathbb{X}_D \sum_{\gamma\in\partial i_v} \mathbb{N}_\gamma \Sigma_s, \\
\mathbb{NP} &= \mathbb{X}_D \sum_{\gamma\in\partial i_v} \mathbb{N}_\gamma \Sigma_s \mathbb{PP}_\gamma^{-1},
\end{aligned}
$$

and,

$$
\begin{aligned}
{}'\mathbf{\Phi}_a &= \mathbb{X}_D \sum_{\gamma\in\partial i_v} \mathbb{N}_\gamma \Sigma_s \, \mathbf{\Phi}_\gamma^s, \\
{}'\mathbf{\Phi}_u &= -{}'\mathbf{\Phi}_G + \frac{1}{V}_i \mathbb{X}_D \sum_{\alpha\in\partial i} \left[\mathbb{I}\mathrm{d} - \mathbb{T}_\alpha\right] \mathbf{J}_{\alpha,-} + \mathbb{X}_D \sum_{\gamma\in\partial i_v} \mathbb{N}_\gamma \boldsymbol{Q}_\gamma^{ext}.
\end{aligned}
$$

We can thus simply write:

$$
\mathbf{\Phi}_{\gamma^\star}^s = \mathbb{PP}_{\gamma^\star}^{-1} {}'\mathbf{\Phi}_{\gamma^\star} + \mathbb{PP}_{\gamma^\star}^{-1} {}'\mathbf{\Phi}_u + \mathbb{PP}_{\gamma^\star}^{-1} {}'\mathbf{\Phi}_a. \tag{6.37}
$$

We multiply equation (6.37) by $\mathbb{N}c$

$$
\mathbb{X}_D \sum_{\gamma\in\partial i_v} \mathbb{N}_\gamma \Sigma_s \mathbf{\Phi}_\gamma^s = \mathbb{X}_D \sum_{\gamma\in\partial i_v} \mathbb{N}_\gamma \Sigma_s \mathbb{PP}_\gamma^{-1} {}'\mathbf{\Phi}_\gamma + \mathbb{NP}{}'\mathbf{\Phi}_u + \mathbb{NP}{}'\mathbf{\Phi}_a. \tag{6.38}
$$

This allows us to define ${}'\mathbf{\Phi}_a$ as

$$
{}'\mathbf{\Phi}_a = \left[\mathbb{I}_\mathrm{d} - \mathbb{NP}\right]^{-1} \left[\mathbb{X}_D \sum_{\gamma\in\partial i_v} \mathbb{N}_\gamma \Sigma_s \mathbb{PP}_\gamma^{-1} {}'\mathbf{\Phi}_\gamma + \mathbb{NP}{}'\mathbf{\Phi}_u\right]. \tag{6.39}
$$

We inject the expressions of ${}'\mathbf{\Phi}_u$ and ${}'\mathbf{\Phi}_a$ in (6.37). It gives:

$$
\begin{aligned}
{}'\mathbf{\Phi}^s_{\gamma^\star} &= {}'\mathbf{\Phi}_{\gamma^\star} + {}'\mathbf{\Phi}_u + \left[\mathbb{I}_\mathrm{d} - \mathbb{NP}\right]^{-1}\left[\mathbb{X}_D \sum_{\gamma\in\partial i_v} \mathbb{N}_\gamma \Sigma_s \mathbb{P}\mathbb{P}_\gamma^{-1}\, {}'\mathbf{\Phi}_\gamma + \mathbb{NP}\,{}'\mathbf{\Phi}_u\right], \\
&= {}'\mathbf{\Phi}_{\gamma^\star} + {}'\mathbf{\Phi}_u + \left[\mathbb{I}_\mathrm{d} - \mathbb{NP}\right]^{-1}\mathbb{X}_D \sum_{\gamma\in\partial i_v} \mathbb{N}_\gamma \Sigma_s \mathbb{P}\mathbb{P}_\gamma^{-1}\, {}'\mathbf{\Phi}_\gamma + \left[\mathbb{I}_\mathrm{d} - \mathbb{NP}\right]^{-1}\mathbb{NP}\,{}'\mathbf{\Phi}_u, \\
&= {}'\mathbf{\Phi}_{\gamma^\star} + \left[\mathbb{I}_\mathrm{d} - \mathbb{NP}\right]^{-1}\mathbb{X}_D \sum_{\gamma\in\partial i_v} \mathbb{N}_\gamma \Sigma_s \mathbb{P}\mathbb{P}_\gamma^{-1}\, {}'\mathbf{\Phi}_\gamma + \left[\mathbb{I}_\mathrm{d} - \mathbb{NP}\right]^{-1}\,{}'\mathbf{\Phi}_u.
\end{aligned}
$$

Next, we need to express ${}'\mathbf{\Phi}_\gamma$ and ${}'\mathbf{\Phi}_u$ in terms of the incoming and outgoing currents, and then combine the terms.

$$
\begin{aligned}
{}'\mathbf{\Phi}^s_{\gamma^\star} &= \mathbb{F}_{\gamma^\star,+}\mathbf{J}_{\gamma^\star,+} + \mathbb{F}_{\gamma^\star,-}\mathbf{J}_{\gamma^\star,-}, \\
&\quad + \left[\mathbb{I}_\mathrm{d} - \mathbb{NP}\right]^{-1}\left[-{}'\mathbf{\Phi}_G + \frac{1}{\mathrm{V}_i}\mathbb{X}_D \sum_{\alpha\in\partial i}\left[\mathbb{Id} - \mathbb{T}_\alpha\right]\mathbf{J}_{\alpha,-} + \mathbb{X}_D \sum_{\gamma\in\partial i_v} \mathbb{N}_\gamma \boldsymbol{Q}^{ext}_\gamma\right], \\
&\quad + \left[\mathbb{I}_\mathrm{d} - \mathbb{NP}\right]^{-1}\left[\mathbb{X}_D \sum_{\gamma\in\partial i_v} \mathbb{N}_\gamma \Sigma_s \mathbb{P}\mathbb{P}_\gamma^{-1}\, {}'\mathbf{\Phi}_\gamma\right].
\end{aligned}
$$

Then, after expanding,

$$
\begin{aligned}
{}'\mathbf{\Phi}^s_{\gamma^\star} &= \sum_{\gamma\in\partial i_v} \delta_{\gamma^\star\gamma}\mathbb{F}_{\gamma,+}\mathbf{J}_{\gamma,+} + \delta_{\gamma^\star\gamma}\mathbb{F}_{\gamma,-}\mathbf{J}_{\gamma,-} \\
&\quad - \sum_{\gamma\in\partial i_v} \left[\mathbb{I}_\mathrm{d} - \mathbb{NP}\right]^{-1}\mathbb{M}_{G,\gamma}\mathbb{P}\mathbb{P}_\gamma^{-1}\left[\mathbb{F}_{\gamma,+}\mathbf{J}_{\gamma,+} + \mathbb{F}_{\gamma,-}\mathbf{J}_{\gamma,-}\right] \\
&\quad + \sum_{\gamma\in\partial i_v} \left[\mathbb{I}_\mathrm{d} - \mathbb{NP}\right]^{-1}\mathbb{X}_D\mathbb{N}_\gamma \boldsymbol{Q}^{ext}_\gamma \\
&\quad + \sum_{\gamma\in\partial i_v} \left[\mathbb{I}_\mathrm{d} - \mathbb{NP}\right]^{-1}\mathbb{X}_D\mathbb{N}_\gamma \Sigma_s \mathbb{P}\mathbb{P}_\gamma^{-1}\left[\mathbb{F}_{\gamma,+}\mathbf{J}_{\gamma,+} + \mathbb{F}_{\gamma,-}\mathbf{J}_{\gamma,-}\right] \\
&\quad + \sum_{\beta\in\partial i} \left[\mathbb{I}_\mathrm{d} - \mathbb{NP}\right]^{-1}\frac{1}{\mathrm{V}_i}\mathbb{X}_D\left[\mathbb{Id} - \mathbb{T}_\beta\right]\mathbf{J}_{\beta,-}.
\end{aligned}
$$

The terms are then grouped into packages

$$
\begin{aligned}
{}'\mathbf{\Phi}^s_{\gamma^\star} = & \sum_{\gamma\in\partial i_v} \left[\delta_{\gamma^\star\gamma}\mathbb{F}_{\gamma,+} + \left[\mathbb{I}_{\mathrm{d}} - \mathbb{NP}\right]^{-1}\left(\mathbb{X}_D\mathbb{N}_\gamma\Sigma_s - \mathbb{M}_{G,\gamma}\right)\mathbb{PP}_\gamma^{-1}\mathbb{F}_{\gamma,+}\right]\mathbf{J}_{\gamma,+} \\
& + \sum_{\gamma\in\partial i_v} \left[\delta_{\gamma^\star\gamma}\mathbb{F}_{\gamma,-} + \left[\mathbb{I}_{\mathrm{d}} - \mathbb{NP}\right]^{-1}\left(\mathbb{X}_D\mathbb{N}_\gamma\Sigma_s - \mathbb{M}_{G,\gamma}\right)\mathbb{PP}_\gamma^{-1}\mathbb{F}_{\gamma,-}\right]\mathbf{J}_{\gamma,-} \\
& + \sum_{\beta\in\partial i} \left[\mathbb{I}_{\mathrm{d}} - \mathbb{NP}\right]^{-1}\frac{1}{\mathrm{V}_i}\mathbb{X}_D\left[\mathbb{I}\mathrm{d} - \mathbb{T}_\beta\right]\mathbf{J}_{\beta,-} \\
& + \sum_{\gamma\in\partial i_v} \left[\mathbb{I}_{\mathrm{d}} - \mathbb{NP}\right]^{-1}\mathbb{X}_D\mathbb{N}_\gamma\boldsymbol{Q}^{ext}_\gamma.
\end{aligned}
$$

Finally, we use the surface matrix $\mathbb{PP}^{-1}_{\gamma^\star}$ to recover the spatial coefficients of the flux

$$
\mathbf{\Phi}^s_{\gamma^\star} = \mathbb{PP}^{-1}_{\gamma^\star}\,{}'\mathbf{\Phi}^s_{\gamma^\star}.
$$

It leads to

$$
\begin{aligned}
\mathbf{\Phi}^s_{\gamma^\star} = & \sum_{\gamma\in\partial i_v} \underbrace{\mathbb{PP}^{-1}_{\gamma^\star}\left[\delta_{\gamma^\star\gamma}\mathbb{F}_{\gamma,+} + \left[\mathbb{I}_{\mathrm{d}} - \mathbb{NP}\right]^{-1}\left(\mathbb{X}_D\mathbb{N}_\gamma\Sigma_s - \mathbb{M}_{G,\gamma}\right)\mathbb{PP}_\gamma^{-1}\mathbb{F}_{\gamma,+}\right]}_{\mathbb{H}^+_{\gamma^\star\gamma}}\mathbf{J}_{\gamma,+} \\
& + \sum_{\gamma\in\partial i_v} \underbrace{\mathbb{PP}^{-1}_{\gamma^\star}\left[\delta_{\gamma^\star\gamma}\mathbb{F}_{\gamma,-} + \left[\mathbb{I}_{\mathrm{d}} - \mathbb{NP}\right]^{-1}\left(\mathbb{X}_D\mathbb{N}_\gamma\Sigma_s - \mathbb{M}_{G,\gamma}\right)\mathbb{PP}_\gamma^{-1}\mathbb{F}_{\gamma,-}\right]}_{\mathbb{H}^-_{\gamma^\star\gamma}}\mathbf{J}_{\gamma,-} \\
& + \sum_{\beta\in\partial i} \underbrace{\mathbb{PP}^{-1}_{\gamma^\star}\left[\mathbb{I}_{\mathrm{d}} - \mathbb{NP}\right]^{-1}\frac{1}{\mathrm{V}_i}\mathbb{X}_D\left[\mathbb{I}\mathrm{d} - \mathbb{T}_\beta\right]}_{\mathbb{I}_{\beta\alpha}}\mathbf{J}_{\beta,-} \\
& + \sum_{\gamma\in\partial i_v} \underbrace{\mathbb{PP}^{-1}_{\gamma^\star}\left[\mathbb{I}_{\mathrm{d}} - \mathbb{NP}\right]^{-1}\mathbb{X}_D\mathbb{N}_\gamma}_{\mathbb{D}_{\gamma^\star\gamma}}\boldsymbol{Q}^{ext}_\gamma.
\end{aligned}
$$

Thus, the balance equation is written as

$$
\mathbf{\Phi}^s_{\gamma^\star} = \sum_{\gamma\in\partial i_v}\mathbb{H}^+_{\gamma^\star\gamma}\mathbf{J}_{\gamma,+} + \sum_{\gamma\in\partial i_v}\mathbb{H}^-_{\gamma^\star\gamma}\mathbf{J}_{\gamma,-} + \sum_{\beta\in\partial i}\mathbb{I}_{\gamma^\star\beta}\mathbf{J}_{\beta,-} + \sum_{\gamma\in\partial i_v}\mathbb{D}_{\gamma^\star\gamma}\boldsymbol{Q}^{ext}_\gamma. \tag{6.40}
$$

In the same manner as for the transmission, the system (6.40) can be written regionally as follows:

$$\boldsymbol{\Phi}_{bd}^{s} = \mathbb{H}^{+}\mathbf{J}_{bd,+} + \tilde{\mathbb{H}}^{-}\mathbf{J}_{bd,-} + \mathbb{D}\boldsymbol{Q}_{bd}^{ext}, \tag{6.41}$$

with

$$\tilde{\mathbb{H}}^{-} = \mathbb{H}^{-} + \mathbb{I}.$$

6.4 . Multi-collisional equation

We now aim to establish an equation that expresses the outgoing currents as a function of the incoming currents and the external source, and an equation that allows updating the corrected surface moments (6.36) from the incoming currents and the external source. To this end, we start from the transmission equation (6.32) and then express the source in terms of the self-scattering component and the external source (fission, up-scattering, and down-scattering). This yields:

$$\mathbf{J}_{bd,+} = \mathbb{T}\mathbf{J}_{bd,-} + \mathbb{E}\Sigma_s\boldsymbol{\Phi}_{bd}^{s} + \mathbb{E}\boldsymbol{Q}_{bd}^{ext}. \tag{6.42}$$

Then, by substituting (6.41) into (6.42), we obtain:

$$\mathbf{J}_{bd,+} = \mathbb{T}\mathbf{J}_{bd,-} + \mathbb{E}\Sigma_s\mathbb{H}^{+}\mathbf{J}_{bd,+} + \mathbb{E}\Sigma_s\tilde{\mathbb{H}}^{-}\mathbf{J}_{bd,-} + \mathbb{E}\Sigma_s\mathbb{D}\boldsymbol{Q}_{bd}^{ext} + \mathbb{E}\boldsymbol{Q}_{bd}^{ext}. \tag{6.43}$$

We isolate the outgoing current on the left side

$$\begin{aligned}\mathbf{J}_{bd,+} = &\left[\mathbb{I}\mathsf{d} - \mathbb{E}\Sigma_s\mathbb{H}^{+}\right]^{-1}\left[\mathbb{T} + \mathbb{E}\Sigma_s\tilde{\mathbb{H}}^{-}\right]\mathbf{J}_{bd,-} \\ &+ \left[\mathbb{I}\mathsf{d} - \mathbb{E}\Sigma_s\mathbb{H}^{+}\right]^{-1}\mathbb{E}\left[\Sigma_s\mathbb{D} + \mathbb{I}\mathsf{d}\right]\boldsymbol{Q}_{bd}^{ext},\end{aligned}$$

then, we set

$$\widehat{\mathbb{T}} = \left[\mathbb{I}\mathsf{d} - \mathbb{E}\Sigma_s\mathbb{H}^{+}\right]^{-1}\left[\mathbb{T} + \mathbb{E}\Sigma_s\tilde{\mathbb{H}}^{-}\right], \tag{6.44}$$

$$\widehat{\mathbb{E}} = \left[\mathbb{I}\mathsf{d} - \mathbb{E}\Sigma_s\mathbb{H}^{+}\right]^{-1}\mathbb{E}\left[\Sigma_s\mathbb{D} + \mathbb{I}\mathsf{d}\right], \tag{6.45}$$

so that we can write:

$$\mathbf{J}_{bd,+} = \widehat{\mathbb{T}}\mathbf{J}_{bd,-} + \widehat{\mathbb{E}}\boldsymbol{Q}_{bd}^{ext}. \tag{6.46}$$

The final form of the matrix to be used along iteration can then be expressed in function of exiting currents only by the use of the geometric relationship connecting the incoming and outgoing currents, ($\mathbf{J}_{bd,-} = \mathbb{G}\mathbf{J}_{bd,+}$), so that

$$\left(\mathbb{I}_{\mathrm{d}} - \mathbb{G}\widehat{\mathbb{T}}\right)\mathbf{J}_{bd,+} = \widehat{\mathbb{E}}\boldsymbol{Q}_{bd}^{ext}. \tag{6.47}$$

The linear system (6.47) is solved using the non-stationary iterative method BiCGSTAB [127] with ILU(0) preconditioning [128] as it has shown better performances compared to the GMRES solver [128, 129]. The final step involves substituting (6.46) into (6.41) in order to update the corrected moments based on the currents and the external source:

$$\boldsymbol{\Phi}_{bd}^{s} = \left[\mathbb{H}^{+}\widehat{\mathbb{T}} + \tilde{\mathbb{H}}^{-}\right]\mathbf{J}_{bd,-} + \left[\mathbb{H}^{+}\widehat{\mathbb{E}} + \mathbb{D}\right]\boldsymbol{Q}_{bd}^{ext}. \tag{6.48}$$

6.5 . Shared memory parallelism

Parallelization with OpenMP is used to construct the matrices of the problem. The strategy is based on the work of a previous thesis on the TDT solver [6]. It consists of two phases : an information retrieval phase and a construction phase.

In the first phase, the threads sweep the trajectories in parallel to retrieve the information necessary for constructing the matrices. For this purpose, a data structure is associated with each 2D region, allowing certain quantities, such as the chord lengths crossing the region, to be stored. In the second phase, each 2D region is assigned to a thread, along with a batch of energy groups. Thus, each thread can independently construct the acceleration matrices associated with this 2D region and these energy groups.

7 - Verifications of the linear surface scheme

Chapter 7 is dedicated to verifying the implementation of the transport scheme and acceleration methods, which are theoretically detailed in Chapters 5 and 6. The chapter is divided into two sections. The first section focuses on performance tests for a PWR cell and a comparison between 2D and 3D calculations. The second section uses a 3x3 PWR assembly to conduct a mesh convergence study between the step and linear surface schemes. In both sections, transport calculations are tested with and without synthetic acceleration.

Contents

7.1 . PWR pin cell test case

7.1.1 . Geometric, material and computational data

The cell is composed of four fuel rings, a cladding ring made of Zircaloy, and water. Finally, the cell is divided into four sectors as shown in figure 7.3. The geometric data are summarized in Table 7.1, and the isotopic composition of these three materials is detailed in Table 7.2.

The calculations are performed according to the 281-energy group structure. All calculations were performed with a quadrature formula of 48 azimuthal angles between $[0, \pi]$ and four polar angles distributed according to the Gauss-Legendre formula. Trajectories share a transversal integration step of 0.003 cm and aa axial one of 0.05 cm. The tolerance for convergence for fission integral and k_{eff} are 1×10^{-05}. All pin cell calculations were performed on Intel(R) Xeon(R) Silver 4216 CPU @ 2.10GHz.

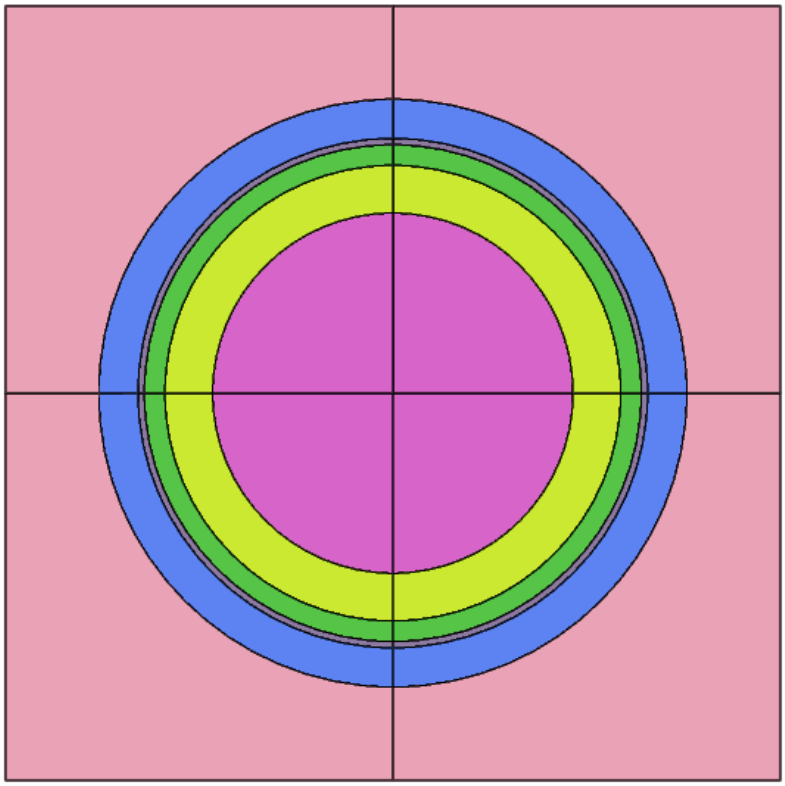

Figure 7.1 – Radial section of the PWR pin cell case.

Table 7.1 – PWR pin cell geometric data.

Lattice cell	Side	1.4122 cm
Fuel pin	First R	0.328451 cm
	Second R	0.415461 cm
	Third R	0.452977 cm
	Outer R	0.4645 cm
Fuel clad	Outer R	0.5360 cm
	Height	0.44 cm

Table 7.2 – Material isotopic composition used for two-/three-dimensional comparisons on a APOLLO3® PWR pin cell case.

Material	Isotope	Concentration (10^{24} at.cm^{-3})
Fuel A	U-235	5.4791E-05
	U-238	2.1944E-02
	0-16	4.5504E-02
	Pu-238	7.8686E-06
	Pu-239	4.5449E-04
	Pu-240	1.7325E-04
	Pu-241	6.4711E-05
	Pu-242	2.9913E-05
	Am-241	8.2290E-06
Fuel B	U-235	5.8051E-05
	U-238	2.1824E-02
	0-16	4.6497E-02
	Pu-238	1.5292E-05
	Pu-239	8.2896E-04
	Pu-240	3.1918E-04
	Pu-241	1.1703E-04
	Pu-242	5.6135E-05
	Am-241	1.4763E-05
Cladding	Zr	4.2909E-06
Water	H2O	2.5320E-02

7.1.2 . Numerical verifications

Initially, some properties of the MOC are studied. We begin by examining the evolution of the classification rate (number of classified chords over the total number of chords) as a function of the geometry height. In this study, we consider a case with two axial planes of equal height, which we vary between 0.1 cm and 200 cm. It is also noted that the side length of the cell is 1.4122 cm. The result is shown in Figure 7.2. It is observed that the classification rate does not fall below 58.6%, but as the ratio (height / cell side) approaches 1 (for example, at a height of 1 cm), the classification rate exceeds 80%. This result is very satisfactory given that, for a PWR assembly, the distance between two axial materials is at least on the order of 10 cm, but can reach the order of a meter in the fuel region. The consequence is that we achieve a high classification rate in the case where $n_p = 2$, and where the material mesh is used axially, as in the thesis [6, 7].

Next, we compare the accuracy and computation time of the linear surface scheme in two and three dimensions with the same axial material composition. To this end, the angu-

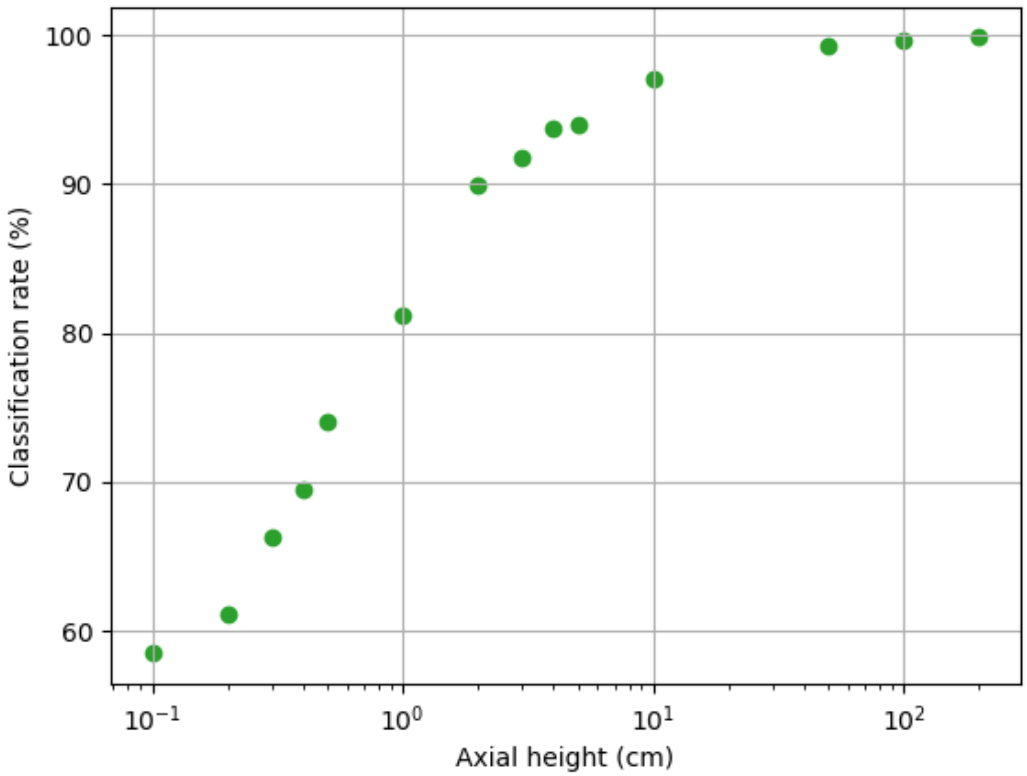

Figure 7.2 – Classification rate for different axial heights for the pin cell case.

lar flux is assumed to be constant in the axial direction ($n_p = 0$). The comparison is made for scattering anisotropy ranging from P_0 to P_3. Finally, given that the 2D method has already been validated on different geometric configurations, the k_{eff} values obtained will be taken as the 'theoretical' reference values. It is noted here that the calculations were run using 50 OpenMP threads.

The results are summarized in Table 7.3. The difference between the 2D and 3D k_{eff} is always less than 11 pcm. Thus, it is considered that the 3D scheme is sufficiently accurate for handling larger geometries. Finally, the 2D calculations take between 6 and 7 seconds, while the 3D calculations take around 2 minutes and 20 seconds.

Table 7.3 – k_{eff} and computing time comparison between two- and three-dimensional (with two axial planes) linear surface schemes on a APOLLO3® PWR pin cell case.

	k_{eff}		Δk_{eff} (pcm)	Time (s)	
Anisotropy	2D	3D ($n_p = 0$)		2D	3D
P_0	1.20554	1.20548	6	6	134
P_1	1.20233	1.20222	11	6	136
P_2	1.20335	1.20341	-7	6	136
P_3	1.20305	1.20310	5	7	146

Next, we compare the accuracy and computation time of the linear scheme between a transport calculation (free), DP_0, and DP_1. For this, the cell dataset is modified by introducing an axial heterogeneity, replacing Fuel A with Fuel B in the upper axial plane. The isotopic compositions are summarized in Table 7.2 . We assume a uniform flux in the axial direction and isotropic scattering.

The results are summarized in Table 7.4 and are the following: the difference between the free and accelerated calculations is at most 6 pcm, in absolute value. Considering the difference in k_{eff} obtained in assembly calculations between deterministic and Monte Carlo methods, which is at least several tens of pcm, this difference can be considered negligible. Regarding the acceleration of the calculations, the computation times are reduced by a factor of 13 for DP_0 acceleration and around 10 DP_1 accelerations. When comparing these reductions in computation time, we observe that they are less significant than those presented in Table 7.4 of reference [7], which are 44 and 45 for 5x5 and 7x7 PWR assemblies, respectively. This difference can be explained as follows: for the cell case, few external iterations, specifically those on the fission source, are required to reach convergence. The transport calculation associated with Table 7.4 was performed with 5 external iterations, compared to 192 and 188 for the 5x5 and 7x7 cases in [7].

In the case where the spatial basis degree equals 2 ($n_p = 2$), the power iteration method diverges for certain cases. To understand this behavior, the cell is entirely filled with Fuel B material, so that we are in a homogeneous configuration. Two parameters are then varied :

Table 7.4 – k_{eff} and computing time comparison between transport, DP_0 and DP_1 calculations on the APOLLO3® three-dimensional PWR pin cell case. The angular flux is supposed constant axially. The anisotropy is ranging from P_0 to P_3. In DP_0 acceleration, only the P_0 calculation is performed, as the flux is assumed to be isotropic.

	Scattering	k_{eff}	Δk_{eff} (pcm)	Time	Speed-up
Free	P_0	1.02014	-	6m23s	-
	P_1	1.01577	-	6m34s	-
	P_2	1.01731	-	6m51s	-
	P_3	1.01698	-	7m22s	-
DP_0	P_0	1.02007	7	30s	12.8
DP_1	P_0	1.02006	8	39s	9.8
	P_1	1.01570	7	40s	9.9
	P_2	1.01724	7	40s	10.3
	P_3	1.01691	7	43s	10.3

the height of the calculation regions Δz and the axial integration step Δs. To investigate this behavior, several quantities are studied : the relative error ξ_1^2 between the volumetric moments and the second-order geometric moments, the relative error ξ_2^2 between the second-order collision terms and the sum of the current term and the higher-order term, and the minimum mean free path across all regions $\langle\tau\rangle_{\text{min}} = \min \langle\tau\rangle$.

Focusing on ξ_2^1 ensures that the geometric source, calculated from the surface source and the geometric operator, is accurately evaluated. Focusing on ξ_2^2 ensures that the current term is correctly integrated numerically. In an infinite homogeneous medium, the current term is negligible (compared to the collision term). Therefore, the closer ξ_2^2 is to 1, the more accurately the current term is integrated. Then, four different heights are chosen : 1 cm, 10 cm, 100 cm, and the limit height Δz_{lim}, to the nearest tenth of a centimeter, which corresponds to the critical height at which the calculation diverges (i.e., above this height, the power iteration method converges). The study is conducted for three axial integration steps : 0.5 cm, 0.1 cm, and 0.05 cm. The results are summarized in table 7.5.

The key observations are as follows : first, for a given axial integration step Δs, as the height increases, the mean optical path also increases, leading to a reduction in errors. Therefore, beyond a certain height limit, where the errors are sufficiently small, transport calculations with $n_p = 2$ converge. Furthermore, for a given height Δz, as the axial integration step decreases, the mean optical path decreases, and the errors reduce accordingly. As a result, the finer the axial integration step, the lower the height limit beyond which the internal iterations converge.

Table 7.5 – Study of the transport convergence with a quadratic axial flux ($n_p = 2$) for the PWR pin cell case, considering various heights Δz and axial integration steps Δs. In each case, the minimum mean free path across all calculation regions is displayed. For this region, the relative errors ξ_1^2 and ξ_2^2 are presented. ξ_1^2 is the relative error between the second-order volumetric moments and the second-order geometric moments. ξ_1^2 is the relative error between the second-order collision terms and the sum of the current term and the higher-order term

$\Delta s = 0.5$ cm				
	$\Delta z = 1$ cm	$\Delta z_{lim} = 6.56$ cm	$\Delta z = 10$ cm	$\Delta z = 100$ cm
$\langle\tau\rangle_{\text{min}}$	1.8 $\times 10^{-08}$	4.7 $\times 10^{-08}$	5.0 $\times 10^{-08}$	1.8 $\times 10^{-07}$
ξ_1^2	4.0 $\times 10^{-03}$	4.6 $\times 10^{-04}$	7.7 $\times 10^{-05}$	4.8 $\times 10^{-06}$
ξ_2^2	1.00003	0.999998	0.999998	1.00000004
$\Delta s = 0.1$ cm				
	$\Delta z = 1$ cm	$\Delta z_{lim} = 5.24$ cm	$\Delta z = 10$ cm	$\Delta z = 100$ cm
$\langle\tau\rangle_{\text{min}}$	1.6 $\times 10^{-08}$	3.3 $\times 10^{-08}$	3.5 $\times 10^{-08}$	4.2 $\times 10^{-08}$
ξ_1^2	3.1 $\times 10^{-04}$	2.9 $\times 10^{-05}$	1.1 $\times 10^{-05}$	1.1 $\times 10^{-06}$
ξ_2^2	0.99992	0.999995	0.9999982	0.9999999931
$\Delta s = 0.05$ cm				
	$\Delta z = 1$ cm	$\Delta z_{lim} = 4.50$ cm	$\Delta z = 10$ cm	$\Delta z = 100$ cm
$\langle\tau\rangle_{\text{min}}$	1.3 $\times 10^{-08}$	1.8 $\times 10^{-08}$	2.2 $\times 10^{-08}$	2.0 $\times 10^{-08}$
ξ_1^2	1.6 $\times 10^{-04}$	2.8 $\times 10^{-05}$	4.8 $\times 10^{-06}$	3.8 $\times 10^{-06}$
ξ_2^2	0.99989	1.000019	0.99999356	0.99999988

7.2 . 3x3 PWR lattice test case

7.2.1 . Geometric, material and computational data

To evaluate the quality of the new LS scheme, we benchmarked it with a 3x3 PWR mini-assembly usually used for validation and verification activities of the APOLLO3® code. The case have been produced to compare 2D MOC schemes [124], and we have extended it to treat 3D geometries. The interest of the work is to study the spatial convergence of the LS method relative to the SC approximation, where the constant source approximation is used as we know that for 2D calculations, the LS scheme achieved better results for industrial meshes [55, 49]. To this end, we will compare the effective multiplication factors k_{eff}, production and absorption reaction rates for different meshes. However, we do not ensure the physical representativeness of our results by comparison with a reference Monte Carlo calculation. This study will be the subject of future work.

The assembly consists of eight UOX cells and an Ag-In-Cd (AIC) control rod. Two configuration cases are considered for the study. One where the control rod isn't inserted for 2D/3D comparisons, named homogeneous as no axial heterogeneities are presents. And one where the control rod is halfway inserted into borated water, named heterogeneous. Two radial planes of height 1 cm are arbitrarily chosen for the two cases. The radial part of the geometry is depicted on figure 7.3. The calculations are performed on a 1/8 geometry to take advantage of the 45° symmetry. Reflective boundary conditions are imposed. Table 7.6 shows the geometric dimensions of the fuel cell and the control rod. The materials' different isotopic concentrations and temperatures are reported in [124].

Self-shielding has been performed with the standard 281-group structure [130] based on the JEFF-3.1.1 cross section library [131]. This fine-group energy mesh assumes a sufficiently refined energy mesh in the lower epithermal domain such that the self-shielding formalism need not to be applied in the range below 24.6 eV. The mutual shielding of the resonant mixtures has been activated for ^{235}U, ^{238}U isotopes in the fuel rod and ^{107}Ag, ^{109}Ag, ^{110}Cd, ^{113}Cd and ^{115}In in the AIC rod.

Table 7.6 – 3x3 PWR test case geometric data.

Lattice cell	Side	1.26 cm
Fuel pin	Outer R	0.40830 cm
Fuel clad	Outer R	0.47750 cm
Fuel He gap	Width	0.00820 cm
	Height	1 cm
AIC rod	Outer R	0.43166 cm
Rod clad	Outer R	0.48400 cm
Rod He gap	Width	0.00534 cm
Guide tube	Inner R	0.55850 cm
-	Outer R	0.62250 cm
	Height	1 cm

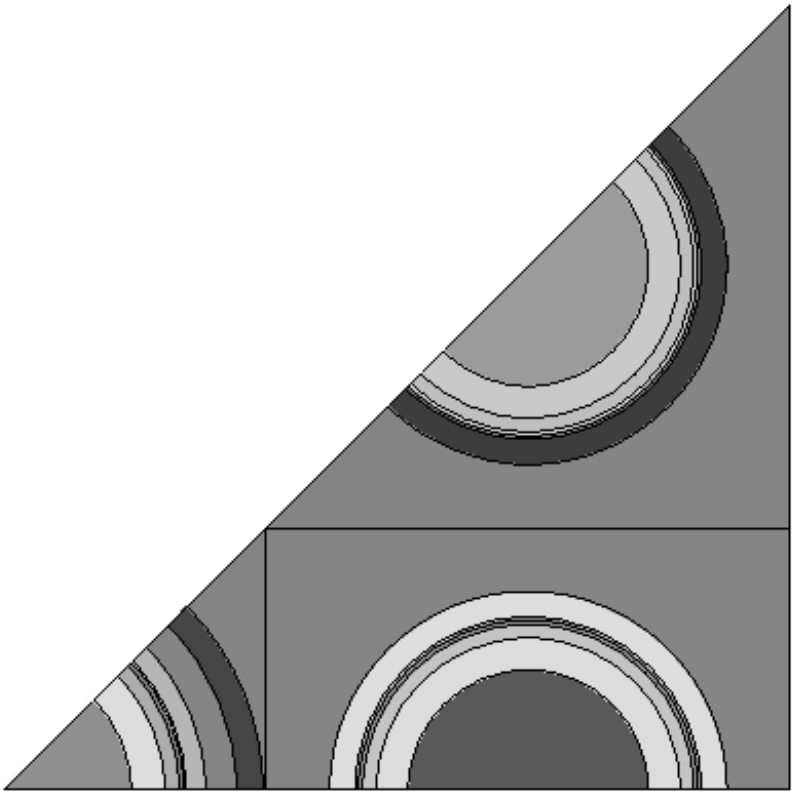

Figure 7.3 – Radial section of the 3x3 PWR assembly test case.

7.2.2 . Numerical verifications

Calculations were performed for six progressively refined grids: MIN, MAV, RAF, HYP, SHYP, and MEG (considered as the reference) as depicted in Fig 7.4. Each plane is composed of 45, 59, 140, 453, 674 and 1454 regions, respectively. Note that the meshes are non-conformal, i.e., the borated water below the control bar shares an identical mesh. A single self-shielded geometry is used for the flux calculations. The relative error on the k_{eff} compared to the reference mesh MEG is studied for each mesh. All calculations were performed with a quadrature formula of 48 azimuthal angles between $[0, \pi]$ and four polar angles distributed according to the Gauss-Legendre formula. The flux is expanded on the polynomial basis with degree 0. P_0 (without transport correction) and P_3 anisotropic scattering are considered and trajectories share a transversal integration step of 0.005 cm and a vertical one of 0.05 cm.

First, calculations were performed in the homogeneous P_0 configuration, both without acceleration (free) and with DP_1 acceleration. For each mesh, the values of k_{eff} and the computation times are provided in Tables 7.7 and 7.8, respectively. In terms of accuracy, the difference between the transport and accelerated calculations is at most 4 pcm. Thus, it can be concluded that the acceleration preserves the k_{eff} of the transport calculations. Regarding computation times, the acceleration reduces the duration by a factor ranging from 5.3 to 7.6. This results in the total computation time for all six cases decreasing from 30h23m42s to 4h52m54s. Practically, with accelerated calculations, multiple studies can be performed within the same day, unlike with non-accelerated calculations. The SC DP_1 accelerated computational times are also reported. These calculations lasted 2h49m22s which is 1.7 times faster than LS calculations. Then, concerning the number of external iterations, both transport and DP calculations took 6 external iterations to converge. To see a bigger difference, one should perform calculations on a bigger 3D case, such as the 5X5 or the 7X7 PWR cases in [7], where the reduction in external iterations is detailed in table 7.4.

Table 7.7 – Comparison of the DP_1 accelerated and free transport k_{eff} for the different meshes of the convergence study in the homogeneous configuration with P_0 anisotropy and constant axial flux ($n_p = 0$).

Mesh	Free k_{eff}	DP_1 k_{eff}	Δk_{eff} (pm)
MIN	0.80759	0.80763	4
MAV	0.80925	0.80928	4
RAF	0.81047	0.81051	4
HYP	0.81080	0.81082	2
SHYP	0.81086	0.81087	1
MEG	0.81088	0.81090	2

Secondly, the mesh convergence of the SC and LS methods is compared. As shown in

Table 7.8 – Comparison of the LS DP_1 accelerated and free transport computational time for the different meshes of the convergence study in the homogeneous configuration with P_0 anisotropy and constant axial flux ($n_p = 0$). The SC DP_1 accelerated computational times are also reported.

Mesh	LS Free Time (s)	LS DP_1 Time (s)	SC DP_1 Time (s)	LS Speed-up
MIN	2h50m36s	25m42s	12m39s	6.6
MAV	2h59m00s	24m27s	15m09s	7.3
RAF	3h20m01s	26m16s	16m39s	7.6
HYP	5h11m15s	45m46s	29m31s	6.8
SHYP	6h27m28s	1h01m46s	36m37s	6.3
MEG	9h35m21s	1h48m57s	58m47s	5.3
Total	30h23m42s	4h52m54s	2h49m22s	6.2

figure 7.5, 7.6, 7.11 and, 7.12, the LS scheme converges faster than the SC one for homogeneous configurations with P_0 and P_3 anisotropy. However, several remarks must be made. First, in each study, the k_{eff} values for the two schemes are not equal for the MEG mesh, the most refined one, although the k_{eff} differences between the SHYP and MEG meshes are only a few pcm. For example, 2 and 10 pcm for the LS and SC schemes, respectively, in the homogeneous P_0 calculation, and 4 and 12 pcm, respectively, in the heterogeneous P_0 calculation. The origin of this discrepancy has not yet been understood. Secondly, starting from the RAF mesh, the differences are on the order of tens of pcm. For example, in the heterogeneous P_3 case, the difference between k_{eff} for the LS and SC schemes is only 6 pcm for the RAF mesh, but it increases to 40 pcm and 20 pcm for the subsequent meshes. In contrast, for the least refined mesh (MIN), the SC scheme shows significant errors, compared to the LS one. For the heterogeneous calculation, the LS and SC k_{eff} errors compared to the reference value are, 295 pcm and 924 pcm for the P_0 calculation, respectively, and 317 pcm and 540 pcm for the P_3 calculation, respectively.

It is possible that, starting from the MAV mesh, the geometry is already too refined for the LS scheme to capture sufficiently significant flux gradients, such that the mesh convergence of the LS scheme becomes even more critical than that of the SC scheme. In other words, the gradients may be so minor that both methods behave similarly.

To assess whether this assertion holds true, a convergence study should be conducted on a larger geometrical configuration, such as the 17x17 assembly presented in Figure 4.7 and 4.8.

Finally, for all four convergence studies (homogeneous, heterogeneous) and (P_0, P_3), the evolution of the relative error in the absorption and production rates is plotted from figure 7.5 to figure 7.12. The fuel pins are numbered from 1 to 6 as follows : the pin cells in the lower plane are numbered 1 to 3 according to the numbering shown in Figure 7.4a. Then,

the pin cells in the upper plane are numbered 4 to 6 following the same numbering order. The LS values are marked with crosses, and the SC values are represented by triangles. The energy condensation is done in two groups.

Key observations are as follows : for each pin cell and mesh, the LS errors are consistently smaller than the SC errors. However, similar to the behavior of k_{eff}, it remains necessary to investigate why the error differences do not tend toward zero. Additionally, it is noticeable that the errors for pin cells with the same isotopic composition overlap, especially in the homogeneous cases where the flux distribution is axially uniform. Finally, starting from the MAV mesh, the errors for each energy group, mesh, anisotropies and material configurations are all below 1 %.

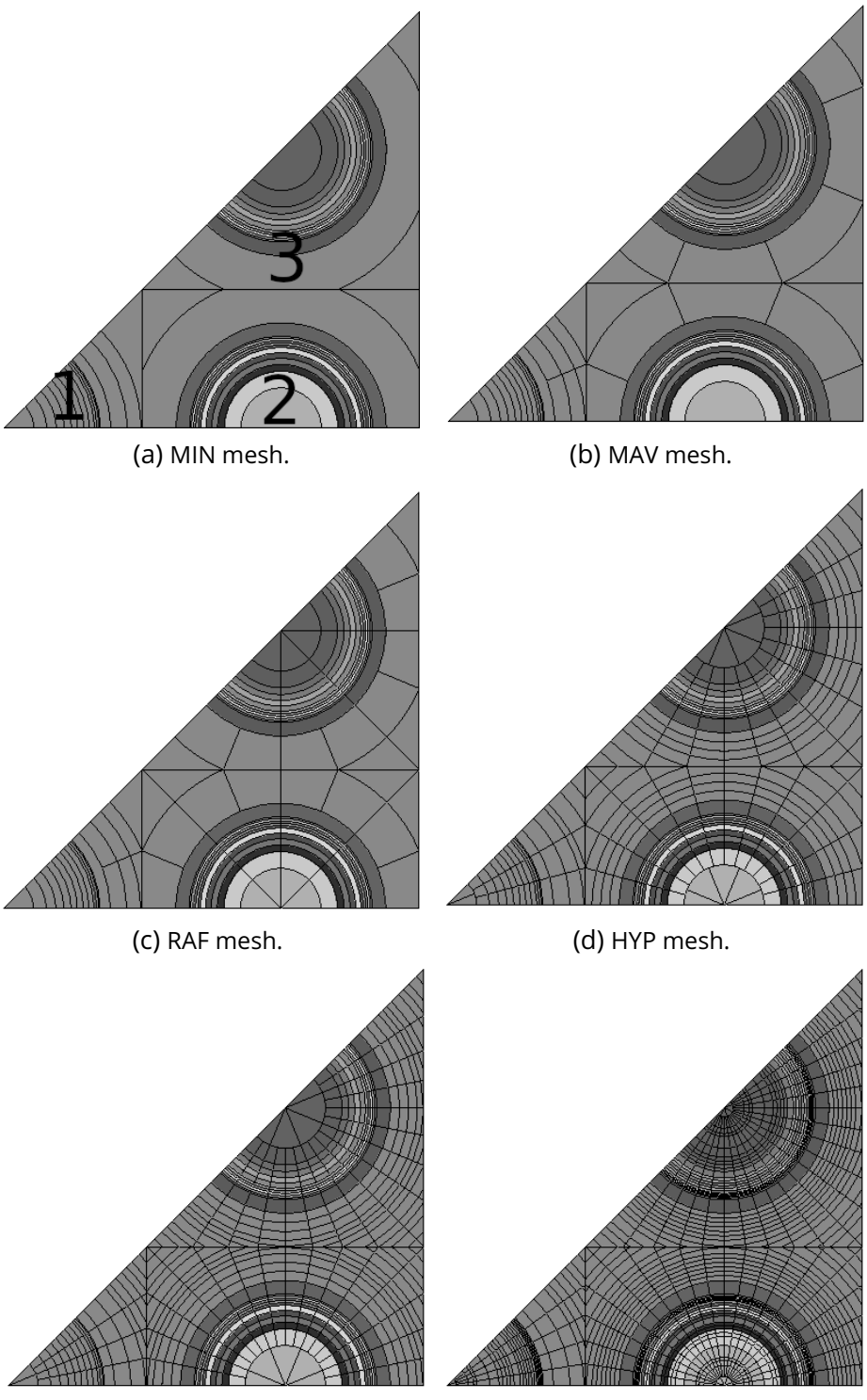

(a) MIN mesh.

(b) MAV mesh.

(c) RAF mesh.

(d) HYP mesh.

(e) SHYP mesh.

(f) MEG mesh.

Figure 7.4 – Flux calculations meshes used for the study of mesh convergence of the three-dimensional linear surface scheme.

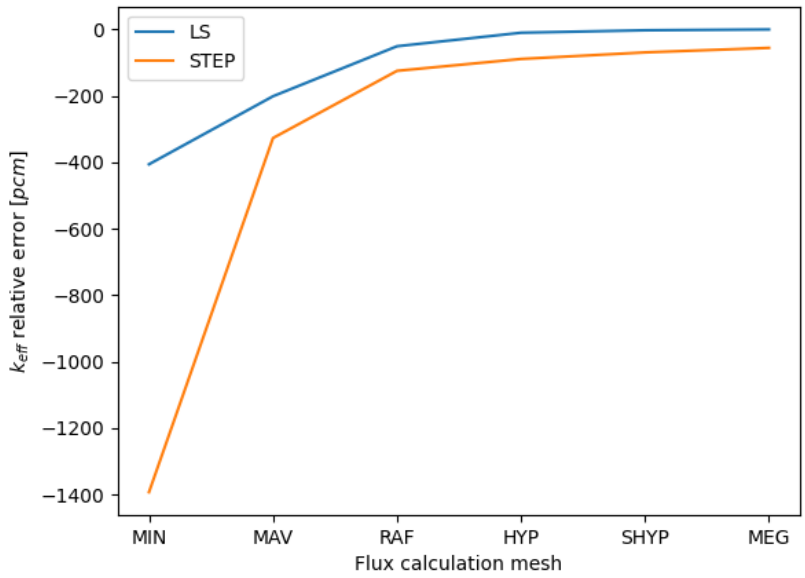

Figure 7.5 – Comparison of the k_{eff} convergence between the SC and LS schemes for the homogeneous configuration with P_0 anisotropy and constant axial flux ($n_p = 0$). The k_{eff} of the MEG mesh for the LS scheme is taken as the reference value.

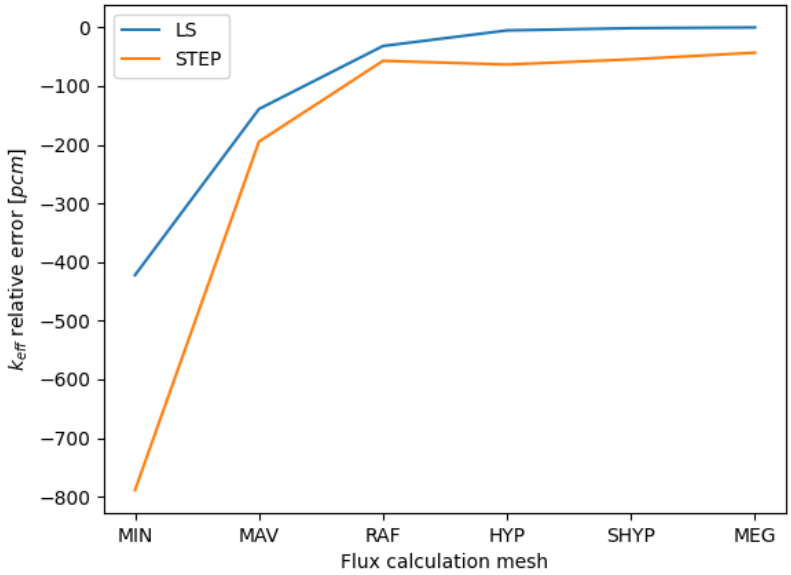

Figure 7.6 – Comparison of the k_{eff} convergence between the SC and LS schemes for the homogeneous configuration with P_3 anisotropy and constant axial flux ($n_p = 0$). The k_{eff} of the MEG mesh for the LS scheme is taken as the reference value.

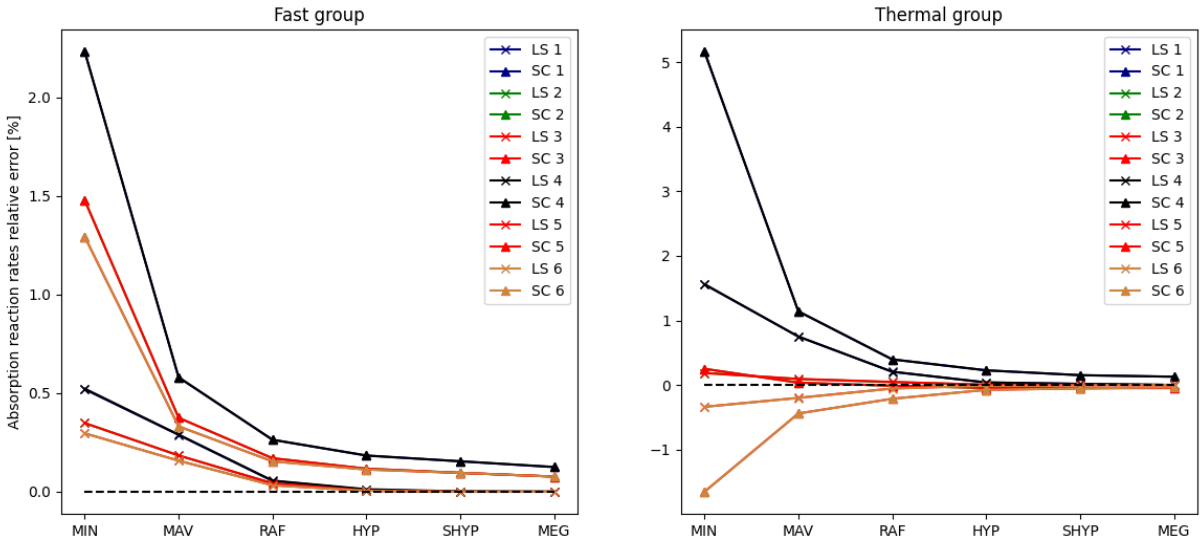

Figure 7.7 – Comparison of the absorption reaction rates relative error convergence between the SC and LS schemes for the homogeneous configuration with P_0 anisotropy and constant axial flux ($n_p = 0$). For each pin cell, the reaction rates of the MEG mesh for the LS scheme is taken as the reference value.

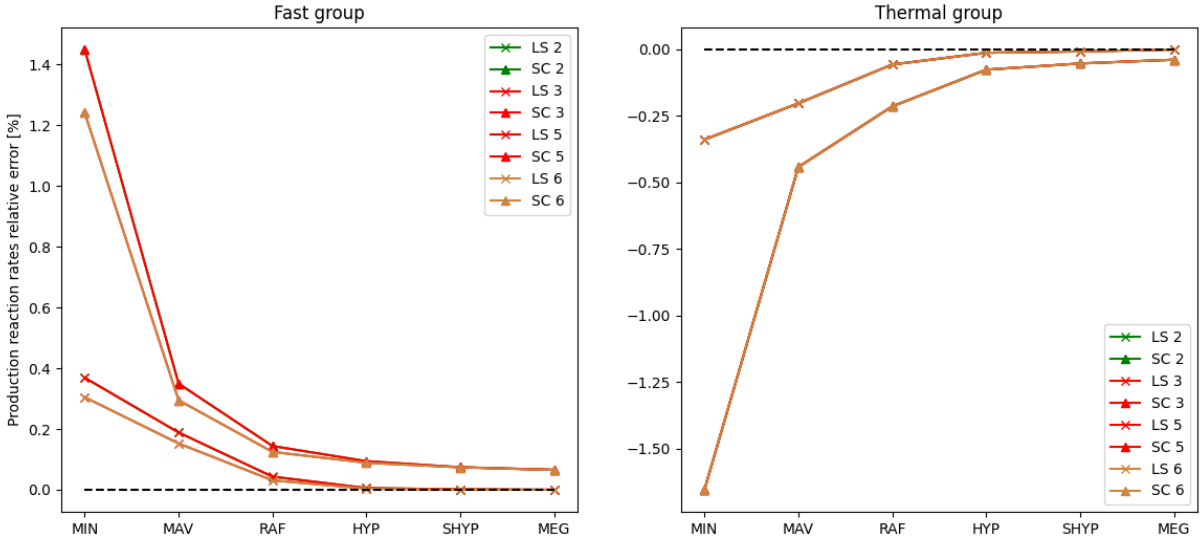

Figure 7.8 – Comparison of the production reaction rates relative error convergence between the SC and LS schemes for the homogeneous configuration with P_0 anisotropy and constant axial flux ($n_p = 0$). For each pin cell, the reaction rates of the MEG mesh for the LS scheme is taken as the reference value.

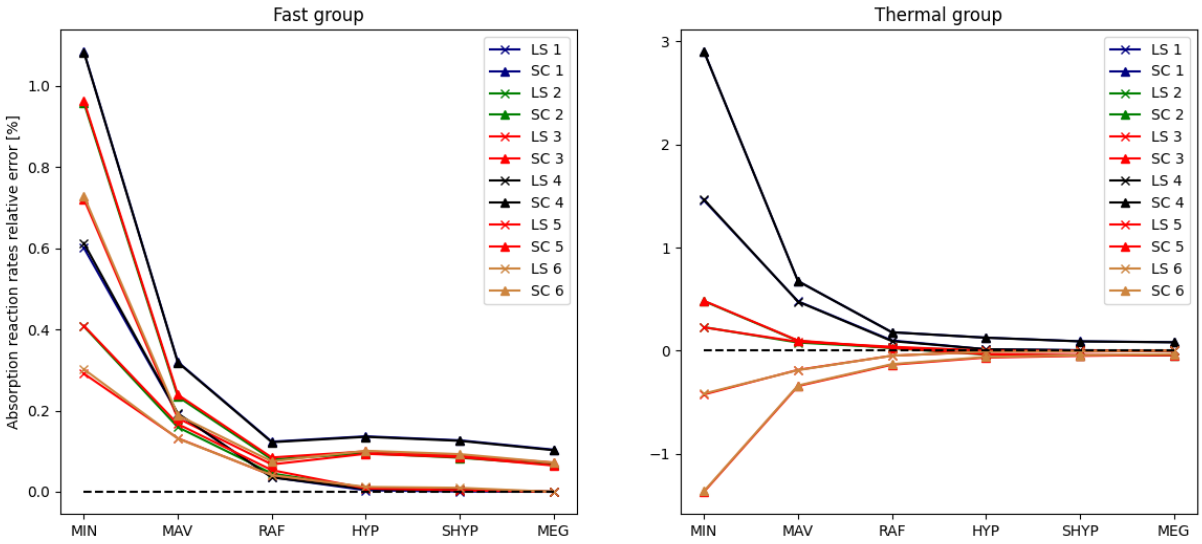

Figure 7.9 – Comparison of the absorption reaction rates relative error convergence between the SC and LS schemes for the homogeneous configuration with P_3 anisotropy and constant axial flux ($n_p = 0$). For each pin cell, the reaction rates of the MEG mesh for the LS scheme is taken as the reference value.

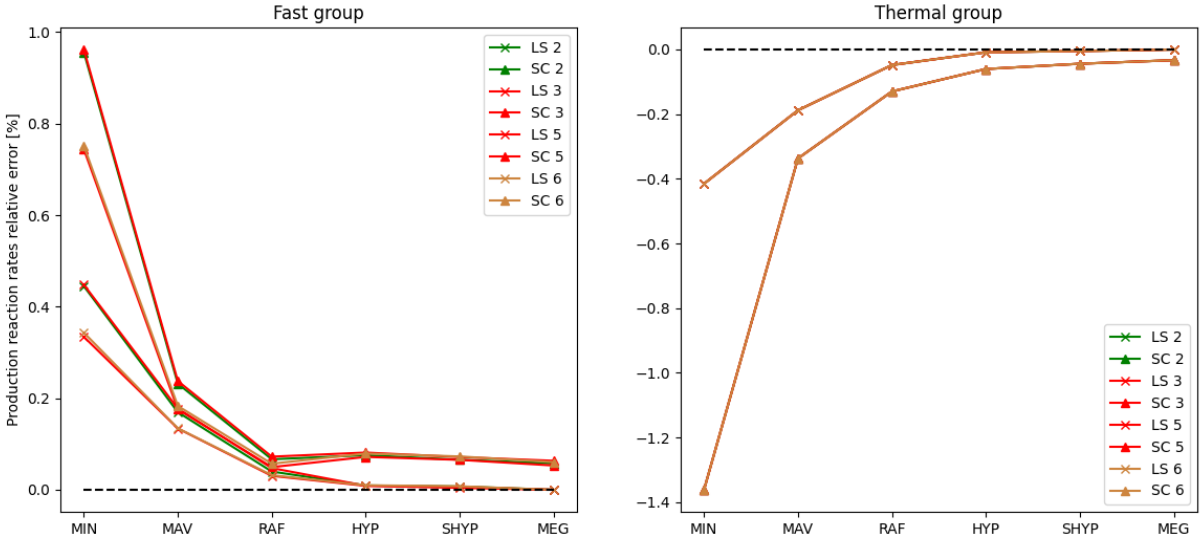

Figure 7.10 – Comparison of the production reaction rates relative error convergence between the SC and LS schemes for the homogeneous configuration with P_3 anisotropy and constant axial flux ($n_p = 0$). For each pin cell, the reaction rates of the MEG mesh for the LS scheme is taken as the reference value.

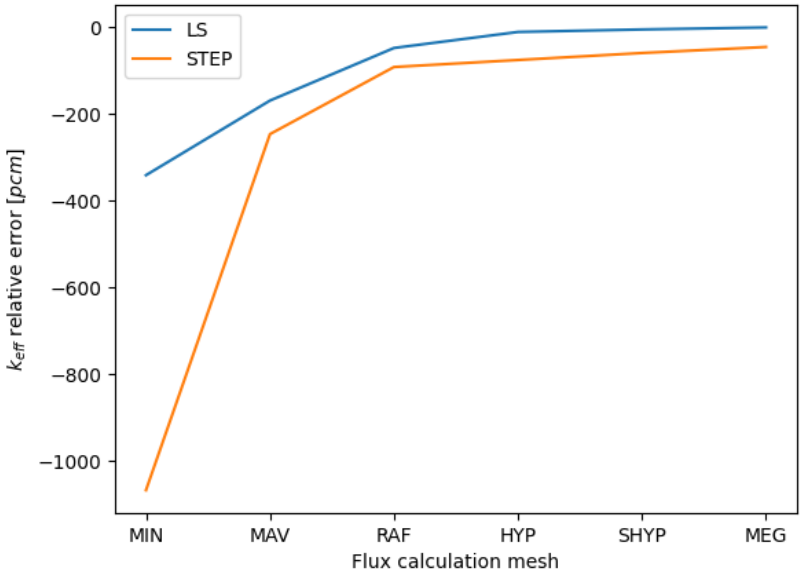

Figure 7.11 – Comparison of the k_{eff} convergence between the SC and LS schemes for the heterogeneous configuration with P_0 anisotropy and constant axial flux ($n_p = 0$). The k_{eff} of the MEG mesh for the LS scheme is taken as the reference value.

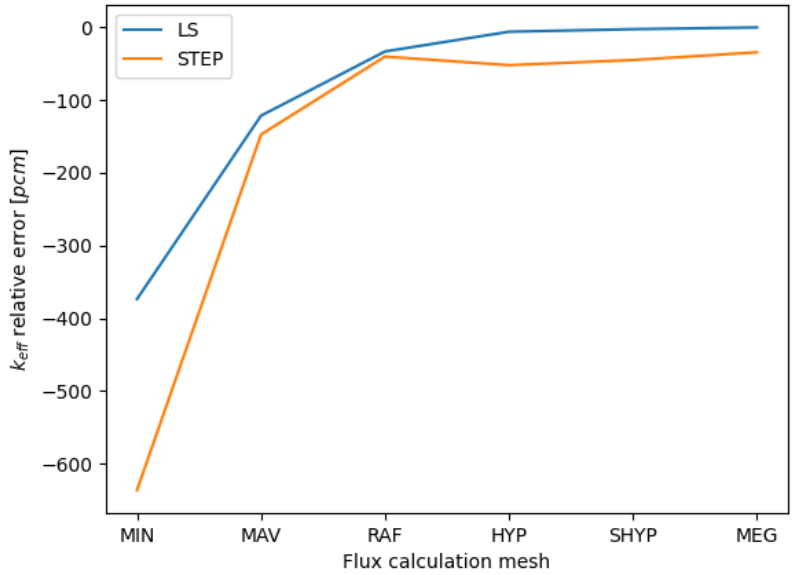

Figure 7.12 – Comparison of the k_{eff} convergence between the SC and LS schemes for the heterogeneous configuration with P_3 anisotropy and constant axial flux ($n_p = 0$). The k_{eff} of the MEG mesh for the LS scheme is taken as the reference value.

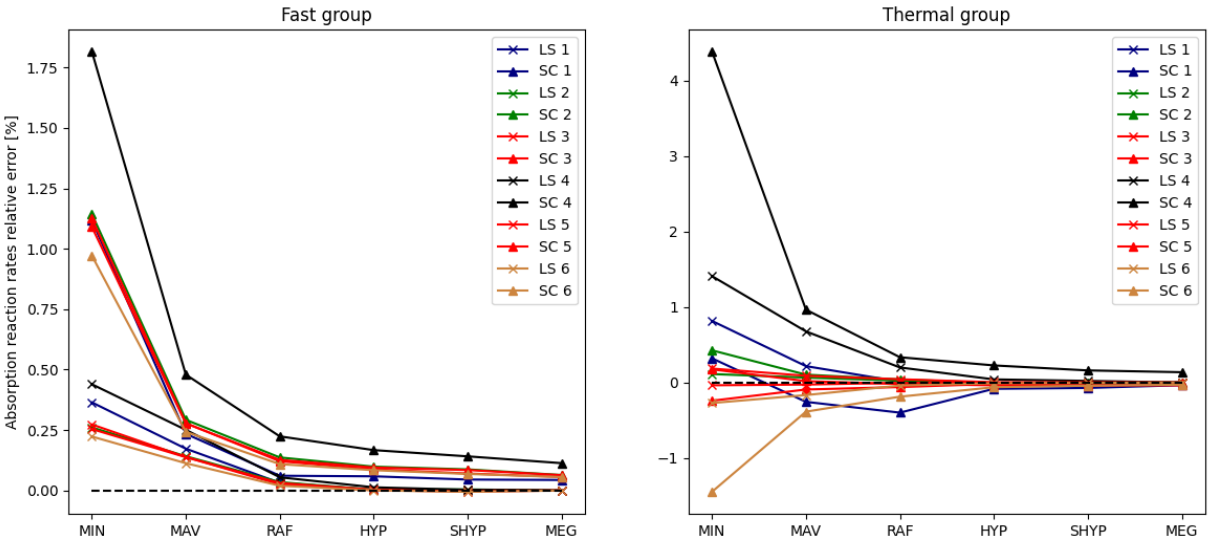

Figure 7.13 – Comparison of the absorption reaction rates relative error convergence between the SC and LS schemes for the heterogeneous configuration with P_0 anisotropy and constant axial flux ($n_p = 0$). For each pin cell, the reaction rates of the MEG mesh for the LS scheme is taken as the reference value.

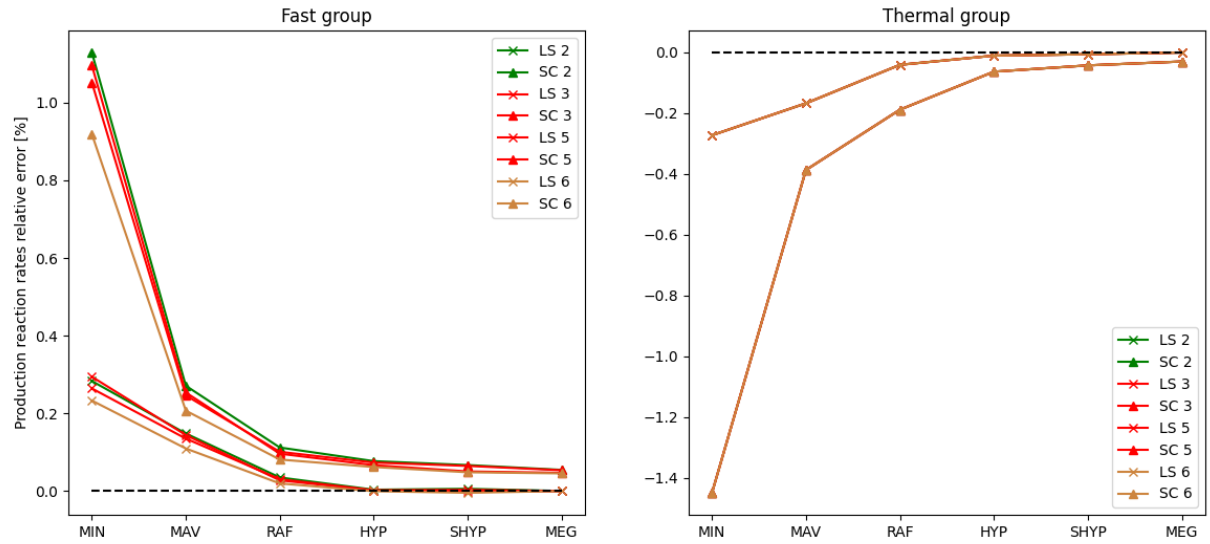

Figure 7.14 – Comparison of the production reaction rates relative error convergence between the SC and LS schemes for the heterogeneous configuration with P_0 anisotropy and constant axial flux ($n_p = 0$). For each pin cell, the reaction rates of the MEG mesh for the LS scheme is taken as the reference value.

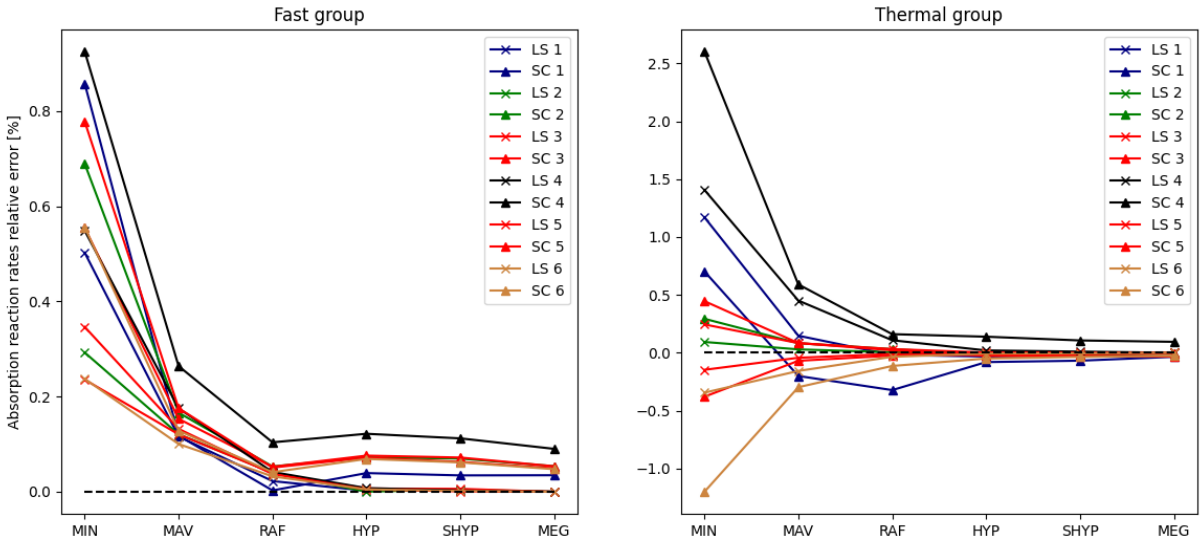

Figure 7.15 – Comparison of the absorption reaction rates relative error convergence between the SC and LS schemes for the heterogeneous configuration with P_3 anisotropy and constant axial flux ($n_p = 0$). For each pin cell, the reaction rates of the MEG mesh for the LS scheme is taken as the reference value.

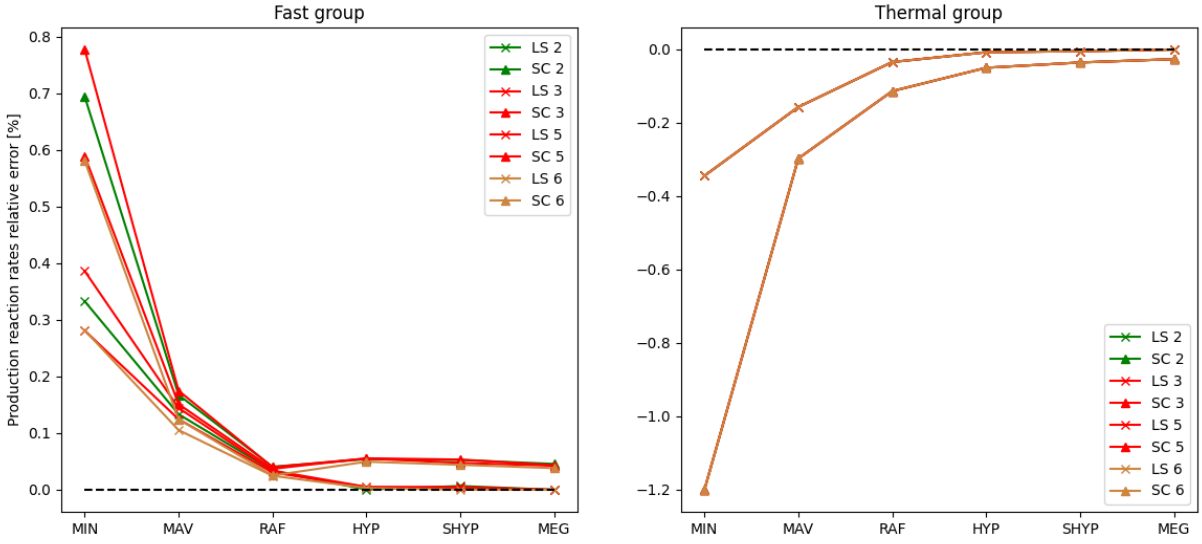

Figure 7.16 – Comparison of the production reaction rates relative error convergence between the SC and LS schemes for the heterogeneous configuration with P_3 anisotropy and constant axial flux ($n_p = 0$). For each pin cell, the reaction rates of the MEG mesh for the LS scheme is taken as the reference value.

8 - Stabilisation of higher-order MOC methods for the TDT solver

Chapter 8 details the theoretical developments aimed at eliminating divergence issues due to the manner the current term and higher-order terms of the balance equation was computed. The equations are elaborated for cases where the source is radially constant, axially polynomial, with uniform cross sections per region or spatially dependent cross sections. Similarly, the theoretical results obtained can be adapted to stabilize the linear surface scheme.

Contents

8.1 . High-order schemes and balance conservation

In the section 7.1.2 divergence behaviors of the transport scheme have been observed. This issue is highlighted in the section 7.1.2, and especially in table 7.5. It is noted that calculations where the flux is expanded on a polynomial basis in the axial direction with $n_p = 2$ diverge when the cell height exceeds a certain limit z_{lim}. To address this problem, a truncation method was developed. This method involves reducing the polynomial degree n_p if conservation in an infinite homogeneous medium is not maintained.

However, even though the origin of these numerical instabilities was clear, no solution had been proposed. This chapter offers a solution in the case where the flux is radially constant, where the same phenomenon have been observed.

To understand the problem, we start by revisiting the balance equation for the spatial moments of the angular flux in the case where the cross sections are uniform (4.20). It is then observed that the streaming term in an infinite homogeneous medium is zero. Indeed, in such medium, the angular flux is uniform, i.e:

$$\boldsymbol{\nabla}\psi(\boldsymbol{r},\boldsymbol{\Omega}) = \mathbb{O}_3.$$

That, by projection on the spatial basis (4.19) and by use of ∇ relations, leads to

$$\Delta\mathbf{J}_i(\boldsymbol{\Omega}) = \mu\mathbb{C}'\boldsymbol{\psi}_i(\boldsymbol{\Omega}). \tag{8.1}$$

In other words, for each spatial order p

$$\Delta\mathrm{J}_{i,p}(\boldsymbol{\Omega}) = \frac{\mu p}{\Delta z/2}{}'\psi_{i,p}(\boldsymbol{\Omega}). \tag{8.2}$$

However, it has been observed in our case that (8.2) is not numerically satisfied for regions where the average optical path length in region i, $\langle\tau\rangle_i$ defined by (8.3), subceeds a certain threshold τ_{lim} (see table 7.5),

$$\langle\tau\rangle_i = \frac{1}{n_{i,t}}\sum_{\boldsymbol{\Omega}_n\in S_n} w_n \sum_{\substack{t||\boldsymbol{\Omega}_n \\ t\cap i}} w_{\perp,t}(\boldsymbol{\Omega}_n)\tau(\boldsymbol{\Omega}_n), \tag{8.3}$$

with $n_{i,t}$ representing the number of trajectories that traverse region i. Thus, it is assumed that improving the numerical equality (8.2) will reduce the divergence phenomena of the

transport scheme. To address the numerical issue, we will revisit the trajectory-based conservation equation [56] in order to cumulate the current and the higher-order terms through an analytical expression. The "local" conservation equation for a trajectory of arbitrary direction $\mathbf{\Omega}$ entering and exiting a region i, through $\boldsymbol{r}_{in}$ and $\boldsymbol{r}_{out}$, respectively writes

$$\Sigma_t \langle \mathbf{P}, \psi \rangle = \mathbf{P}(z_{in})\psi(\boldsymbol{r}_{in}, \mathbf{\Omega}) - \mathbf{P}(z_{out})\psi(\boldsymbol{r}_{out}, \mathbf{\Omega}) + \langle \mathbf{P}, Q \rangle + \left\langle \frac{\partial \mathbf{P}}{\partial t}, \psi \right\rangle. \tag{8.4}$$

Then, let's introduce a corrected current term for spatial order p, denoted as $\Delta \mathrm{J}^*_{p,t}$, defined as follows:

$$\Delta \mathrm{J}^*_{p,t} = \mathrm{P}_p(z_{in})\psi(\boldsymbol{r}_{in}, \mathbf{\Omega}) - \mathrm{P}_p(z_{out})\psi(\boldsymbol{r}_{out}, \mathbf{\Omega}) + \left\langle \frac{\partial \mathrm{P}_p}{\partial t}, \psi \right\rangle. \tag{8.5}$$

8.2 . Case with a polynomial basis of degree 1 for the angular flux

8.2.1 . With constant cross sections by spatial region

This section is structured as follows: first, we express the sum and difference between the incoming and outgoing fluxes in terms of the incoming flux and the source term. Next, we derive an expression for $\Delta \mathrm{J}^*_{1,t}$. Finally, the current term is integrated over space and energy to calculate the moments of the flux. The transmission equation (4.15) allows us to obtain

$$\psi(\boldsymbol{r}_{in}, \mathbf{\Omega}) - \psi(\boldsymbol{r}_{out}, \mathbf{\Omega}) = \left(1 - e^{-\tau(l)}\right) \psi(\boldsymbol{r}_{in}, \mathbf{\Omega}) - \mathbf{P} \cdot \mathbf{T}(\mathbf{\Omega}), \tag{8.6}$$

$$\psi(\boldsymbol{r}_{in}, \mathbf{\Omega}) + \psi(\boldsymbol{r}_{out}, \mathbf{\Omega}) = \left(1 + e^{-\tau(l)}\right) \psi(\boldsymbol{r}_{in}, \mathbf{\Omega}) + \mathbf{P} \cdot \mathbf{T}(\mathbf{\Omega}). \tag{8.7}$$

We now aim to determine an expression for $\Delta \mathrm{J}^*_{1,t}$ (8.5). First, we note that $\mathrm{P}_1(z_{out}) = \tilde{z}(l)$ and $\mathrm{P}_1(z_{in}) = \tilde{z}(0)$, which we express as

$$z_{in} = z_m - \frac{l}{2}\mu, \tag{8.8}$$

$$z_{out} = z_m + \frac{l}{2}\mu, \tag{8.9}$$

with z_m being the axial coordinate of the midpoint of the chord of length l and μ the cosine of the angle between the chord and the z-axis. Using the previous expressions (8.8) and (8.9), and setting $\gamma = (\Delta z/2)^{-1}$, the term $\Delta \mathrm{J}_{1,t}$ can be written as

$$\begin{aligned}\Delta \mathrm{J}_{1,t} &= \mathrm{P}_1(z_{in})\psi(\boldsymbol{r}_{in}, \boldsymbol{\Omega}) - \mathrm{P}_1(z_{out})\psi(\boldsymbol{r}_{out}, \boldsymbol{\Omega}),\\ &= \gamma(z_{in} - \bar{z})\psi(\boldsymbol{r}_{in}, \boldsymbol{\Omega}) - \gamma(z_{out} - \bar{z})\psi(\boldsymbol{r}_{out}, \boldsymbol{\Omega}).,\\ &= \gamma(z_m - \bar{z})\left[\psi(\boldsymbol{r}_{in}, \boldsymbol{\Omega}) - \psi(\boldsymbol{r}_{out}, \boldsymbol{\Omega})\right],\\ &- \gamma\frac{l}{2}\mu\left[\psi(\boldsymbol{r}_{in}, \boldsymbol{\Omega}) + \psi(\boldsymbol{r}_{out}, \boldsymbol{\Omega})\right].\end{aligned}$$

On the other hand, still at first order, we expand the higher-order term as

$$\begin{aligned}\left\langle \frac{\partial \mathrm{P}_1}{\partial t}, \psi \right\rangle &= \gamma\mu \int_0^l \mathrm{d}t\psi(\boldsymbol{r}_t, \boldsymbol{\Omega}),\\ &= \gamma\mu l\overline{\psi}_0.\end{aligned}$$

Finally, using the two previous results, the sum of the current and higher-order terms can be rewritten as

$$\Delta \mathrm{J}^*_{1,t} = \gamma(z_m - \bar{z})\left[\psi(\boldsymbol{r}_{in}, \boldsymbol{\Omega}) - \psi(\boldsymbol{r}_{out}, \boldsymbol{\Omega})\right] + \gamma l\mu\left(\overline{\psi}_0 - \frac{\psi(\boldsymbol{r}_{in}, \boldsymbol{\Omega}) + \psi(\boldsymbol{r}_{out}, \boldsymbol{\Omega})}{2}\right). \quad (8.10)$$

The task now is to group the terms of $\Delta \mathrm{J}^*_{1,t}$ in such a way as to obtain an expression that requires the fewest floating-point operations possible and addresses the issue that arises for very small optical paths. Using (8.6), (8.6), and (10.15), $\Delta \mathrm{J}^*_{1,t}$ can be expressed as a function of the optical path τ, the incoming and outgoing fluxes, a source term $S(\boldsymbol{\Omega})$, and geometric parameters:

$$\Delta \mathrm{J}^*_{1,t} = \gamma(z_m - \bar{z})\Delta\psi_t(\boldsymbol{\Omega}) - \gamma l\mu \mathrm{G}(\tau)\psi(\boldsymbol{r}_{in}, \boldsymbol{\Omega}) + S(\boldsymbol{\Omega}). \quad (8.11)$$

with $\Delta\psi_t(\boldsymbol{\Omega}) = \psi(\boldsymbol{r}_{in}, \boldsymbol{\Omega}) - \psi(\boldsymbol{r}_{out}, \boldsymbol{\Omega})$ and $\mathrm{G}(\tau)$ expressed as

$$\mathrm{G}(\tau) = \left[\frac{1 + e^{-\tau}}{2} - \frac{1 - e^{-\tau}}{\tau}\right], \quad (8.12)$$

and the source term $S(\mathbf{\Omega})$ as

$$S(\mathbf{\Omega}) = -\gamma l\mu \left[\frac{1}{\tau} + \frac{1}{2}\right] \mathbf{P} \cdot \mathbf{T}(\mathbf{\Omega}) + \frac{\gamma l\mu}{\tau} \left(\mathbb{PP}_t(\mathbf{\Omega}) \cdot \boldsymbol{Q}(\mathbf{\Omega})\right)_0 . \tag{8.13}$$

We now need to rewrite the source term in order to classify the quantity according to the type of chord. To do this, let us start from the equation for the current term (8.11). Recall that $\mathbf{P} \cdot \mathbf{T}(\mathbf{\Omega})$ can be expressed as

$$\mathbf{P} \cdot \mathbf{T}(\mathbf{\Omega}) = \sum_{k=0}^{n_p} \left[\frac{z_0 - \tilde{z}}{\Delta z/2}\right]^k \underbrace{\sum_{p=k}^{n_p} \binom{p}{k} \left(\frac{2\mu}{\Delta z}\right)^{p-k} \mathrm{E}_{p-k}(\tau) \frac{Q^p(\mathbf{\Omega})}{\Sigma_t}}_{\mathrm{T}_k} . \tag{8.14}$$

Then, by applying equation (10.30) for $j = 0$, it can be shown that $\left(\mathbb{PP}_t(\mathbf{\Omega}) \cdot \boldsymbol{Q}(\mathbf{\Omega})\right)_0$ can be expressed, provided that the order of summation is changed, as

$$\left(\mathbb{PP}_t(\mathbf{\Omega}) \cdot \boldsymbol{Q}(\mathbf{\Omega})\right)_0 = \sum_{p=0}^{n_p} \sum_{k=0}^{p} \binom{p}{k} \left[\frac{z_0 - \tilde{z}}{\Delta z/2}\right]^k \left(\frac{2\mu}{\Delta z}\right)^{p-k} \frac{l^{p-k+1}}{p-k+1} \cdot Q^p(\mathbf{\Omega}),$$

which can be rewritten in the form

$$\begin{aligned}
\left(\mathbb{PP}_t(\mathbf{\Omega}) \cdot \boldsymbol{Q}(\mathbf{\Omega})\right)_0 &= \sum_{k=0}^{n_p} \left[\frac{z_0 - \tilde{z}}{\Delta z/2}\right]^k \sum_{p=k}^{n_p} \binom{p}{k} \left(\frac{2\mu}{\Delta z}\right)^{p-k} \frac{l^{p-k+1}}{p-k+1} Q^p(\mathbf{\Omega}), \\
&= \tau \sum_{k=0}^{n_p} \left[\frac{z_0 - \tilde{z}}{\Delta z/2}\right]^k \underbrace{\sum_{p=k}^{n_p} \binom{p}{k} \left(\frac{2\mu}{\Delta z}\right)^{p-k} \frac{l^{p-k}}{p-k+1} \frac{Q^p(\mathbf{\Omega})}{\Sigma_t}}_{\mathrm{V}_k}, \\
&= \tau\, \mathbf{P} \cdot \mathbf{V}.
\end{aligned}$$

Thus, by defining $\widetilde{\mathbf{T}}(\mathbf{\Omega}) = \gamma l\mu \left[\mathbf{V} - \left(\frac{1}{\tau} + \frac{1}{2}\right) \mathbf{T}(\mathbf{\Omega})\right]$, the current term $\Delta \mathrm{J}_1^*$ can be rewritten as

$$\Delta \mathrm{J}_{1,t}^* = \gamma(z_m - \bar{z}) \Delta\psi_t(\mathbf{\Omega}) - \gamma l\mu \mathrm{G}(\tau) \psi(\boldsymbol{r}_{in}, \mathbf{\Omega}) + \mathbf{P} \cdot \widetilde{\mathbf{T}}(\mathbf{\Omega}). \tag{8.15}$$

(8.15) represents the general expression for the contribution of a chord to the modified current term. However, the main idea is to find an expression in the case where the optical

path is small. Therefore, we study the behavior of $\mathrm{G}(\tau)$ and $\mathbf{P}\cdot\widetilde{\mathbf{T}}(\mathbf{\Omega})$ as $\tau\to 0$. We begin with $\mathrm{G}(\tau)$, starting from equation (8.12). It is noteworthy that $\frac{1-e^{-\tau}}{\tau}$ and $\frac{1+e^{-\tau}}{2}$ approach 1 as τ approaches 0. If the contributions of these terms are accumulated separately, we observe that the two sums over the set of associated chords are no longer equal, although the asymptotic expansion shows that the difference tends to 0 like τ^2.

This discrepancy is due to the number of significant digits (single precision, double precision) of the chosen variables relative to the order of magnitude of τ^2 for small chords. This phenomenon is known as catastrophic cancellation. Expressing the difference as an asymptotic development helps to resolve the issue.

$$\lim_{\tau\to 0} 1-e^{-\tau} = \tau - \frac{1}{2}\tau^2 + \frac{1}{6}\tau^3 - \frac{1}{24}\tau^4 + o(\tau^4), \tag{8.16}$$

and

$$\lim_{\tau\to 0} \frac{1+e^{-\tau}}{2} = 1 - \frac{1}{2}\tau + \frac{1}{4}\tau^2 - \frac{1}{12}\tau^3 + o(\tau^3), \tag{8.17}$$

such that

$$\lim_{\tau\to 0} G(\tau) = \frac{1}{12}\tau^2 - \frac{1}{24}\tau^3 + o(\tau^3). \tag{8.18}$$

We still have to deal with the term $\mathbf{P}\cdot\widetilde{\mathbf{T}}(\mathbf{\Omega})$. The k^{th} component of the vector $\widetilde{\mathbf{T}}$ writes:

$$\widetilde{\mathrm{T}}_k = \sum_{p=k}^{n_p} \binom{p}{k} \left(\frac{2\mu}{\Delta z}\right)^{p-k} \underbrace{\left[\frac{l^{p-k}}{p-k+1} - \left(\frac{1}{\tau}+\frac{1}{2}\right)\mathrm{E}_{p-k}(\tau)\right]}_{\widetilde{\mathrm{E}}_{p-k}(\tau)} \frac{Q^p(\mathbf{\Omega})}{\Sigma_t}. \tag{8.19}$$

As detailed in the section, the calculation of $\mathrm{E}_{p-k}(\tau)$ is performed based on $\mathrm{E}_k^T(\tau)$. We can thus use the known results to find an expression for $\widetilde{\mathrm{E}}_{p-k}(\tau)$ in the case of small optical paths. We begin by writing

$$\begin{aligned}\forall k\in\mathbb{N},\ \widetilde{\mathrm{E}}_k(\tau) &= l^k\left[\frac{1}{k+1} - \left(\frac{1}{\tau}+\frac{1}{2}\right)\mathrm{E}_k^T(\tau)\right],\\ &= l^k\left[\frac{1}{k+1} - \left(\frac{2+\tau}{2\tau}\right)\mathrm{E}_k^T(\tau)\right].\end{aligned}$$

We then use the recurrence relation

$$\mathrm{E}_k^T(\tau) = \frac{\tau}{k+1}\left[1 - \mathrm{E}_{k+1}^T(\tau)\right], \tag{8.20}$$

which is obtained by integration by parts and then substituted into the previous relation to write

$$\begin{aligned}
\forall k \in \mathbb{N},\ \widetilde{\mathrm{E}}_k(\tau) &= l^k \left[\frac{1}{k+1} - \left(\frac{2+\tau}{2\tau}\right)\frac{\tau}{k+1}\left[1 - \mathrm{E}_{k+1}^T(\tau)\right]\right], \\
&= \frac{l^k}{k+1}\left[1 - \left(\frac{2+\tau}{2}\right)\left[1 - \mathrm{E}_{k+1}^T(\tau)\right]\right], \\
&\underset{0}{\to} \frac{l^k}{k+1}\mathrm{E}_{k+1}^T(\tau),
\end{aligned}$$

so that for small chords we can write

$$\widetilde{\mathrm{T}}_k(\boldsymbol{\Omega}) \underset{\tau\to 0}{=} \sum_{p=k}^{n_p} \binom{p}{k}\left(\frac{2\mu}{\Delta z}\right)^{p-k} \frac{l^{p-k}}{p-k+1}\mathrm{E}_{p-k+1}^T(\tau)\frac{Q^p(\boldsymbol{\Omega})}{\Sigma_t}. \tag{8.21}$$

We now need to integrate (8.15) over all chords in the direction $\boldsymbol{\Omega}$, and then over all directions belonging to the set of directions. We write:

$$\Sigma_t{}'\boldsymbol{\Phi}_{i,1} = \Delta\mathbf{J}_{i,1}^* + {}'\boldsymbol{Q}_{i,1}. \tag{8.22}$$

We then obtain an equation similar to (5.56), but where the source term ${}'\boldsymbol{Q}_{i,1}$ is the second component of the vector defined by (5.58) and the current term are combined into $\Delta\mathbf{J}_{i,1}^*$, defined as

$$\Delta\mathbf{J}_{i,1}^* = \frac{1}{4\pi}\int_{\mathbb{S}_2} \mathrm{d}\boldsymbol{\Omega}\boldsymbol{A}(\boldsymbol{\Omega})\Delta\mathbf{J}_{i,1}^*(\boldsymbol{\Omega}), \tag{8.23}$$

with

$$\Delta\mathbf{J}_{i,1}^*(\boldsymbol{\Omega}) = \frac{1}{\mathrm{V}_i(\boldsymbol{\Omega})}\sum_{\substack{t||\Omega \\ t\cap i}} w_{\perp,t}\Delta\mathrm{J}_{1,t}^*. \tag{8.24}$$

8.2.2 . With polynomial cross sections by spatial region

In order to address the case where the cross sections depend on space, we start again from the conservation equation for the spatial moments of the angular flux. At first order, we recall that

$$\Sigma_{t,0}{}'\psi_{i,0}(\boldsymbol{\Omega}) + \Sigma_1{}'\psi_{i,1}(\boldsymbol{\Omega}) = \left(\mathbb{PP}^{2n_p}(\boldsymbol{\Omega}) \cdot \boldsymbol{Q}(\boldsymbol{\Omega})\right)_0 - \Delta \mathrm{J}_{i,0}(\boldsymbol{\Omega}), \tag{8.25}$$

$$\Sigma_{t,0}{}'\psi_{i,1}(\boldsymbol{\Omega}) + \Sigma_{t,1}{}'\psi_{i,2}(\boldsymbol{\Omega}) = \left(\mathbb{PP}^{2n_p}(\boldsymbol{\Omega}) \cdot \boldsymbol{Q}(\boldsymbol{\Omega})\right)_1 - \Delta \mathrm{J}_{i,1}(\boldsymbol{\Omega}) + \gamma\mu'\psi_{i,0}(\boldsymbol{\Omega}). \tag{8.26}$$

As in section (4.3.3), we observe that the system of equations (8.25) and (8.26) consists of two equations and three unknowns. As it stands, it is impossible to solve. The method employed in the dedicated chapter involved using a system of equations with the spatial coefficients of the angular flux as the unknowns.

In (8.26), the same problem of numerical cancellation arises as in the case where the cross sections are constant within each region. Furthermore, it was shown in Appendix (10.2) that it is also possible to derive a conservation equation along a chord when the cross sections depend on space. Therefore, we can follow the same method as in the previous section, which involved combining the contributions of each chord into a single term that includes both the current and higher-order terms.

However, a simple analytical expression for $\overline{\psi}_0(\boldsymbol{\Omega})$ has not been found for an arbitrary optical path, but only for small optical path. Note that practically, this would mean that a conditional test should be implemented to distinguish chords with a sufficiently small optical path from others. This strategy cannot be employed, as such a test would slow down the sweep process, which is the most time-consuming phase in MOC transport. For small optical path, we can use the relation (10.3.2) to write the transmission equation as:

$$\psi(\boldsymbol{r}_{out}, \boldsymbol{\Omega}) \underset{\tau \to 0}{=} \psi(\boldsymbol{r}_{in}, \boldsymbol{\Omega}) e^{-\tau_0} + \int_0^l \mathrm{d}t\, Q(\boldsymbol{r}_{in} + t\boldsymbol{\Omega})\, e^{-[\tau_0 - \tau(t)]}. \tag{8.27}$$

We can therefore write

$$\overline{\psi}_0(\boldsymbol{\Omega}) \underset{\tau \to 0}{=} \frac{1}{\tau_0} \left[\psi(\boldsymbol{r}_{in}, \boldsymbol{\Omega}) - \psi(\boldsymbol{r}_{out}, \boldsymbol{\Omega}) + \left(\mathbb{PP}_t^{2n_p}(\boldsymbol{\Omega}) \cdot \boldsymbol{Q}(\boldsymbol{\Omega})\right)_0\right], \tag{8.28}$$

with,

$$\mathbb{PP}_t^{2n_p}(\mathbf{\Omega}) = \int_0^l \mathrm{d}t \mathbf{P}(z_t) \otimes \mathbf{P}(z_t). \tag{8.29}$$

Thus, knowing (8.10), (8.28), and (10.14), we can write, in the case where the macroscopic cross sections are expanded to first order:

$$\Delta \mathrm{J}_{1,t}^* \underset{\tau \to 0}{=} \gamma(z_m - \bar{z}) \Delta\psi_t(\mathbf{\Omega}) - \gamma l \mu \mathrm{G}_{\mathsf{XS}}(\tau)\psi(\boldsymbol{r}_{in}, \mathbf{\Omega}) + S_{\mathsf{XS}}(\mathbf{\Omega}), \tag{8.30}$$

with,

$$\mathrm{G}_{\mathsf{XS}}(\tau) = \left[\frac{1+e^{-\tau}}{2} - \frac{1-e^{-\tau}}{\tau_0}\right], \tag{8.31}$$

$$S_{\mathsf{XS}}(\mathbf{\Omega}) = -\gamma l \mu \left[\frac{1}{\tau_0} + \frac{1}{2}\right] \mathbf{P} \cdot \mathbf{T} + \frac{\gamma l \mu}{\tau_0} \left(\mathbb{PP}_t^{2n_p}(\mathbf{\Omega}) \cdot \boldsymbol{Q}(\mathbf{\Omega})\right)_0. \tag{8.32}$$

Unlike the case where the cross section is spatially independent, we cannot directly tabulate the function G_{XS} here. To address this issue, we write:

$$\mathrm{G}_{\mathsf{XS}}(\tau) = \mathrm{G}(\tau) + (1 - e^{-\tau}) \left[\frac{\tau_0 - \tau}{\tau_0 \tau}\right]. \tag{8.33}$$

G is tabulable, as we saw in the previous section. Similarly, the function $g : \tau \longmapsto 1 - e^{-\tau}$ also tabulable. Therefore, G_{XS} can be computed on-the-fly. Il reste à s'occuper du terme $S_{\mathsf{XS}}(\mathbf{\Omega})$. To this end, we observe that:

$$\left(\mathbb{PP}_t^{2n_p}(\mathbf{\Omega}) \cdot \boldsymbol{Q}(\mathbf{\Omega})\right)_0 \underset{\tau \to 0}{=} \tau_0 \, \mathbf{P} \cdot \mathbf{V}. \tag{8.34}$$

with $\mathbf{V}$ the vector of $2n_p + 1$ of component defined as

$$\mathrm{V}_k = \sum_{p=k}^{2n_p} \binom{p}{k} \left(\frac{2\mu}{\Delta z}\right)^{p-k} \frac{l^{p-k+1}}{p-k+1} \frac{Q^p(\mathbf{\Omega})}{\Sigma_{t,0}}, \tag{8.35}$$

such that,

$$S_{\mathsf{XS}}(\mathbf{\Omega}) = -\gamma l \mu \left[\frac{1}{\tau_0} + \frac{1}{2}\right] \mathbf{P} \cdot \mathbf{T} + \gamma \mu \mathbf{P} \cdot \mathbf{V}. \tag{8.36}$$

In the same manner as in [125], $\mathbf{P}\cdot\mathbf{T}$ is calculated using a Gauss-Legendre quadrature. We have $\mathbf{P}\cdot\mathbf{T}=\boldsymbol{Q}(\boldsymbol{\Omega})\cdot\mathbf{E}_0$ with the component (5.55). We follow the same logic to calculate $\mathbf{P}\cdot\mathbf{V}$, which is written as:

$$\mathbf{P}\cdot\mathbf{V}=\boldsymbol{Q}(\boldsymbol{\Omega})\cdot\mathbf{F}_0, \tag{8.37}$$

with $\mathbf{F}_0$ a vector of $2n_p+1$ components defined as

$$\mathrm{F}_{0,k}\simeq\frac{l}{2}\sum_{j=1}^{m}w_j\left[\mathrm{P}_1(z_{in})+\mu\frac{l/2(1+x_j)}{\Delta z/2}\right]^k. \tag{8.38}$$

8.3 . Case with a polynomial basis of degree 2 for the angular flux

8.3.1 . With constant cross sections by spatial region

No solution has yet been found in the case where the spatial basis is of degree 2 and where the cross-sections are constant within regions. However, the problem is introduced. The idea is to start from (4.20) while using the result on the expression of the stabilized current at order 1 (8.24). The system of equations is given by:

$$\Sigma_t{}'\psi_{i,0}(\mathbf{\Omega}) = (\mathbb{PP}(\mathbf{\Omega}) \cdot \boldsymbol{Q}_i(\mathbf{\Omega}))_0 - \Delta \mathrm{J}_{i,0}(\mathbf{\Omega}), \tag{8.39}$$

$$\Sigma_t{}'\psi_{i,1}(\mathbf{\Omega}) = (\mathbb{PP}(\mathbf{\Omega}) \cdot \boldsymbol{Q}_i(\mathbf{\Omega}))_1 + \Delta \mathbf{J}^*_{i,1}(\mathbf{\Omega}), \tag{8.40}$$

$$\Sigma_t{}'\psi_{i,2}(\mathbf{\Omega}) = (\mathbb{PP}(\mathbf{\Omega}) \cdot \boldsymbol{Q}_i(\mathbf{\Omega}))_2 - \Delta \mathrm{J}_{i,2}(\mathbf{\Omega}) + 2\gamma\mu'\psi_{i,1}(\mathbf{\Omega}). \tag{8.41}$$

To stabilize (8.41), the logic is the same as for $n_p = 1$. We aim to group the contributions for each chord from the current and higher-order terms, and then to determine a general analytical expression as well as an asymptotic expression for the new term in the case of small chords. To this end, we start from the conservation equation along a chord (8.5) applied for $p = 2$ to express the current and higher-order terms as:

$$\Delta \mathrm{J}^*_{2,t} = \mathrm{P}_2(z_{in})\psi(\boldsymbol{r}_{in}, \mathbf{\Omega}) - \mathrm{P}_2(z_{out})\psi(\boldsymbol{r}_{out}, \mathbf{\Omega}) + \left\langle \frac{\partial \mathrm{P}_2}{\partial t}, \psi \right\rangle, \tag{8.42}$$

with

$$\left\langle \frac{\partial \mathrm{P}_2}{\partial t}, \psi \right\rangle = 2\mu\gamma \left\langle \mathrm{P}_1, \psi \right\rangle, \tag{8.43}$$

that we can know compute properly knowing that the conservation equation per chords at order 1 have been stabilized. At present, the expression of (8.42) in a form that allows for the elimination of divergence behaviors, particularly in regions where $\langle \tau \rangle_i < \tau_{lim}$, **has not yet been determined**.

8.3.2 . With polynomial cross sections by spatial region

In the case where the cross-sections depend on space, the system of equations for the spatial moments of the angular flux is written as follows:

$$\Sigma_{t,0}{}'\psi_{i,0}(\boldsymbol{\Omega}) + \Sigma_1{}'\psi_{i,1}(\boldsymbol{\Omega}) + \Sigma_{t,2}{}'\psi_{i,2}(\boldsymbol{\Omega}) = \left(\mathbb{PP}^{2n_p}(\boldsymbol{\Omega}) \cdot \boldsymbol{Q}_i(\boldsymbol{\Omega})\right)_0 - \Delta \mathrm{J}_{i,0}(\boldsymbol{\Omega}), \tag{8.44}$$

$$\Sigma_{t,0}{}'\psi_{i,1}(\boldsymbol{\Omega}) + \Sigma_{t,1}{}'\psi_{i,2}(\boldsymbol{\Omega}) + \Sigma_{t,2}{}'\psi_3(\boldsymbol{\Omega}) = \left(\mathbb{PP}^{2n_p}(\boldsymbol{\Omega}) \cdot \boldsymbol{Q}_i(\boldsymbol{\Omega})\right)_1 - \Delta \mathrm{J}_{i,1}(\boldsymbol{\Omega}) + \gamma\mu'\psi_{i,0}(\boldsymbol{\Omega}), \tag{8.45}$$

$$\Sigma_{t,0}{}'\psi_{i,2}(\boldsymbol{\Omega}) + \Sigma_{t,1}{}'\psi_3(\boldsymbol{\Omega}) + \Sigma_{t,2}{}'\psi_4(\boldsymbol{\Omega}) = \left(\mathbb{PP}^{2n_p}(\boldsymbol{\Omega}) \cdot \boldsymbol{Q}_i(\boldsymbol{\Omega})\right)_2 - \Delta \mathrm{J}_{i,2}(\boldsymbol{\Omega}) + \gamma\mu'\psi_{i,1}(\boldsymbol{\Omega}). \tag{8.46}$$

It is recalled that an analytical expression for the current term and higher order is obtained only in the case of a small optical path, and it is practically unimplementable because it would slow down the sweep. Furthermore, the system consists of 3 equations and 5 unknowns; as such, the system is non-invertible. The trick is to work with the flux coefficients. Finally, to date, no solution has been developed to stabilize (8.46).

9 - Conclusion

The work in this thesis focused on extending the surface linear scheme for solving the transport equation in 3D geometries. Based on the initial assumptions of the scheme, the transmission and conservation equations were derived and subsequently adapted.

However, unlike in 2D geometries, trajectories can cross horizontal surfaces, which, for a given set of tracking parameters, will always be less accurately integrated than vertical surfaces. To address this integration issue, the decision was made to compute the sources defined on horizontal surfaces through a linear interpolation between the sources defined on vertical surfaces.

Regarding the conservation equation, its particularity lies in the fact that the source term is constructed from a geometric operator that allows for the construction of a volumetric source based on the source defined on the vertical surfaces of the geometry. During the thesis, the geometric operator was adapted to account for the polynomial dependence of the angular flux in the axial direction.

Finally, synthetic accelerations DP_0 and DP_1 were implemented to speed up the convergence of transport calculations. The DP_n methods are based on the expansion of the angular flux in spherical harmonics over the surfaces of the computational regions. However, the same assumptions about flux variation as those used in transport are applied. Lastly, as with the MOC, the method relies on the integral form of the transport equation to evaluate the flux along the trajectories.

Once all these implementations were completed, various verification calculations were carried out. In the case where the flux is uniform axially, we demonstrated that the k_{eff} values for the 3D geometry match those obtained for the 2D geometries. Then, still for a uniform flux, we verified that the DP_0 and DP_1 accelerations correctly reproduce the transport results with a reduction in computation time. In the pin cell case, the acceleration reduces the computation time by a factor between 10 and 13 regardless of the anisotropy.

After these preliminary results, a convergence study was carried out on a 3X3 PWR assembly, with two axial planes, and a control rod made of AIC at the center of the assembly. The study was conducted for a case where the control rod is fully inserted (called the homogeneous case) and a case where the control rod is half-inserted (called the heterogeneous case) for the anisotropies P0 and P3. For all four cases, we focused on the evolution of the k_{eff}, absorption rate, and production rate.

The results clearly show that the LS scheme converges spatially faster than the SC scheme. However, starting from the RAF mesh, it seems that the improvement in precision diminishes.

One hypothesis for this behavior is that the flux gradients within each calculation region become so minimal that the gain in pcm between LS and SC calculations becomes negligible. To determine if this hypothesis holds for configurations with more steep gradients, it is planned to conduct the study on a larger 3D 17x17 assembly. However, in order to reduce the computation time for this study and minimize the number of axial mesh layers, it would be beneficial to finalize the implementation of synthetic acceleration for the case where the angular flux follows a parabolic profile in the axial direction.

Once these final implementations and studies are completed, several potential avenues for further work emerge.

Firstly, the equations implemented so far only allow calculations at Beginning Of Cycle. In order to account for the influence of spatial flux variation on the evolution of isotopic concentrations, it would be necessary to implement the transmission and conservation equations in the case where the cross-sections vary spatially.

Moreover, it is important to note that the LS scheme calculates moments on surfaces, whereas the linear schemes implemented in the solvers of codes such as CASMO5®, OpenMOC®, or DRAGON® are volumetric schemes, which calculate flux moments along the -x and -y directions. The advantage of such a surface-based scheme is that the number of degrees of freedom per calculation region is greater than that of volumetric schemes. This suggests that flux gradients are better accounted for. However, for given tracking parameters, the surfaces of a calculation region will always be less well integrated than the volumes. Consequently, the surface moments in the LS scheme will be less accurately integrated than the volumetric moments, which could negatively affect the precision of k_{eff}, absorption and production rates. An adaptive tracking approach, already implemented in the 2D part of the TDT solver, can be developed for 3D geometries to address this issue [124]. The principle is to add local trajectories to the tracking to reduce surface integration errors.

Regarding the acceleration of the transport scheme, several avenues for research and development can be pursued. First, synthetic acceleration is currently limited to DP_1, but the advantages or disadvantages of a DP_2 acceleration have not yet been studied. To this end, it would be interesting to compare both approximations on realistic cases with a number of external transport iterations on the order of hundreds. However, several hundred GB of memory would be required to store the DP_2 matrices, as a DP_1 calculation on a half 17x17 assembly (with one height symmetry) with a parabolic flux axially required around 120 GB of memory to store the matrices of the synthetic acceleration (see Table 7.6 of [7]).

Furthermore, the memory cost of the matrices can be reduced using non-linear fitting or multi-output gaussian processes. Non-linear fitting has already been implemented in TDT and is based on the Gauss-Newton method [6, 7]. Indeed, for the same assembly calculation as mentioned earlier, this technique allowed reducing the memory required to store

the acceleration matrices from 120 GB to 52 GB. The latter strategy has been used to reduce the storage of few-groups homogenized cross-sections libraries in the context of two-step reactor simulations [132]. Compared to the standard method (multi-linear interpolation), this probabilistic approach reduces the number of tabulated points by a factor of 20 for core calculations at a given precision. When applied to the evaluation of DP_n matrices, this approach could potentially decrease the number of energy groups for which acceleration matrices are evaluated prior to regression, and thus the memory requirements.

Next, it would be interesting to extend the implementation of macro-domains to 3D geometries [97]. The idea is to apply synthetic acceleration over a set of "transport" calculation regions. This strategy increases the average optical path per calculation region, which decreases the spectral radius of the synthetic operator, thereby accelerating convergence [59].

Finally, since most MOC solvers rely on CMFD acceleration, it would be interesting to compare this method with synthetic acceleration using the same MOC solver for transport. This study could be conducted on a realistic case, such as the EPR [14] or the BEAVRS reactor [133], to compare the stability, computational time gains, and memory costs of the two acceleration methods.

10 - APPENDIX

10.1 . Special case of horizontal trajectories

As the flux and macroscopic cross sections only depend on the axial coordinate, the emission density and cross sections are constant along horizontal chords. If we consider a point $\boldsymbol{r}$ in region i crossed by a horizontal trajectory entering through $\boldsymbol{r}_{in}$ and with $\boldsymbol{\Omega}_h$ as direction, we can write :

$$\Sigma_\rho(\boldsymbol{r}) = \Sigma_\rho(\boldsymbol{r}_{in}), \tag{10.1}$$

and

$$Q(\boldsymbol{r}, \boldsymbol{\Omega}) = Q(\boldsymbol{r}_{in}, \boldsymbol{\Omega}). \tag{10.2}$$

Equation (10.1) and Equation (10.2) make it possible to integrate the optical path length and the source term of the transmission equation (see Equation (4.15)) directly, yielding

$$\psi(\boldsymbol{r}_{out}, \boldsymbol{\Omega}_h) = \psi(\boldsymbol{r}_{in}, \boldsymbol{\Omega}_h)\, e^{-\Sigma_t(z_{in})\, l} + (1 - e^{-\Sigma_t(z_{in})\, l})\, \frac{Q(z_{in}, \boldsymbol{\Omega}_h)}{\Sigma_t(z_{in})}. \tag{10.3}$$

The transmission equation is the same as in the case where the cross sections and emission density are assumed constant per region. Then, one can compare the evaluation of the exiting flux $\psi(\boldsymbol{r}_{out}, \boldsymbol{\Omega}_h)$ with Equation (4.41), and Equation (10.3) to show that the horizontal transmission requires fewer floating point operations compared to other directions. First, one must remark that only the computation of the source term differs. The evaluation of the source term with Equation (4.41) requires at least the computation of $Q_0(\boldsymbol{\Omega})\tilde{\mathrm{E}}_0$ for $p = 0$, where $\tilde{\mathrm{E}}_0$ according to the Equation (4.43). Since the order of quadrature is equal to five in most cases, its evaluation requires at least five multiplications and five additions. Then, a multiplication by the source $Q_0(\boldsymbol{\Omega})$ is required. Moreover, if $n_p \geq 1$, the cost to compute the source term increases. Using the Equation (10.3), only three multiplications are required as $1 - e^{-\Sigma_t(z_{in})\, l}$ is retrieved from tabulated values, regardless of the value of n_p. Thus, it always makes the sweep for the horizontal direction equal or cheaper in terms of floating-point operations than other directions. Additionally, the computational strategy of the angular current term has been modified. We recall that the p-th spatial component is defined as :

$$\Delta \mathrm{J}_{i,p}(\boldsymbol{\Omega}) = \frac{1}{\mathrm{V}_i} \int_{\partial i_+} \mathrm{d}\boldsymbol{r}\, |\boldsymbol{\Omega} \cdot \boldsymbol{n}|\, \left[\mathrm{P}_p(\boldsymbol{r}_{out})\psi(\boldsymbol{r}_{out}, \boldsymbol{\Omega}) - \mathrm{P}_p(\boldsymbol{r}_{in})\psi(\boldsymbol{r}_{in}, \boldsymbol{\Omega})\right], \tag{10.4}$$

where $\boldsymbol{r}_{in}$ and $\boldsymbol{r}_{out}$ designate the entering and exiting points crossed by the considered trajectory, respectively. Along a horizontal chord, each point shares the same axial coordinate. Then :

$$\mathrm{P}_p(\boldsymbol{r}_{in}) = \mathrm{P}_p(\boldsymbol{r}_{out}).$$

The current term can therefore be written as :

$$\Delta \mathrm{J}_{i,p}(\boldsymbol{\Omega}) = \frac{1}{\mathrm{V}_i} \int_{\partial i_+} \mathrm{d}\boldsymbol{r}\, |\boldsymbol{\Omega} \cdot \boldsymbol{n}|\, \mathrm{P}_p(\boldsymbol{r}_{out}) \left[\psi(\boldsymbol{r}_{out}, \boldsymbol{\Omega}) - \psi(\boldsymbol{r}_{in}, \boldsymbol{\Omega})\right]. \tag{10.5}$$

We decompose the integral on the boundary ∂i_+ (where $\boldsymbol{\Omega} \cdot \boldsymbol{n} \geq 0$) into the vertical and radial surfaces :

$$\int_{\partial i_+} \mathrm{d}\boldsymbol{r} = \int_{\partial z} dz \int_{\partial i_{+,\mathrm{2D}}} \mathrm{d}\boldsymbol{r}_{\mathrm{2D}}.$$

Then, we use the definition of $\tilde{z}$ given by Equation (4.25) to make a change of variable such that

$$\int_{\partial i_+} \mathrm{d}\boldsymbol{r} = \frac{\Delta z_r}{2} \int_{-1}^{1} d\tilde{z} \int_{\partial i_{+,\mathrm{2D}}} \mathrm{d}\boldsymbol{r}_{\mathrm{2D}}.$$

We call $\mathcal{P}_{2D}(z, \boldsymbol{\Omega}_h)$ the plane that crosses the region i containing the direction and of height z. If we consider a chord of length l comprised between $\boldsymbol{r}_{in}$ and $\boldsymbol{r}_{out}$,

$$\Delta \mathrm{J}_{i,p}(\boldsymbol{\Omega}_h) = \frac{\Delta z_r}{2\mathrm{V}_i} \int_{-1}^{1} \mathrm{d}\tilde{z} \sum_{\substack{t \in \mathcal{P}_{2D}(z, \boldsymbol{\Omega}_h) \\ t \cap r}} \Delta_\perp(\boldsymbol{\Omega}_h)\, \tilde{z}^{\,p} \left[\psi(\boldsymbol{r}_{out}, \boldsymbol{\Omega}_h) - \psi(\boldsymbol{r}_{out}, \boldsymbol{\Omega}_h)\right], \tag{10.6}$$

where $\Delta_\perp$ is the 2D integration weight equal to the distance between the projections of 3D characteristics on the radial place. Then, we use Equation (10.3) to express the difference $\psi(\boldsymbol{r}_{out}, \boldsymbol{\Omega}_h) - \psi(\boldsymbol{r}_{in}, \boldsymbol{\Omega}_h)$. We get :

$$\Delta \mathrm{J}_{i,p}(\mathbf{\Omega}_h) = \frac{\Delta z_r \, \Delta_\perp}{2\mathrm{V}_i} \sum_{\substack{t \in \mathcal{P}_{2D}(z,\mathbf{\Omega}_h) \\ t \cap r}} \int_{-1}^{1} \mathrm{d}\tilde{z} \, \tilde{z}^{\,p} \left[(1 - e^{-\Sigma(z)l}) \left[\frac{Q(\mathbf{\Omega}_h)}{\Sigma(z)} - \psi(\boldsymbol{r}_{in}, \mathbf{\Omega}_h) \right] \right]. \quad (10.7)$$

The last integration is made thanks to a Gauss-Legendre quadrature. Denoting by m the quadrature order, the integrand needs to be evaluated at every quadrature abscissa $\tilde{z}_j$ of weight w_j such that :

$$\Delta \mathrm{J}_{i,p}(\mathbf{\Omega}_h) \approx \frac{\Delta z_r \, \Delta_\perp}{2\mathrm{V}_i} \sum_{\substack{t \in \mathcal{P}_{2D}(z,\mathbf{\Omega}_h) \\ t \cap r}} \sum_{j=1}^{m} w_j \, z_j^p \left[(1 - e^{-\Sigma(z_j)l}) \left[\frac{Q(z_j, \mathbf{\Omega}_h)}{\Sigma(z_j)} - \psi(\boldsymbol{r}_{in}, \mathbf{\Omega}_h) \right] \right]. \quad (10.8)$$

The tracking-based integration is only made on each radial plane $\mathcal{P}_{2D}(z, \mathbf{\Omega}_h)$.

10.2 . Trajectory-based balance equation in the case of spatially dependent cross sections

If one consider a chord of length l entering the region in $\boldsymbol{r}_{\text{in}}$, each point that belongs to will be written as $\boldsymbol{r}_t = \boldsymbol{r}_{in} + t\mathbf{\Omega}$ with t between 0 and l. Its coordinate will be noted (x_t, y_t, z_t). In particular $\boldsymbol{r}_0 = \boldsymbol{r}_{in}$. If one wants to know the angular flux $\psi(\boldsymbol{r}_t, \mathbf{\Omega})$, he can use the transmission equation

$$\psi(\boldsymbol{r}_t, \mathbf{\Omega}) = \psi(\boldsymbol{r}_{in}, \mathbf{\Omega}) e^{-\tau(l)} + \int_0^t \mathrm{d}t' \, Q(\boldsymbol{r}_{in} + t'\mathbf{\Omega}) \, e^{-[\tau(t) - \tau(t')]} \quad (10.9)$$

that we multiply by the total macroscopic cross section $\Sigma_t(\boldsymbol{r}_t)$. We multiply the result by $\mathbf{P}$ and integrate over a chord of length l. This gives :

$$\begin{aligned} \langle \mathbf{P}, \Sigma_t \psi \rangle &= \psi(\boldsymbol{r}_{in}, \mathbf{\Omega}) \int_0^l \mathrm{d}t \mathbf{P}(z_t) \Sigma_t(\boldsymbol{r}_t) e^{-\tau(t)} \\ &+ \int_0^l \mathrm{d}t \mathbf{P}(z_t) \Sigma_t(\boldsymbol{r}_t) \int_0^t \mathrm{d}t' Q(\boldsymbol{r}_{t'}, \mathbf{\Omega}) e^{-(\tau(t) - \tau(t'))}. \end{aligned} \quad (10.10)$$

The first term is integrated by part :

$$\psi(\boldsymbol{r}_{in},\boldsymbol{\Omega})\int_0^l \mathrm{d}t\mathbf{P}(z_t)\Sigma_t(\boldsymbol{r}_t)e^{-\tau(t)} = \psi(\boldsymbol{r}_{in},\boldsymbol{\Omega})\left[\mathbf{P}(z_0)-\mathbf{P}(z_l)e^{-\tau(l)}\right]+ \psi(\boldsymbol{r}_{in},\boldsymbol{\Omega})\int_0^l \mathrm{d}t\mathbf{P}'(t)e^{-\tau(t)}. \tag{10.11}$$

The second term is integrated by inverting the integration order. The integration of t' between 0 and t, for t in 0 to l equals the integration of t between t' and l, for t' in 0 and l.

$$\begin{aligned}\left\langle \mathbf{P}, \int_0^t \mathrm{d}t'\Sigma_t(\boldsymbol{r}_t)Q(\boldsymbol{r}'_t,\boldsymbol{\Omega})e^{-(\tau(t)-\tau(t'))}\right\rangle &= \int_0^l \mathrm{d}t\int_0^t \mathrm{d}t'\mathbf{P}(z_t)\Sigma_t(\boldsymbol{r}_t)Q(\boldsymbol{r}_{t'},\boldsymbol{\Omega})e^{-(\tau(t)-\tau(t'))},\\ &= \int_0^l \mathrm{d}t'\int_{t'}^l \mathrm{d}t\mathbf{P}(z_t)\Sigma_t(\boldsymbol{r}_t)Q(\boldsymbol{r}_{t'},\boldsymbol{\Omega})e^{-(\tau(t)-\tau(t'))},\\ &= \int_0^l \mathrm{d}t'Q(\boldsymbol{r}_{t'},\boldsymbol{\Omega})e^{\tau(t')}\int_{t'}^l \mathrm{d}t\mathbf{P}(z_t)\Sigma_t(\boldsymbol{r}_t)e^{-\tau(t)},\\ &= \int_0^l \mathrm{d}tQ(\boldsymbol{r}_t,\boldsymbol{\Omega})e^{\tau(t)}\int_t^l \mathrm{d}t'\mathbf{P}(z_{t'})\Sigma_t(\boldsymbol{r}_{t'})e^{-\tau(t')}.\end{aligned}$$

The integral between t and l is integrated by part.

$$\int_t^l \mathrm{d}t'\mathbf{P}(z_{t'})\Sigma_t(\boldsymbol{r}_{t'})e^{-\tau(t')} = \left[\mathbf{P}(z_t)e^{-\tau(t)}-\mathbf{P}(z_{out})e^{-\tau(l)}\right]+\int_t^l \mathrm{d}t'\mathbf{P}'(z_t)e^{-\tau(t')}. \tag{10.12}$$

Then, we multiply (10.12) by the integral of the source term and we inverse the integration order of the last term :

$$\begin{aligned}\int_0^l \mathrm{d}tQ(\boldsymbol{r}_t,\boldsymbol{\Omega})e^{\tau(t)}\int_t^l \mathrm{d}t'\mathbf{P}(z_{t'})e^{-\tau(t')} &= \int_0^l \mathrm{d}t\mathbf{P}(z_t)Q(\boldsymbol{r}_t,\boldsymbol{\Omega})\\ &\quad -\mathbf{P}(l)\int_0^l \mathrm{d}tQ(\boldsymbol{r}_t,\boldsymbol{\Omega})e^{-(\tau(l)-\tau(t))}\\ &\quad +\int_0^l \mathrm{d}t\int_0^t \mathrm{d}t'\mathbf{P}'(t)Q(\boldsymbol{r}'_t,\boldsymbol{\Omega})e^{-(\tau(t)-\tau(t'))}.\end{aligned} \tag{10.13}$$

Finally, one obtains :

$$\langle \mathbf{P},\Sigma_t\psi\rangle = \mathbf{P}(z_{in})\psi(\boldsymbol{r}_{in},\boldsymbol{\Omega})-\mathbf{P}(z_{out})\psi(\boldsymbol{r}_{out},\boldsymbol{\Omega})+\langle \mathbf{P},Q\rangle+\left\langle \mathbf{P}',\psi\right\rangle. \tag{10.14}$$

10.3 . Useful relations

10.3.1 . Average of the angular flux over a trajectory

Let $\boldsymbol{r}_t$ be a point along a chord of length l and direction $\boldsymbol{\Omega}$ that traverses region i between the entry point $\boldsymbol{r}_{in}$ and the exit point $\boldsymbol{r}_{out}$. For $t \in [0, l]$, $\boldsymbol{r}_t$ is defined as $\boldsymbol{r}_t = \boldsymbol{r}_{in} + t\boldsymbol{\Omega}$. In the case where the cross sections are constant within regions, it can be shown that:

$$\overline{\psi}_0(\boldsymbol{\Omega}) = \frac{1}{\tau}\left[\psi(\boldsymbol{r}_{in}, \boldsymbol{\Omega}) - \psi(\boldsymbol{r}_{out}, \boldsymbol{\Omega}) + \left(\mathbb{PP}_t(\boldsymbol{\Omega}) \cdot \boldsymbol{Q}(\boldsymbol{\Omega})\right)_0\right], \tag{10.15}$$

with,

$$\mathbb{PP}_t(\boldsymbol{\Omega}) = \int_0^l \mathrm{d}t \mathbf{P}(z_t) \otimes \mathbf{P}(z_t). \tag{10.16}$$

Demonstration: The idea is to start from the definition of the average flux along a chord and then express the flux at a point using the transport equation. Thus, we can write:

$$\begin{aligned} l\overline{\psi}_0(\boldsymbol{\Omega}) &= \int_0^l \mathrm{d}t \psi(\boldsymbol{r}_t, \boldsymbol{\Omega}), \\ &= \psi(\boldsymbol{r}_{in}, \boldsymbol{\Omega}) \int_0^l \mathrm{d}t e^{-\tau(t)} + \int_0^l \mathrm{d}t \int_0^t \mathrm{d}t' Q(\boldsymbol{r}_{in} + t'\boldsymbol{\Omega}) e^{-(\tau(t)-\tau(t'))}. \end{aligned}$$

The first term integrates naturally. For the second term, we use the fact that integrating t' from 0 to t, where t ranges from 0 to l, is equivalent to integrating t from t' to l, with t' ranging from 0 to l. Therefore:

$$\begin{aligned} \int_0^l \mathrm{d}t \int_0^t \mathrm{d}t' Q(\boldsymbol{r}_{in} + t'\boldsymbol{\Omega}) e^{-(\tau(t)-\tau(t'))} &= \int_0^l \mathrm{d}t' \int_{t'}^l \mathrm{d}t Q(\boldsymbol{r}_{in} + t'\boldsymbol{\Omega}) e^{-(\tau(t)-\tau(t'))}, \\ &= \frac{1}{\Sigma_t}\left(\mathbb{PP}_t(\boldsymbol{\Omega}) \cdot \boldsymbol{Q}(\boldsymbol{\Omega})\right)_0 \\ &\quad - \frac{1}{\Sigma_t} \int_0^l \mathrm{d}t Q(\boldsymbol{r}_{in} + t\boldsymbol{\Omega}) e^{-(\tau(l)-\tau(t))}. \end{aligned}$$

Thus,

$$\overline{\psi}_0(\boldsymbol{\Omega}) = \frac{1}{\tau}\left[\psi(\boldsymbol{r}_{in}, \boldsymbol{\Omega}) - \psi(\boldsymbol{r}_{out}, \boldsymbol{\Omega}) + \left(\mathbb{PP}_t(\boldsymbol{\Omega}) \cdot \boldsymbol{Q}(\boldsymbol{\Omega})\right)_0\right].$$

10.3.2 . Asymptotic expansion of optical path in 0

When the cross sections are polynomially expanded within each region

$$\forall t \in \mathbb{R}, \tau(t) \underset{0}{=} \tau_0(t) + o(\tau_0(t)), \text{ with } \tau_0(t) = \Sigma_{t,0} t \tag{10.17}$$

Demonstration: Let $n_p \in \mathbb{N}$ be the polynomial degree of the cross sections. We can then write

$$\forall \boldsymbol{r} \in \mathbb{R}^3, \Sigma_t(\boldsymbol{r}) = \Sigma_{t,0} + \Sigma_{t,1}\tilde{z}_r + \Sigma_{t,2}\tilde{z}_r^2 + \ldots + \Sigma_{t,n_p}\tilde{z}_r^{n_p}. \tag{10.18}$$

There are two situations in which τ approaches 0. Either the swept chord is small ($\tilde{z}_r$ approaches 0), or the medium being considered is empty. In the first case, we can write

$$\Sigma_t(\boldsymbol{r}) \underset{0}{=} \Sigma_{t,0} + o(\Sigma_{t,0}),$$

Then, by integrating over a chord of length l,

$$\tau(t) \underset{0}{=} \tau_0 + o(\tau_0).$$

In the case of a void region, $\Sigma_t = 0$, it directly follows that

$$\lim_{\Sigma_t \to 0} (\tau - \tau_0) = 0,$$

Which, by definition, means that

$$\tau(t) \underset{0}{=} \tau_0 + o(\tau_0).$$

Subsequently, and unless necessary, we will no longer specify whether we are dealing with an empty medium or a chord of sufficiently small length.

10.3.3 . Asymptotic expansion of the escape factors for small optical path and uniform cross sections

In the case where the cross sections are constant within regions, it can be shown that $\mathrm{E}_j(\tau)$ defined as 4.18, writes:

$$\forall j \in \mathbb{N},\ \mathrm{E}_j(\tau) \underset{0}{=} \sum_{i=1}^{\infty} (-1)^{i+1} \frac{j!}{(j+i)!} \tau^i l^j. \tag{10.19}$$

Demonstration: Soit $j \in \mathbb{N}$,

To start, we recall the definition of $\mathrm{E}_j(\tau)$:

$$\mathrm{E}_j(\tau) = \frac{1}{\Sigma_t^j} \int_0^\tau d\tau'\, \tau'^{,j} e^{\tau'-\tau} \tag{10.20}$$

We first focus on $\mathrm{E}_j^{\mathrm{T}}(\tau) = \frac{1}{l^j}\mathrm{E}_j(\tau)$, which is defined as:

$$\mathrm{E}_j^{\mathrm{T}}(\tau) = \frac{1}{\tau^j} \int_0^\tau d\tau'\, \tau'^{,j} e^{\tau'-\tau}. \tag{10.21}$$

Besides, a integration by part of (10.21) leads to the relation

$$\mathrm{E}_j^{\mathrm{T}}(\tau) = 1 - \frac{j}{\tau}\mathrm{E}_{j-1}^{\mathrm{T}}(\tau). \tag{10.22}$$

We use this relationship to show by recurrence that

$$\forall j \in \mathbb{N},\ \mathrm{E}_j^{\mathrm{T}}(\tau) \underset{0}{=} \sum_{i=1}^{\infty} (-1)^{i+1} \frac{j!}{(j+i)!} \tau^i. \tag{10.23}$$

Indeed

$$
\begin{aligned}
\mathrm{E}_{j+1}^{\mathrm{T}}(\tau) &= 1 - \frac{j+1}{\tau}\mathrm{E}_{j}^{\mathrm{T}}(\tau), \\
&= 1 - \frac{j+1}{\tau}\sum_{i=1}^{\infty}(-1)^{i+1}\,\frac{j!}{(j+i)!}\tau^{i}, \\
&= 1 + \sum_{i=1}^{\infty}(-1)^{i+2}\,\frac{(j+1)!}{(j+i)!}\tau^{i-1}, \\
&= \sum_{i=2}^{\infty}(-1)^{i+2}\,\frac{(j+1)!}{(j+i)!}\tau^{i-1}, \\
&= \sum_{i=1}^{\infty}(-1)^{i+1}\,\frac{(j+1)!}{(j+i+1)!}\tau^{i}
\end{aligned}
$$

.

It naturally follows that

$$
\forall j \in \mathbb{N},\ \mathrm{E}_j(\tau) \underset{0}{=} \sum_{i=1}^{\infty}(-1)^{i+1}\,\frac{j!}{(j+i)!}\tau^{i}l^{j},
$$

and that if we want an equivalent, we can take

$$
\forall j \in \mathbb{N},\ \mathrm{E}_j(\tau) \underset{0}{\simeq} \frac{1}{1+j}\tau l^{j} \tag{10.24}
$$

10.3.4 . Asymptotic expansion of the escape factors for small optical path and spatially dependent cross sections

In the case where the effective sections are developed on the base, we can show that:

$$
\forall j \in \mathbb{N},\ \mathrm{E}_j(t) \underset{0}{=} \frac{1}{\Sigma_{t,0}}\left[\frac{1}{j+1}\tau_0 + o(\tau_0)\right] l^{j} \tag{10.25}
$$

Demonstration: We use result 10.3.2 to show that

$$
e^{\tau(t)} \underset{0}{=} 1 + \tau_0 + o(\tau_0),
$$

then,

$$
t^{j}e^{\tau(t)} \underset{0}{=} t^{j} + \Sigma_{t,0}t^{j+1} + o(t^{j+1}),
$$

and finally,

$$\mathrm{E}_j(t) = e^{-\tau(l)} \int_0^l \mathrm{d}t\, t^j e^{\tau(t)} \underset{0}{=} \frac{1}{\Sigma_{t,0}} \left[\frac{1}{j+1} \tau_0 + o(\tau_0) \right] l^j.$$

10.3.5 . Equality between transmission equation source term and trajectory source term for small optical path

In the case where the cross sections are constant per region, we can show that:

$$\forall j \in \mathbb{N},\ \lim_{\tau \to 0} \mathbf{P}^j \cdot \mathbf{T} = \left(\mathbb{PP}_t(\mathbf{\Omega}) \cdot \boldsymbol{Q}(\mathbf{\Omega}) \right)_j . \tag{10.26}$$

Demonstration: We begin by determining an expression for $\left(\mathbb{PP}_t(\mathbf{\Omega}) \cdot \boldsymbol{Q}(\mathbf{\Omega}) \right)_j$. It can be demonstrated using the binomial theorem and then integrating that the element in row p and column p' can be expressed as

$$\overline{\mathbb{PP}}_{pp'} = \int_0^l \mathrm{d}t \left[\frac{z_0 - \tilde{z} + \mu t}{\Delta z/2} \right]^{p+p'}, \tag{10.27}$$

$$= \sum_{k=0}^{p+p'} \binom{p+p'}{k} \left[\frac{z_0 - \tilde{z}}{\Delta z/2} \right]^{p+p'-k} \left(\frac{2\mu}{\Delta z} \right)^k \frac{l^{k+1}}{k+1}, \tag{10.28}$$

$$= \sum_{k=0}^{p+p'} \binom{p+p'}{k} \left[\frac{z_0 - \tilde{z}}{\Delta z/2} \right]^{k} \left(\frac{2\mu}{\Delta z} \right)^{p+p'-k} \frac{l^{p+p'-k+1}}{p+p'-k+1}. \tag{10.29}$$

What we are interested in is the $(j+1)^{\text{th}}$ term of the vector $\left(\mathbb{PP}_t(\mathbf{\Omega}) \cdot \boldsymbol{Q}(\mathbf{\Omega}) \right)_j$. This corresponds to the dot product between the source and the $(j+1)^{\text{th}}$ row of the matrix $\mathbb{PP}_t(\mathbf{\Omega})$. By applying the binomial formula and interchanging the order of summation, we obtain:

$$\left(\mathbb{PP}_t(\mathbf{\Omega}) \cdot \boldsymbol{Q}(\mathbf{\Omega}) \right)_j = \sum_{p=0}^{n_p} \sum_{k=0}^{p+j} \binom{p+j}{k} \left[\frac{z_0 - \tilde{z}}{\Delta z/2} \right]^{p+j-k} \left(\frac{2\mu}{\Delta z} \right)^k Q^p(\mathbf{\Omega}) \frac{l^{k+1}}{k+1}, \tag{10.30}$$

Now, let $\mathbf{P}^j \cdot \mathbf{T}$ denote the integral

$$\mathbf{P}^j \cdot \mathbf{T} = \int_0^l \mathrm{d}t \mathrm{P}_j Q(\boldsymbol{r}_{in} + t\mathbf{\Omega}) e^{-(\tau(l) - \tau(t))}. \tag{10.31}$$

By expanding the source according to its polynomial approximation and then carrying out the calculations, we obtain the following expressions:

$$\begin{aligned}\mathbf{P}^j \cdot \mathbf{T} &= \int_0^l \mathrm{d}t \sum_{p=0}^{n_p} \left[\frac{z_0 - \tilde{z} + \mu t}{\Delta z/2}\right]^{p+j} Q^p(\mathbf{\Omega}) e^{-(\tau(l)-\tau(t))}, \\ &= \sum_{p=0}^{n_p}\sum_{k=0}^{p+j} \binom{p+j}{k} \left[\frac{z_0 - \tilde{z}}{\Delta z/2}\right]^{p+j-k} \left(\frac{2\mu}{\Delta z}\right)^k \frac{Q^p(\mathbf{\Omega})}{\Sigma_t} \mathrm{E}_k(\tau),\end{aligned}$$

Knowing from the the result 10.3.3 that

$$\lim_{\tau\to 0} \frac{1}{\Sigma_t}\mathrm{E}_k(\tau) \simeq \frac{l_t^{k+1}}{k+1},$$

we have shown that

$$\forall j \in \mathbb{N},\ \lim_{\tau\to 0} \mathbf{P}^j \cdot \mathbf{T} = \left(\mathbb{PP}_t(\mathbf{\Omega}) \cdot \boldsymbol{Q}(\mathbf{\Omega})\right)_j .$$

10.4 . Mathematical functions

10.4.1 . Legendre polynomials

The sequence of Legendre polynomials $(\mathcal{P}_k)_{k\in\mathbb{N}}$ encompasses all solutions on $[-1,1]$ of the Legendre differential equation (homogeneous and second-order) :

$$\frac{d}{d\mu}\left[(1-\mu^2)\frac{d}{d\mu}\mathcal{P}_k(\mu)\right]+k(k+1)\mathcal{P}_k(\mu)=0. \tag{10.32}$$

The polynomial functions are also defined as follows :

$$\mathcal{P}_0(\mu)=1, \tag{10.33}$$

$$\mathcal{P}_k(\mu)=\frac{1}{2^k k!}\frac{d^k}{d\mu^k}(\mu^2-1). \tag{10.34}$$

Their algebraic expressions can also be derived from the recurrence formula :

$$(k+1)P_{k+1}(\mu)=(2k+1)\mu P_k(\mu)+kP_{k-1}(\mu). \tag{10.35}$$

A graphical representation of the Legendre polynomials up to order 4 is provided in the figure 10.1. Now, let's discuss some properties.

Parity property

$$\mathcal{P}_k(-\mu)=(-1)^k\mathcal{P}_k(\mu). \tag{10.36}$$

Orthogonality property

$$\int_{-1}^{1}\mathrm{d}\mu\mathcal{P}_k(\mu)\mathcal{P}'_k(\mu)=\frac{2}{2k+1}\delta_{k,k'}. \tag{10.37}$$

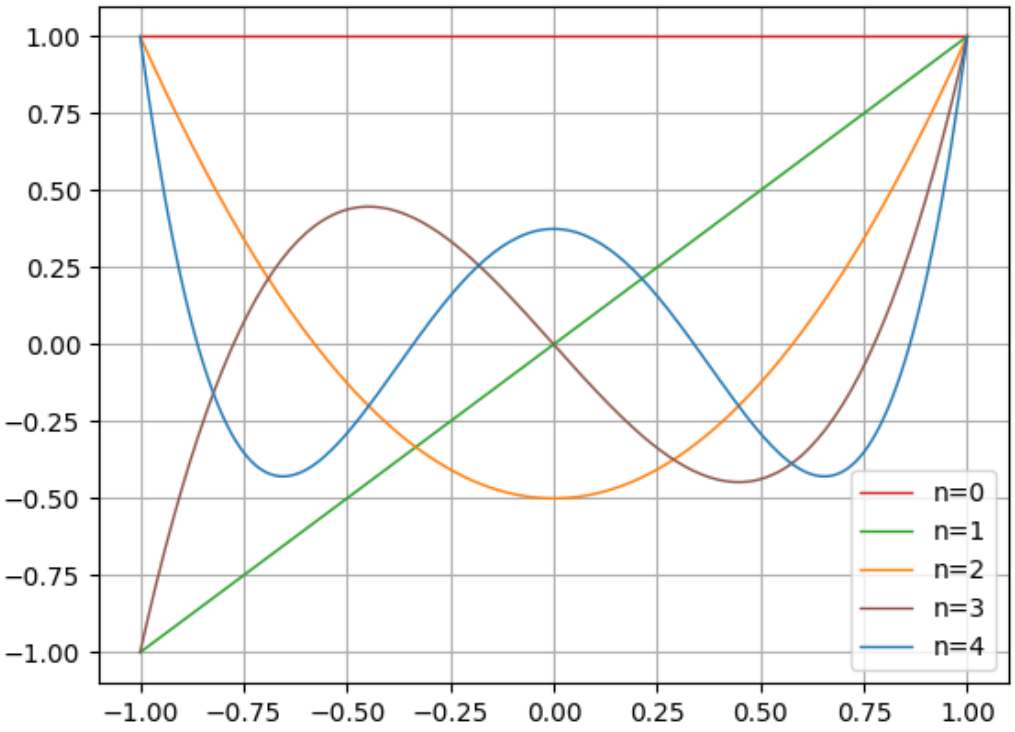

Figure 10.1 – Graphical representation of the Legendre polynomials up to the order 4.

10.4.2 . Real spherical harmonics

The real spherical harmonics are defined based on the associated Legendre polynomials. The associated Legendre polynomials $(\mathcal{P}_k^l)_{k\in\mathbb{N}}^{l\in[\![0,k]\!]}$ are themselves defined from the Legendre polynomials as follows :

$$\mathcal{P}_k^0(\mu) = \mathcal{P}_k(\mu), \tag{10.38}$$

$$\mathcal{P}_k^l(\mu) = (-1)^l(1-\mu)^{l/2}\frac{\mathrm{d}^l}{\mathrm{d}\mu^l}\mathcal{P}_k(\mu). \tag{10.39}$$

Parity property

$$\mathcal{P}_k^l(-\mu) = (-1)^{k+l}\mathcal{P}_k^l(\mu). \tag{10.40}$$

Orthogonality property

$$\int_{-1}^{1} \mathrm{d}\mu \mathcal{P}_k^l(\mu)\mathcal{P}_{k'}^l(\mu) = \frac{2(k+l)!}{(2k+1)(k-l)!}\delta_{k,k'}. \tag{10.41}$$

We can now define the real spherical harmonics as :

$$A_k^l(\mathbf{\Omega}) = \begin{cases} \sqrt{2}\sqrt{\frac{(2k+1)}{(4\pi)}\frac{(k-l)!}{(k+l)!}}P_k^l(cos(\theta))cos(l\varphi), & \text{if l>0,} \\ \sqrt{\frac{(2k+1)}{(4\pi)}}P_k^0(cos(\theta)), & \text{if l=0,} \\ \sqrt{2}\sqrt{\frac{(2k+1)}{(4\pi)}\frac{(k-l)!}{(k+l)!}}P_k^{|l|}(cos(\theta))sin(|l|\varphi), & \text{if l<0.} \end{cases} \tag{10.42}$$

11 - Résumé en français

Le travail de cette thèse se divise en deux volets distincts. Le premier est consacré à la conception d'un schéma combinant transport et accélération, basé sur une approximation linéaire surfacique, destiné à résoudre l'équation du transport sur des géométries 3D extrudées. Actuellement, seule une approximation constante est disponible. La principale distinction entre ces deux approches réside dans la vitesse de convergence par rapport au maillage : elle est linéaire pour l'approximation constante et devient quadratique avec l'approximation surfacique linéaire. Concrètement, cette dernière permet d'obtenir une précision équivalente tout en réduisant le nombre de mailles nécessaires, ce qui diminue significativement le temps de calcul. De plus, le schéma proposé doit permettre le développement du flux selon une base polynomiale dans la direction axiale ainsi que celui des sections efficaces, nécessaire pour les calculs en évolution. Contrairement aux méthodes linéaires classiques, la source de neutron est ici définie sur les surfaces verticales des régions de calcul, tandis que sa valeur sur les surfaces horizontales est déterminée par interpolation linéaire à partir des valeurs verticales. Cette approche présente l'avantage d'éliminer la nécessité de l'intégration par traçage sur les surfaces horizontales.

Ensuite, de manière à évaluer la convergence des itérations internes, un bilan sur les moments volumiques du flux angulaire est réalisé. Un opérateur géométrique est alors conçu afin de générer une source volumique à partir de la source surfacique, avec une conservation imposée par une correction.

Concernant l'accélération du transport, l'option retenue est l'implémentation d'une accélération synthétique de type DP_n. Cette méthode repose sur le développement du flux angulaire en harmoniques sphériques sur les surfaces des régions de calcul, et peut être interprétée comme un préconditionnement d'un schéma itératif de type Richardson. Ce choix est motivé par plusieurs facteurs : d'une part, le rayon spectral de l'opérateur associé est plus faible que celui d'autres techniques d'accélération comme la Diffusion Synthetic Acceleration (DSA) ou les méthodes non linéaires du type Coarse Mesh Finite Difference (CMFD), même dans des milieux à fortes longueurs de parcours optiques. D'autre part, la construction du système d'équations repose sur la même discrétisation spatiale que celle utilisée pour le transport, réduisant ainsi les besoins de normalisation de certaines grandeurs, problème fréquent avec d'autres méthodes. Enfin, l'usage de la forme intégrale de l'équation de transport rend cette approche intéressante pour des géométries complexes et des maillages non structurés.

La seconde partie du travail s'attache à corriger les instabilités numériques qui surgissent avec l'augmentation de l'ordre de développement spatial du flux. Dans un milieu homogène infini, le terme de fuite issu de l'équation intégro-différentielle devrait être nul. Or, dans certaines régions de calcul où le nombre de trajectoires à faible chemin optique dépasse un

seuil critique, ce terme devient non négligeable, compromettant la convergence des méthodes TDT-MOC, voire la rendant impossible si ce phénomène est trop prononcé. De manière à contourner le problème, une solution théorique est proposée où le terme de courant est cumulé directement avec le terme d'ordre supérieur, corde par corde. En suivant cette approche, il est possible d'évaluer correctement ces termes pour les cordes avec un faible chemin optique en s'appuyant sur des développements limités. Actuellement, ce travail est réalisé juqu'aux équations bilans concernant les seconds moments spatiaux du flux, i.e. les moments linéaires en espace.

Une fois toutes les implémentations achevées, plusieurs calculs de vérifications ont été réalisés. Dans le cas où le flux est uniforme selon l'axe axial, nous avons démontré que les valeurs de k_{eff} pour la géométrie 3D correspondent à celles obtenues pour les géométries 2D - la différence de k_{eff} est inférieur à 11 pcm. Ensuite, toujours pour un flux uniforme, nous avons vérifié que les accélérations DP_0 et DP_1 reproduisent correctement les résultats du transport tout en réduisant le temps de calcul. Dans le cas de la cellule combustible, l'accélération permet de diminuer le temps de calcul par un facteur compris entre 10 et 13, quel que soit l'ordre d'anisotropie.

Après ces résultats préliminaires, une étude de convergence a été menée sur un assemblage PWR 3×3, comportant deux plans axiaux et une barre de commande en AIC placée au centre de l'assemblage. L'étude a été réalisée pour deux configurations : une où la barre de commande est entièrement insérée (appelée cas homogène axial) et une où elle est insérée à moitié (appelée cas hétérogène axial), pour les anisotropies P0 et P3. Pour ces quatre cas, l'analyse a porté sur l'évolution de k_{eff}, du taux d'absorption et du taux de production.

Les résultats montrent clairement que le schéma linéaire surfacique (LS) converge spatialement plus rapidement que le schéma step constant (SC). Toutefois, à partir du maillage RAF, l'amélioration de la précision semble s'atténuer. Une hypothèse avancée pour expliquer ce comportement est que les gradients de flux à l'intérieur de chaque région de calcul deviennent si faibles que le gain en pcm entre les calculs LS et SC devient négligeable. Pour vérifier si cette hypothèse se confirme dans des configurations présentant des gradients plus marqués, il est prévu de poursuivre l'étude sur un assemblage 3D plus grand de type 17×17. De cette manière, on pourrait vérifier la performance, en temps et en précision, de ce schéma sur des configurations géométriques industrielles.

Bibliographie

[1] K. Assogba, *Résolution numérique de l'équation du transport de neutrons par la méthode des harmoniques sphériques et une méthode de Galerkin discontinue*. Theses, Institut Polytechnique de Paris, 2023.

[2] P. K. Romano, N. E. Horelik, B. R. Herman, A. G. Nelson, B. Forget, and K. Smith, "Openmc : A state-of-the-art monte carlo code for research and development," *Annals of Nuclear Energy*, vol. 82, pp. 90–97, 2015. Joint International Conference on Supercomputing in Nuclear Applications and Monte Carlo 2013, SNA + MC 2013. Pluri- and Trans-disciplinarity, Towards New Modeling and Numerical Simulation Paradigms.

[3] C. Jeannesson, *Development of a methodology to exploit nuclear data in the unresolved resonance range and the impact on criticality safety and reactor applications*. Theses, Université Paris-Saclay, 2020.

[4] B. Becker, *On the influence of the resonance scattering treatment in Monte Carlo codes on high temperature reactor characteristics*. PhD thesis, 2010.

[5] D. Sciannandrone, S. Santandrea, and R. Sanchez, "Optimized tracking strategies for step MOC calculations in extruded 3d axial geometries," *Annals of Nuclear Energy*, vol. 87, pp. 49–60.

[6] L. Graziano, *An axial polynomial expansion and acceleration of the characteristics method for the solution of the Neutron Transport Equation*. Theses, Université Paris Saclay (COmUE), 2018.

[7] A. Gammicchia, *Development and acceleration of a 3D characteristics method including an axial polynomial expansion of cross sections*. Theses, Université Paris-Saclay, 2021.

[8] A. Le Bars, D. Tomatis, and I. Zmijarevic, "Apollo3 calculation of bwr fuel assembly of a burn-up credit criticality benchmark," *PHYSOR, Pittsburgh*, pp. 3634–3643, 2022.

[9] O. Hahn and F. Strassmann, "Über die entstehung von radiumisotopen aus uran durch bestrahlen mit schnellen und verlangsamten neutronen," *Naturwissenschaften*, vol. 26, no. 46, pp. 755–756, 1938.

[10] A. Hessenbruch, "Lise meitner - a life in physics," *European Journal of Physics*, vol. 17, no. 6, p. 021, 1996.

[11] D. Cooper and E. Fermi, *Enrico Fermi : And the Revolutions of Modern Physics*. (Accad. nazionale dei Lincei. Problemi attuali di scienza e di cultura), Oxford University Press, USA, 1999.

[12] M. F. James, "Energy released in fission," *Journal of Nuclear Energy*, vol. 23, no. 9, pp. 517–536.

[13] S. Marguet, *The Technology of Pressurized Water Reactors*. Springer Cham, 2022.

[14] D. Lago and F. Rahnema, "Benchmark description of a stylized three-dimensional european pressurized reactor (epr) problem," *Progress in Nuclear Energy*, vol. 93, pp. 18–46, 2016.

[15] A. W. Solbrig, Jr, "Doppler effect in neutron absorption resonances," *American Journal of Physics (U.S.)*.

[16] G. Grimmett, D. Grimmett, and D. Stirzaker, *Probability and Random Processes : Fourth Edition*. Oxford University Press, 2020.

[17] E. Brun, F. Damian, C. M. Diop, E. Dumonteil, F. X. Hugot, C. Jouanne, Y. K. Lee, F. Malvagi, A. Mazzolo, O. Petit, J. C. Trama, T. Visonneau, and A. Zoia, "TRIPOLI-4®, CEA, EDF and AREVA reference monte carlo code," *Annals of Nuclear Energy*, vol. 82, pp. 151–160.

[18] Mancusi, Davide, Brun, Emeric, Dechenaux, Benjamin, Fröhlicher, Kévin, Gonçalves, Thomas, Jinaphanh, Alexis, Kowalski, Mikolaj Adam, Larmier, Coline, Malvagi, Fausto, Millasseau, Grégory, Monange, Wilfried, Petit, Odile, and Zoia, Andrea, "Overview of tripoli-5, a monte carlo code for hpc," *EPJ Nuclear Sci. Technol.*, vol. 10, p. 26, 2024.

[19] M. Rising *et al.*, "MCNP® Code Version 6.3.0 Release Notes," Tech. Rep. LA-UR-22-33103, Rev. 1, Los Alamos National Laboratory, Los Alamos, NM, USA, 2023.

[20] J. A. Kulesza *et al.*, "MCNP® Code Version 6.3.0 Theory & User Manual," Tech. Rep. LA-UR-22-30006, Rev. 1, Los Alamos National Laboratory, Los Alamos, NM, USA, 2022.

[21] J. Leppänen *et al.*, "Serpent - a continuous-energy monte carlo reactor physics burnup calculation code," *VTT Technical Research Centre of Finland*, vol. 4, no. 455, pp. 2023–09, 2013.

[22] W. Boyd, S. Shaner, L. Li, B. Forget, and K. Smith, "The openmoc method of characteristics neutral particle transport code," *Annals of Nuclear Energy*, vol. 68, pp. 43–52, 2014.

[23] G. Gunow, B. Forget, and K. Smith, "Full core 3d simulation of the BEAVRS benchmark with OpenMOC," *Annals of Nuclear Energy*, vol. 134, pp. 299–304.

[24] J. Cho, K. Kim, H. Kim, C. Lee, S. Zee, and H. Joo, "Decart v1. 2 user's manual," 2007.

[25] J.-Y. Cho, K.-S. Kim, C.-C. Lee, S.-Q. Zee, and H.-G. Joo, "Axial spn and radial moc coupled whole core transport calculation," *Journal of nuclear science and technology*, vol. 44, no. 9, pp. 1156–1171, 2007.

[26] Y. S. Jung, C. B. Shim, C. H. Lim, and H. G. Joo, "Practical numerical reactor employing direct whole core neutron transport and subchannel thermal/hydraulic solvers," *Annals of Nuclear Energy*, vol. 62, pp. 357–374, 2013.

[27] N. Choi, H. Park, H. Lee, S. Jae, S. Jeon, and H. Joo, "Recent capability and performance enhancements of the whole-core transport code ntracer," *The European Physical Journal Conferences*, vol. 247, p. 06033, 2021.

[28] D. R. Gaston, B. Forget, K. S. Smith, L. H. Harbour, G. K. Ridley, and G. G. Giudicelli, "Method of characteristics for 3d, full-core neutron transport on unstructured mesh," *Nuclear Technology*, vol. 207, no. 7, pp. 931–953, 2021.

[29] D. Schneider, F. Dolci, F. Gabriel, J.-M. Palau, M. Guillo, and B. Pothet, "APOLLO3® CEA/DEN deterministic multi-purpose code for reactor physics analysis," in *PHYSOR 2016 – Unifying Theory and Experiments in the 21st Century*, (Sun Valley, United States), 2016. APOLLO3® is a registered trademark of CEA.

[30] P. Mosca *et al.*, "APOLLO3® : Overview of the new code capabilities for reactor physics analysis," in *M&C 2023*, (NIAGARA FALLS, Canada), 2023.

[31] A. Hébert, "Dragon and donjon : A legacy open-source reactor physics project at polytechnique montreal," *Technical Meeting on the Development and Application of Open-Source Modelling and Simulation Tools for Nuclear Reactors, Milan*, 2022.

[32] J. Rhodes, K. Smith, and D. Lee, "Casmo-5 development and applications," *PHYSOR, Vancouver*, 2006.

[33] T. Bahadir and S.-Ö. Lindahl, "Studsvik's next generation nodal code simulate-5," *Advances in Nuclear Fuel Management IV (ANFM 2009)*, 2009.

[34] P. Mosca *et al.*, "Apollo3® : Overview of the new code capabilities for reactor physics analysis," *Nuclear Science and Engineering*, pp. 1–14, 2024.

[35] R. Sanchez, "Assembly homogenization techniques for core calculations," *Progress in Nuclear Energy*, vol. 51, no. 1, pp. 14–31, 2009.

[36] L. Mao and I. Zmijarevic, "A new tone's method in apollo3® and its application to fast and thermal reactor calculations," *Nuclear Engineering and Technology*, vol. 49, no. 6, pp. 1269–1286, 2017. Special Issue on International Conference on Mathematics and Computational Methods Applied to Nuclear Science and Engineering 2017 (MC 2017).

[37] L. Mao, I. Zmijarevic, and R. Sanchez, "A subgroup method based on the equivalent dancoff-factor cell technique in apollo3® for thermal reactor calculations," *Annals of Nuclear Energy*, vol. 139, p. 107212, 2019.

[38] E. Rosier, L. Mao, R. Sanchez, L. Leal, and I. Zmijarevic, "An analysis of a coarse-group subgroup method based on the physical probability tables in apollo3®," *Nuclear Science and Engineering*, pp. 1–14, 2024.

[39] L. Bourhrara, "A new numerical method for solving the boltzmann transport equation using the pn method and the discontinuous finite elements on unstructured and curved meshes," *Journal of Computational Physics*, vol. 397, p. 108801, 2019.

[40] L. Bourhrara, "New variational formulations for the neutron transport equation," *Transport Theory and Statistical Physics*, vol. 33, no. 2, pp. 93–124, 2004.

[41] K. Assogba, L. Bourhrara, I. Zmijarevic, G. Allaire, and A. Galia, "Spherical harmonics and discontinuous galerkin finite element methods for the three-dimensional neutron transport equation : Application to core and lattice calculation," *Nuclear Science and Engineering*, vol. 197, no. 8, pp. 1584–1599, 2023.

[42] K. Assogba, G. Allaire, and L. Bourhrara, "Analysis of a combined spherical harmonics and discontinuous Galerkin discretization for the Boltzmann transport equation." 2023.

[43] E. Masiello, R. Sanchez, and I. Zmijarevic, "New numerical solution with the method of short characteristics for 2-d heterogeneous cartesian cells in the apollo2 code : Numerical analysis and tests," *Nuclear Science and Engineering*, vol. 161, no. 3, pp. 257–278, 2009.

[44] F. Filiciotto, E. Masiello, S. Cochet-Lapuerta, and R. Lenain, "Incomplete parabolic short characteristics in idt," *The International Conference on Mathematics and Computational Methods Applied to Nuclear Science and Engineering, Niagara Falls*, 2023.

[45] E. Masiello, F. Filiciotto, S. Lapuerta-Cochet, and R. Lenain, "Asymptotic expansion of the angular flux applied to discrete-ordinates source iterations in lattice depletion calculations," *Nuclear Science and Engineering*, vol. 197, no. 9, pp. 2404–2424, 2023.

[46] F. Filiciotto, E. Masiello, S. Cochet-Lapuerta, and R. Lenain, "Nonconforming three-dimensional model for pwr control rod movements without homogenization and cusping effect," *Nuclear Science and Engineering*, vol. 197, no. 9, pp. 2425–2445, 2023.

[47] F. Filiciotto, E. Masiello, S. Lapuerta-Cochet, and R. Lenain, "New modelling capabilities in idt," *PHYSOR, Pittsburgh*, 2022.

[48] A. Chetaine, R. Sanchez, and L. Erradi, "The use of the characteristics method to solve the transport equation in unstructured geometries," *Radiation Physics and Chemistry*, vol. 61, no. 3, pp. 763–765.

[49] S. Santandrea, J. C. Jaboulay, P. Bellier, F. Fevotte, and H. Golfier, "Improvements and validation of the linear surface characteristics scheme," *Annals of Nuclear Energy*, vol. 36, no. 1, pp. 46–59.

[50] S. Santandrea and R. Sanchez, "Acceleration techniques for the characteristic method in unstructured meshes," *Annals of Nuclear Energy*, vol. 29, no. 4, pp. 323–352, 2002.

[51] D. Sciannandrone, *Acceleration and higher order schemes of a characteristic solver for the solution of the neutron transport equation in 3D axial geometries*. Theses, Université Paris Sud - Paris XI, 2015.

[52] A.-M. Baudron and J.-J. Lautard, "Minos : A simplified pn solver for core calculation," *Nuclear Science and Engineering*, vol. 155, no. 2, pp. 250–263, 2007.

[53] J.-Y. Moller and J.-J. Lautard, "Minaret, a deterministic neutron transport solver for nuclear core calculations," *International Conference on Mathematics and Computational Methods Applied to Nuclear Science and Engineering, Rio de Janeiro*, 2011.

[54] A.-M. Baudron, J.-J. Lautard, M. Y, and O. Mula, "Minaret : Towards a time-dependent neutron transport parallel solver," in *SNA + MC 2013 - Joint International Conference on Supercomputing in Nuclear Applications + Monte Carlo* (Array, ed.), 2014.

[55] S. Santandrea, R. Sanchez, and P. Mosca, "A linear surface characteristics approximation for neutron transport in unstructured meshes," *Nuclear Science and Engineering*, vol. 160, no. 1, pp. 23–40, 2008.

[56] S. Santandrea, L. Graziano, and D. Sciannandrone, "Accelerated polynomial axial expansions for full 3d neutron transport MOC in the APOLLO3® code system as applied to the ASTRID fast breeder reactor," *Annals of Nuclear Energy*, vol. 113, pp. 194–236.

[57] A. Gammicchia, S. Santandrea, and S. Dulla, "Cross sections polynomial axial expansion within the apollo3® 3d characteristics method," *Annals of Nuclear Energy*, vol. 165, p. 108673, 2022.

[58] R. Sanchez and A. Chetaine, "A synthetic acceleration for a two-dimensional characteristic method in unstructured meshes," *Nuclear Science and Engineering*, vol. 136, no. 1, pp. 122–139, 2000.

[59] S. Santandrea and R. Sanchez, "Analysis and improvements of the dpn acceleration technique for the method of characteristics in unstructured meshes," *Annals of Nuclear Energy*, vol. 32, no. 2, pp. 163–193, 2005.

[60] S. Santandrea, D. Sciannandrone, R. Sanchez, L. Mao, and L. Graziano, "A neutron transport characteristics method for 3d axially extruded geometries coupled with a fine group self-shielding environment," *Nuclear Science and Engineering*, vol. 186, no. 3, pp. 239–276, 2017.

[61] D. Tomatis, F. Bidault, A. Bruneton, and Z. Stankovski, "Overview of serma's graphical user interfaces for lattice transport calculations," *Energies*, vol. 15, no. 4, 2022.

[62] C. Diop and C. Jouanne, *Eléments de physique nucléaire*. EDP sciences, 2024.

[63] B. E. Watt, "Energy spectrum of neutrons from thermal fission of u^{235}," *Phys. Rev.*, vol. 87, pp. 1037–1041, 1952.

[64] L. Cranberg, G. Frye, N. Nereson, and L. Rosen, "Fission neutron spectrum of u^{235}," *Phys. Rev.*, vol. 103, pp. 662–670, 1956.

[65] G. Bell and S. Glasstone, *Nuclear Reactor Theory*. Van Nostrand Reinhold Company, 1970.

[66] A. Hébert, *Applied Reactor Physics*. Cursus (Presses internationales Polytechnique), Presses internationales Polytechnique, 2020.

[67] M. Beni, T. Hau, D. Krstic, D. Nikezic, and P. Yu, "Monte carlo studies on neutron interactions in radiobiological experiments," *PLOS ONE*, vol. 12, p. e0181281, 2017.

[68] C. P. Society. and H. Bateman, *The solution of a system of differential equations occurring in the theory of radioactive transforma- tions, Proceedings - Cambridge Philosophical Society Mathematical and physical sciences*, vol. v.15 (1908-1910). Cambridge [etc.], Cambridge Philosophical Society [etc.]„ 1908. https ://www.biodiversitylibrary.org/bibliography/39008.

[69] S. Lahaye, A. Tsilanizara, P. Bellier, and T. Bittar, "Implementation of a CRAM solver in MENDEL Depletion Code System," in *International Conference on Mathematics and Computational Methods Applied to Nuclear Science and Engineering (M&C - 2017)*, (Jeju, South Korea), 2017.

[70] J. Butcher, *Numerical Methods for Ordinary Differential Equations*. Wiley, 2016.

[71] P. Maria, "Higher-order chebyshev rational approximation method and application to burnup equations," *Nuclear Science and Engineering*, vol. 182, no. 3, pp. 297–318, 2016.

[72] S. Lahaye, P. Bellier, H. Mao, A. Tsilanizara, and Y. Kawamoto, "First verification and validation steps of mendel release 1.0 cycle code system," *PHYSOR, Kyoto*, 2014.

[73] P. Reuss, *Neutron Physics*. Nuclear engineering, EDP Sciences, 2008.

[74] A. Santamarina and N. Hfaiedh, "The shem energy mesh for accurate fuel depletion and buc calculations," *International Conference on Nuclear Criticality-Safety ICNC2007, St-Petersburg*, 2007.

[75] A. Santamarina, C. Collignon, and C. Garat, "French calculation schemes for light water reactor analysis," *PHYSOR, Chicago*, 2004.

[76] A. Hébert and A. Santamarina, "Refinement of the santamarina-hfaiedh energy mesh between 22.5 ev and 11.4 kev," *International Conference on the Physics of Reactors 2008, PHYSOR 08*, vol. 2, pp. 929–938, 2008.

[77] M. Edenius, K. Ekberg, B. H. Forssén, and D. Knott, "Casmo-4, a fuel assembly burnup program, user's manual," *StudsvikoSOA-9501, Studsvik of America, Inc*, 1995.

[78] R. Ferrer and J. Rhodes, "Generation and initial validation of a new casmo5 endf/b-viii.0 nuclear data library," *EPJ Web Conf.*, vol. 247, p. 09001, 2021.

[79] J. L. Conlin, A. Kahler, A. P. McCartney, and D. A. Rehn, "Njoy21 : Next generation nuclear data processing capabilities," *EPJ Web Conf.*, vol. 146, p. 09040, 2017.

[80] C. Mattoon, B. Beck, and G. Gert, "Managing and processing nuclear data libraries with fudge," *EPJ Web of Conf.*, vol. 284, p. 14010, 2023.

[81] M. Coste-Delclaux, C. Jouanne, and C. Mounier, "Current status of the verification and processing system galilÉe-1 for evaluated data," *EPJ Web Conf.*, vol. 239, p. 10002, 2020.

[82] C. Jouanne and M. Coste-Delclaux, "Recent developments in the galilee-1 processing code," *EPJ Web of Conf.*, vol. 294, p. 06003, 2024.

[83] W. Boyd, N. Gibson, B. Forget, and K. Smith, "An analysis of condensation errors in multi-group cross section generation for fine-mesh neutron transport calculations," *Annals of Nuclear Energy*, vol. 112, pp. 267–276, 2018.

[84] S. Choi, K. Smith, H. Kim, T. Tak, and D. Lee, "On the diffusion coefficient calculation in two-step light water reactor core analysis," *Journal of Nuclear Science and Technology*, vol. 54, no. 6, pp. 705–715, 2017.

[85] J. Leppänen, M. Pusa, and E. Fridman, "Overview of methodology for spatial homogenization in the serpent 2 monte carlo code," *Annals of Nuclear Energy*, vol. 96, pp. 126–136, 2016.

[86] E. Dorval, "Directional diffusion coefficients and leakage-corrected discontinuity factors : Implementation in serpent and tests," *Annals of Nuclear Energy*, vol. 87, pp. 101–112, 2016.

[87] E. Larsen, "Asymptotic diffusion limits of the multigroup neutron transport equations," *Nuclear Science and Engineering*, vol. 197, no. 2, pp. 145–163, 2023.

[88] W. Wu, G. Giudicelli, K. Smith, B. Forget, D. Yao, and Q. Luo, "Improvements of the cmfd acceleration capability of openmoc," *Nuclear Engineering and Technology*, vol. 52, no. 10, pp. 2162–2172, 2020.

[89] M. J. Halsall, "The wims subgroup method for resonance absorption," *Transactions of the American Nuclear Society*, vol. 72, 1995.

[90] N. Sugimura and A. Yamamoto, "Resonance treatment based on ultra-fine-group spectrum calculation in the aegis code," *Journal of Nuclear Science and Technology*, vol. 44, no. 7, pp. 958–966, 2007.

[91] H. Lee, C. Lim, and H. Joo, "Improvement to the resonance calculation using energy spectrum expansion method for direct whole-core calculation," *The International Conference on Mathematics and Computational Methods Applied to Nuclear Science and Engineering, Niagara Falls*, 2023.

[92] A. Hébert, "A collision probability formulation of the resonance spectrum expansion (rse) self-shielding method," *PHYSOR, San Francisco*, 2024.

[93] K. S. Smith, "Nodal method storage reduction by nonlinear iteration," *Trans. Am. Nucl. Soc.; (United States)*.

[94] J. Cho, H. Joo, K. S. Kim, and S. Zee, "Cell based cmfd formulation for acceleration of whole-core method of characteristics calculations," *Nuclear Engineering and Technology*, vol. 34, 2002.

[95] A. Z. M. Jarrett, B. Kochunas and T. Downar, "Analysis of stabilization techniques for cmfd acceleration of neutron transport problems," *Nuclear Science and Engineering*, vol. 184, no. 2, pp. 208–227, 2016.

[96] M. L. Adams and E. W. Larsen, "Fast iterative methods for discrete-ordinates particle transport calculations," *Progress in Nuclear Energy*, vol. 40, no. 1, pp. 3–159.

[97] S. Santandrea, "An integral multidomain dpn operator as acceleration tool for the method of characteristics in unstructured meshes," *Nuclear Science and Engineering*, vol. 155, no. 2, pp. 223–235, 2007.

[98] E. Larsen, "Diffusion-synthetic acceleration methods for the discrete-ordinates equations." Publication Title : American Nuclear Society topical conference on computational methods, Salt Lake City, UT, USA, 28 Mar 1983 Type : Article.

[99] I. R. Suslov, "Solution of transport in 2- and 3-dimensional irregular geometry by the method of characteristics," in *International Conference on Mathematical Methods and Supercomputing in Nuclear Applications*, 1993.

[100] R. L. Tellier and A. Hébert, "An improved algebraic collapsing acceleration with general boundary conditions for the characteristics method," *Nuclear Science and Engineering*, vol. 156, no. 2, pp. 121–138, 2007.

[101] K. M. Khattab and E. W. Larsen, "Synthetic acceleration methods for linear transport problems with highly anisotropic scattering," *Nuclear Science and Engineering*, vol. 107, no. 3, pp. 217–227, 1991.

[102] E. W. Larsen and B. W. Kelley, "The relationship between the coarse-mesh finite difference and the coarse-mesh diffusion synthetic acceleration methods," *Nuclear Science and Engineering*, vol. 178, no. 1, pp. 1–15, 2014.

[103] W. S. Y. Guangchun Zhang, Albert Hsieh and Y. S. Jung, "Consistent pcmfd acceleration schemes of the three-dimensional transport code proteus-moc," *Nuclear Science and Engineering*, vol. 193, no. 8, pp. 828–853, 2019.

[104] Y. Chan and S. Xiao, "Implementation and performance study of lpcmfd acceleration method for multi-energy group k-eigenvalue neutron transport problem in hexagonal geometry," *Annals of Nuclear Energy*, vol. 139, p. 107220, 2020.

[105] Y. Chan and S. Xiao, "Convergence study of variants of cmfd acceleration schemes for fixed source neutron transport problems in 2d cartesian geometry with fourier analysis," *Annals of Nuclear Energy*, vol. 134, pp. 273–283, 2019.

[106] H. Joo, J. Cho, K. S. Kim, C. Lee, and S. Zee, "Methods and performance of a three-dimensional whole-core transport code decart," *Proceedings of the PHYSOR 2004 : The Physics of Fuel Cycles and Advanced Nuclear Systems - Global Developments*, 2004.

[107] J. Cho, K. Kim, C. Lee, S. Zee, and H. Joo, "Axial spn and radial moc coupled whole core transport calculation," *Journal of Nuclear Science and Technology*, vol. 44, no. 9, pp. 1156–1171, 2007.

[108] J. Y. S. L. C. H. Ryu, Min and H. G. Joo, "Incorporation of anisotropic scattering in ntracer," *Transactions of the Korean Nuclear Society*, 2014.

[109] Y. S. Jung, C. B. Shim, C. H. Lim, and H. G. Joo, "Practical numerical reactor employing direct whole core neutron transport and subchannel thermal/hydraulic solvers," *Annals of Nuclear Energy*, vol. 62, pp. 357–374, 2013.

[110] K. M. Kim, J. Lee, N. Choi, and H. Joo, "Performance assessment of gpu-based ntracer/escot coupled simulations," *Transactions of the Korean Nuclear Society*, 07 2020.

[111] S. Choi, A. Fitzgerald, N. Herring, and B. Kochunas, "Linear source approximation in mpact for efficient and robust multiphysics whole-core simulations," *Nuclear Science and Engineering*, vol. 198, no. 4, pp. 914–944, 2024.

[112] E. Larsen, B. Collins, B. Kochunas, A. Graham, and S. Stimpson, "Mpact theory manual (v.4.3),"

[113] B. Collins, S. Stimpson, B. W. Kelley, M. T. H. Young, B. Kochunas, A. Graham, E. W. Larsen, T. Downar, and A. Godfrey, "Stability and accuracy of 3d neutron transport simulations using the 2d/1d method in MPACT," *Journal of Computational Physics*, vol. 326, pp. 612–628.

[114] B. Yee, E. Larsen, and B. Kochunas, "An analytical derivation of transport-corrected p0 cross sections and diffusion coefficients," *PHYSOR*, 05 2016.

[115] G. Gunow, B. Forget, and K. Smith, "Stabilization of multi-group neutron transport with transport-corrected cross-sections," *Annals of Nuclear Energy*, vol. 126, pp. 211–219, 2019.

[116] G. Giudicelli, A. Lindsay, L. Harbour, C. Icenhour, M. Li, J. E. Hansel, P. German, P. Behne, O. Marin, R. H. Stogner, J. M. Miller, D. Schwen, Y. Wang, L. Munday, S. Schunert, B. W. Spencer, D. Yushu, A. Recuero, Z. M. Prince, M. Nezdyur, T. Hu, Y. Miao, Y. S. Jung, C. Matthews, A. Novak, B. Langley, T. Truster, N. Nobre, B. Alger, D. Andrš, F. Kong, R. Carlsen, A. E. Slaughter, J. W. Peterson, D. Gaston, and C. Permann, "3.0 - MOOSE : Enabling massively parallel multiphysics simulations," *SoftwareX*, vol. 26, p. 101690, 2024.

[117] J. R. Tramm, K. S. Smith, B. Forget, and A. R. Siegel, "The random ray method for neutral particle transport," *Journal of Computational Physics*, vol. 342, pp. 229–252, 2017.

[118] J. R. Tramm, K. S. Smith, B. Forget, and A. R. Siegel, "Arrc : A random ray neutron transport code for nuclear reactor simulation," *Annals of Nuclear Energy*, vol. 112, pp. 693–714, 2018.

[119] M. A. Kowalski, P. Cosgrove, J. Broman, and E. Shwageraus, "Scone : A student-oriented modifiable monte carlo particle transport framework," *Journal of Nuclear Engineering*, vol. 2, no. 1, pp. 57–64, 2021.

[120] P. Cosgrove and J. R. Tramm, "The random ray method versus multigroup monte carlo : The method of characteristics in openmc and scone," *Nuclear Science and Engineering*, vol. 0, no. 0, pp. 1–20, 2023.

[121] R. L. Tellier and A. Hébert, "Anisotropy and particle conservation for trajectory-based deterministic methods," *Nuclear Science and Engineering*, vol. 158, no. 1, pp. 28–39, 2008.

[122] R. Sanchez, L. Mao, and S. Santandrea, "Treatment of boundary conditions in trajectory-based deterministic transport methods," *Nuclear Science and Engineering*, vol. 140, no. 1, pp. 23–50, 2002.

[123] A. L. Bars, A. Gammicchia, and S. Santandrea, "Optimizations of the accelerated axial polynomial method of characteristics of the apollo3® deterministic neutron transport code," *Nuclear Science and Engineering*, pp. 1–16, 2024.

[124] M. Tiberga and S. Santandrea, "A novel high-order surface characteristics scheme for the neutron transport equation in 2d unstructured meshes," *Nuclear Science and Engineering*, vol. 198, 2023.

[125] A. Le Bars, A. Gammicchia, and S. Santandrea, "Optimizations of the accelerated axial polynomial method of characteristics of the apollo3® deterministic neutron transport code," *Nuclear Science and Engineering*, pp. 1–16, 2024.

[126] S. Santandrea, D. Sciannandrone, R. Sanchez, L. Mao, and L. Graziano, "A neutron transport characteristics method for 3d axially extruded geometries coupled with a fine group self-shielding environment," *Nuclear Science and Engineering*, vol. 186, no. 3, pp. 239–276.

[127] H. A. van der Vorst, "Bicgstab : A fast and smoothly converging variant of bi-cg for the solution of nonsymmetric linear systems," *SIAM Journal on Scientific and Statistical Computing*, vol. 13, no. 2, pp. 631–644, 1992.

[128] Y. Saad, *Numerical Methods for Large Eigenvalue Problems : Revised Edition*. Classics in Applied Mathematics, Society for Industrial and Applied Mathematics, 2011.

[129] S. Santandrea, "Personal communication on the comparison in computation time between the bicgstab and gmres solvers for solving the synthetic problem," 2024.

[130] A. Santamarina, N. Hfaiedh, R. Letellier, V. Marotte, S. Misu, A. Sargeni, C. Vaglio, and I. Zmijarevic, "Advanced neutronics tools for bwr design calculations," *Nuclear Engineering and Design*, vol. 238, no. 8, pp. 1965–1974, 2008. ICONE-14 - 14th International Conference on Nuclear Energy.

[131] A. Santamarina, D. Bernard, P. Blaise, M. Coste, A. Courcelle, T. Huynh, C. Jouanne, P. Leconte, O. Litaize, S. Mengelle, G. Noguere, J. Ruggieri, O. Serot, J. Tommasi, C. Vaglio-Gaudard, and J.-F. Vidal, "The jeff-3.1.1 nuclear data library. validation results from jef-2.2 to jeff-3.1.1," *OECD 2009 NEA No. 6807, ISBN 978-92-64-99074-6*, 2009.

[132] Truffinet, Olivier, Ammar, Karim, Argaud, Jean-Philippe, Gérard Castaing, Nicolas, and Bouriquet, Bertrand, "Multi-output gaussian processes for the reconstruction of homogenized cross-sections," *EPJ Web Conf.*, vol. 302, p. 02006, 2024.

[133] N. Horelik, B. Herman, B. Forget, and K. Smith, "Benchmark for evaluation and validation of reactor simulations," *International Conference on Mathematics and Computational Methods Applied to Nuclear Science and Engineering, Sun Valley, ID*, 2013.